UNIVERSITY OF CALIFORNIA, SAN DIEGO

Dissociation Dynamics of Transient Molecules Studied by Photoelectron-Photofragment Coincidence Spectroscopy

A dissertation submitted in partial satisfaction of the requirements

for the degree Doctor of Philosophy

in

Chemistry

by

Amelia W. Ray

Committee in charge:

Professor Robert E. Continetti, Chair
Professor Tadeusz F. Molinski
Professor Kimberly A. Prather
Professor Kalyanasundaram Seshadri
Professor Amitabha Sinha

2016

The Dissertation of Amelia W. Ray is approved and it is acceptable in quality and form for publication on microfilm and electronically:

_____

_____

_____

_____

_____

Chair

University of California, San Diego

2016

DEDICATION

To my family John Ray, Linda Wolpert,

Peter Ray and Hillary Henthorn

TABLE OF CONTENTS

LIST OF FIGURES

LIST OF TABLES

ACKNOWLEDGEMENTS

Many people have offered help, guidance and support along the way. First and foremost I would like to thank my advisor Bob Continetti. He took me into his lab and helped me grow as both a person and a scientist. I was honestly quite intimidated by our lab when I first joined as a rotation student, but Bob made it easy to find a home on campus. I am especially grateful that he was around when needed to offer an extra set of hand, a piece of advice or to sit down and have a conversation about the data. Sometimes he was too much in our hair, but I'll take that over the alternative. Also thank you for fixing the laser after we flooded it, my PhD would have taken far longer otherwise.

I would also especially like to thank the Continetti lab members past and present. When I first joined the lab Berwyck Poad was kind enough to take me under his wing and teach me how to run Machine C and the laser, while Chris Johnson offered wisdom and guidance on how to navigate our lab. I would not have been able to complete this dissertation without Ben Shen who was by my side fixing Machine C when it was broken (often) and helping me run the machine overnight when needed. I could always count on his calm demeanor to keep me grounded, and I very much appreciate the sound boarding and coffee walks. Rico Otto was instrumental in the implementation of the IR laser system and we had a good time working together on the machine. I was sad to lose him first to the back room and then to Illumina, but I know he's off doing good work and I wish him continued success. I've enjoyed working with Katharine Lunny and Yanice Benitez, who were unlucky enough to spend their first year in the lab fixing the EIBT. May the rest of your graduate careers be less eventful and more productive, and may the machine treat you kindly.

I also enjoyed working with other members of the Continetti lab. Although their time in our lab was short, I wish Joel Rivera and Jen Daluz all the best and I'm happy you both found a good lab home. Although our projects are quite different, I have learned a lot from the AIM team including Morgan Miller, Katherine Nadler and, more recently, Brian Adamson. I always enjoyed trying out new puns on both Morgan and Brian, and my students appreciate it too I'm sure. I've enjoyed conversations with Jemma Gibbard and I hope Machine A continues to treat her well. Finally, our staff scientist Joseph Taulane for his kind feedback and technical knowhow. I always appreciated that he never assumed I couldn't help move heavy things, even if I was sore the next day.

I also need to thank the various people on campus who have helped with the logistics side of my time in graduate school. I always enjoyed my conversations with Carmen Alfaro and appreciated her work as our program assistant. Everyone in the Chemistry office, in particular Jeanine for keeping us all on track and Jeff for always having time to help me out, even when it wasn't technically his job. I also thank the guys in the machine shop, in particular Don and Bob, for keeping an eye on all of us and for saving my butt more than once when we didn't have the right tool or part.

Additionally I would like to thank our theory collaborators. I have very much enjoyed the rich back and forth our work has provided. In particular, Hua Guo's lab for their quantum dynamics work and our continued collaborative efforts, and Jay Agarwal and H. F. Schaefer for their work on the F + $HOCH_3$ system. Finally, Andrew Cooksy and John Stanton for their work on the propiolyl system, including many good conversations.

Finally I would like to thank my family and friends who have supported me along the way. My parents always encouraged me to aim high, while my brother and his wife Hillary are always good for a sympathetic ear. Among others, Don, Noelle, Lizzy, Michelle, Thien, and Kate have all been there when I needed them and I really enjoyed our monthly dinner parties. Alix and Jerome for reminding me to go outside from time to time. Sharon for encouraging me to come here to UCSD and helping me navigate around San Diego when I got here. Libby and Jeff for helping to keep the process fun and offering me a place to stay when things got really tough. I love you all and thank you.

Chapter 3, in full, is a reprint of the material as it appeared in Ray, A. W.; Shen, B. B.; Poad, B. L. J.; Continetti, R. E. "State-Resolved Predissociation Dynamics of the Formyloxyl Radical," *Chemical Physics Letters*, 2014, *592*, 30–35; doi:10.1016/j.cplett.2013.11.06. The dissertation author is the primary author and the dissertation advisor is the corresponding author.

Chapter 6, in full, is a reprint of the material as it appeared in Ray, A. W.; Agarwal, J.; Shen, B. B.; Schaefer, H. F.; Continetti, R. E. "Energetics and Transition-State Dynamics of the F + $HOCH_3$ → HF + OCH_3 Reaction," *Physical Chemistry Chemical Physics*, in press (2016); doi: 10.1039/c6cp06409d. The dissertation author is the primary author and the dissertation advisor is the corresponding author.

VITA

2007	Bachelor of Arts, Scripps College
2008 – 2010	Research Assistant, University of San Francisco
2010	Master of Science, University of San Francisco
2010 – 2016	Research Assistant, University of California, San Diego
2016	Doctor of Philosophy, University of California, San Diego

PUBLICATIONS

Ray, A. W.; Otto, R.; Continetti, R. E. "Effects of Vibrational Excitation on the F + $H_2O \rightarrow FH + OH$ Reaction: Dissociative Photodetachment of Overtone-Excited $[F–H–OH]^-$," *In preparation.*

Ray, A. W.; Rabidoux, S. M.; Ichino, T.; Stanton, J. F.; Cooksy, A.; Continetti, R. E. "Dissociative Photodetachment of $HC_3O_2^-$ and stability of the Propiolyl Radical HC_3O_2," *In preparation.*

Otto, R.; Ma, J.; Ray, A. W.; Li, J. Guo, H.; Continetti, R. E. "Imaging the Dynamics of a Four-Atom System: Experimental and Theoretical Studies of the Dissociative Photodetachment of the Isotopologs of $F^-(H_2O)$," *In preparation.*

Ray, A. W.; Agarwal, J.; Shen, B. B.; Schaefer, H. F.; Continetti, R. E. "Energetics and Transition-State Dynamics of the the F + $HOCH_3 \rightarrow HF + OCH_3$ Reaction," *Physical Chemistry Chemical Physics*, in press (2016); doi: 10.1039/c6cp06409d.

Otto, R.; Ray, A. W.; Daluz, J. S.; Continetti, R. E. "Direct IR Excitation in a Fast Ion Beam: Application to NO^- Photodetachment Cross Sections," *EPJ Techniques and Instrumentation*, 2014, *1:3*; doi: 10.1186/epjti3

Otto, R.; Ma, J.; Ray, A. W.; Daluz, J. S.; Li, J.; Guo, H.; Continetti, R. E. "Imaging Dynamics on the F + $H_2O \rightarrow HF + OH$ Potential Energy Surfaces from Wells to Barriers," *Science*, 2014, *343*, 396–399; doi:10.1126/science.1247424

Ray, A. W.; Shen, B. B.; Poad, B. L. J.; Continetti, R. E. "State-Resolved Predissociation Dynamics of the Formyloxyl Radical," *Chemical Physics Letters*, 2014, *592*, 30–35; doi:10.1016/j.cplett.2013.11.06

Poad, B. L. J.; Ray, A. W.; Continetti, R. E. "Dissociative Photodetachment of the Ethoxide Anion and Stability of the Ethoxy Radical $CH_3CH_2O^{\bullet}$," *Journal of Physical Chemistry A*, 2013, *117*, 12035–12041; doi:10.1021/jp404343w

Ray, A. W.; Taatjes, C. A.; Welz, O.; Osborn, D. L.; Meloni, G. "Synchrotron Photoionization Measurements of OH-initiated Cyclohexene Oxidation: Ring-Preserving Products in OH + Cyclohexene and Hydroxycyclohexyl + O_2 Reactions," *Journal of Physical Chemistry A*, 2012, *116*, 6720–6730; doi: 10.1021/jp3022437

FIELDS OF STUDY

Major Field: Physical Chemistry

Studies in Organic Chemistry
Professor Thomas Poon, Scripps College

Studies in Physical Chemistry
Professor Giovanni Meloni, University of San Francisco

Studies in Physical Chemistry
Professor Robert E. Continetti, University of California, San Diego

ABSTRACT OF THE DISSERTATION

Dissociation Dynamics of Transient Molecules Studied by Photoelectron-Photofragment Coincidence Spectroscopy

by

Amelia W. Ray

Doctor of Philosophy in Chemistry

University of California, San Diego, 2016

Professor Robert E. Continetti, Chair

As the simplest carboxyl free radical the formyloxyl radical, HCO_2, serves as a prototype for more complex carboxyl free radicals such as CH_3CO_2, $C_6H_5CO_2$ and HC_2CO_2. It is also an intermediate in the OH + CO ⟶ H + CO_2 reaction, of increasing interest for both atmospheric and combustion chemistry. The predissociation dynamics for the $DCO_2^- + h\nu \rightarrow D + CO_2 + e^-$ reaction were studied by DPD of DCO_2^-.

Photodetachment near threshold (hν = 4.27 eV) accesses all three of the lowest-lying electronic states ($^2B_2$, $^2A_1$, and $^2A_2$) of the formyloxyl radical. The photoelectron spectrum indicates vibrational excitation dominated by the O–C–O bending mode in the $^2A_1$. In the PPC spectra for DCO_2^-, each vibrational state of the nascent neutral is coupled to bending excitation in the resulting CO_2 product observed in the eKE-gated state-resolved translational energy distribution. Each CO_2 product-state distribution exhibits a substantial level of bending excitation, more than predicted by recent quantum-dynamics calculations on an *ab initio* potential energy surface.

Extending our work on carboxyl free radicals, the dissociation dynamics of the propiolyl radical, $HCCCO_2$, and its related isomer $CCCO_2H$ were studied by DPD of their respective anions using PPC spectroscopy. At hν = 4.27 eV, the $HCCCO_2^-$ anions is found to readily dissociate to HCC + CO_2. Similar to the formyloxyl radical, dissociation to HCC + CO_2 results in a series of resolved peaks in the translational energy release spectrum corresponding to the O–C–O bending mode in the CO_2 fragment. The isomeric $CCCO_2H$ were not observed. High level *ab initio* calculations and Franck-Condon simulations were carried out to reproduce the stable photoelectron spectrum.

Extending the recent work on the F + H_2O benchmark F initiated hydrogen abstraction reaction, the effects of vibrational excitation of the precursor anion was explored. To carry out this experiment, an IR laser was coupled into the existing PPC spectrometer using a mirror on the existing neutral beam block. Excitation of the internal hydrogen bond F—H—OH of the anion causes a noticeable change in dissociation dynamics, increasing access to the HF + OH products. Finally, the effects of

intramolecular vibrational relaxation of the excited anions was explored by looking at how the anions aged during confinement in the electrostatic ion beam trap.

Finally, the $F + HOCH_3 \rightarrow HF + OCH_3$ reaction was studied; expanding our work on F initiated hydrogen abstraction reactions. The HF product is formed with considerable excitation while the OCH_3 product behaves as a spectator to the reaction. Both the metastable reactant channel van der Waals complex and stable product hydrogen bonded complexes were observed, along with a series of long-lived metastable vibrational Feshbach resonances.

Chapter 1 : Introduction and Background

The second industrial revolution was spurred by the introduction of the internal combustion engine in the 19th century, dramatically changing the world. At the time, knowledge of the complex chemistry of combustion and the effects of resulting pollutants on our atmosphere was largely limited to the basic definition of combustion:

$$\text{Fuel} + \text{Air} \rightarrow \text{Heat} + CO_2 + \text{Water} \qquad (1.1)$$

In practice, however, combustion is far more complex than this basic definition suggests, actually comprising hundreds of different free radical reactions. Furthermore, incomplete combustion can result in complex pollutants entering the atmosphere where they can continue to react. Thus, although combustion and atmospheric reactions occur at noticeably different pressure and temperature regimes, they have many free radicals and short-lived species in common. As we continue to develop ever-more-efficient engine technologies, explore alternative fuels, and deal with climate change, it is important that we strive to gain insight into not just which chemical reactions are important, but how they proceed. This second criteria is covered by the field of dynamics, which provides a molecular-level description of a chemical reaction.

Recent strides in the theoretical realms of quantum dynamics and high-accuracy, sophisticated computational methods make the need for good fundamental experimental observation more important than ever. To date, three-atom systems, such as the elementary atom-diatom reaction $F + H_2 \rightarrow FH + H$,[1-3] have been the most fruitful

experimental proving grounds for theory, resulting in fairly detailed quantum mechanical understanding of these systems. Expansion of the experimental proving ground to larger systems, however, is problematic. This is because system complexity, taken as the number of degrees of freedom or the number of coordinates needed to fully describe a system, grows as $3N - 6$ for non-linear systems ($3N - 5$ for linear systems) where the number of atoms is N, and so increases dramatically with increasing number of atoms. By this reckoning, three-atom systems of course have at minimum three degrees of freedom. Four-atom systems are far more complex, with six degrees of freedom, and represent the current frontier for quantum dynamics. For such systems, detailed experimental observables such as product energetics, branching ratios, and general reaction dynamics of key benchmark systems are needed as tests for quantum chemical and dynamics theories.

To this aim, this thesis focuses on the experimental study of energetics and reaction dynamics of small transient neutral species, relevant to atmospheric and combustion processes, that represent ideal candidates for comparison to theory. Specifically, focus is on simple carboxyl free radicals and hydrogen abstraction by fluorine reactions, which proceed through both reactant and product complexes and a shared-hydrogen F−H−X intermediate. This first chapter outlines methods and techniques used to study reactive species, including an overview of our experimental approach that combines anion photoelectron spectroscopy with photofragment translational spectroscopy in coincidence using the technique of photoelectron-photofragment coincidence (PPC) spectroscopy.[4, 5]

1.1. Short-Lived Species: Reactive Free Radicals and Reaction Intermediates

The transient species discussed in this thesis fall into two categories: reactive free radicals and reaction intermediates. Free radicals are atoms and molecules with an unpaired electron — like the ·OH radical, which is known to be particularly important in initiation of free radical reactions in both the atmosphere and combustion. The carboxyl free radicals discussed in Chapters 3 and 4 are examples of free radicals with an unpaired electron localized on the carboxyl group, giving rise to multiple low-lying electronic states depending on the location of the unpaired electron.

For reaction intermediates, it is useful to consider the following generic chemical reaction:

$$AB + C \rightarrow [ABC] \rightarrow A + BC \tag{1.2}$$

where A, B, and C are atoms or molecules and [ABC] is either the activated complex/transition state or a reaction intermediate. The difference between a transition state and a reaction intermediate is as follows. A transition state has a lifetime on the order of just a single molecular vibration and exists at a potential energy maximum on the potential energy surface (PES). A reaction with a transition state is considered to be an elementary reaction that cannot be broken down into simpler reaction steps. In contrast, a reaction intermediate has a lifetime appreciably longer than a single molecular vibration. Common types of reaction intermediates include van der Waals (vdW) complexes (consisting of atoms and/or molecules bound by weak van der Waals forces) and

hydrogen-bonded complexes. A reaction with a reaction intermediate is considered to be a stepwise combination of elementary reactions. Unlike a transition state, a reaction intermediate appears as a global or local minimum on the PES. The presence of a reaction intermediate can dramatically influence the overall dynamics and kinetics of a reaction.

1.2. Experimental Techniques for Studying Reaction Intermediates and Free Radicals

Due to their short lifetimes, transient reaction intermediates and free radicals can be difficult to study directly. Traditional approaches have focused largely on bulk observations or kinetic measurements, inferring the presence of a reaction intermediate based on appearance of certain products and/or rates at which a specific product appears. Recent advances in ion-beam and ion-imaging technology have made it possible to study individual reactions or dissociation events, gaining important information on the dynamics of such systems. Supersonic sources, for example, allow for the production of both fast *and* very cold molecular beams.[6] These work by passing gases from high pressure to low pressure though a small nozzle producing a hydrodynamic flow. As a result, the molecules are accelerated in the forward direction with a net transfer of energy from translational and internal degrees of freedom into this forward acceleration to produce a cold molecular beam.

Current experimental dynamics techniques include, but are not limited to, molecular beam scattering, state-resolved spectroscopic techniques, and precursor-ion neutralization techniques.[7] These last techniques are the focus of this thesis and will be discussed in more detail below. Briefly, many free radicals can be stabilized by the addition/removal of an electron to form a closed-shell anion/cation and these transient

neutrals can then be probed using various techniques. For example, anion precursors can be probed using a fixed-wavelength laser to eject a photoelectron as is done in photoelectron spectroscopy,[8] discussed in detail in Section 1.3. Alternatively, cation precursors can be neutralized by either dissociative recombination[9] or charge exchange[10] which, like anion photoelectron spectroscopy, probes the neutral PES.

1.3. Photoelectron Spectroscopy

Anion photoelectron spectroscopy has proven to be a useful technique for studying short-lived or unstable species.[11-14] Here, negative ions are probed using a pulsed laser at a fixed wavelength with sufficient energy to neutralize the anion as follows:

$$ABC^- \xrightarrow{h\upsilon} ABC + e^- \tag{1.3}$$

Although limited to systems with a stable anion, the additional stability gained by neutralization can greatly extend species lifetimes, and has the added benefit that the species can be steered and manipulated in the usual ways. Although excess energy can partition into internal energy in the resulting neutral, the bulk typically partitions into the departing photoelectron in the form of kinetic energy as follows:

$$eKE = h\upsilon - AEA - E_{int} \tag{1.4}$$

where eKE is electron kinetic energy, AEA is adiabatic electron affinity, and E_{int} is internal energy. The eKE and photoelectron angular distribution (PAD) of the resulting photoelectron are measured, providing information on the AEA and E_{int} partitioning in the resulting neutral. This technique can, in principle, be performed on any stable anion

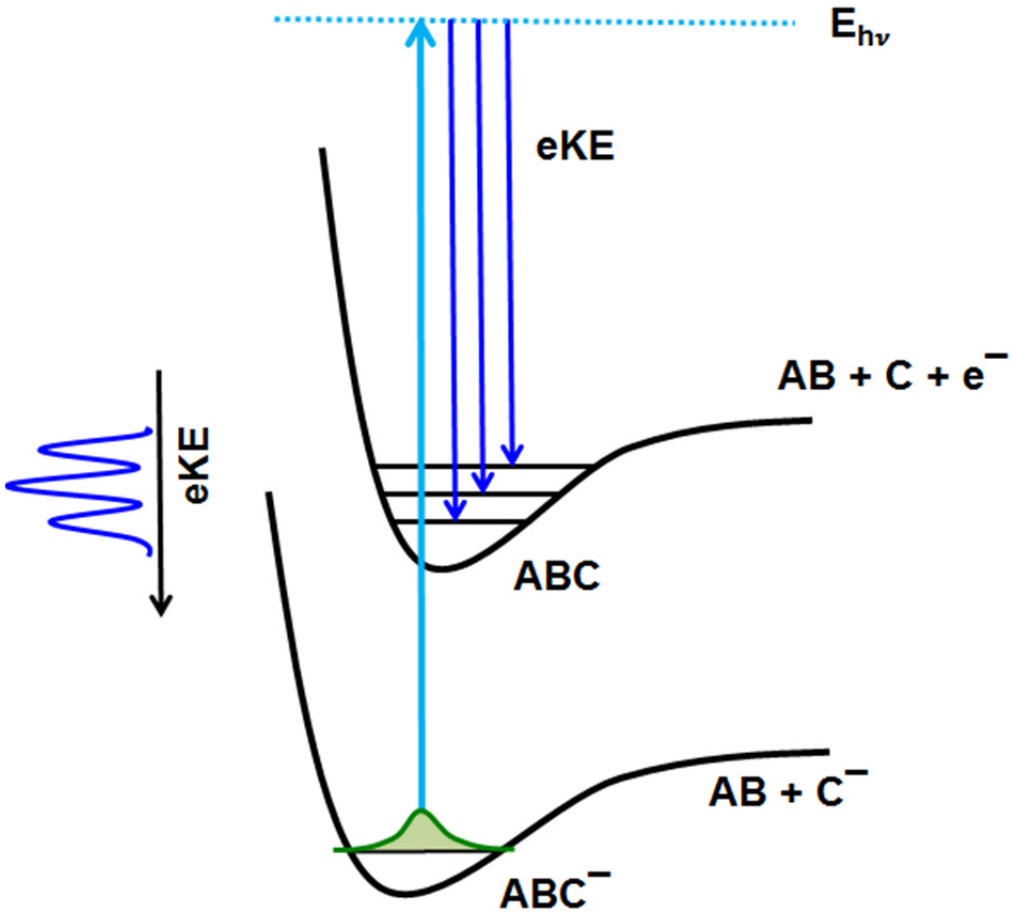

Figure 1.1. Principle of anion photoelectron spectroscopy. Absorption of a photon (light blue) produces a neutral product and a photoelectron that carries away excess energy (dark blue). The resulting photoelectron spectrum is shown to the left.

with a positive AEA, making it ideal for probing free radicals and even some closed-shell molecules.

Anion photoelectron spectroscopy is shown schematically in Figure 1.1 for direct photodetachment, where the resulting neutral surface is bound. The experimental photoelectron spectrum, plotted vertically along the energy axis, provides information on internal energy partitioning into vibrational and rotational degrees of freedom. In this case, information on the accessible vibrational modes can be extracted by looking at the relative peak positions in the resulting spectrum, while unresolved rotational excitation contributes to peak width. Although peak spacing provides direct information on the neutral, peak intensities are more complicated because they depend on both the anion and neutral potential energy surfaces, and need to be discussed in more detail.

The Franck-Condon principle states that electronic transitions occur nearly instantaneously relative to nuclear motion, and thus nuclei can be treated as "frozen" during electronic transitions.[15, 16] Schematically, the electronic transition is represented by a vertical arrow in Figure 1.1, and the geometry of the lower-energy electronic state (anion in this case) is projected onto that of the higher-energy electronic state (neutral). Combining the Franck-Condon principle with the Born-Oppenheimer approximation,[17] which states that wavefunctions for nuclear and electronic components are separable ($\psi_{en} = \psi_e \psi_n$), the intensity of an electronic transition can be described by the overlap of anion and neutral electronic wavefunctions (ψ'_{el} and ψ_{el}):

$$I = \int \psi'^{*}_{el} \, \mu_{el} \psi_{el} d\tau_e \int S'^{*}_{vib} S_{vib} \, dR \qquad (1.5)$$

where the first integral is the electronic-transition dipole moment and the second integral is the vibrational-overlap integral. The first integral generally implies the electronic-dipole transition selection rule of $\Delta l = \pm 1$, although this is only rigorously defined for atomic systems and is relaxed for molecular systems. The second integral in equation 1.5 governs the intensity of each vibronic transition, and its square is called the Franck-Condon (FC) factor. That is, the square of the electronic-transition dipole moment dictates the intrinsic strength of the electronic transition, while FC factors govern the distribution of this intensity among the vibrational states on the higher-energy electronic surface. The selection rules for vibrational transitions in electronic spectroscopy are $\Delta n = 0, \pm 1, \pm 2, \ldots$ where, in the absence of vibronic interactions, only totally symmetric modes will produce a non-zero transition moment integral. This means, for example, that bending modes with odd quanta will not be populated, as was seen in the early quantum dynamics simulations of the formyloxyl radical.[18] These selection rules are relaxed from the purely vibrational spectroscopy case as S'_{vib} and S_{vib} represent vibrational wavefunctions for different electronic states, making the overlap integral non-zero for a larger number of conditions.

FC factors are depicted schematically in Figure 1.2. In particular, this figure shows how sensitive these factors are to overlap in geometry between the two electronic states. When anion and neutral geometries are very similar, as for the ground electronic state in Figure 1.2, FC overlap between the two states should be excellent. As a result, intense peaks will be observed for the ground state $0 \leftarrow 0$ and other $\Delta v = 0$ transitions such as $1 \leftarrow 1$, $2 \leftarrow 2$, and so on. As an experimental note, the contribution of the $1 \leftarrow 1$

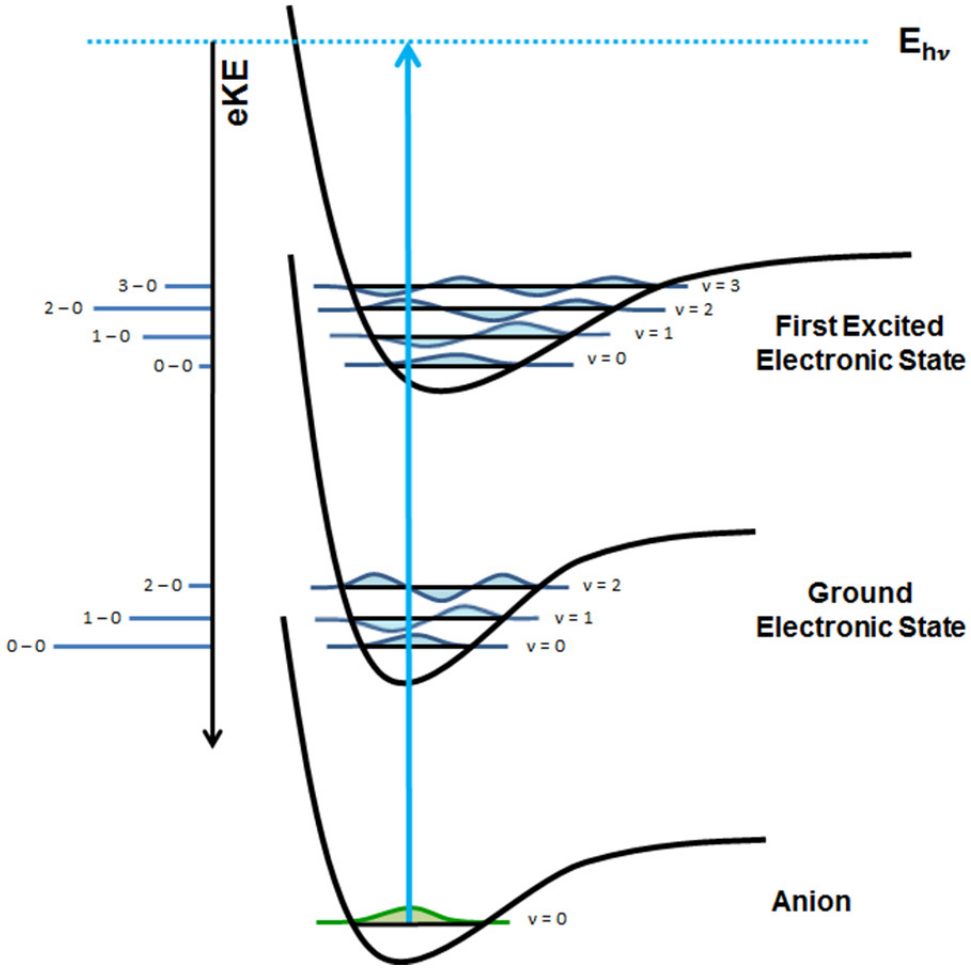

Figure 1.2. Schematic diagram illustrating Franck-Condon factors, represented as vibrational stick structures along the left side, for two different electronic states. The ground electronic state is depicted with good geometry overlap (middle) while the first excited electronic state is depicted with relatively poor geometry overlap (upper). The most intense transitions are, for the first case, the 0–0 transition and, for the second case, the 2–0 transition.

and other transitions from excited vibrational levels in the anion, collectively referred to as "hot bands," should be minor as long as cold precursor anions are used. In contrast, when anion and neutral geometries are considerably different, as for the excited electronic state in Figure 1.2, the intensity of the $\Delta v = 0$ transitions may be quite small and the most intense transition may no longer be to the ground vibrational state. Thus, in addition to obtaining useful information about the vibrational states of the neutral potential energy surface, photoelectron spectroscopy also allows for valuable comparison of anion and neutral geometries.

Recent improvements in photoelectron spectroscopy resolution have been achieved using two new technologies: the technically challenging anion zero electron kinetic energy (ZEKE) spectroscopy and the more versatile slow electron velocity-map imaging (SEVI) spectroscopy.[19] With ZEKE, a tunable laser is used for photodetachment near the threshold for ion-neutral transitions and only those electrons with nearly zero kinetic energy are detected. Although energy resolution better than 1 meV has been achieved, [20] this technique is applicable only to a limited number of anions due to the near-threshold nature of the experiment.[11, 21] With SEVI, photoelectrons are collected over a greater, though still narrow, energy range to produce a high-resolution spectrum (2 – 3 meV). Spectra are taken over a discrete number of detachment wavelengths and then "stitched" together to form a composite spectrum. SEVI is applicable to a broader range of species than is ZEKE, while still providing enhanced resolution compared to more traditional photoelectron spectroscopy. The near threshold approach of SEVI has been

utilized to good effect in our PPC experiment,[22] but with smaller gains in resolution owing to the experimental constraints imposed by coincidence measurements.

1.4. Cross Sections and Photoelectron Angular Distributions

The probability of observing the bound-free transition from an anion to the corresponding neutral and free electron is given by the photodetachment cross section, which corresponds to the sum of all allowed transitions (vibronic and electronic) at a given wavelength and, in general, increase monotonically with energy above threshold. Near threshold, Wigner[23] showed that the energy dependence of this cross section (for two particles) depends only on the long-range forces between the products, giving the following relationship for the photodetachment cross section near threshold for atomic anions

$$\sigma(E) \propto (\Delta E)^{l+(1/2)} \tag{1.6}$$

where ΔE is the energy above threshold and l represents the quanta of angular momentum in the photoelectron. Reed and coworkers[24] extended this cross section to polyatomic anions by replacing the atomic orbital quantum number with an effective angular moment quantum number l' describing the highest occupied molecular orbital (HOMO) from which the electron is detached to give

$$\sigma(E) \propto (\Delta E)^{l^*+(1/2)} \tag{1.7}$$

for polyatomic anions. Here l^* is the angular momentum of the departing photoelectron ejected from the HOMO where $l^* = l' \pm 1$, which adjusts for the dipole selection rules.

In the atomic case, this threshold law dictates that only isotropic s-wave photodetachment occurs with any appreciable cross section near threshold. These relationships break down above threshold, where the detached electron can be more accurately described as a free continuum electron with essentially arbitrary angular momentum. This allows for observation of excited neutral states that would be forbidden in traditional optical spectroscopy, for example.[25]

During the process of photodetachment, angular momentum is conserved and can provide useful information on the anion orbital from which the photoelectron was ejected.[24, 26] The photoelectron angular distribution (PAD) with respect to the laser polarization vector of a linearly polarized laser is given by

$$I(\theta) \propto 1 + \beta_2 P_2(\cos\theta) \tag{1.8}$$

where θ is the angle between the laser-polarization vector and the electron-velocity vector, β_2 is the asymmetry parameter, and $P_2(cos\,\theta) = \frac{1}{2}(3cos^2\theta - 1)$. The asymmetry parameter β_2 corresponds to angular distributions ranging from $cos^2\theta$ to $sin^2\theta$ where the corresponding β_2 ranges from 2 to −1. Fitting of energy-resolved PADs gives a plot of the electron kinetic energy dependence of β_2. Although β_2 is qualitative only for molecular systems, it provides a useful tool to aid in, for example, distinguishing between photodetachment to different electronic states.

1.5. Photofragment Translational Spectroscopy

So far, this discussion of photoelectron spectroscopy has focused on direct photodetachment, where the electronic transition accesses a bound neutral state. If,

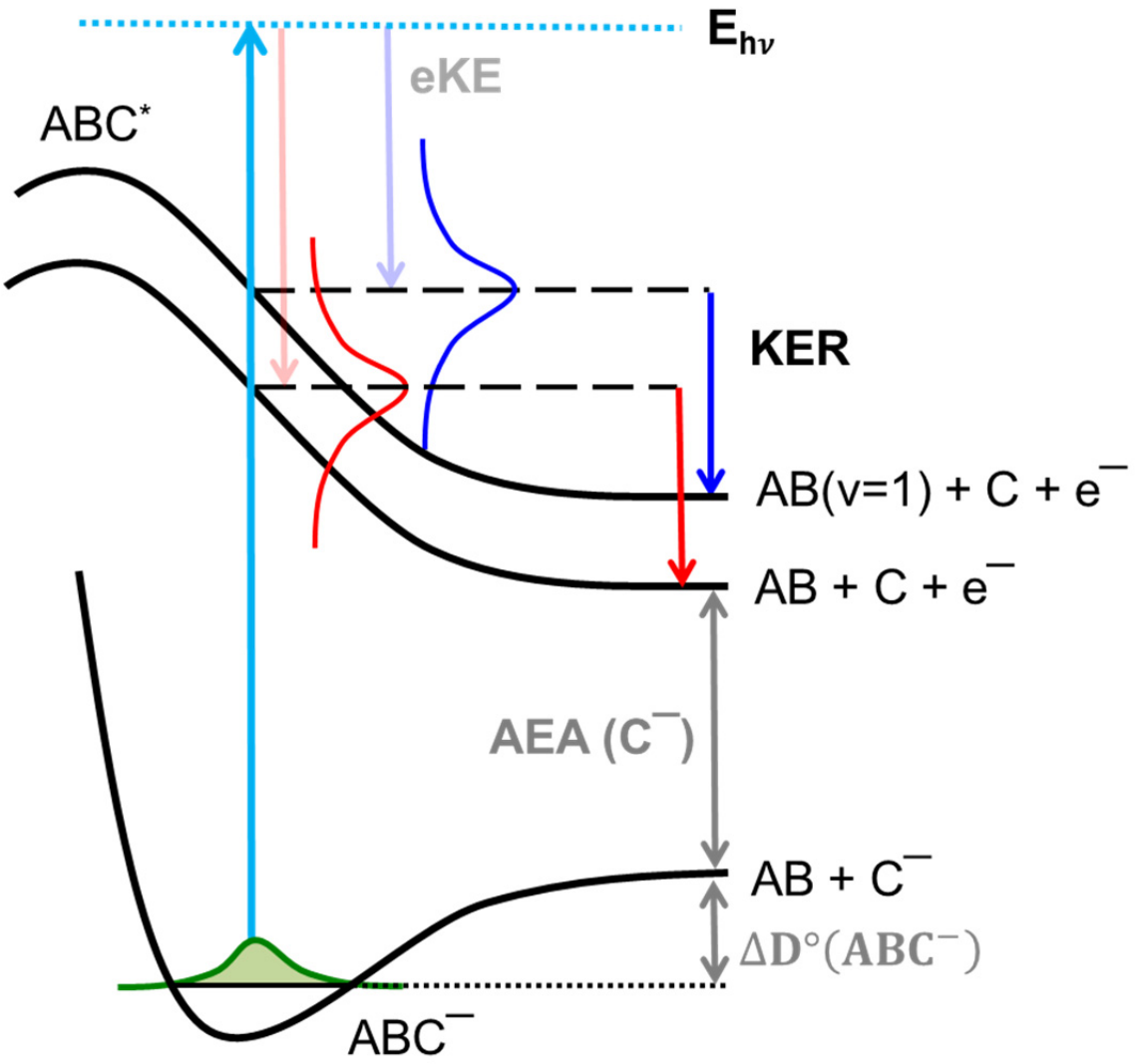

Figure 1.3. Schematic diagram of photofragment translational spectroscopy. Absorption of a photon (light blue) accesses a dissociative curve where excess energy is carried away by the departing photoelectron (eKE).

however, the neutral state is not bound but, rather, repulsive, as shown in Figure 1.3, the resulting neutral species fragments upon photodetachment in a process called dissociative photodetachment. It is informative to collect the resulting neutral fragments and study the partitioning of kinetic energy

$$KER = \mathrm{E_{h\upsilon}} - eKE - \Delta D°(ABC^-) - AEA(C^-) - E_{int} \quad (1.9)$$

where KER is the kinetic energy release of the resulting fragments and is defined relative to the bond dissociation energy $\Delta D°(ABC^-)$ of the anion, the AEA of the fragment anion and the energy partitioning into internal degrees of freedom of the fragments E_{int}. A more general form is given by

$$KER = \mathrm{E_{h\upsilon}} - eKE - E_{products} - E_{int} \quad (1.10)$$

where $E_{products}$ is the energy of the resulting products relative to the anion, providing an equation which is still good even when there is no well-defined AEA for C^-, for example. Additionally, upon dissociation, energy may partition into the internal degrees of freedom of the resulting fragment, as shown in the upper curve in Figure 1.3.

This direct photodetachment is shown schematically in Figure 1.4 for a fast-ion-beam experiment like the ones carried out in our lab. The resulting fragments still retain the center-of-mass (COM) velocity of the parent ion while the products leave with their own recoil velocities. Each recoil velocity can be determined relative to the COM and the KER extracted, as explained in greater detail in Chapter 2.

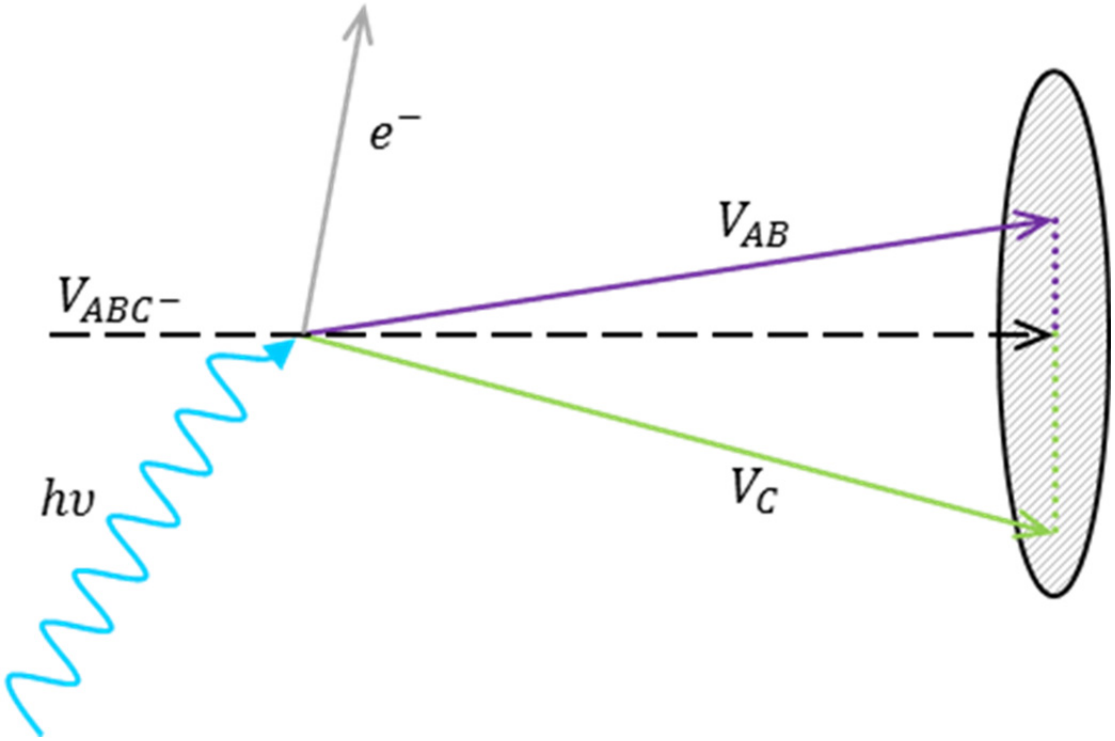

Figure 1.4. Direct dissociative photodetachment in a fast ion beam experiment. Product kinetic energy release (KER) is observed as translational energy of the fragments relative to the COM velocity.

As suggested in equations 1.9 and 1.10, useful information on energy partitioning to the internal degrees of freedom of the resulting products can be gleaned from a KER spectrum. In addition, KER distributions provide valuable insight into relative barrier heights when probing near a transition state. Finally, because product KER from the COM depends on both velocity and mass, observation of product KER upon dissociative photodetachment allows for identification of accessible dissociative pathways, particularly if more than one fragmentation pathway is available.

1.6. Photoelectron-Photofragment Coincidence Spectroscopy

In this thesis, photoelectron-photofragment coincidence spectroscopy (PPC), a combination of photoelectron and photofragment spectroscopic techniques, is used to gain significant insight into the dissociation dynamics of transient neutrals.[4, 5] Here the kinetic energy release (KER) (sometimes also referred to as translational energy release (E_T)) for the resulting fragments is measured in coincidence with a photoelectron, providing information on the nascent neutral, the resulting products, and the reaction dynamics of the system. The coincidence spectrum can provide additional insight not obtainable from the individual eKE and KER data. For instance, all products that end up at the same final state appear as a diagonal in the coincidence spectrum, shown schematically in Figure 1.5. The position along that diagonal provides information on the Franck-Condon region of a dissociative curve and, as is the case for the F + H_2O system, allows for observation of the FC region for more than one asymptotically near-degenerate electronic state.

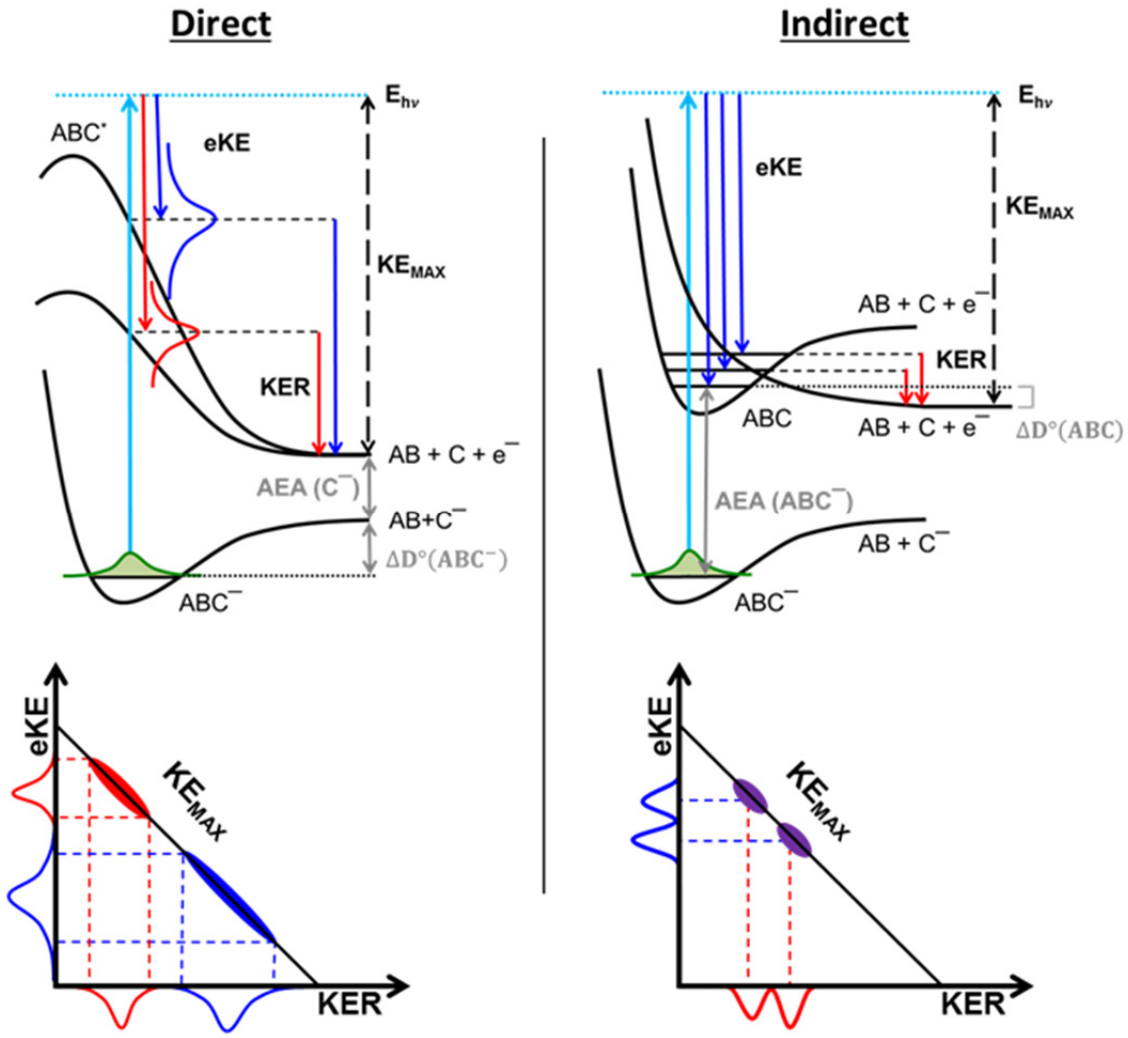

Figure 1.5. Schematics for direct (left) and indirect (right) dissociative photodetachment and schematics of the corresponding photoelectron-photofragment coincidence plots below.

Example schematics of a coincidence measurement are shown in Figure 1.5 for both direct and indirect dissociation pathways. For both cases, the diagonal line along which these bands fall corresponds to the maximum kinetic energy (KE_{MAX}) where the products are formed in their ground vibrational and rotational states. In this case the following pertains:

$$KE_{MAX} = E_{h\upsilon} - AEA(C^-) - \Delta D°(ABC^-) \quad (1.11)$$

where E_{hv} is the energy of the photodetachment laser, AEA is the adiabatic electron affinity of the fragment anion, and ΔD° is the dissociation energy of the ABC^- anion. For the case of indirect dissociative photodetachment, equation 1.11 can also be given by:

$$KE_{MAX} = E_{h\upsilon} - AEA(ABC^-) - \Delta D°(ABC) \quad (1.12)$$

defined relative to the AEA of the ABC^- anion and the $\Delta D°(ABC)$ of the resulting neutral. As shown on the left side of Figure 1.5, direct dissociative photodetachment involves accessing purely repulsive surfaces, in this case corresponding asymptotically to the same final products. A schematic of the resulting coincidence plot is shown in Figure 1.5; eKE is shown on the vertical axis, product KER is shown on the horizontal axis, and the corresponding signals show as diagonal bands.

The right side of Figure 1.5 shows indirect dissociative photodetachment where photodetachment accesses a bound intermediate crossed by a repulsive curve. The resulting photoelectron spectrum in this example now contains peaks corresponding to vibrations in the metastable neutral, provided that this intermediate has a lifetime greater than a vibration. Vibrational states that fall above the dissociative curve can cross and

then dissociate, resulting in a series of diagonal peaks in the corresponding coincidence plot schematic.

More complicated dissociative processes — such as electron autodetachment following direct ionic photodissociation, multiphoton processes, and decaying metastable states—all exhibit unique characteristics in the coincidence spectrum while remaining elusive or impossible to disentangle with single-dimensional techniques. For example, electron autodetachment following a photodissociation event appears as a series of horizontal stripes at low eKE. Decaying metastable states can appear in the coincidence spectrum as horizontal bands, as for the F^-H_2O system, or as a series of dots if sufficient vibrational resolution is observed in both eKE and KER spectra, as for the formate anion discussed in Chapter 3.

1.7. Thesis Outline

This introductory chapter presents background information needed to understand information presented later in the thesis. Subsequent chapters describe the experimental apparatus, including the recent introduction of a tunable IR laser system for controlled vibrational pumping of precursor anions, as well as detector calibration and data-analysis techniques. Experimental results start with our study of carboxyl free radicals, looking specifically at formyloxyl radical HCO_2 and propiolyl radical HC_3O_2 systems. Experimental results continue with our study of proton abstraction by fluorine, starting with the $F + HOCH_3 \rightarrow HF + OCH_3$ system and culminating with implementation of a tunable IR light source for controlled vibrational pumping of the precursor F^-H_2O anion and its effects on the dissociation dynamics of the $F + H_2O \rightarrow HF + OH$ system.

1.8. References

1. Kim, J. B.; Weichman, M. L.; Sjolander, T. F.; Neumark, D. M.; Kłos, J.; Alexander, M. H.; Manolopoulos, D. E., Spectroscopic Observation of Resonances in the F + H_2 Reaction. *Science* **2015,** *349* (6247), 510-513.

2. Yang, X.; Zhang, D. H., Dynamical Resonances in the Fluorine Atom Reaction with the Hydrogen Molecule. *Accounts of Chemical Research* **2008,** *41* (8), 981-989.

3. Liu, K., Quantum Dynamical Resonances in Chemical Reactions: From A + BC to Polyatomic Systems. In *Advances in Chemical Physics*, John Wiley & Sons, Inc.: 2012; p 1-46.

4. Continetti, R. E., Photoelectron-Photofragment Coincidence Studies of Dissociation Dynamics. *International Reviews in Physical Chemistry* **1998,** *17* (2), 227-260.

5. Continetti, R. E., Coincidence Spectroscopy. *Annual Review of Physical Chemistry* **2001,** *52* (1), 165-192.

6. Smalley, R. E.; Wharton, L.; Levy, D. H., Molecular Optical Spectroscopy with Supersonic Beams and Jets. *Accounts of Chemical Research* **1977,** *10* (4), 139-145.

7. Steinfeld, J. I.; Francisco, J. S.; Hase, W. L., *Chemical Kinetics and Dynamics*. 2nd ed.; Prentice Hall: Upper Saddle River, N.J., 1999; 518 pages.

8. Neumark, D. M., Probing the Transition State with Negative Ion Photodetachment: Experiment and Theory. *Physical Chemistry Chemical Physics* **2005,** *7* (3), 433-442.

9. Thomas, R. D., When Electrons Meet Molecular Ions and What Happens Next: Dissociative Recombination from Interstellar Molecular Clouds to Internal Combustion Engines. *Mass Spectrometry Reviews* **2008,** *27* (5), 485-530.

10. Savee, J. D.; Mann, J. E.; Laperle, C. M.; Continetti, R. E., Experimental Probes of Transient Neutral Species Using Dissociative Charge Exchange. *International Reviews in Physical Chemistry* **2011,** *30* (1), 79-113.

11. Kitsopoulos, T. N.; Waller, I. M.; Loeser, J. G.; Neumark, D. M., High Resolution Threshold Photodetachment Spectroscopy of Negative Ions. *Chemical Physics Letters* **1989,** *159* (4), 300-306.

12. Hüfner, S., *Photoelectron Spectroscopy: Principles and Applications*. 3rd rev. and enlarged ed.; Springer: New York, 2003; 662 pages.

13. Brehm, B.; Gusinow, M. A.; Hall, J. L., Electron Affinity of Helium Via Laser Photodetachment of its Negative Ion. *Physical Review Letters* **1967,** *19* (13), 737-741.

14. Sanov, A.; Mabbs, R., Photoelectron Imaging of Negative Ions. *International Reviews in Physical Chemistry* **2008,** *27* (1), 53-85.

15. McQuarrie, D. A., *Quantum Chemistry*. University Science Books: Mill Valley, Calif., 1983; 517 pages.

16. Condon, E. U., Nuclear Motions Associated with Electron Transitions in Diatomic Molecules. *Physical Review* **1928,** *32* (6), 858-872.

17. Born, M.; Oppenheimer, R., Zur Quantentheorie der Molekeln. *Annalen der Physik* **1927,** *389* (20), 457-484.

18. Ma, J.; Guo, H., Full-Dimensional Quantum State Resolved Predissociation Dynamics of HCO_2 Prepared by Photodetaching HCO_2^-. *Chemical Physics Letters* **2011,** *511* (4–6), 193-195.

19. Neumark, D. M., Slow Electron Velocity-Map Imaging of Negative Ions: Applications to Spectroscopy and Dynamics. *The Journal of Physical Chemistry A* **2008,** *112* (51), 13287-13301.

20. Waller, I. M.; Kitsopoulos, T. N.; Neumark, D. M., Threshold Photodetachment Spectroscopy of the Iodine Atom + Hydrogen Iodide Transition-State Region. *The Journal of Physical Chemistry* **1990,** *94* (6), 2240-2242.

21. Wetzel, D. M.; Brauman, J. I., Electron Photodetachment Spectroscopy of Trapped Negative Ions. *Chemical Reviews* **1987,** *87* (3), 607-622.

22. Johnson, C. J.; Harding, M. E.; Poad, B. L. J.; Stanton, J. F.; Continetti, R. E., Electron Affinities, Well Depths, and Vibrational Spectroscopy of cis- and trans-HOCO. *Journal of the American Chemical Society* **2011,** *133* (49), 19606-19609.

23. Wigner, E. P., On the Behavior of Cross Sections Near Thresholds. *Physical Review* **1948,** *73* (9), 1002-1009.

24. Reed, K. J.; Zimmerman, A. H.; Andersen, H. C.; Brauman, J. I., Cross Sections for Photodetachment of Electrons from Negative Ions Near Threshold. *The Journal of Chemical Physics* **1976,** *64* (4), 1368-1375.

25. Weaver, A.; Metz, R. B.; Bradforth, S. E.; Neumark, D. M., Observation of the $\tilde{A}(^2B_2)$ and $\tilde{C}(^2A_2)$ States of NO_2 by Negative Ion Photoelectron Spectroscopy of NO^-_2. *The Journal of Chemical Physics* **1989,** *90* (3), 2070-2071.

26. Sanov, A., Laboratory-Frame Photoelectron Angular Distributions in Anion Photodetachment: Insight into Electronic Structure and Intermolecular Interactions. *Annual Review of Physical Chemistry* **2014,** *65* (1), 341-363.

Chapter 2 : Experimental Methods and Data Analysis

The experiments presented in this thesis were carried out on a fast-ion-beam photoelectron-photofragment coincidence (PPC) spectrometer, discussed in detail elsewhere.[1, 2] This chapter presents a brief description of the major components of the apparatus and is followed by a more detailed discussion of installation of an IR laser system used for vibrational pumping of precursor anions prior to carrying out PPC experiments. Finally, the chapter concludes with a discussion of data analysis, calibration, and needed modifications to these procedures for the IR/vibrational excitation experiment.

2.1. Experimental Apparatus Overview

The instrument was constructed and designed specifically to carry out coincidence measurements of single molecules with high detection efficiency.[1, 3] Detection of neutral products is achieved by utilizing a fast (keV) ion beam followed by photodetachment of the precursor anions with ~ 50% detection efficiency observed for a microchannel-plate-based detector.[4] The use of a fast ion beam has the added advantage that, due to conservation of momentum, neutral products are constrained to a limited angular range in the laboratory frame. In most cases this allows for detection of the full 4π solid angle in the center-of-mass (CM) frame using a single detector. Discussed in more detail in Section 2.3.2, product mass ratios, scattering angles, and CM translational energy release (KER) for dissociative events are determined the time and position of arrival on the

neutral particle detector and information on the parent mass and velocity.[5] Upon photodetachment, the resulting photoelectron is extracted perpendicular to the fast ion beam axis using a space-focusing time-of-flight detection scheme coupled to a time- and position-sensitive detector. Discussed in more detail in Section 2.3.1, the photoelectron spectrum is determined from the radial and temporal distributions of electrons on the detector. Coincidence measurements dictate photodetachment and detection of a single molecule at a time, which can be controlled for by limiting the experimental rate to no more than one event per photodetachment laser shot.

A schematic cross-section of the PPC spectrometer is shown in Figure 2.1 and a discussion of the experiment and spectrometer follows below. The spectrometer consists of the following differentially pumped chambers: source, acceleration, time-of-flight (TOF), mass gate, electrostatic ion-beam trap (EIBT), and detector. Each chamber is separated from its neighbors by an aperture (diameters ranging over 3–5 mm) and selective chambers are separated by gate valves (GV) to allow for selective partial venting of the instrument for maintenance purposes.

Ions are created in the source using a coaxial-pulsed discharge (typically 500–700 V, 30–50 μs pulse width) acting upon a pulsed (10–20 Hz) supersonic expansion of desired gas mixture. The expansion is then crossed by an electron beam (1 keV) that provides an additional source of secondary low-energy electrons formed through collisions of the expansion with the high-energy electron beam. One advantage to using a supersonic expansion is that it results in cooling of internal degrees of freedom through

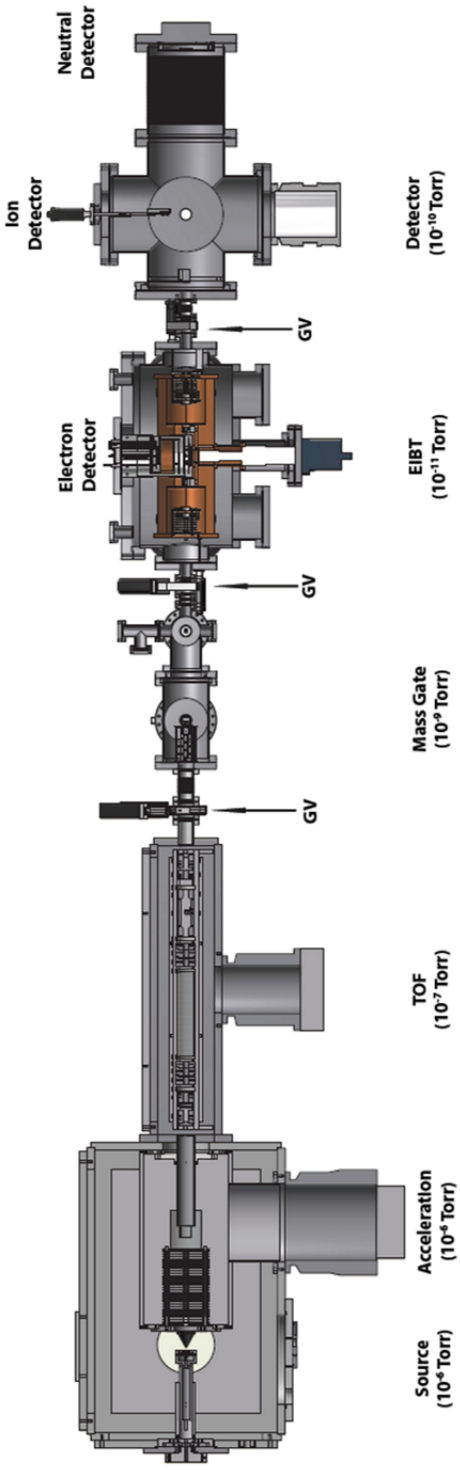

Figure 2.1. Simplified schematic of the PPC spectrometer.

inelastic collisions with the buffer/carrier gas to typical vibrational temperatures of <100K and rotational temperatures of <20K near the center of expansion.[6]

The actual discharge-initiated chemistry in the expansion typically occurs via either of two mechanisms: (1) fragmentation of species in the discharge followed by collisions of energetic molecules or (2) attachment of free low-energy electrons. Note that molecular anion formation, especially late in the expansion where there is less collisional cooling, can yield anions with significant internal excitation.[7, 8] Implementation of the EIBT has dramatically improved our ability to produce cold anions, largely through the stronger expansions possible from using a 10 Hz source compared to a 1 kHz source,[9] but it is still important to take special care to find source conditions for the production of cold ions. As discussed in section 2.5 production of cold ions is especially important for IR pumping of precursor ions in the F^-H_2O system. After ion production, the coldest portion of the expansion is selected using a conical skimmer (3 mm) located between the differentially pumped source and acceleration chambers.

The ions are accelerated to 4–7 keV using a stack of plates with holes (diameter 5 cm) centered along the ion-beam axis with monotonically increasing positive potential. They then enter a cylinder (length 30 cm) with endcaps with apertures (entrance diameter 3 mm, exit diameter 5 mm) along the center line, floated at the acceleration potential. Once the anion packet is contained within the cylinder, the cylinder's high voltage potential is rapidly (~30 ns) switched to zero, re-referencing the anion packet to ground so that the rest of the instrument need not be floated at the acceleration potential. Included in the acceleration stack is an einzel lens, discussed in more detail below, to

help focus the ion packet. The resulting collimated beam has a small energy spread and can be easily guided through the rest of the instrument.

The accelerated ions are separated by their mass/charge (m/z) ratio in the subsequent differentially pumped region (time-of-flight, or TOF). At fixed beam energy, time-of-flight over a given distance is proportional to the $\sqrt{m/z}$, allowing for temporal separation of masses with the same charge. TOF information relative to the high-voltage switch allows for identification of anion species created in the source and, later, for selection of the anion of interest in the mass gate region. Ion-beam steering and focusing is achieved with a series of ion optics, including two sets of vertical and horizontal ion deflectors located at the beginning and end of the TOF chamber and two electrostatic einzel lenses. These lenses consist of three coaxial cylindrical electrodes, where the outer electrodes are held at ground and the center electrode is held at potential, allowing for focusing of the ion beam without changing its energy.[10] Before entering the differentially pumped mass gate region, the beam is deflected over a neutral-beam block centered along the ion-beam axis and then returned to its original trajectory. The beam block serves to reduce the number of residual fast neutrals that were formed by collisional electron detachment with the background gas in the source and now make it to the neutral-particle detector. This neutral-beam block is discussed in more detail in Section 2.4, where modifications that enable use as a turning mirror for coupling an IR laser into the instrument are outlined.

Although experiments can be readily carried out on more than one mass simultaneously using the EIBT (this use is known as multi-mass mode), it is often more

practical to select a single mass or small range of masses using a mass gate beforehand. In the current configuration, the mass gate consists of two parallel plates held at equal and opposite voltages to deflect undesired ions out of the beam. The mass or masses of interest are selected by rapidly dropping the potential of the mass gate to ground to let a specific m/z pass, then raising the plates to potential again. Increasing the length of time that the mass gate is held at ground allows for selection of a greater number of species that can be loaded into the EIBT, though typically only a single mass was selected during an experimental run. Also housed within the mass gate region is an ion detector that can be translated in and out of the ion beam.

The EIBT consists of two focusing electrostatic mirrors used to store the fast ions with a stable orbiting trajectory. The entrance mirror is held at ground to allow ions to be injected into the EIBT and is then raised to potential before the ions complete their first round trip, trapping the oscillating ions in the cavity. Ions can remain trapped for more than 5 seconds,[2] during which their primary loss mechanism is charge exchange with background gas. The entire trap assembly is cooled to cryogenic temperatures such that the electrostatic mirrors are at ~ 20 K, allowing, in principle, the stored ions to cool radiatively during confinement.

At the center of the trap is the ion-laser interaction region and electron detector assembly. The trapped ion packet is repetitively probed with the output of a 1 kHz laser, as discussed in more detail in Section 2.2.1. The photoelectron is velocity-mapped[11] onto a time- and position-sensitive electron detector, while the resulting neutrals are no longer held by the trap potential and recoil out of the trap toward the neutral particle detector.

Compared to traditional single-shot PPC experimental techniques, use of such a trap effectively decouples the source from the photodetachment process, allowing for greater flexibility in carrying out this complex experiment. Primarily this means that the ion source is run at 10 Hz, allowing for better cooling in the supersonic expansion, while the photodetachment laser still probes the trapped, oscillating ion packet in the EIBT at 1 kHz.

Over the course of the trap cycle, the slight kinetic energy spread of the ion packet and any Coulomb interactions of the ions (particularly in the turnaround regions) causes the ion packet to elongate and spread, ultimately filling the entire cavity, resulting in a net lowering of the ion density that the photodetachment laser encounters during crossing. To counteract this effect, a small cylindrical RF-bunching electrode is placed inside the trap along the ion beamline. Application of a sinusoidal RF voltage, phase-locked to the master oscillator of the laser at a frequency close to the natural oscillation frequency of the ions, helps to "bunch" the ion packet – that is, limit ion packet spread over the course of the trap confinement resulting from the inherent ensemble of velocities contained within. In addition, bunching helps ensure that the ions travel toward the neutral particle detector when photodetachment occurs, dramatically increasing the experimental rate.

The detector chamber houses both the multi-particle neutral detector as well as an ion detector used to measure TOF spectra of ions during ion tuning and beam optimization. The neutral particle detector, described in more detail in Section 2.3.2, is mounted in the beam axis on a vertical translator mount attached by bellows to the main

detector chamber. This allows flexibility in fine-tuning the ion beam center-of-mass position on the detector face.

The ion beam is monitored at the ion detector using an electrostatic deflector consisting of parallel plates that deflects ions out of the beam-line up to a stack of two microchannel plates (MCPs; diameter 1"). The emitted charge is collected by a stainless steel anode and amplified by a high-speed preamplifier (Ortec VT-120). The ion deflector serves double duty by also causing all ions to be deflected out of the beam axis, ensuring that only neutrals are detected at the neutral particle detector.

Collisions of anions in the fast beam with background gas molecules can either result in heating of internal degrees of freedom in the anion or deflection of the anion from the stable trajectories needed to traverse the length of the instrument. Differential pumping, provided by high performance vacuum technology, is used to limit these interactions. The source, acceleration and TOF comprise the high vacuum system, each with typical pressures of $\sim 10^{-8}$ Torr. Each chamber in the high vacuum system is separated from the next by a small aperture (typical diameter of 3 mm) allowing for differential pumping, which becomes increasingly more important when the pulsed valve is running in the source causing typical source pressures of 10^{-5} Torr. The remaining chambers make up the ultra-high vacuum portion of the instrument with typical pressures of $<10^{-9}$ Torr for the mass gate, 10^{-11} Torr for the EIBT and 10^{-10} Torr for the detector chamber. Beam line gate valves are used to isolate the ultra-high vacuum system from the high vacuum system, allowing for selective venting of the source, acceleration and TOF regions when maintenance is needed. Additional beam line gate valves are located at both

the entrance and exit of the EIBT allowing for selective venting of the mass gate, EIBT and detector chambers if needed.

In the high vacuum system each source is evacuated by magnetically-levitated turbomolecular pumps (TMP) with pumping speeds of 3200 L/s (source, Edwards STP-XA3203C), 2200 L/s (acceleration, Edwards STP-A2503PV), and 800 L/s (TOF, Edwards STP-A803WAV-U). All three are backed by a shared foreline evacuated by a roots blower backed by a rotary vane mechanical pump (Edwards EH500 with E2M80, 110 L/s). During the course of this thesis project, the mechanical pump was replaced by an oil free scroll pump (Edwards XDS 35i, 9.7 L/s).

In the ultra-high vacuum system the detector and mass gate chambers share a foreline evacuated by a scroll pump (Edwards nXDS 10i, 3.2 L/s). The mass gate is evacuated using two 250 L/s TMPs, which helps ensure that the high gas load used in the source does not effect the ultra-high vacuum requirements of the EIBT in particular. The detector chamber is pumped by a magnetically levitated 400 L/s TMP backed by a 250 L/s TMP to ensure adequate pumping of hydrogen and helium with which TMPs can struggle. Finally, the EIBT chamber itself is evacuated using a cryopump (Oxford Instruments, Cryo-Plex 8) and cold head (Oxford Instruments, 1020 Cold Head), reaching the $< 10^{-10}$ Torr needed for the extended flight path of the trapped ions. Roughing valves for both the EIBT chamber and the cryogenic pump are backed by the same foreline as the mass gate and detector regions to help limit the effects of gas permeation through the Viton O-rings. Finally, the EIBT also can be evacuated with a home-built, 3000 L/s

titanium sublimation pump (TSP), but this is typically only needed if the EIBT chamber has been open for long periods of time for extended maintenance.

2.2. Laser Systems

The photodetachment/dissociative photodetachment studies described in this thesis require the use of a short-pulse picosecond laser with a high repetition rate. The system used for these studies is a cavity-dumped, mode-locked Titanium:Sapphire-based regenerative amplifier, described in section 2.2.1.

In addition, to achieve vibrational pumping of precursor anions before photodetachment requires the use of an optical-parametric-oscillator/optical-parametric-amplifier (OPO/OPA) tunable-IR laser system. The system used for these studies is described in section 2.2.2. How this system was coupled into the instrument and data acquisition is described in section 2.5.

2.2.1. Photodetachment: Clark Titanium:Sapphire CPA System

Photodetachment in these experiments is carried out using a Clark MXR CPA-2000 Ti:Sapphire regenerative amplifier system. The fundamental output of 775.5 nm light has pulse width 1.1 ps, 400 μJ/pulse, repetition rate 1.037 kHz. In general, such short pulses have a very high peak power, which limits power amplification in laser systems due to the damage threshold of the gain medium and optics. Consequently a chirped-pulse-amplification (CPA) approach is used, where laser pulses are elongated temporally by use of a dispersive grating that stretches the pulse width to tens of picoseconds. These elongated pulses now have a lower peak height and are safe for

amplification in the laser cavity, after which the well-defined pulse can be recompressed using a similar dispersive system to recover an amplified short pulse.

Briefly, the regenerative amplification system used herein to amplify the Ti:Sapphire output is a mode-locked diode-pumped fiber laser producing picosecond seed pulses (nJ/pulse, 43.58 MHz). Seed pulses are first stretched (making them safe for amplification), then injected at 1.037 kHz into the Ti:Sapphire amplifier cavity. The Ti:Sapphire crystal is pumped by a high-power Q-switched Nd:YAG laser, allowing amplification of the seed pulse over several passes through the cavity. Once the maximum energy is reached, the pulse is ejected from the cavity through a polarizer using a Pockels cell (fast-polarization rotator), then recompressed using a grating to produce the final output pulse.

Once the fundamental 775.5 nm (1.60 eV) light exits the laser cavity, it can either be used directly for photodetachment experiments or converted to other wavelengths by use of nonlinear optics. Frequency doubling in beta-Barium-Borate (BBO) produces 387.8 nm (3.20 eV) light that, if desired, can be used to pump a traveling-wave parametric amplifier of superfluorescence (TOPAS) system to produce tunable radiation over the ranges 460 – 720 nm and 830 nm – 2 μm. The TOPAS system consists of a superfluorescence generator, three preamplifiers, and a power-amplification stage arranged such that only a single nonlinear BBO crystal is needed to produce tunable radiation. The output of the TOPAS system can be frequency doubled using an additional BBO crystal mounted just outside the exit aperture of the TOPAS unit. The majority of results presented in this thesis were obtained using 258.5 nm (4.80 eV) light, produced by

frequency tripling the Ti:Sapphire fundamental (with a commensurate reduction in power per pulse) using a BBO crystal to combine frequency doubled 387.8 nm light with residual 775.5 nm light overlapped spatially and temporally through use of a delay-line setup.

Because high intensity 258.5 nm light can overcome the work function of surfaces in our electrostatic ion beam trap (EIBT), a series of concentric baffles was installed in the trap chamber on the vacuum side of the entrance and exit laser windows to reduce scattered light and spurious photoelectrons. This necessitated implementation of a telescoping lens assembly before the EIBT, replacing the focusing lens (focal length 500 mm) used at longer wavelengths. That is, the laser beam is now collimated through the trap instead of being focused in the interaction region at the center of the EIBT. For this thesis, data at 258.5 nm was collected with the telescope, while data at longer wavelengths was collected with the focusing lens.

2.2.2. Vibrational Pumping: LaserVision OPO/OPA IR System

The major instrumentation modification undertaken for this thesis was the implementation of a new tunable-IR laser system used to pump specific vibrational modes in the precursor anion packet before the PPC experiment is performed. This section describes the IR laser system. Implementation of this system with the PPC spectrometer is discussed in Section 2.5.

The IR laser system consists of a pump laser and an OPO/OPA system.[12] The pump laser is a Continuum Surelite EX Nd:YAG laser producing 1064-nm light with the

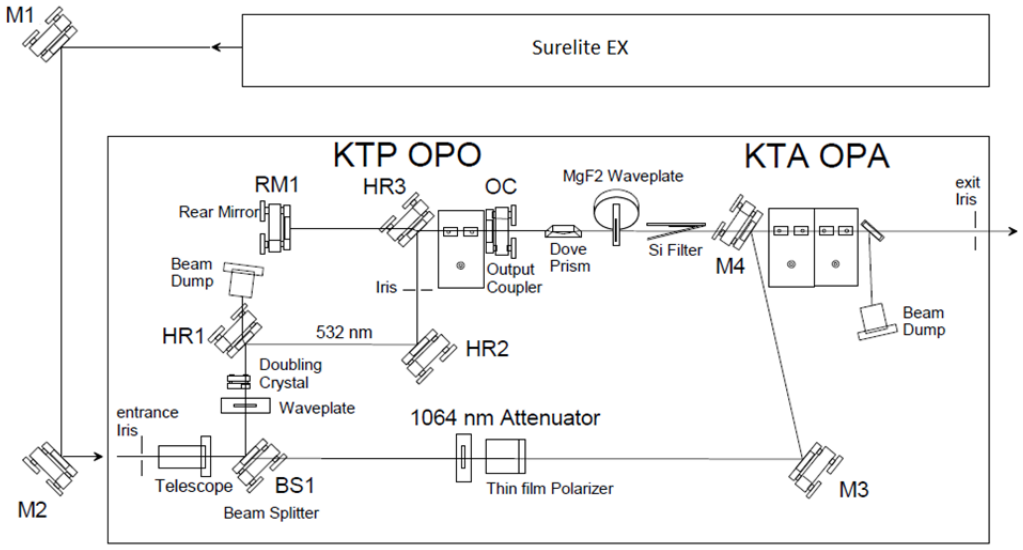

Figure 2.2. Schematic of the LaserVision OPO/OPA IR system including the Surelite EX Nd:YAG pump laser. The pump beam is split at BS1; the reflected beam is doubled to 532 nm, then split into Signal and Idler photon beams in the OPO stage. Finally, the Signal and Idler photon beams are amplified using the passed-though 1064 nm light in the OPA stage.[12]

following characteristics: pulse width 5 ns, power 740 mJ/pulse, repetition rate 10 Hz. IR radiation is produced using a LaserVision OPO/OPA system operating at the repetition rate of the pump laser and can be tuned over the ranges 710 – 885 nm (14000 – 11300 cm^{-1}) and 1.35 – 5.0 μm (7400 – 2000 cm^{-1}); within the second range, average power is 12 mJ/pulse over the range 1.5 – 3.0 μm but only 4 mJ/pulse at 4 μm. A schematic of the LaserVision system is shown in Figure 2.2.

Briefly, the fundamental 1064 nm pump is first split into two beams using a beam splitter (BS1). The two beams then proceed as follows: one beam is frequency doubled to 532 nm and enters the OPO, which consists of two matched potassium titanyl phosphate (KTP) crystals, producing two new tunable beams called the Signal (near-IR, 1400 – 2000 nm) and Idler (855 – 720 nm) photon beams. By conservation of energy, the sum of these two beams must equal that of the 532 nm pump beam, per the relationship $\omega_{532} = \omega_{\text{signal}} + \omega_{\text{idler}}$. Tunability is achieved by matched rotation of the KTP crystals to ensure phase matching. The near-IR Signal beam then enters the OPA, where it passes through four matched potassium titanyl arsenate (KTA) crystals. The other beam produced at BS1 is used to pump this OPA chain, amplifying the near-IR beam and generating another photon in the range 4300 – 2200 nm (ω_{IR}) where, by conservation of energy, $\omega_{1064} = \omega_{\text{signal}} + \omega_{\text{IR}}$. Similarly, the ω_{IR} photon is selected for by matched rotation and phase-matching of the KTA crystals. Judicious use of filters at the exit of the LaserVision box allows for selection of ω_{IR} produced from either ω_{signal} or ω_{idler}, expanding the tunable range of the system. Power is measured and optimized using a

power meter located just outside the exit of the LaserVision box, and the wavelength of ω_{IR} is verified using an Ocean Optics spectrometer (HR2000+).

2.3. Detectors

The time- and position-sensitive electron and neutral particle detectors mentioned in the general overview of the instrument in Section 2.1 generally work in a similar fashion, in that they make use of microchannel plates (MCPs) to amplify single incident particles (high energy (keV) neutrals or electrons) into electron clouds of ~10^7 electrons. Information regarding the electron and neutral particles over the full 4π solid angle distribution of recoiling particles is collected. For the electron detector a set of velocity-map-imaging (VMI) extraction optics are used to map the detached electron up to the MCPs and wedge-and-strip anode. Neutrals retain the momentum of their parent anion and therefore the center-of-mass (COM) of the recoiling particles is projected onto the neutral detector at keV energies in the lab frame. The neutral particle detector consists of a four-quadrant crossed delay-line anode, allowing for detection of up to eight neutral particles in coincidence during a single dissociative event. The three-dimensional velocity spread of each particle is mapped onto its respective time- and position-sensitive detector, allowing for easy conversion to particle velocities.

2.3.1. Time- and Position-Sensitive Electron Detector

Photoelectrons are extracted perpendicular to the laser ion beam plane in the interaction region and velocity-map-imaged onto the plane of the electron detector, shown in Figure 2.3. The VMI setup and electron detector are described in detail elsewhere.[2, 9, 11] Briefly, the VMI extraction optics consist of a repeller plate (negative

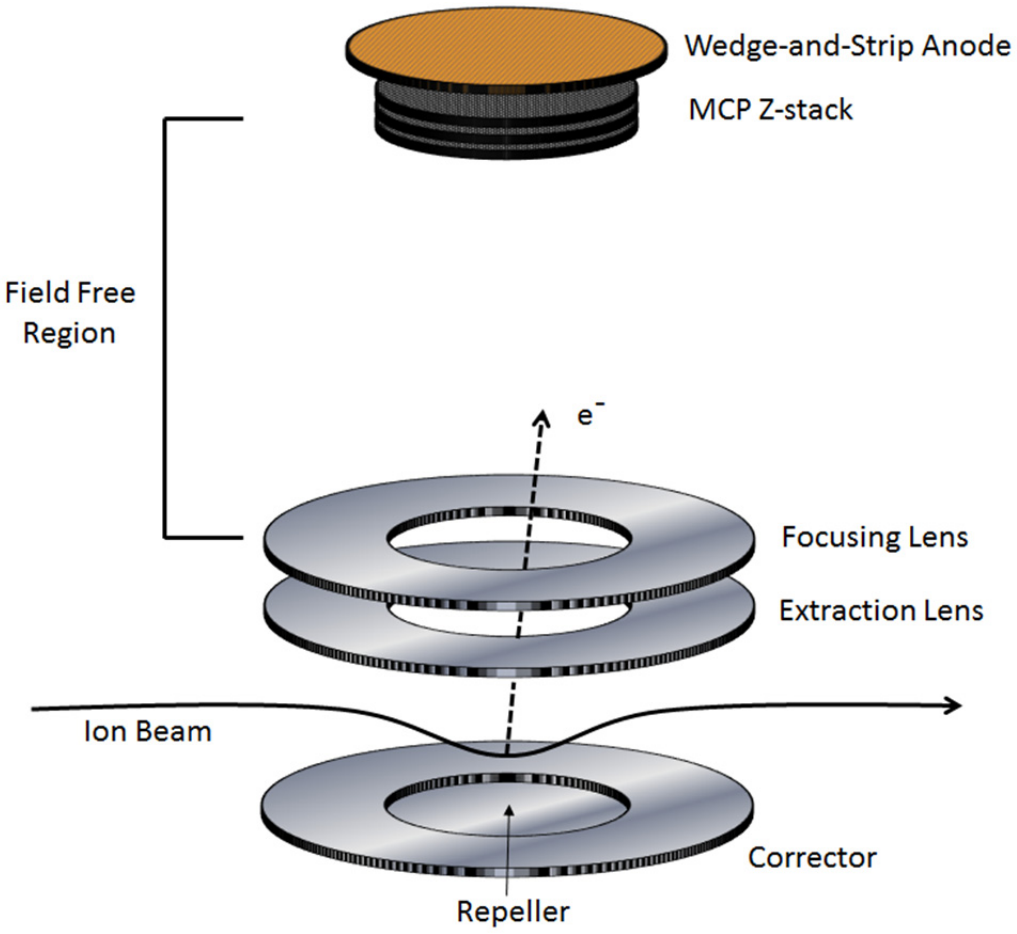

Figure 2.3. Schematic of the velocity-map-imaging (VMI) extraction optics.

bias), an extraction lens (grounded), a focusing lens (positive bias), a field-free-flight region, and a z-stack of three MCPs mounted above a "wedge-and-strip" anode, shown in Figure 2.4.[13] Additionally, a corrector plate (positive bias), not found in traditional VMI setups, is included to correct for deflection of the anion beam by the repeller plate voltage. Because the interaction region is located at the center of the EIBT, the repeller, corrector, and extraction-lens plates are held at ~20 K while the electron detector is held at room temperature.

The wedge-and-strip anode shown in Figure 2.4 consists of three electrodes: the wedge electrode (a comb of tapered fingers), the interlaced strip electrode (another comb of parallel fingers of increasing thickness), and the remaining zig-zag electrode (filling the space between the wedge and the strip). For ensure detection in both the x and y dimensions, the impinging electron cloud must be large enough to cover at least one finger on each electrode element. The x and y position of arrival is determined by charge division:

$$x \propto \frac{Q_W}{Q_W + Q_S + Q_Z} \tag{2.1}$$

$$y \propto \frac{Q_S}{Q_W + Q_S + Q_Z} \tag{2.2}$$

where the ratio of charge on the wedge (Q_W) relative to the total charge gives position along the directions of the wedge fingers, and the ratio of charge on the strip (Q_S) gives position perpendicular to the wedge fingers due to the increasing width of the strips in that direction. The zig-zag electrode ensures proper charge normalization by capturing

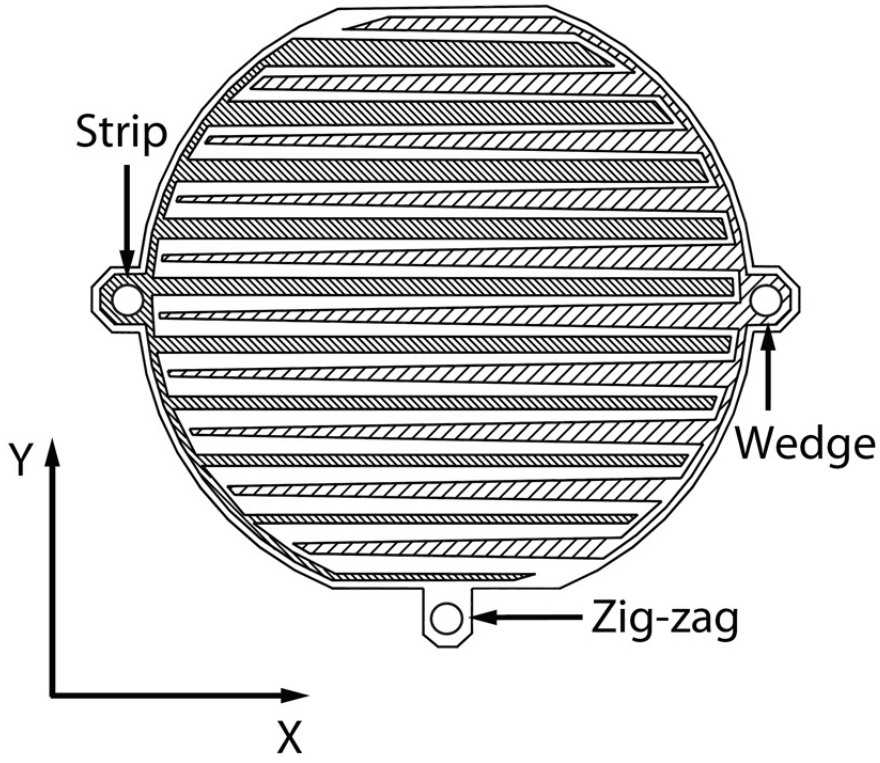

Figure 2.4. Simplified schematic of a wedge-and-strip anode. The strip electrode provides information on the y-axis, the wedge electrode provides information on the x-axis, and the zig-zag electrode ensures proper charge normalization.

those electrons that miss either the wedge or strip electrodes where $Q_{Tot} = Q_W + Q_S + Q_Z$. Additional calculations and calibration of the detector are discussed in Section 2.4.2.

The signal from each electrode is amplified using a combination charge-sensitive preamplifier and shaping amplifier (Siegmund Scientific) before digitization using three channels on a 13-bit Ortec AD413 peak-sensing analog-to-digital converter (ADC). Timing information is pulled off of the wedge electrode using a capacitively coupled high-speed preamplifier (Ortec VT120). Electron time-of-flight information is determined by taking the difference between the photodetachment laser pulse, measured at the output of the Ti:Sapphire laser, and the arrival time of the electron using a time-to-amplitude converter with 50 ns full scale. Both the laser and electron timing signals are passed through a constant-fraction discriminator (CFD Ortec 935) set to trigger at 20% peak height for each signal. These triggers are then converted to a voltage proportional to the difference in time between the start and stop signals using a time-to-amplitude converter (TAC, Ortec 566), which is then digitized using another channel of the 13-bit Ortec AD413 peak-sensing ADC. The ADCs and TDCs are housed in a Computer-Automated Measurement and Control (CAMAC) crate which interfaces to a PC where a custom-written LabVIEW acquisition code polls and continuously reads in events. The data is then discriminated, histogrammed and written to the hard drive for later use.

2.3.2. Time- and Position-Sensitive Multi-Particle Neutral Detector

In a single photodetachment event, ideally we want to collect a single electron in coincidence with one or more neutral products. The wedge-and-strip anode's charge-detection scheme does not allow for collection of more than one particle, precluding it as

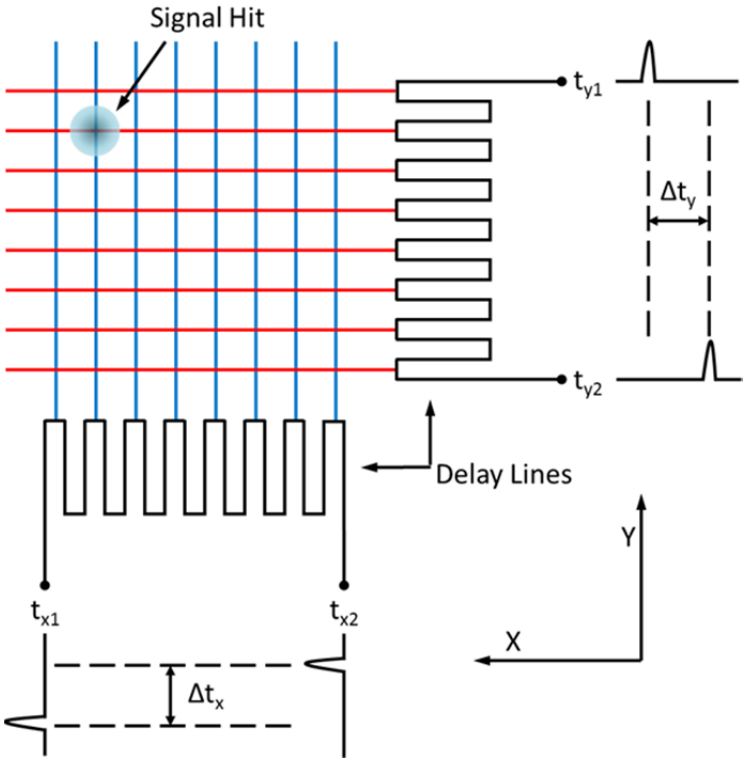

Figure 2.5. Schematic of a crossed delay-line (XDL) anode. The signal hit/incident charge is sampled on both delay lines, giving signal at both ends of a single line. Particle position is then determined from the differences in pulse arrival times.

an ideal option for our neutral detector. Among alternatives, a split wedge-and-strip anode, divided into two halves, has been used successfully to detect two-particle events, but detection of additional particles quickly becomes nontrivial.[14] A better alternative is a crossed delay-line (XDL) anode,[15, 16] instrumented to allow for detection of more than one particle on a single anode.[1] A simple schematic of an XDL anode is shown in Figure 2.5. The anode consists of overlaid, isolated wire grids of wire fingers attached to serpentine delay lines in the x and y directions.

The position of arrival of the amplified electron cloud from the MCPs is determined by measuring the arrival time of the resulting charge at either end of the delay line. In the x dimension, the arrival times of the charge signal at the two ends of the delay line are given by t_{x1} and t_{x2}, the length of the delay line is l, and the position is x. The time difference between the delay-line ends is given in equation 2.3 and the final position x is a given by equation 2.4.

$$\Delta t_x = t_{x1} - t_{x2} = \left[\left(\frac{\frac{1}{2}l+x_1}{V_{charge}}\right) - \left(\frac{\frac{1}{2}l+x_2}{V_{charge}}\right)\right] \tag{2.3}$$

$$x = \left(\frac{v_{charge}\cdot\Delta t_x}{2}\right) \tag{2.4}$$

In the y dimension, the position of arrival is calculated in the same way using the timing information from the y-axis delay line. Further calculations and calibration of the detector are discussed in Section 2.4.3.

The neutral multiparticle detector consists of a z-stack of three MCPs mounted above a four- quadrant crossed delay-line anode (QXDL) anode, shown schematically in Figure 2.6. Construction of the QXDL anode has been discussed in detail previously and is discussed only briefly here.[1] The QXDL anode is comprised of four XDL anodes laid

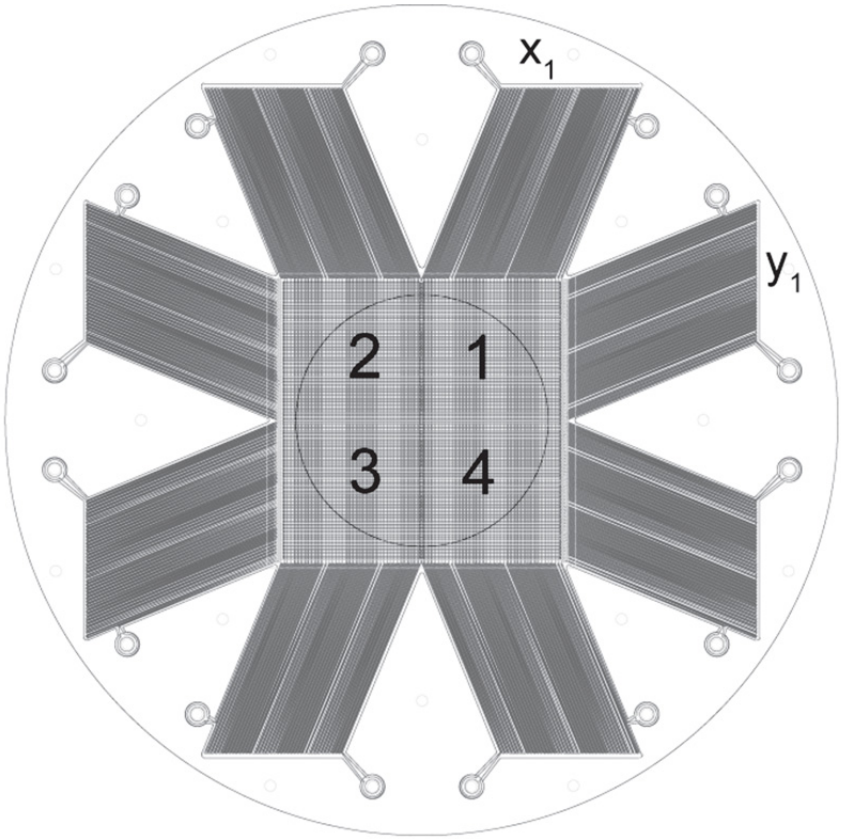

Figure 2.6. Schematic of a four quadrant crossed delay-line (QXDL) anode used for detection of coincident neutral particles in the PPC spectrometer.[1]

out in four independent isolated quadrants. Each quadrant of the anode can detect up to two particles provided that the second particle arrives after the minimum dead time of the electronics (~20 ns). Because the quadrants are independent, there is no dead time for events hitting different quadrants simultaneously. Thus, conceivably, up to four neutral particles can be detected at the same time. With sufficient temporal separation, up to eight neutral particles can be detected from a single dissociative event. In practice, and for this thesis, the typical dissociative event is confined to studies of two neutral fragments.

Delay signals from each quadrant are independently amplified using fast preamps, then sent to custom cascaded two-hit CFD/TACs (Siegmund Scientific). The output voltages are digitized using two 8-channel LeCroy Model 3351 12-bit peak-sensing ADC's. Timing information for each quadrant is provided from a TDC triggered by a delayed start pulse after laser shot, to account for the heavy particle time-of-flight, and stop pulses are taken from the start CFDs for the y-coordinate TACs for both particles one and two. The timing information is encoded using a LeCroy 3371 12-bit TDC. The total MCP charge and individual quadrant charges are then amplified and digitized with another LeCroy 3351 ADC. Like the photoelectron detector, the ADCs and TDCs for the neutral detector are also housed the CAMAC crate which interfaces with a PC. For the neutral detector x, y, and t values for each quadrant, as well as the total charge, are discriminated, histogrammed and written out using a custom-written LabVIEW data acquisition system, outlined in more detail in the thesis of Chris Johnson.[9] In addition to the ADC and TDCs for each detector, the CAMAC crate also houses a laser shot counter used to store the number of laser shots over a trapping cycle. The laser shot information

is also recorded using a hex scaler (Kinetic Systems 3615) housed in the CAMAC crate and can be used in order to sort events by trapping time.

2.4. Data Analysis and Calibration

Once raw data is collected, it needs to be sorted, processed from raw digital form into position and time information, and converted into relevant velocity and coincidence information. Each data set collected contains a large amount of information. The following sections describe the calculations involved to extract this information using an analysis code written in the Interactive Data Language (IDL).

2.4.1. Data Discrimination and Sorting

Before particle-velocity calculations are performed, data are discriminated by excluding neutral events without valid x, y, and t information from the QXDL and electrons without valid charge information from the wedge (Q_W), strip (Q_S), and zig-zag (Q_Z) or without time information from the electron detector.

Data are then sorted by desired multiplicity into the following three groups: (1) electron-only events, (2) N-heavy-particle-only events, and (3) N-particle events in coincidence with an electron. For example, in a data set, a stable channel is selected for by sorting for an electron in coincidence with one heavy particle (e^- + 1TAC); similarly, a dissociative channel is selected for by sorting for an electron in coincidence with two heavy particles (e^- + 2TAC).

The sorted data are written to new data files, loaded into the analysis code PATTI, and processed by a second discrimination step that removes contributions from electrons

not correlated with neutral events and neutrals from other parent masses, among other known concerns. Additional discrimination, such as charge-gating on the neutral-particle detector can be implemented after calibration.

2.4.2. Photoelectrons: Calibration and Kinematics

The raw data are then calibrated and converted into position and time information as outlined here. Determination of the position of arrival of the photoelectron cloud on the electron detector wedge-and-strip anode is determined by charge division between the wedge, strip, and zig-zag conductors is discussed earlier in section 2.3, where x and y positions are determined using equations 2.1 and 2.2.

In practice, capacitive coupling between the anode electrodes, known as "crosstalk," significantly complicates position determination. Crosstalk can be accounted for by careful calibration, as discussed in detail in the thesis of Chris Johnson.[9] An electron's time of arrival (z dimension) and thus its time of flight is determined as follows:

$$TOF = DMC_t * N + DAC_t \tag{2.5}$$

The multiplicative DMC_t and additive-offset DAC_t constants are determined by careful calibration using species with well-known electron affinities and electronic states such as F^-, O^-, I^-, or O_2^-. Inhomogeneous fields in the VMI detection setup require that calibration files be taken frequently and that each electron data set be carefully corrected and calibrated.

Electron-recoil velocities are determined from this position information using a scaled TOF. The x- and y-velocity components are given by:

$$v_x = \frac{x}{TOF - t_{cal}} \tag{2.6}$$

$$v_y = \frac{y}{TOF - t_{cal}} \tag{2.7}$$

The z-velocity component is determined relative to the effective TOF for a zero-energy electron, TOF_0:

$$v_z = \frac{\Delta v_z}{\Delta(TOF - t_{cal})}(TOF - t_{cal} - TOF_0) \tag{2.8}$$

Finally, electron kinetic energy eKE and the recoil angle from the polarization axis of the laser are calculated by:

$$eKE = \tfrac{1}{2} m_e\left(v_x^2 + v_y^2 + v_z^2\right) \tag{2.9}$$

$$\theta = arccos\left(\frac{v_y}{\sqrt{v_x^2 + v_y^2 + v_z^2}}\right) \tag{2.10}$$

2.4.3. Neutral Particles: Calibration and Kinematics

Although the neutral-particle detector is capable of detecting up to eight neutral particles in coincidence with a photoelectron, only two-body neutral dissociation events are discussed in this thesis. Therefore, discussion here is limited to only two-particle events. Details on three-body dissociation can be found in the thesis of John Savee[17] and symmetric four-body dissociation in the thesis of Todd Clements.[18]

Conversion of raw uncalibrated data for the neutral-particle detector is comparatively simple, involving a linear relationship between temporal/spatial coordinates and the recorded laboratory-frame values:

$$x_i = DMC_{x_i} * \Delta t_{x_i} + DAC_{x_i} \tag{2.11}$$

$$y_i = DMC_{y_i} * \Delta t_{y_i} + DAC_{y_i} \tag{2.12}$$

where *DMC* and *DAC* are multiplicative and additive-offset constants, respectively and Δt_{x_i} and Δt_{y_i} were determined using equation 2.3. The laboratory-frame positions are then converted to positions in the CM frame, x_{CM} and y_{CM}, using the following equations:

$$x_{CM} = x_i - x_0 \tag{2.13}$$

$$y_{CM} = y_i - y_0 \tag{2.14}$$

where x_0 and y_0 are offsets corresponding to the CM dissociation relative to the center of the detector. These offsets are set manually using an iterative process during the calibration step and provide flexibility in the beam centering on the QXDL.

Similarly, the CM time-of-flight t_{CM} for each particle is determined from the time of arrival t_{meas}:

$$t_{CM} = DMC_t * \Delta t_{meas} + DAC_t - \Delta t_{det} * |y_i| \tag{2.15}$$

where Δt_{det} is a correction factor to take into account the time required for a pulse to travel through a delay line and is experimentally determined. Using the ion beam velocity v_{beam} calculated from the beam energy E_{beam} as follows:

$$v_{beam} = \sqrt{\frac{2*E_{beam}}{M_{parent}}} \tag{2.16}$$

where M_{parent} is the mass of the parent ion. The timing information t_{CM} is then converted into a z position in the CM frame z_{CM} :

$$z_{CM} = v_{beam} * t_{CM} \tag{2.17}$$

The time-of-flight of the center-of-mass TOF_{CM} can now be determined using v_{beam} and the distance between the interaction region and the QXDL L, which is currently 1.347 m.

$$TOF_{CM} = \frac{L}{v_{beam}} \tag{2.18}$$

Using TOF_{CM} , the velocity vectors in the CM frame for each dimension are determined for each particle from the CM frame positions

$$v_x = \frac{x_{CM}}{TOF_{CM}} \tag{2.19}$$

where v_y and v_z are calculated in a similar way.

These velocity calculations work well to first order, but do not take into account the perturbation of measured recoil distances for particles ejected either forward or backward along the ion-beam axis arising from the projection of a three-dimensional sphere on the two-dimensional surface of the detector. That is, a particle ejected forward toward the QXDL arrives before the CM, causing underestimation of the particle-velocity vector. Conversely, a particle ejected backward away from the QXDL arrives after the CM, causing overestimation of the particle-velocity vector. This effect of “crushing” the three-dimensional sphere of recoiling particles onto the two-dimensional circular detector

surface is relatively small for KER < 1 eV, but additional geometric corrections are now implemented in the code. The crushing algorithm is outlined in detail in the thesis of John Savee.[17]

Typically the masses of a particular dissociation channel of interest are known and these products, denoted m_i for i fragments, are then used to calculated the kinetic energy of the fragment. However, on occasion, it is useful to calculate the masses of the fragments using the three-dimensional recoil radius at the detector and the parent mass.

$$m_{calc,i} = M_{parent} * \frac{d_1}{d_1+d_2} \tag{2.20}$$

$$d_i = \sqrt{x_{CM}^2 + y_{CM}^2 + z_{CM}^2} \tag{2.21}$$

These calculated masses can be particularly useful for identification of additional dissociation channels or to help differentiate between expected dissociation channels.

With the CM velocity vectors in hand, calculation of the CM kinetic energy release is determined using

$$KER = \tfrac{1}{2}\sum m_i * v_i^2 \tag{2.22}$$

From here, center-of-mass gating, discussed in the next section, is used to limit the contributions of false coincidence or competing mass channels.

2.4.4. Gating

The data can now be gated in various ways to improve resolution and examine various parameters of interest, including but not limited to, eKE, KER, total kinetic

energy (E_{TOT} = eKE + KER), the photoelectron-photofragment coincidence spectrum as well as various product angular distributions. To start, contributions from false-coincidence events or competing mass channels are minimized by centroid gating. Centroids are based on the conservation of momentum between particles as defined in equation 2.23 for the *z* dimension, are calculated in terms of position-of-arrival of the CM at the detector in the *x*, *y* and *z* dimensions.

$$centroid_z = \sum m_i * v_{z,i} \tag{2.23}$$

Here m_i is the assigned mass, $v_{z,i}$ is the CM velocity in the z direction and centroids for the *x*, and *y* dimensions are calculated in a similar way. Ideally, the centroid for two fragments from the same event from the assigned mass channel should have a centroid value of zero. However, centroids can deviate from zero due to the finite velocity and angular distributions of the parent ion beam, the presence of other fragment channels, false coincidences and the inherent resolution of the detector. For example, when a single m/z is trapped, photodetachment from more than one anion can lead to detection of one photoelectron and an uncorrelated neutral, as one example of false-coincidence. In multi-mass mode false-coincidence events can arise from detection of other m/z ions. In either case, a narrow gate is used to minimize these false-coincidence events by filtering out events beyond the gate.

The total charge picked off the MCPs of the QXDL is proportional to the number of neutral events hitting the detector. Charge gating provides an additional gating mechanism to help limit the effects of false-coincidence events, in particular boarder hits. For example, a heavy particle landing on the border between QXDL quadrants can

register a hit on both quadrants and will therefore be sorted as two heavy particle event. However, this single particle will only have a single charge event on the MCPs and can therefore be removed with charge gating.

In the case where the product masses for a dissociative channel are dramatically disparate or when two competing product channels are present, it can be advantageous to implement a second iteration of CM gating where ranges of apparent mass matching the dissociation channel of interest are defined. Events outside these separate mass-gates are discarded. Although this additional mass-gating can be useful for diminishing the effects of false coincidence, for example, it is only useful for resolving mass channels that can already be resolved with reasonable CM gating.

Data can also be gated along the trap-time dimension, providing information on the time-dependence of the internal energy of ions confined in a cryogenic environment. For example, this potentially allows for an examination of the effects of radiative cooling of precursor anions, including changing FC overlap. For the IR excitation experiments discussed in Section 2.5 and Chapter 5, the effects of intramolecular vibrational relaxation (IVR) on the excited ions can be explored by gating along the trap-time dimension.

Finally, additional resolution can be gained from the eKE spectrum by slicing along the z dimension due to the relatively poor time resolution of our electron detector and the nonlinearities in the time to v_z conversion discussed in Section 2.3. Optimum

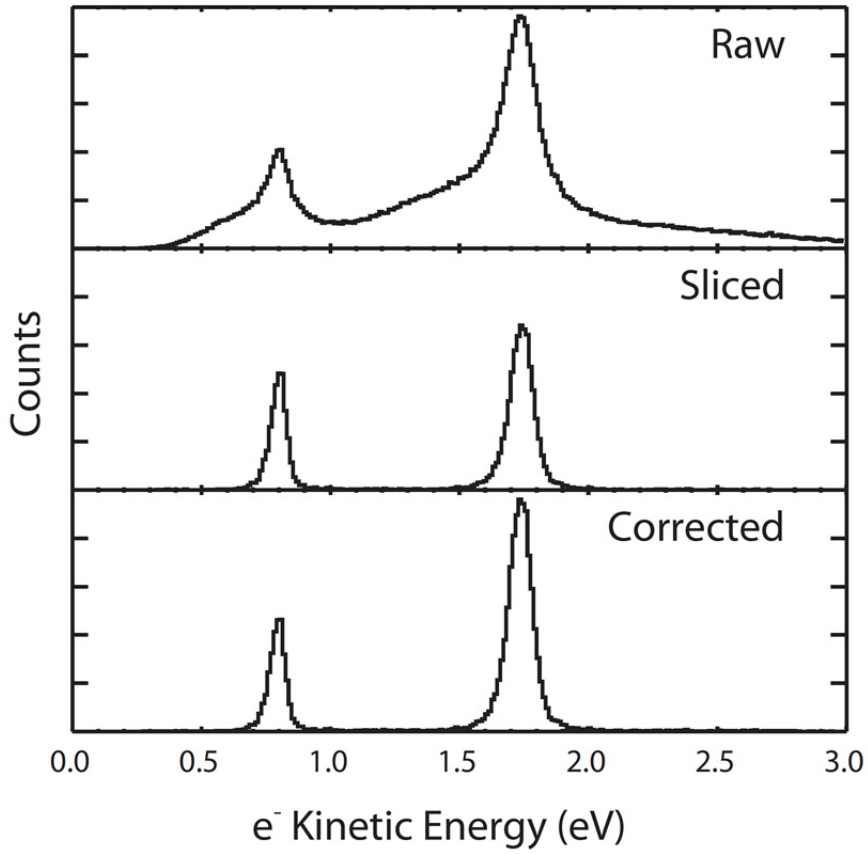

Figure 2.7. Effects of slicing and slice correcting for I^- at 258 nm. The raw spectrum is shown on top, the sliced in the middle, and the sliced and corrected on the bottom. Note the effect of slicing on the peaking weighting, and the retrieval of proper weighting with addition of correction.

resolution is achieved by selecting an equatorial z slice about $v_z \sim 0$ at the cost of signal-to-noise and an induced detector acceptance function (DAF). The DAF depends on both eKE and ejection angle θ, resulting in an underrepresentation of apparent intensities of electrons with high eKE. The corrected relative intensities as a function of energy and θ are recovered by DAF correction as follows:

$$DAF = \begin{cases} \frac{|v| \sin\theta}{v_z^{slice}}, & |v| > v_z^{slice}, \theta(|v|) > \theta^{slice}(|v|) \\ 1, & |v| \leq v_z^{slice} \\ 1, & \theta(|v|) \leq \theta^{slice}(|v|) \end{cases} \quad (2.24)$$

The effects of DAF correction are shown in Figure 2.7 for the photoelectron spectrum of I^- at 258 nm. The resolution of the peaks corresponding to the two spin orbit states $^2P_{1/2}$ and $^2P_{3/2}$ are considerably improved from ΔeKE/eKE ~ 11% to ~ 3.5 % at eKE = 0.797 eV and ΔeKE/eKE ~ 7.3% to ~ 2.5 % at eKE = 1.74 eV electron kinetic energy upon z-velocity slicing, respectively. Notice that z-slicing without correction induces a decrease in the relative intensity of the higher-eKE ground-state peak at 1.74 eV and that the correction properly retrieves the relative intensity of the two features.

2.4.5. Coincidence Calculations

The total kinetic energy release E_{TOT} can now be calculated from the electron kinetic energy and fragment kinetic energies by the relationship:

$$E_{TOT} = eKE + KER \quad (2.25)$$

from which the internal energy of the fragments can be determined, assuming the following relationships:

$$E_{TOT} = KE_{MAX} - E_{int} \quad (2.26)$$

where KE_{MAX} was defined in equations 1.11 and 1.12 in Chapter 1. Features observed in the E_{TOT} spectrum directly reflect internal-energy partitioning in the fragments. In the case where one fragment acts as a spectator to the reaction, the spectrum reflects partitioning of internal energy in the other, excited fragment. This is the case for both the carboxyl free radicals and F-initiated hydrogen-abstraction reactions discussed in the following chapters.

It can be informative to examine the photoelectron-photofragment coincidence (PPC) spectrum, a two-dimensional histogram of the correlated eKE and KER data, N(eKE,KER). These spectra directly display the partitioning of kinetic energy between the photoelectron and the photofragments. Schematic examples of PPC spectra for direct and indirect photodetachment are shown in Figure 1.5 and are discussed in some detail Chapter 1.

2.5. Implementation of IR Excitation/Vibrational Pumping

The major instrumentation development for this thesis was implementation of the tunable-IR laser system. The laser system itself is discussed in detail in Section 2.2.2. This section focuses on experimental modifications needed to couple the new laser system into the existing PPC spectrometer, including introduction of a mirrored neutral-beam block in the TOF region[19] and implementation of an interleaved data acquisition sequence. The additional data processing necessary for these IR excitation experiments is also discussed.

2.5.1. Mirrored Neutral-Beam Block and Laser Alignment

Pulsed, tunable-IR radiation was steered from the laser system to the PPC instrument via protected gold turning mirrors, then the beam was collimated and decreased in size using a telescope setup consisting of two concave mirrors, and finally entered the instrument by means of a periscope. Because of fairly substantial power loss (due to water-line absorption), the entire beam path was enclosed and dried using an FT-IR purge gas generator (Parker, flow 56 LPM) to lower the relative humidity of the laser-beam path at room temperature to ~1−5%. The IR radiation then entered the TOF region through a 2 inch CaF_2 window on the side of the vacuum chamber. The laser pulse entered the chamber at a 50° angle relative to the ion-beam axis, and was coupled into the experiment via a gold mirror (1 x 3 cm) mounted at roughly 25° relative to the ion-beam axis so that the radiation was counter-propagated along the ion-beam axis. The mirror itself was mounted on the aluminum L-bracket (1 x 2 in.) of the existing neutral-beam block electrode, shown in Figure 2.8. This configuration allowed for maximal overlap with the elongated ion packet (~30 cm, dictated by the length of the HV switch).

Counter-propagating the laser pulse relative to the direction of ion travel enabled anions with velocity v_{anion} to interact with Doppler-shifted photons with energy $\tilde{\upsilon}'$. This Doppler shift is taken into account by the following relation when setting the IR-wavelength output of the laser, $\tilde{\upsilon}$:

$$\tilde{\upsilon}' = \tilde{\upsilon}\left(1 - \frac{v_{anion}}{c}\right) \tag{2.27}$$

Under our experimental condition ($\tilde{\upsilon}$ ~3000 cm^{-1}, anion-beam energy ~7 keV), the Doppler shift is only a ~2 cm^{-1}. The IR wavelengths reported

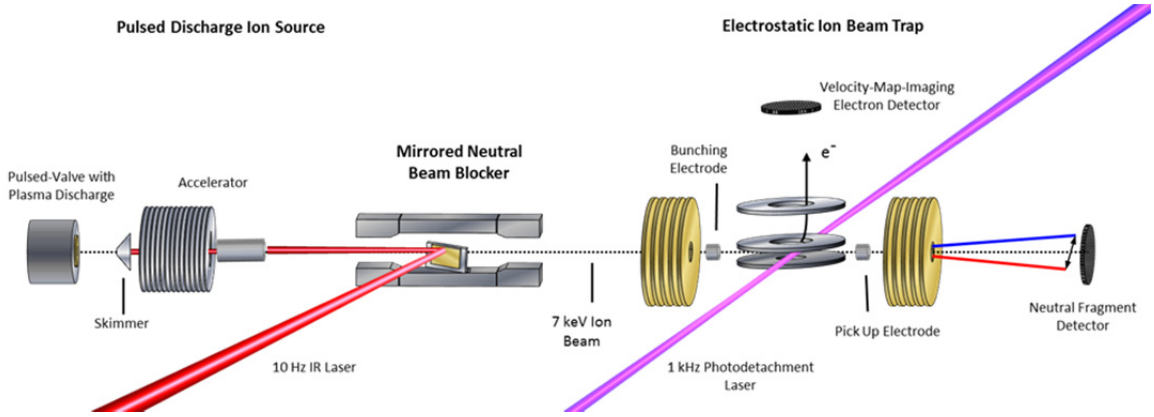

Figure 2.8. Simplified schematic of the PPC spectrometer including the new mirrored neutral beam blocker (MNBB) used for counter-propagation of the IR laser beam relative to the fast ion beam.

throughout this thesis correspond to the frequency observed by the anions, $\tilde{\upsilon}'$, corrected accordingly from the IR laser output.

Optimization of IR overlap spatially and temporally with the anion packet was carried out using photodetachment of NO^-, measured using ion signal intensity on an ion detector placed directly into the beam axis in the mass-gate region.[19] Quick alignment checks were carried out on a regular basis, looking at the decrease in ion intensity on the detector-region ion detector normally used during ion tuning, and achieving up to 90% photodepletion of the anion beam. The IR-excitation setup was characterized by measuring photodetachment cross-sections of NO^- as measured by anion photodepletion using the ion detector in the mass gate region, averaging over 64 laser on/off cycles to account for any fluctuations in the ion source. The measured cross-section, including pronounced autodetachment features, was found to be in good agreement with previous literature.[19] Although far less complicated than a PPC experiment, this photodetachment cross-section measurement showed that the laser system was calibrated and the experimental setup optimized.

2.5.2. Interleaved Experimental Setup

In the case of direct absorption in an ion beam, the transition probability of exciting a particular anion vibrational mode is limited to a maximum of 50% for a two level system based on the rates of absorption compared to spontaneous and stimulated emission.[20] Although techniques such as rapid adiabatic passage have been shown to achieve 100% excitation,[21] these techniques need 1) a very narrow bandwidth tunable monochromatic light source and 2) the vibrational frequency of the molecule to excite

needs to be known precisely. Although the second requirement can be achieved by scanning through a range of frequencies with a tunable light source, the bandwidth of our tunable laser system (Surelite EX pumped LaserVision OPO/OPA system, width > 1 cm^{-1}) is not narrow enough to carry out a rapid adiabatic passage excitation. Thus, PPC experiments carried out on an IR-irradiated anion packet contain data from both excited and nonexcited (cold) anions. It is therefore necessary to perform some type of background subtraction to remove contributions from nonexcited anions. However, the intensity of ions formed in the source prior to IR irradiation can fluctuate over the course of an experimental run. In order to minimize the effects of source drift, an interleaved 20 Hz experimental setup was implemented for IR excitation.

One benefit of implementing the EIBT into the PPC spectrometer has been the decoupling of the source-laser and photodetachment-laser repetition rates. As mentioned in section 2.1, the source laser typically ran at 10 Hz, while the experimental photodetachment laser operated at 1 kHz. Decoupling the source and experimental repetition rates provides flexibility in the rate at which the source can run and offers an ideal means for introducing an interleaved experimental setup. In the IR experiments, the source operated at 20 Hz, with the IR laser at 10 Hz (to ensure that every other ion packet is irradiated). This configuration allowed the PPC experiment to still be carried out at 1KHz, but with a correspondingly shorter trapping time in the EIBT (50 ms, instead of the 100 ms used for a 10 Hz experiment). The PPC experiment was otherwise carried out in the normal way.

In order to distinguish between data collected with and without IR (designated IR, no-IR), an IR-flag signal was produced every time the IR laser triggers and sent to a channel in the hex scaler (Kinetic Systems 3615) housed in the CAMAC crate. This flag was read in by the data acquisition computer and was recorded with the rest of the PPC data as an additional column in the raw data file later used to separate the interleaved experimental data.

2.5.3. IR Vibrational Excitation Data Analysis

The IR and no-IR data sets were first sorted using the IR-flag into new individual data files for IR or no-IR events. These data files were then calibrated and processed in the usual way, as outlined in Section 2.4. Calibrations for IR and no-IR data from a single file are identical, as the data in each were collected over the same time period, so calibration done after separation is not as cumbersome as it might appear.

Once calibrated, the no-IR data was background-subtracted from the IR data to remove the contribution of unexcited anions (the unexcited fraction $n_{no\text{-}IR}$) as part of the process of determining the effects of IR irradiation. A difference plot is produced by direct subtraction, IR – no-IR, with no weighting to adjust for the excitation fraction. An example for the F^-H_2O system discussed in Chapter 5 is shown in Figure 2.9. Here, negative features correspond to areas of greater intensity in the no-IR spectrum, and positive features correspond to areas of increased intensity in the IR spectrum.

One of the major concerns for these experiments was whether the observed difference plot (Figure 2.10) showed statistically significant events. Even in the case of a

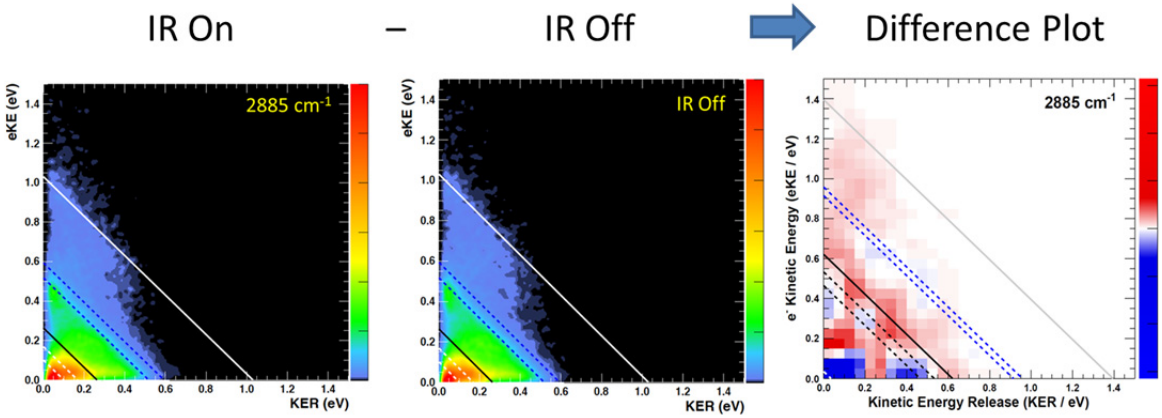

Figure 2.9. IR, no-IR, and difference plots for $F^{-}H_2O$ at ν_{IR} = 2885 cm^{-1}.

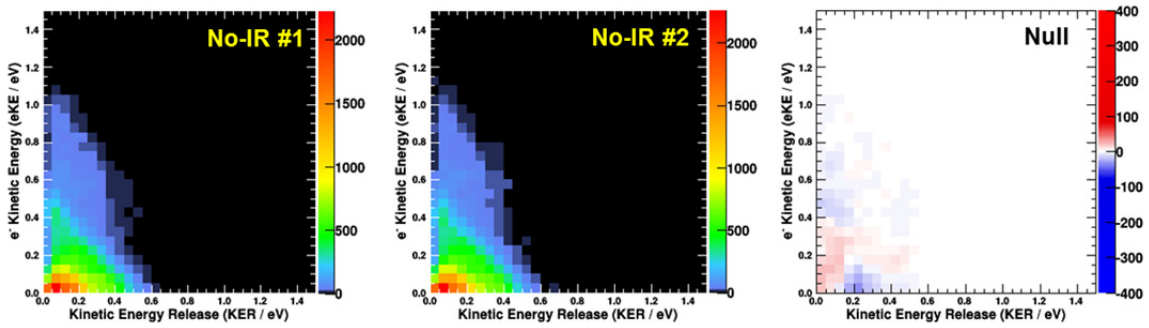

Figure 2.10. Experimental null difference plot. Each no-IR plot contains ~ 39,000 events, differing by ~100 events, within the expected experimental uncertainty.

null experiment where data is obtained in an interleaved fashion but the anion packet is not irradiated, subtraction of one spectrum from another yields a difference spectrum owing to the Poisson error per histogram bin ($\sqrt{n}$) associated with this counting experiment. Shown in Figure 2.10 the null difference plot produces non-zero values resulting in mottled pattern of positive and negative features. Encouragingly, this mottled pattern is different from the difference plot obtained for 2885 cm^{-1}.

In order to assess what fractional excitation of the anion packet was required to produce a reliable signature in the difference plots, Monte Carlo simulations were carried out for both a null experiment and by estimating an induced change, scaled by an excitation fraction f. The approach taken here is to simulate two coincidence spectra, using two random distributions D_1 and D_2 where D_1 represents a no-IR case and D_2 an IR case with n_{IR} events corresponding to an excited fraction which are as follows:

$$n_{IR} = f(n_{total}) \tag{2.28}$$

$$n_{no\text{-}IR} = (1 - f)n_{total} \tag{2.29}$$

$$D_2 = n_{IR} + n_{no\text{-}IR} \tag{2.30}$$

where $n_{no\text{-}IR}$ is the remaining unexcited events in D_2 and n_{total} is the total number of events in D_2. From these a difference plot can be calculated and compared to the programmed changes (true changes plot) where n_{IR} events are moved from one set of Gaussian distributions (no-IR), representing the cold spectrum, to a second set of Gaussian distributions (IR) representing the IR excited spectrum. Thus the true changes plot will

show this shuffling of the n_{IR} events as programed and, for a null plot, this means $n_{IR} = 0$ and there will be no change due to excitation.

Each random distribution consists of a 2D histogram with 30x30 bins (900 bins total) with a bin width of 0.05 eV on a side. These histograms are each filled using a random number generator with n=220,000 events, consistent with the amount of data in the unsliced 2885 cm^{-1} experimental data used to produce the difference plots shown in Figure 2.9 and discussed in detail in Chapter 5. D_1 consists of 198000 events (90% of n) distributed in a 2D Gaussian centered at (KER,eKE) = (0.2 eV, 0.15 eV), with widths on the KER axis of 0.25 eV and on the eKE axis of 0.15 eV. The remaining 22000 (10% of n) events are distributed in a second Gaussian centered (KER,eKE) = (0.15 eV, 0.65 eV), with widths on the KER axis of 0.15 eV and on the eKE axis of 0.10 eV. The centers of these Gaussians are marked with an x in Figure 2.11. This process is repeated for the D_2 using the same Gaussian centers, widths and fractions. These two distributions now represent an interleaved experiment.

The two random distributions are then subtracted ($D_2 - D_1$) to produce the difference plot for the null experiment shown in Figure 2.11(d). Logically, if the two distributions are identical (i.e. not randomized from each other), taking the difference would produce the true changes plot (Figure 2.11(c)) where no change is observed. The mottled pattern of positive and negative events observed in the difference plot therefore reflects the randomization implemented when filling the Gaussians in each histogram, consisting of fewer than 8000 events (sum of the absolute value of each bin over all bins

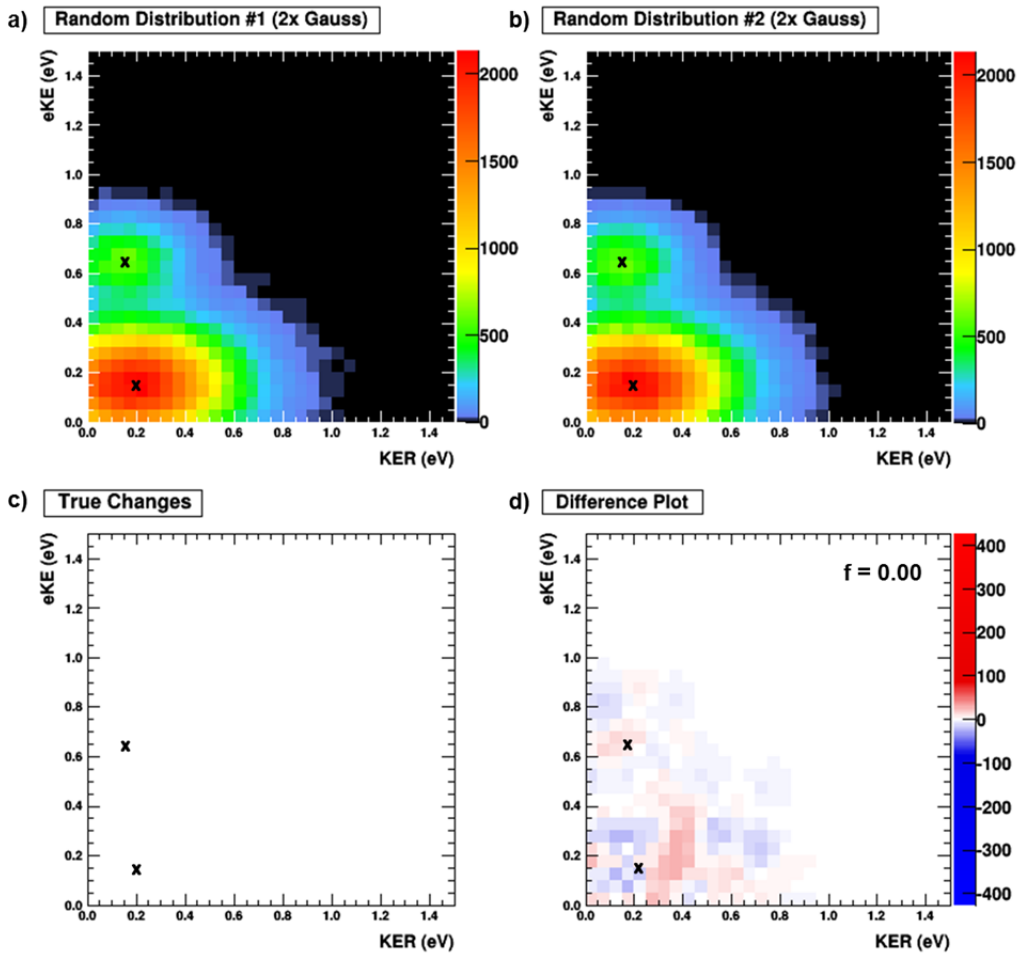

Figure 2.11. Monte Carlo simulation and difference plots for a null (no-change) experiment where each random distribution plot (a and b) consists of two Gaussians (centers marked with a black x) filled with 220,000 events using a random number generator. For the null plot $n_{IR} = 0$ and therefore the true changes plot (c) is blank. The difference plot (d) is formed by subtracting D_1 from D_2.

in the difference plot) out of the 440,000 events included in the difference plot (220,000 from each random distribution histogram).

A simulated difference plot using an "IR" experiment with an excitation fraction of f = 0.05 is shown in Figure 2.12. The D_1, representing the "no-IR" plot, is first filled as described above with 220,000 events using a random number generator and the two original no-IR Gaussian distributions. To simulate the effects of IR excitation, a small fraction of events (f = 0.05, or 11,000 events) are removed from these two no-IR Gaussians again using a random number generator, representing the loss of the original distribution due to IR excitation, these are then distributed into two additional IR Gaussians representing the coincidence spectrum for IR-excited anions. These additional Gaussian distributions are shifted from the original two by eKE = 0.3 eV and KER = 0.05 eV to reflect the energy of the IR photon (2885 cm^{-1}, 0.35 eV), representing the excited fraction n_{IR} in the raw "IR" spectrum shown in D2. Specifically, the IR Gaussians are centered at (KER,eKE) = (0.25 eV, 0.45 eV) and (0.2 eV, 0.95 eV) with the same KER-widths (0.25 and 0.15 eV, respectively) and eKE-widths (0.15 and 0.10 eV, respectively) as the two no-IR Gaussians in the random distribution. The centers of the no-IR Gaussians are again marked with a black x in Figure 2.12 and the centers of the new IR Gaussians are now marked with a red and white x. This shuffling of events is carried out so that the overall number of events in the D_2/"IR" histogram is still 220,000 events, equal to the number in the D_1/"no-IR" histogram. Although there are some noticeable differences between the random distributions, particularly in areas where there was little to no signal in the "no-IR" spectrum that are now populated in the "IR" spectrum, the

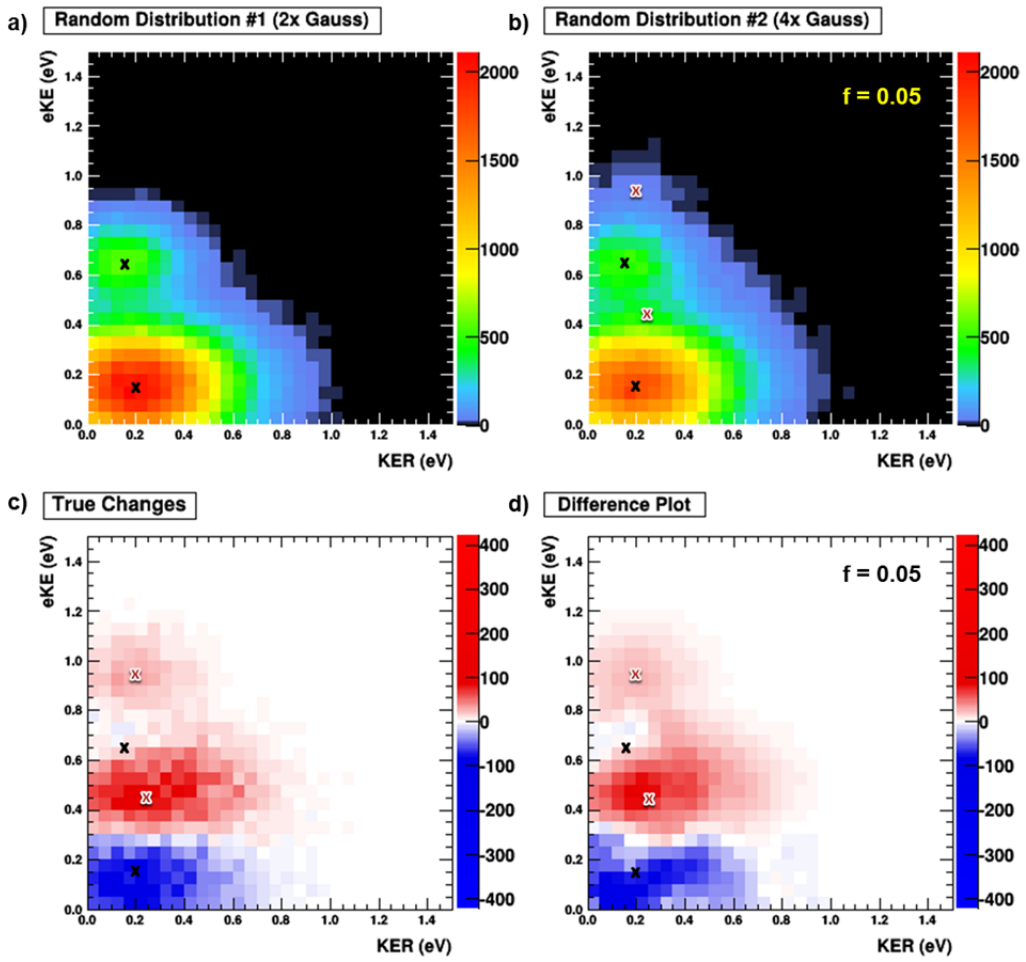

Figure 2.12. Monte Carlo simulation and difference plots for a f = 0.05 experiment where each random distribution plot consists of the two no-IR Gaussians (centers marked with a black x) filled with 220,000 events using a random number generator. 5% of the events in D_2 were then shuffled into the two additional IR Gaussians (centers marked with a red and white x). The true changes are dependent on the excitation fraction f = 0.05 and represent the programmed shuffling of n_{IR}. The difference plot is formed by subtracting D_1 from D_2.

overall shape remains largely the same and is still dominated (as expected) by the unexcited fraction.

The IR difference plot is again produced by subtracting the random distributions (D_2 - D_1 or "IR" – "no-IR") and a simulated difference plot using an excitation fraction of f = 0.05 is shown in Figure 2.12(d). The programmed shuffling of n_{IR} events is shown in the true changes histogram in Figure 2.12(c), representing the actual differences that are expected to be recovered in the difference plot. In this case, the difference plot consists of two prominent areas of suppression and two prominent areas of enhancement in remarkably good agreement with the expected true changes, recovering the general shape of the implemented changes.

A fraction of f = 0.05 corresponds to the shuffling of 11,000 events for a total of 22,000 events in the true changes plot (11,000 enhancement/positive events and 11,000 suppression/negative events). Integration over the absolute value of events shown in the true changes plot only recovers ~13,500 events. given the overlap between enhancement and suppression features, this is reasonable. For comparison, integration over the absolute value of events in the difference plot gives ~ 17,000 events for f = 0.05, indicating a contribution from the background uncertainty resulting from the randomization of the spectra (ie. what was observed for the null plot). Integration over all values for both the true changes and difference plots was zero, as expected.

To answer the question of what is the smallest excitation fraction needed to observe an actual difference in the difference plot, simulations at f = 0.01, 0.02, 0.05 and 0.1 were carried out. The simulated difference plots for each are shown in Figure 2.13.

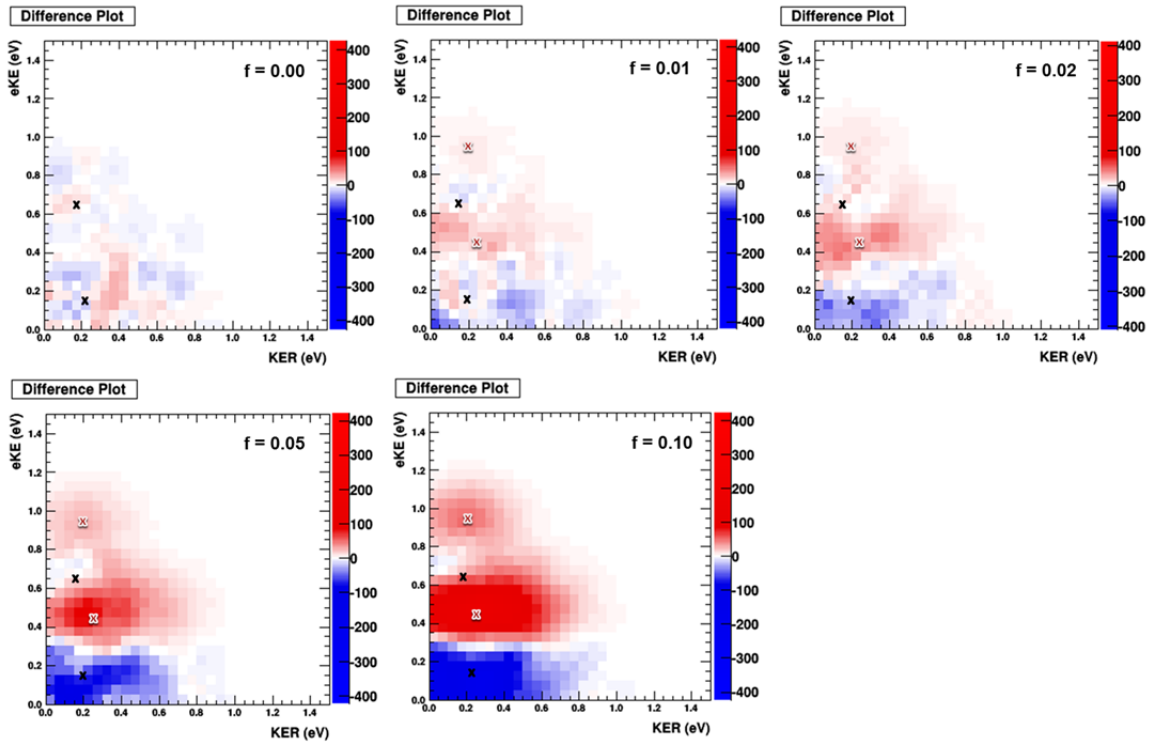

Figure 2.13. Comparison of simulated differences plots for f = 0.00, 0.01, 0.02, 0.05 and 0.10. Monte Carlo simulation and difference plots for various f values where each random distribution plot consists of two no-IR Gaussians (centers marked with a black x) filled with 220,000 events using a random number generator. The indicated fraction of events in D_2 were then shuffled into two additional IR Gaussians (centers marked with a red and white x). The difference plot is formed by subtracting D_1 from D_2.

Although there are hints of the pattern for the programmed shuffling of n_{IR} in the f = 0.01 plot, the differences are still noisy without clear distinction between positive and negative Gaussians. By the time f = 0.02 the pattern of changes is starting to become clear in the difference plot, although the edges between the enhancement and suppression features are not well defined like they are in in the f = 0.05 and f = 0.10 difference plots.

These MC simulations show that it is possible to recover the implemented changes using a difference plot for fractions as small as f = 0.02 from an interleaved experiment. However, a true discussion of these simulations would not be complete without a discussion of their limitations and the simplifications implemented during their design. One major simplification was assuming that the random distributions representing the interleaved experiment have exactly the same number of events. Although careful consideration was taken to ensure that the interleaved IR and no-IR experiments were carried out in as identical a way as possible, even without IR excitation the data can vary in number of events between the two interleaved raw data sets due to the expected Poisson error leading to a larger number of events in the difference plot. This uncertainty is partially accounted for in the simulation by using the random number generator to simulate this uncertainty on a bin by bin basis, as can be seen in the null plot, but does not directly address any overall differences in numbers of events. Experimentally these differences in counts were found to be within the expected error and did not systematically favor either the IR or no-IR cases. Encouragingly, the simulated null plot (Figure 2.11) is very similar to the experimental null plot (Figure 2.10) and thus these

differences in counts are not expected to play a major role in the experimental difference plots.

A related simplification is the assumption that the photodetachment cross sections for both the ground state and vibrationally excited anions are the same. The shuffling of an equal number of events from the first two no-IR Gaussians (suppression) into the additional IR Gaussians (enhancement) in the "IR" histogram assumes that the likelihood of detecting these events is the same, corresponding to equivalent cross sections for the two states. If, however, the photodetachment cross section for the excited anions (represented by the n_{IR} portion of D_2) is larger, the assumption that n_{IR} events are shuffled from the no-IR Gaussians directly to the IR Gaussians breaks down.

If the excitation fraction f is well known, the IR-excited spectrum could be extracted by scaling the no-IR spectrum with f. In practice, however, determination of f is nontrivial. Ideally what is needed is a feature that is absent from the excited spectrum but appears in the nonexcited spectrum, in a unique portion where it is easy to distinguish. Unfortunately, however, the F^-H_2O system contains no easily discernable feature that meets these requirements. Instead, it is necessary to rely on the appearance of signal at greater energies than accessible in the nonexcited spectrum and to work back to an excitation fraction. Clearly, determination of the excitation fraction of ions must be addressed on a system-by-system basis.

2.6. Conclusion

This chapter has briefly described the major components of the fast-ion-beam photoelectron-photofragment coincidence spectrometer, including both the

photodetachment and vibrational pumping laser systems. The implementation of an IR laser system for vibrational pumping, including the modifications to the neutral beam block for coupling into the existing instrument were discussed. A brief outline of data calibration and analysis was presented for both the traditional PPC experiments and for PPC experiments with the addition of vibrational excitation. Finally, MC simulations of the IR difference plots were carried out, demonstrating that even with small excitation fractions ($f \geq 0.02$) the general effects of excitation are easily observable in the difference plot.

2.7. References

1. Hanold, K. A.; Luong, A. K.; Clements, T. G.; Continetti, R. E., Photoelectron-Multiple-Photofragment Coincidence Spectrometer. *Review of Scientific Instruments* **1999,** *70* (5), 2268-2276.

2. Johnson, C. J.; Shen, B. B.; Poad, B. L. J.; Continetti, R. E., Photoelectron-Photofragment Coincidence Spectroscopy in a Cryogenically Cooled Linear Electrostatic Ion Beam Trap. *Review of Scientific Instruments* **2011,** *82* (10), 105105.

3. Continetti, R. E., Coincidence Spectroscopy. *Annual Review of Physical Chemistry* **2001,** *52* (1), 165-192.

4. Wiza, J. L., Microchannel Plate Detectors. *Nuclear Instruments and Methods 162*, 587-601.

5. de Bruijn, D. P.; Los, J., Time and Position-Sensitive Detector for Dissociative Processes in Fast Beams. *Review of Scientific Instruments* **1982,** *53* (7), 1020-1026.

6. Levy, D. H., Laser Spectroscopy of Cold Gas-Phase Molecules. *Annual Review of Physical Chemistry* **1980,** *31* (1), 197-225.

7. Lu, Z.; Continetti, R. E., Dynamics of the Acetyloxyl Radical Studied by Dissociative Photodetachment of the Acetate Anion. *The Journal of Physical Chemistry A* **2004,** *108* (45), 9962-9969.

8. Lu, Z.; Hu, Q.; Oakman, J. E.; Continetti, R. E., Dynamics on the HOCO Potential Energy Surface Studied by Dissociative Photodetachment of $HOCO^-$ and $DOCO^-$. *The Journal of Chemical Physics* **2007,** *126* (19), 194305.

9. Johnson, C. J. Investigation of the reaction of OH and CO to form H and CO_2 by Photoelectron-Photofragment Coincidence spectroscopy in a cryogenic ion beam trap Investigation of the Reaction of OH and CO to form H and CO_2 by Photoelectron-Photofragment Coincidence Spectroscopy in a Cryogenic Ion Beam Trap. University of California San Diego, 2011.

10. Moore, J. H.; Davis, C. C.; Coplan, M. A.; Greer, S. C., *Building Scientific Apparatus*. 4th ed.; Cambridge University Press: Cambridge, UK ; New York, 2009; 647 pages.

11. Eppink, A. T. J. B.; Parker, D. H., Velocity Map Imaging of Ions and Electrons Using Electrostatic Lenses: Application in Photoelectron and Photofragment Ion Imaging of Molecular Oxygen. *Review of Scientific Instruments* **1997,** *68* (9), 3477-3484.

12. Guyer, D. R., LaserVision OPO User Manual. 2011; p 2.

13. Martin, C.; Jelinsky, P.; Lampton, M.; Malina, R. F.; Anger, H. O., Wedge-and-Strip Anodes for Centroid-Finding Position-Sensitive Photon and Particle Detectors. *Review of Scientific Instruments* **1981,** *52* (7), 1067-1074.

14. Continetti, R. E.; Cyr, D. R.; Osborn, D. L.; Leahy, D. J.; Neumark, D. M., Photodissociation Dynamics of the N3 Radical. *The Journal of Chemical Physics* **1993,** *99* (4), 2616-2631.

15. Friedman, P. G.; Cuza, R. A.; Fleischman, J. R.; Martin, C.; Schiminovich, D.; Doyle, D. J., Multilayer Anode with Crossed Serpentine Delay Lines for High Spatial Resolution Readout of Microchannel Plate Detectors. *Review of Scientific Instruments* **1996,** *67* (2), 596-608.

16. Siegmund, O. H. W.; Treason, A. S.; Vallerga, J. V.; Hull, J., Cross Strip Imaging Anodes for Microchannel Plate Detectors. *IEEE Transactions on Nuclear Science* **2001,** *48* (3), 430-434.

17. Savee, J. D. An Experimental Probe of Electronic Interactions in Excited Molecules Produced By Charge Exchange. University of California, San Diego, 2009.

18. Clements, T. G. Multi-Body Dissociative Photodetachment Dynamics of Small Molecular and Cluster Anions. University of California, San Diego, 2002.

19. Otto, R.; Ray, A. W.; Daluz, J. S.; Continetti, R. E., Direct IR Excitation in a Fast Ion Beam: Application to NO^- Photodetachment Cross Sections. *EPJ Techniques and Instrumentation* **2014,** *1* (1), 3.

20. Bernath, P. F., *Spectra of Atoms and Molecules*. 2nd ed.; Oxford University Press: Oxford ; New York, 2005; p xiv, 439 pages.

21. Liedenbaum, C.; Stolte, S.; Reuss, J., Inversion Produced and Reversed by Adiabatic Passage. *Physics Reports* **1989,** *178* (1), 1-24.

Chapter 3: State-Resolved Predissociation Dynamics of the Formyloxyl Radical

3.1. Introduction

As an intermediate in the reaction OH + CO → H + CO_2, the formyloxyl radical (HCO_2) is of particular interest for both atmospheric and combustion chemistry.[1-4] It also serves as a prototype for more complex carboxyl free radicals such as CH_3CO_2,[5] $C_6H_5CO_2$, and HC_2CO_2. However, the formyloxyl radical has proven difficult to characterize, both experimentally and theoretically. Experimentally this radical presents a challenge as it has a short lifetime and is metastable with respect to dissociation to H + CO_2.[6-9] Kim *et al.* carried out the first photoelectron spectroscopy study of the system, revealing the presence of three low-lying electronic states ($^2A_1$, $^2B_2$, and $^2A_2$) as predicted by Peyerimhoff *et al.* and Feller *et al.* in the 1980's.[10, 11] Theoretical treatments of the HCO_2 radical are difficult owing to the presence of these three low-lying electronic states.[10-17] The near degeneracy of these states makes determination of the ground state difficult, requiring high levels of theory because of strong vibronic coupling. These interactions result in strong pseudo-Jahn-Teller (PJT) coupling that distorts the expected C_{2V} ground-state equilibrium geometry.[18, 19] High-resolution measurements by Garand *et al.* using slow photoelectron velocity-map imaging (SEVI) spectroscopy coupled with high-level *ab initio* calculations have recently assigned many of the vibrational features in the experimental spectra, and unambiguously assigned the $^2A_1$ state as the ground state for both HCO_2 and its isotopolog DCO_2.[9]

The most challenging aspect of studying the neutral formyloxyl radical is the rapid predissociation $HCO_2 \longrightarrow H + CO_2$. Previously, the dynamics of this process have been studied by examining the dissociative photodetachment (DPD) of HCO_2^- / DCO_2^- anions using photoelectron–photofragment coincidence (PPC) spectroscopy.[8] It was found that all three low-lying electronic states dissociate to $H + CO_2$, with resolved bending progressions in the $^2A_1/^2B_2$ region of the photoelectron spectrum. Moreover, the CO_2 product was produced with low rotational excitation allowing excitation in the O−C−O bending mode ($\nu_2 = 2, 3, 4, \ldots$) to be observed in the photofragment translational energy release spectrum. Subsequently, Ma and Guo carried out a full-dimensional quantum-dynamics study of the photodetachment of HCO_2^- using an exact wavepacket method on the Lakin–Troya–Schatz–Harding (LTSH) potential energy surface (PES) for the reaction $OH + CO \longrightarrow H + CO_2$.[3, 20] Their calculated absorption spectrum for HCO_2^- captured elements of the experimental photoelectron spectra, but more interestingly predicted distributions for the product CO_2 vibrational states resulting from the predissociation of different vibrational levels in the neutral formyloxyl radical. In contrast to the earlier experiments,[8] their calculations predicted that at low levels of formyloxyl radical excitation the ground vibrational state of the CO_2 fragment is the most populated.

To further examine the dissociation dynamics of the formyloxyl radical, the previous study of the DPD of HCO_2^- / DCO_2^- anions has been extended using a cryogenically cooled electrostatic ion-beam trap (EIBT) coupled with a PPC spectrometer. The experiments reported here were carried out at a photon energy of 4.27 eV (290 nm), close to the photodetachment threshold (EA (DCO_2) = 3.52 eV),[9] and are restricted to the deuterated anion DCO_2^- as a result of detection efficiency. From these

results, experimental ν_2 bending vibrational-state distributions for the CO_2 product as a function of internal energy in the DCO_2 radical intermediate were extracted. Although the intermediate-radical electronic and vibrational states are not fully resolved in the photoelectron spectrum, a strong dependence on internal energy and significant excitation in the CO_2 products are observed, providing a direct experimental comparison to the product state distributions predicted by Ma and Guo.[20]

3.2. Experimental Methods

These experiments were carried out on a purpose-built PPC spectrometer, described in detail elsewhere.[21, 22] The deuterated formate precursor anion, DCO_2^-, was synthesized using a coaxial-pulsed discharge acting upon a supersonic expansion of O_2 passed over perdeuterated formic acid held at room temperature and then crossed by a 1-keV electron beam. The anions were accelerated to 7 keV, re-referenced to ground, mass-selected by time-of-flight, and then confined in a cryogenically cooled EIBT for 500 ms. The trapped oscillating ions were phase-locked to the output from a Ti:Sa regenerative amplifier (Clark MXR CPA-2000 ; λ = 774.4 nm, repetition rate 1037 Hz, pulse width 1.8 ps) and probed with 290 nm (4.27 eV) radiation produced by doubling the fundamental to 388 nm, which is used to pump an optical parametric amplifier (Light Conversion TOPAS). Detached photoelectrons were collected on an event-by-event basis using an electrostatic velocity-map imaging lens and focused onto a time- and position-sensitive photoelectron detector. The center-of-mass (CM), electron kinetic energy (eKE), and recoil angle in the laboratory frame were obtained from the arrival time and position of each photoelectron. The resulting photoelectron spectrum was then

equatorially sliced to select photoelectrons with minimal *z*-velocity to obtain optimum resolution. However, this imposed effective detector-acceptance function (DAF) affects the signal intensity distributions of the sliced photoelectron spectrum, reducing the apparent intensity at higher photoelectron velocities. The DAF corrected intensity distribution, $P(eKE)$, was determined by dividing the experimental distribution, $N(eKE)$, by the acceptance function of the slice.[23] Calibration of the photoelectron detector using I^- showed a sliced *z*-velocity component resolution of $\Delta E/E \sim 4.4\%$ at 1.2 eV and ~ 6.6 % at 0.3 eV electron kinetic energy. Following photodetachment, the nascent neutral species recoiled out of the trap and were detected in coincidence with the electron using a time- and position-sensitive multiparticle detector. From this information, product masses and translational energy release (E_T) were determined on an event-by-event basis for momentum-matched neutral particles. The multiparticle detector was determined to have a resolution of $\Delta E/E \sim 10\%$ by calibration using the dissociative photodetachment of O_4^-.[21]

The angular acceptance of coincidence events on the neutral particle detector is small (approximately 0.6% for HCO_2 and 1.2% for DCO_2 for the current setup) due to the finite size of the detector and the large difference in mass between the H/D and CO_2 fragments, resulting in large CM velocities. Product translational energy distributions, $P(E_T)$, were obtained by using Monte Carlo simulations to determine the DAF, $N(E_{T,MC})$, and then dividing the experimental distribution, $N(E_T)$, by $N(E_{T,MC})$.[24] The primary result of this correction is to amplify features with larger translational energies. This correction is done on the PPC spectrum so that the eKE-selected $P(E_T)$ distributions can be used to extract the $CO_2(\nu_2)$ product state distributions. The dissociation of DCO_2 produced by

photodetachment of a 7 keV ion beam of DCO_2^- yields D atoms with a laboratory frame energy of 320 eV where the detection efficiency with the MCP-based detector is still as large as ~20%, making this experiment feasible.[25]

3.3. Results

PPC spectroscopy enables detection of photoelectrons and neutral fragments in coincidence, providing additional information on the dissociation dynamics beyond either photoelectron kinetic-energy or photofragment translational-energy release spectra alone. If a structured photoelectron spectrum is observed and assigned, determination of the state-to-state resolved dissociation dynamics of transient species is possible. In the case of DCO_2^-, this limit is nearly achieved, with a structured yet highly overlapping photoelectron spectrum observed. In the following paragraphs the measured photoelectron spectrum, translational-energy release spectrum, PPC spectrum, and eKE-gated photofragment energy $P(E_T)$ spectra will be presented.

The top panel in Figure 3.1 shows the photoelectron kinetic-energy spectrum, $P(eKE)$, for DCO_2 recorded at a photon energy of 4.27 eV in coincidence with one neutral fragment and the experimental product translational-energy release, $N(E_T)$, is shown in the bottom panel. Due to the kinematic and detection constraints mentioned earlier, at most 0.25% of dissociating events are expected to result in detection of two neutral particles in coincidence with an electron. This means that the $P(eKE)$ spectrum measured in coincidence with one neutral fragment will consist of a combination of (1) any stable channel, defined as a species with a reactive lifetime longer than the flight time

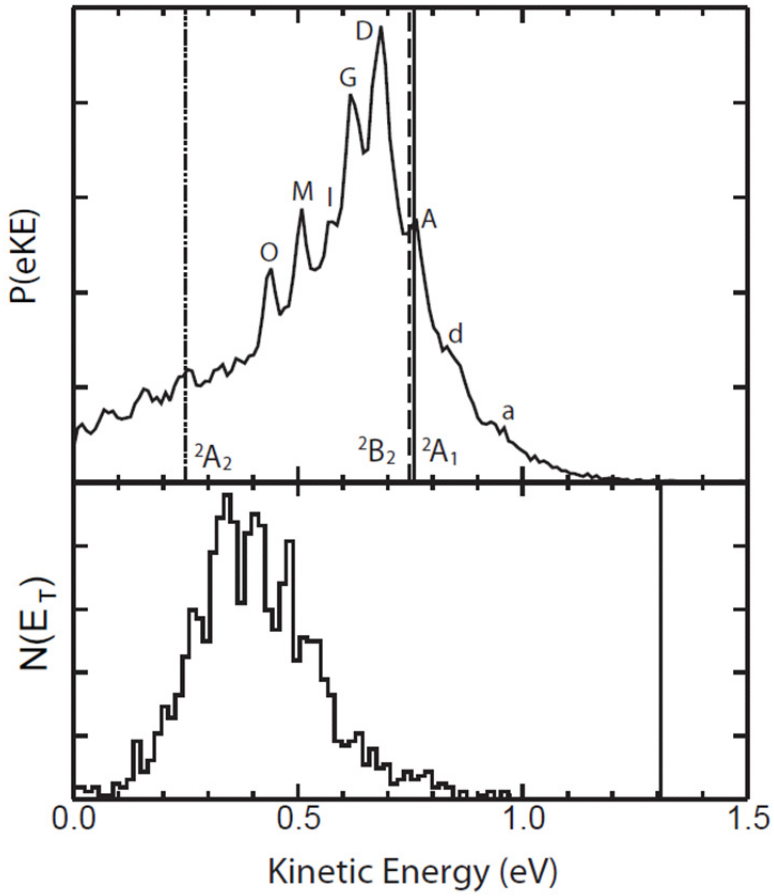

Figure 3.1. Photoelectron kinetic-energy spectrum of DCO_2^- at 290 nm in coincidence with one neutral particle (top panel) and translational-energy release for two neutral particles in coincidence with an electron (bottom panel). Peak assignments in *P*(*eKE*) are based on those of Garand *et al.* and are indicated in Table 3.1.[9] Electron affinities for the three lowest-lying electronic states are indicated by a solid line ($^2A_1$), a dashed line ($^2B_2$), and a dash-dot-dot line ($^2A_2$). For $N(E_T)$, KE_{max} is indicated by a solid line.

Table 3.1. DCO_2^- electron kinetic-energy, *P*(*eKE*), spectral-peak positions for the $^2A_1/^2B_2$ region, the respective eKE-gates used to examine the state-resolved $P(E_T)$ distributions, and corresponding peak assignments based on those of Garand *et al.*[9] All energies reported are in eV.

Peak	*P*(*eKE*)	*P*(*eKE*) Gate	Assignment
a	0.93	0.89-1.02	3_2^0 ($^2A_1$)
d	0.83	0.80-0.88	3_1^0 ($^2A_1$)
A	0.76	0.72-0.79	0_0^0 ($^2A_1$)
D	0.69	0.65-0.71	3_0^1 ($^2A_1$)
G	0.63	0.61-0.65	3_0^2 ($^2A_1$)
I	0.59	0.55-0.60	3_0^2 ($^2B_2$)
M	0.51	0.48-0.53	Highly mixed
O	0.44	0.41-0.48	

of the radical from the laser–ion interaction region to the delay-line detector (~ 7 μs for DCO_2 at an ion-beam energy of 7 keV), and (2) the dissociative channel, where only the heavier CO_2 fragment is detected because the lighter D product recoils out of the detector frame. *P*(*eKE*) spectra recorded in coincidence with either one or two neutral particles are identical within the signal-to-noise ratio, indicating that the *P*(*eKE*) spectra are for dissociative products, with no detectable stable channel. This is consistent with the earlier PPC experiments. [8]

The peak assignments in Figure 3.1 are based on those of Garand *et al.*[9] Photodetachment at this photon energy accesses the three lowest-lying electronic states ($^2A_1$, $^2B_2$, and $^2A_2$) of the formyloxyl radical, and the resolved structure in the $^2A_1/^2B_2$ region is dominated by the O−C−O bending mode (ω_3) in the $^2A_1$ state (Table 3.1). As in the previous studies of this system,[7-9] hot bands are observed above the adiabatic electron affinity, with resolved peaks attributed to excitation in the totally symmetric O−C−O bending mode of the parent anion (ω'_3 = 743 cm^{-1}).[9] These hot bands do not undergo radiative cooling during the 500 ms trapping time in the EIBT.

Figure 3.2 shows the PPC spectrum for the $DCO_2^- + h\nu \rightarrow D + CO_2 + e^-$ reaction, providing a more complete picture of the energy partitioning in this dissociative process. The *P(eKE)* spectrum (vertical axis) and $P(E_T)$ spectrum (horizontal axis) are generated by integration over the complementary variable. The signal-to-noise in the $P(E_T)$ spectrum is reduced relative to the $N(E_T)$ spectrum shown in Figure 3.1 as a result of fewer electron + momentum-matched fragment coincidence events and the DAF correction procedure. The rightmost diagonal line in the coincidence plot corresponds to

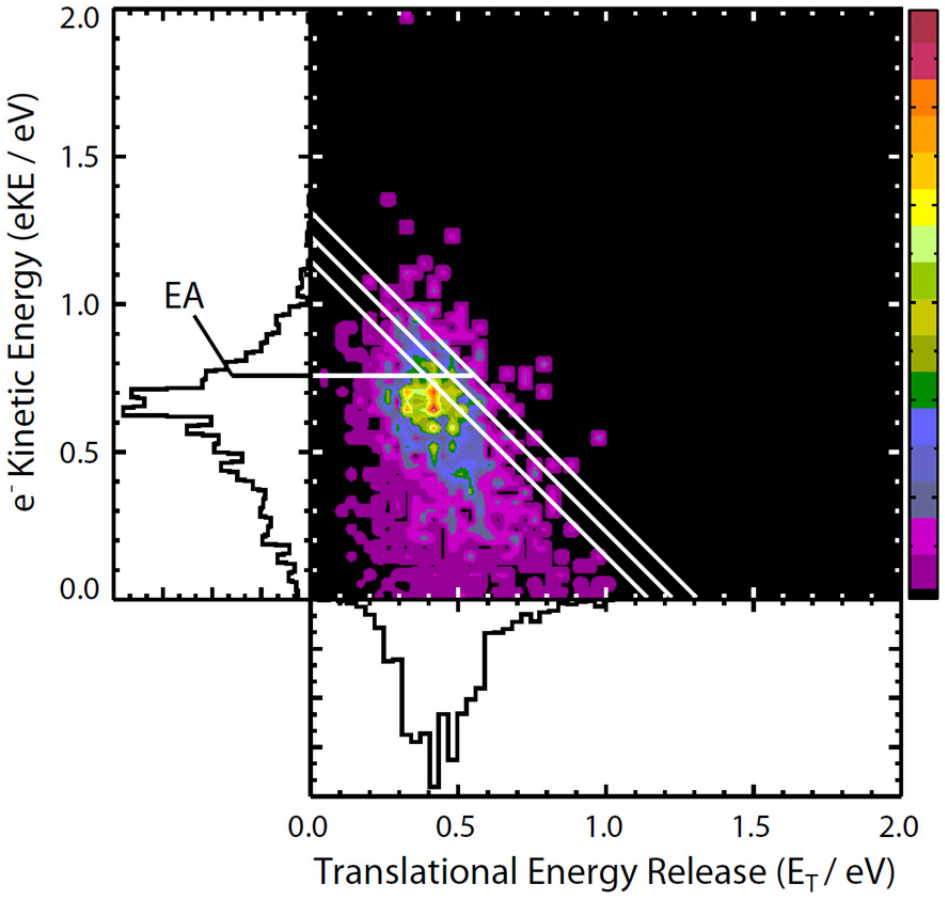

Figure 3.2. Photoelectron-photofragment coincidence spectrum for the reaction $DCO_2^- + h\nu \rightarrow D + CO_2 + e^-$ at 290 nm. The rightmost diagonal line corresponds to KE_{max} for the $^2A_1$ electronic state.

the maximum kinetic-energy release (KE_{max}) for dissociation from the $^2A_1$ electronic state of the formyloxl radical, where the D + CO_2 products are in their ground rotational, vibrational and electronic states ($KE_{max}(DCO_2, {}^2A_1) = h\nu - EA - \Delta D_o = 1.30$ eV). The H-CO_2 bond dissociation energy, ΔD_o, was estimated by Neumark and coworkers to be – 0.58 ± 0.13 eV,[7] indicating that HCO_2 is unstable with respect to the H + CO_2 products. With the inclusion of the zero-point energy correction to ΔD_o of 0.04 eV for DCO_2,[8] the calculated KE_{max} is in excellent agreement with the experimental results and the previous ΔD_o error estimation is an upper bound. Additional diagonal lines corresponding to $\nu_2 = 1$ and $\nu_2 = 2$ in the CO_2 product bending mode are also plotted, using the literature value for the O−C−O bending frequency for free CO_2 (667.4 cm^{-1}/83 meV).[26] The coincidence spectrum shows evidence for a series of vertical bands that correspond to the peaks in the *P(E_T)* spectrum and have similar spacing to the peaks in the *P*(*eKE*) spectrum in Figure 3.1 (top panel). Shown more clearly in the *N*(E_T) spectrum, bottom panel of Figure 3.1, these E_T peaks have an average spacing of 71 meV, consistent with the previous study of DCO_2, and are assigned to a progression in the ν_2 bending mode. While the signal-to-noise in the coincidence spectrum is limited, the fact that resolved peaks are seen in the *N*(E_T) spectrum proves that this is the case.[8]

The two-dimensional PPC spectrum contains detailed information about the dependence of the dissociation dynamics on the initial electronic and vibrational state of the DCO_2 radical produced in the photodetachment process. The experimental resolution and signal-to-noise limits our ability to get true state-to-state dynamical information, but, by examining eKE-gated *P*(E_T) spectra, product CO_2 bending vibration (ν_2) distributions can be extracted from the data. These spectra are obtained by integrating the coincidence

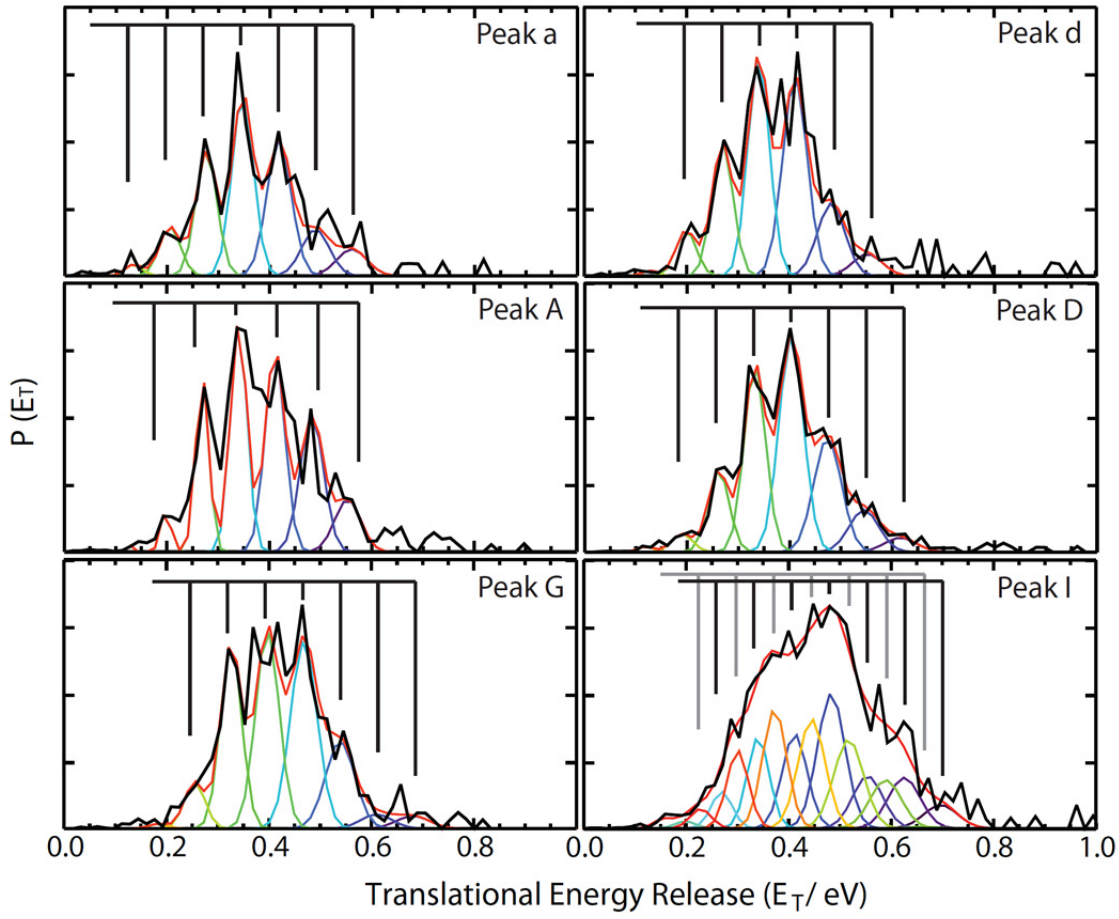

Figure 3.3. eKE-gated $P(E_T)$ CO_2 product bending (ν_2) distributions (black line) for selected peaks from Table 3.1 corresponding to the O−C−O bending mode ω_3 in the $^2A_1$ state (black comb) and $^2B_2$ state (grey comb). Peak progressions are fit using Gaussians with an average $P(E_T)$ peak spacing of 71 meV.

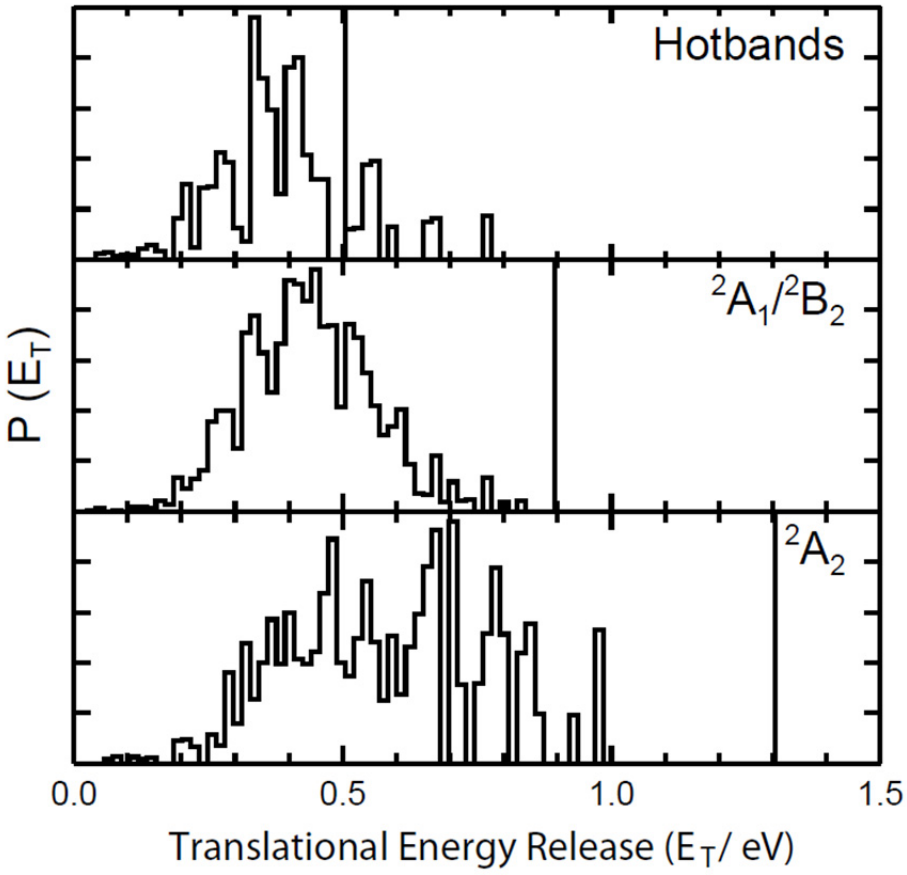

Figure 3.4. eKE-gated $P(E_T)$ distributions for the hot-band region (top), the $^2A_1/^2B_2$ region (middle), and the $^2A_2$ region (bottom) for the reaction $DCO_2^- + h\nu \rightarrow D + CO_2 + e^-$ at 290 nm. Translational energy release spectra were obtained by integration of the PPC plot over the eKE for the following ranges: ≥ 0.80 eV, 0.41 – 0.79 eV, and ≤ 0.25eV. For each region, the corresponding KE_{max} is indicated with a solid vertical line.

spectrum over each peak, with the width of each non-overlapping gate determined by the width of the peak as indicated in Table 3.1. It is important to note here that these $P(E_T)$ spectra have been corrected by the DAF for detection of D + CO_2 products in order to extract product state distributions. Using this method to examine individual peaks in the $^2A_1/^2B_2$ region, vibrationally resolved eKE-gated $P(E_T)$ spectra were extracted for assigned peaks in the photoelectron spectrum, shown in Figure 3.3. The eKE-gated $P(E_T)$ for peaks corresponding to the O−C−O bending mode in the $^2A_1$ state (peaks A, D and the hot bands a and d) yield nicely resolved $P(E_T)$ spectra with peaks spaced ~71 meV. These are the peaks that give rise to the resolved E_T observed in the $^2A_1/^2B_2$ region of the coincidence spectrum (Figure 3.2). The $P(E_T)$ spectra for peak G is not as nicely resolved, and that for peak I is more convoluted still, with what looks like two overlaid vibrational progressions. In the region of the coincidence spectrum corresponding to photodetachment to the $^2A_2$ state in DCO_2 (eKE < 0.25 eV) there is no evidence for resolved CO_2 bending excitation, indicating a change in the dissociation dynamics for this excited electronic state seen in Figure 3.4.

3.4. Discussion

Ma and Guo recently reported a full-dimensional quantum-state-resolved study of the predissociation dynamics of the $HCO_2^- + h\nu \rightarrow H + CO_2 + e^-$ reaction proceeding on the ground $^2A'$ state of the HCO_2 radical, essentially modeling the PPC experiment, complete with a calculated HCO_2^- absorption spectrum and predicted CO_2 product state distributions.[20] The calculated absorption spectrum is in relatively poor agreement with the SEVI spectrum from Garand *et al.*,[9] with quantitative differences in signal

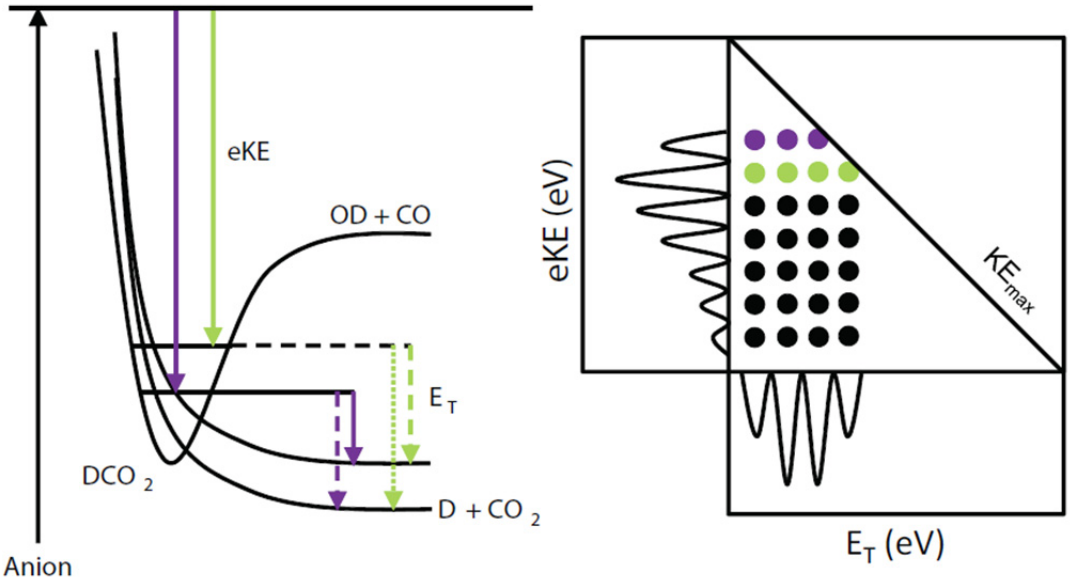

Figure 3.5. Schematic potential energy surface illustrating the predissociation dynamics of DCO_2 (left) and how these dynamics manifest in the corresponding PPC spectrum (right). In the schematic potential energy surface predissociation to only the two lowest $CO_2(\nu_2)$ states are shown for clarity and the photodetached electron is not explicitly shown.

intensities and peak positions attributed to inaccuracies in the LTSH neutral PES[3] used and the neglect of the other low-lying electronic states of HCO_2. As an example, the calculated absorption spectrum was found to underestimate the O−C−O bending frequency in the formyloxyl radical as compared to experimental values obtained by Garand *et al*. The PPC experimental results presented here allow for a direct comparison to the quantum dynamics calculations of Ma and Guo of the subsequent predissociation of the formyloxyl radical, as a further test of both the dynamics calculations and the LTSH surface.

Previously it was demonstrated that the vertical bands observed in the coincidence spectrum of DCO_2 correspond to predissociation sequence bands.[8] In other words, each predissociated vibrational state in the neutral formyloxyl radical can access several CO_2 product vibrational states with low rotational excitation, as shown schematically in Figure 3.5. The vertical alignment of the peaks, leading to the resolution observed in E_T, results from the fact that the peak spacing in the dominant O−C−O bending mode (ω_3) of the formyloxyl radical is nearly degenerate with respect to the O−C−O bending mode (ν_2) of the resulting CO_2 fragment. The observed predissociation bands in the $^2A_1/^2B_2$ region of the PPC spectrum (Figure 3.2) result from the characteristic dissociation dynamics of this system. In the present data, the evidence for these predissociation sequence bands is most easily observed in the eKE-gated $P(E_T)$ spectra shown in Figure 3.3.

Figure 3.3 shows that in the $^2A_1/^2B_2$ region, the eKE-gated $P(E_T)$ for selected peaks in the PPC spectrum exhibit well-resolved peak progressions (peaks A, D, G and I), also seen in the eKE-gated $P(E_T)$ spectra for the hot-band transitions (peaks a and d).

Table 3.2. eKE-gated $P(E_T)$ $CO_2(\nu_2)$ product state distributions determined from the fits in Figure 3.3, given in percentages, for each formyloxyl O−C−O bending state. The assignment of $P(eKE)$ peaks to states in DCO_2 are indicated.[9] E_T values for each CO_2 (ν_2) product state, in eV, are given in parentheses as determined by the conservation of energy (see text). All states (except for peak I) result from the $^2A_1$ state of the formyloxyl radical. Peak I population distributions are the sum of those from the $^2B_2$ and $^2A_1$ states, where E_T positions for peak I are indicated as ($^2B_2/^2A_1$).

ν_2	a (3_2^0)	d (3_1^0)	A (3_0^0)	D (3_0^1)	G (3_0^2)	I (3_0^2)
0	4.6 (0.56)	3.1 (0.55)	6.2 (0.55)	2.1 (0.62)	1.7 (0.68)	2.6 (0.70/0.72)
1	8.0 (0.49)	10.3 (0.48)	16.2 (0.47)	6.2 (0.54)	1.9 (0.60)	10.3 (0.63/0.64)
2	23.5 (0.42)	28.2 (0.41)	23.8 (0.40)	16.8 (0.47)	11.8 (0.53)	14.6 (0.56/0.57)
3	31.3 (0.35)	31.4 (0.33)	26.9 (0.33)	31.8 (0.40)	25.5 (0.46)	25.3 (0.49/0.50)
4	21.6 (0.28)	19.1 (0.26)	20.8 (0.26)	27.5 (0.33)	26.9 (0.39)	22.2 (0.41/0.43)
5	8.5 (0.21)	6.5(0.19)	5.0 (0.19)	12.2 (0.26)	25.2 (0.32)	17.5 (0.34/0.36)
6	2.0 (0.13)	0.8 (0.12)	0.8 (0.12)	2.7 (0.19)	6.3 (0.25)	5.8 (0.27/0.29)
7	0.5 (0.06)	0.5 (0.05)	0.4 (0.05)	0.8 (0.12)	0.6 (0.18)	1.7 (0.20/0.22)

Each eKE-gated $P(E_T)$ spectrum was fit using a series of Gaussians spaced by the observed average E_T-peak spacing of 71 meV (570 cm^{-1}). The fit $P(E_T)$ peak positions for a given eKE-gated $P(E_T)$ spectrum from the $^2A_1$ electronic are determined by conservation of energy using the following relation: E_T ($^2A_1$; ν_2 = n) = KE_{max} ($^2A_1$) – eKE($^2A_1$; ω_3 = m) – $nE_{int}^{CO_2}(\nu_2)$, where n and m correspond to vibrational quanta in the O−C−O bending mode of the CO_2 product and the neutral formyloxyl radical, respectively. The fit $P(E_T)$ peak positions from the $^2B_2$ state are calculated in a similar fashion, using a KE_{max} ($^2B_2$) value of 1.29 eV. The fits to the data yield the CO_2 product vibrational distributions in Table 3.2, showing inverted bending vibration distributions, with peak values ranging from ν_2 = 2 for the lowest energy radical states up to ν_2 = 4. The $P(E_T)$ spectrum from peak G is not as well fit, most notably around 0.4 eV, indicating that there are likely contributions from other states in the formyloxyl radical. Peak I, assigned by Garand *et al.* as belonging to the $^2B_2$ state, results in a $P(E_T)$ spectrum that cannot entirely be explained by CO_2 fragments coming from only this electronic state and is fit better by including a contribution from the $^2A_1$ state as shown in Figure 3.3. Understandably, peaks corresponding to highly mixed states—that is, not dominated by a single state—do not exhibit the same vibrational resolution (peaks M and O) and are therefore not fit well by just the O−C−O bending mode from $^2A_1$ (Figure 3.6). Finally, there is no evidence in the fits for preferential excitation of even bending quanta, in spite of the well-known Fermi resonance between $2\nu_2$ and the ν_1 symmetric stretch of CO_2.[20, 27]

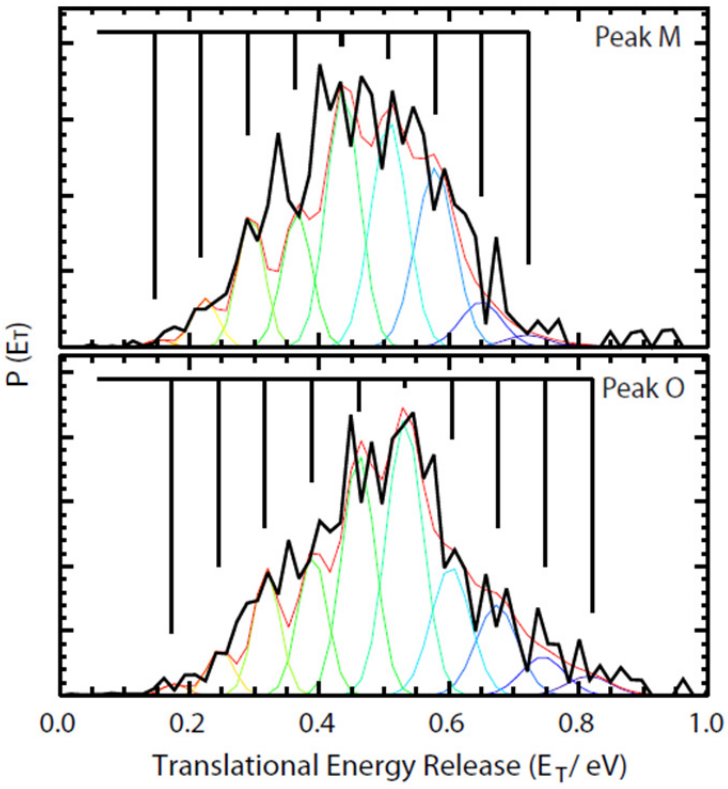

Figure 3.6. eKE-gated $P(E_T)$ CO_2 product distributions for the highly mixed peaks M and O from Table 3.1, fit using Gaussians with an average $P(E_T)$ peak spacing of 71 meV. The fit peak progressions correspond only to the O−C−O bending mode in the $^2A_1$ state and do not take into account that these peaks are identified as being highly mixed.

As indicated in the coincidence spectrum, considerable excitation was found in the resulting CO_2 product, as even the ground state of the neutral formyloxyl radical (peak A) yielded CO_2 products with significant populations in ν_2 = 2, 3, and 4, consistent with our previous findings.[8] This result is contrary to the calculated vibrational product state distributions reported by Ma and Guo,[20] who found significantly less CO_2 product vibrational excitation from the lowest resonances on the radical potential energy surface. Figure 3.7 shows the predicted CO_2 product state distributions for the 3_0^0 and 3_0^1 transitions from the anion ground state to ω_3 in the $^2A_1$ radical ground state, plotted in terms of E_T and convoluted with Gaussians at the experimental resolution. For comparison, the overall fits for the experimentally determined CO_2 product state distributions for the corresponding features, peaks A and D, are also included. Odd bending quanta were not included in the predicuted distributions in the total J=0 calculations carried out by Ma and Guo. From this comparison it is readily apparent that the high degree of vibrational excitation in the experimental results for the lowest metastable levels of DCO_2 is not captured by the theoretical predictions. At much higher levels of excitation in the radical (1600 cm^{-1} of internal energy) the calculations predicted a vibrational inversion (peaking at ν_2 = 2), however it is difficult to compare that directly to experiment as the spectrum becomes congested. In any case, a sharp change in the level of product vibrational excitation in the region where the $^2A_1$ and $^2B_2$ states of DCO_2 dominate the spectrum is not experimentally observed.

Possible reasons for the discrepancies between experiment and theory are several. These experiments were carried out on DCO_2 for experimental reasons, while the calculations were performed on HCO_2. However, the change in reduced mass from H-

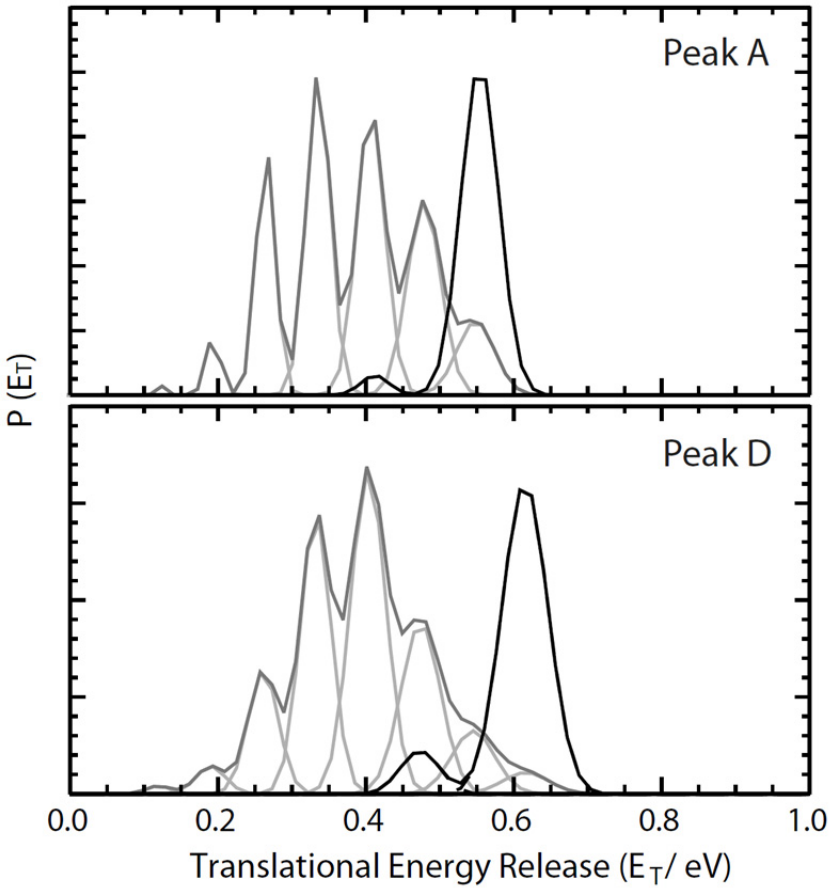

Figure 3.7. Comparison of experimental fits for eKE-gated $P(E_T)$ CO_2 product state distributions (grey) to theoretical distributions predicted by Ma and Guo (black) for the 3_0^0 and 3_0^1 transitions from the anion ground state to ω_3 in the $^2A_1$ radical ground state (peaks A and D, respectively).[20]

CO_2 to D-CO_2 is not expected to lead to a significant change in product bending excitation, as experimentally confirmed by the $P(E_T)$ distributions reported for both HCO_2 and DCO_2 in earlier work from this laboratory at a photon energy of 4.80 eV.[8] Ma and Guo commented on how the difference in intensity and peak positions between their calculated absorption spectrum and experimental photoelectron spectra[7, 9] could be attributed to inaccuracies in the LTSH neutral potential energy surface.[3, 20] Significantly improved potential energy surfaces for the HOCO system are now available, so it would be of interest to test the new global potential energy surfaces for the OH + CO ⟶ H + CO_2 reaction recently reported by Li *et al.* and Chen *et al.*[28, 29] A recent examination of CO_2 product state distributions resulting from a quasiclassical trajectory study of H + CO_2 collisions carried out by Corchado *et al.*,[30] performed on the latest surface from Li and coworkers, indicated significant excitation of the O-C-O bend in the CO_2 products. It should be noted that although these results most certainly involve the HCO_2 well, significant rotational excitation is also observed, more consistent with dissociation from the related HOCO radical. These theoretical results are in qualitative agreement with hot atom collision experiments carried out by Flynn and Weston,[31] indicating that the H + CO_2 portion of this new surface at high total energies is reasonable. It will be valuable, therefore, to examine the performance of this new surface at the lower total energies probed by the predissociating formyloxyl radical.

As noted in the introduction and evident in the discussion of the low-lying electronic states of DCO_2 involved in these phenomena, vibronic and electronic interactions in this predissociating system are also of great importance. Evidence for the differing dissociation dynamics as a function of electronic state are seen in the present

data by examination of the region of the coincidence spectrum corresponding to photodetachment to the $^2A_2$ state in the neutral DCO_2 radical (eKE < 0.25 eV). Although the $^2A_2$ state of DCO_2 is also dissociative, it does not show the same state-resolved distributions as do the $^2A_1$ or $^2B_2$ states (Figure S1); this indicates that predissociation of the $^2A_2$ state involves other vibrational modes and very likely also involves greater distortion of the C_{2V} framework, with resulting rotational excitation of the CO_2 broadening the product translational energy distribution. A complete theoretical understanding of this system will have to address all the low-lying electronic states and the rich vibronic interactions documented by Burton *et al.* and Klein *et al*.[13, 19]

3.5. Conclusion

In conclusion, photodetachment of DCO_2^- produces the DCO_2 radical in low-lying electronic states accompanied by O-C-O bending excitation. These states rapidly predissociate into a range of D + $CO_2(\nu_2)$ product states leading to predissociation sequence bands in the the $^2A_1/^2B_2$ region of the PPC spectrum. The eKE-gated $P(E_T)$ spectra in the $^2A_1/^2B_2$ region provide formyloxyl radical state-specific experimental determination of $CO_2(\nu_2)$ product state distributions. The experimental results indicate a much greater degree of excitation in the O−C−O bending mode than found in quantum dynamics calculations on the LTSH potential energy surface by Ma and Guo.[20] Additionally, evidence for differing dissociation dynamics as a function of electronic state were observed, particularly in the broad, unresolved $P(E_T)$ distributions from the higher-lying $^2A_2$ electronic state, further illustrating the complexity of vibronic and electronic interactions in the predissociating formyloxyl radical. A complete theoretical

picture will necessarily need to include all three low-lying electronic states in order to accurately capture the complex dynamics observed experimentally.

Acknowledgments

This work was supported by the U.S. Department of Energy under grant number DE-FG03-98ER14879. AWR acknowledges support from GAANN grant P200A120223 from the U.S. Dept. of Education.

Chapter 3, in full, is a reprint of the material as it appeared in Ray, A. W.; Shen, B. B.; Poad, B. L. J.; Continetti, R. E. "State-Resolved Predissociation Dynamics of the Formyloxyl Radical," *Chemical Physics Letters*, 2014, *592*, 30–35; doi:10.1016/j.cplett.2013.11.06. The dissertation author is the primary author and the dissertation advisor is the corresponding author.

3.6. References

1. Schatz, G. C.; Fitzcharles, M. S.; Harding, L. B., State-to-State Chemistry with Fast Hydrogen Atoms. Reaction and Collisional Excitation in H + CO_2. *Faraday Discussions of the Chemical Society* **1987,** *84* (0), 359-369.

2. Kudla, K.; Schatz, G. C.; Wagner, A. F., A Quasiclassical Trajectory Study of the OH + CO Reaction. *The Journal of Chemical Physics* **1991,** *95* (3), 1635-1647.

3. Lakin, M. J.; Troya, D.; Schatz, G. C.; Harding, L. B., A Quasiclassical Trajectory Study of the Reaction OH + CO $\rightarrow$ H + CO_2. *The Journal of Chemical Physics* **2003,** *119* (12), 5848-5859.

4. Duncan, T. V.; Miller, C. E., The HCO_2 Potential Energy Surface: Stationary Point Energetics and the HOCO Heat of Formation. *The Journal of Chemical Physics* **2000,** *113* (13), 5138-5140.

5. Lu, Z.; Continetti, R. E., Dynamics of the Acetyloxyl Radical Studied by Dissociative Photodetachment of the Acetate Anion. *The Journal of Physical Chemistry A* **2004,** *108* (45), 9962-9969.

6. Ruscic, B.; Schwarz, M.; Berkowitz, J., A Photoionization Study of the COOH Species. *The Journal of Chemical Physics* **1989,** *91* (11), 6780-6785.

7. Kim, E. H.; Bradforth, S. E.; Arnold, D. W.; Metz, R. B.; Neumark, D. M., Study of HCO_2 and DCO_2 by Negative Ion Photoelectron Spectroscopy. *The Journal of Chemical Physics* **1995,** *103* (18), 7801-7814.

8. Clements, T. G.; Continetti, R. E., Predissociation Dynamics of Formyloxyl Radical Studied by the Dissociative Photodetachment of HCO_2^- /DCO_2^- + hν → H/D + CO_2 + e^-. *The Journal of Chemical Physics* **2001,** *115* (12), 5345-5348.

9. Garand, E.; Klein, K.; Stanton, J. F.; Zhou, J.; Yacovitch, T. I.; Neumark, D. M., Vibronic Structure of the Formyloxyl Radical (HCO_2) via Slow Photoelectron Velocity-Map Imaging Spectroscopy and Model Hamiltonian Calculations. *The Journal of Physical Chemistry A* **2009,** *114* (3), 1374-1383.

10. Peyerimhoff, S. D.; Skell, P. S.; May, D. D.; Buenker, R. J., Configuration Interaction Study of the Three Lowest Electronic States in the Formyl and Acetyl Radicals. *Journal of the American Chemical Society* **1982,** *104* (17), 4515-4520.

11. Feller, D.; Huyser, E. S.; Borden, W. T.; Davidson, E. R., MCSCF/CI Investigation of the Low-Lying Potential Energy Surfaces of the Formyloxyl Radical, HCO_2·. *Journal of the American Chemical Society* **1983,** *105* (6), 1459-1466.

12. McLean, A. D.; Lengsfield III, B. H.; Pacansky, J.; Ellinger, Y., Symmetry Breaking in Molecular Calculations and the Reliable Prediction of Equilibrium Geometries. The Formyloxyl Radical as an Example. *The Journal of Chemical Physics* **1985,** *83* (7), 3567-3576.

13. Burton, N. A.; Yamaguchi, Y.; Alberts, I. L.; Schaefer Iii, H. F., Interpretation of Excited State Hartree-Fock Analytic Derivative Anomalies for NO_2 and HCO_2 Using the Molecular Orbital Hessian. *The Journal of Chemical Physics* **1991,** *95* (10), 7466-7478.

14. Rauk, A.; Yu, D.; Borowski, P.; Roos, B., CASSCF, CASPT2, and MRCI Investigations of Formyloxyl Radical (HCOO·). *Chemical Physics* **1995,** *197* (1), 73-80.

15. Stanton, J. F.; Kadagathur, N. S., Pseudorotational Interconversion of the $^2A_1$ and $^2B_2$ states of HCOO. *Journal of Molecular Structure* **1996,** *376* (1–3), 469-474.

16. Ayala, P. Y.; Schlegel, H. B., A Nonorthogonal CI Treatment of Symmetry Breaking in Sigma Formyloxyl Radical. *The Journal of Chemical Physics* **1998,** *108* (18), 7560-7567.

17. Kieninger, M.; Ventura, O. N.; Suhai, S., Density Functional Investigations of Carboxyl Free Radicals: Formyloxyl, Acetyloxyl, and Benzoyloxyl Radicals. *International Journal of Quantum Chemistry* **1998,** *70* (2), 253-267.

18. Feller, D.; Dixon, D. A.; Francisco, J. S., Coupled Cluster Theory Determination of the Heats of Formation of Combustion-Related Compounds: CO, HCO, CO_2, HCO_2, HOCO, HC(O)OH, and HC(O)OOH. *The Journal of Physical Chemistry A* **2003,** *107* (10), 1604-1617.

19. Klein, K.; Garand, E.; Ichino, T.; Neumark, D.; Gauss, J.; Stanton, J., Quantitative Vibronic Coupling Calculations: the Formyloxyl Radical. *Theoretical Chemistry Accounts* **2011,** *129* (3-5), 527-543.

20. Ma, J.; Guo, H., Full-Dimensional Quantum State Resolved Predissociation Dynamics of HCO_2 Prepared by Photodetaching HCO_2^-. *Chemical Physics Letters* **2011,** *511* (4–6), 193-195.

21. Hanold, K. A.; Luong, A. K.; Clements, T. G.; Continetti, R. E., Photoelectron-Multiple-Photofragment Coincidence Spectrometer. *Review of Scientific Instruments* **1999,** *70* (5), 2268-2276.

22. Johnson, C. J.; Shen, B. B.; Poad, B. L. J.; Continetti, R. E., Photoelectron-Photofragment Coincidence Spectroscopy in a Cryogenically Cooled Linear Electrostatic Ion Beam Trap. *Review of Scientific Instruments* **2011,** *82* (10), 105105.

23. Bowen, M. S.; Continetti, R. E., Photodetachment Imaging Study of the Vinoxide Anion. *The Journal of Physical Chemistry A* **2004,** *108* (39), 7827-7831.

24. Sherwood, C. R.; Hanold, K. A.; Garner, M. C.; Strong, K. M.; Continetti, R. E., Translational Spectroscopy Studies of the Photodissociation Dynamics of O_4^-. *The Journal of Chemical Physics* **1996,** *105* (24), 10803-10811.

25. Peko, B. L.; Stephen, T. M., Absolute Detection Efficiencies of Low Energy H, H^-, H^+, H_2^+ and H_3^+ Incident on a Multichannel Plate Detector. *Nuclear Instruments and Methods in Physics Research Section B: Beam Interactions with Materials and Atoms* **2000,** *171* (4), 597-604.

26. Herzberg, G., Molecular Spectra and Molecular Structure III. Electronic Spectra and Electronic Structure of Polyatomic Molecules. Krieger Publishing: Malabar, 1991.

27. Rodriguez-Garcia, V.; Hirata, S.; Yagi, K.; Hirao, K.; Taketsugu, T.; Schweigert, I.; Tasumi, M., Fermi Resonance in CO_2: A Combined Electronic Coupled-Cluster and Vibrational Configuration-Interaction Prediction. *The Journal of Chemical Physics* **2007,** *126* (12), 124303-6.

28. Li, J.; Wang, Y.; Jiang, B.; Ma, J.; Dawes, R.; Xie, D.; Bowman, J. M.; Guo, H., Communication: A chemically Accurate Global Potential Energy Surface for the HO + CO → H + CO_2 Reaction. *The Journal of Chemical Physics* **2012,** *136* (4), 041103-4.

29. Chen, J.; Xu, X.; Zhang, D. H., Communication: An Accurate Global Potential Energy Surface for the OH + CO → H + CO_2 Reaction Using Neural Networks. *The Journal of Chemical Physics* **2013,** *138* (22), 221104-4.

30. Corchado, J. C.; Espinosa-Garcia, J.; Li, J.; Guo, H., CO2 Vibrational State Distributions From Quasi-Classical Trajectory Studies of the HO + CO → H + CO_2 Reaction and H + CO_2 Inelastic Collision. *The Journal of Physical Chemistry A* **2012**.

31. Flynn, G. W.; Weston, R. E., Diode Laser Studies of Collisional Energy Transfer. *The Journal of Physical Chemistry* **1993,** *97* (31), 8116-8127.

Chapter 4: Dissociative Photodetachment of $HCCCO_2^-$ and Stability of the Propiolyl Radical $HCCCO_2$

4.1. Introduction

Carboxyl radicals $RCO_2\cdot$ are widely used in synthetic organic chemistry and are known to readily decompose to CO_2 and a free radical $R\cdot$. The simplest carboxyl radicals formyloxyl (HCO_2) and acetyloxyl (CH_3CO_2) have been extensively studied both experimentally [1-6] and computationally [7-20]. Not only do both of these carboxyl radicals readily dissociate to CO_2 and a free radical, as expected, but for both the CO_2 fragment forms with considerable internal energy.[3, 4, 6, 18] The study and analysis of these radicals are complicated by the presence of multiple low-lying electronic states, owing to the geometry of the CO_2 group. This complexity makes these systems an excellent test for theory, and it is of interest to study the effects of substitution on the dissociation dynamics and energetics of the low-lying electronic states of carboxyl radicals. Here we extend previous work carried out in our lab on the dissociation dynamics of HCO_2[3, 6] and CH_3CO_2[4] to that of the relatively unexplored propiolyl radical, HC_3O_2. For reference, the structures and shorthand labels for the propiolyl radical and the related structural isomers, anti- and syn-C_3O_2H, are shown in Figure 4.1.

Although not widely studied, the propiolate anion, $HC_3O_2^-$, has been observed experimentally by Fourier-transform infrared spectroscopy (FT-IR) as a decarboxylation product of aqueous acetylenedicarboxylic acid.[21] Decarboxylation of gaseous

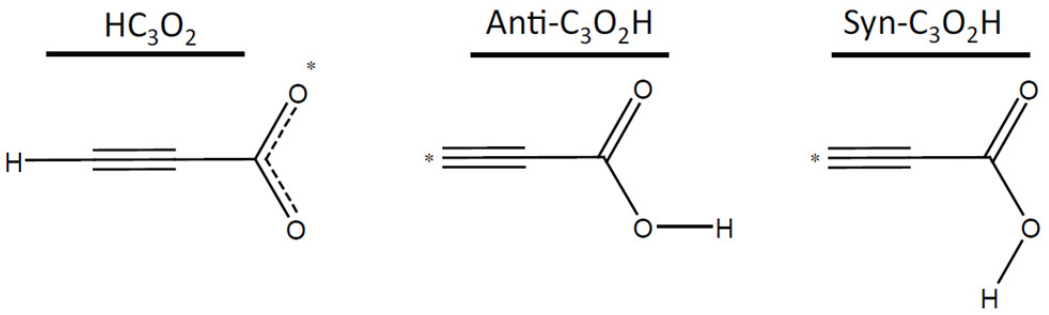

Figure 4.1. Nominal structures of the propiolyl radical, HC_3O_2, and its isomers, anti- and syn-C_3O_2H.

acetylenedicarboxylate anions has been shown to form a $C_3O_2^-$ radical anion.[22] The $HC_3O_2^-$ anion has also been studied more directly by noncontact atomic-force microscopy of propiolate prepared on a TiO_2 surface.[23] The neutral propiolyl radical HC_3O_2 and the isomeric C_3O_2H (syn- and anti- conformers) carbon radicals have been studied experimentally by Fitzgerald and coworkers using neutralization-reionization mass spectrometry;[24] in this case the experimental work was complimented by *ab initio* calculations of the stationary points and barriers to isomerization on both the anion and neutral surfaces, carried out at the coupled-cluster singles-and-doubles plus perturbative triples (CCSD(T)) level using the aug-cc-pVDZ basis set on B3LYP/6-31G(d) optimized geometries. The primary focus of their computational work was to determine the relative stability of each isomer and the isomerization barriers, in addition to the energetics for possible neutral and anionic dissociation pathways for each isomer. The calculations predict that anions for all three isomers should be stable relative to the corresponding neutrals, and that the barriers to isomerization on the anion surface are relatively large (0.36 – 1.21 eV). Neutralization-reionization using collisional ionization to observe the resulting fragments of $HC_3O_2^-$ results in the formation of energized HC_3O_2, which was found to readily dissociate to $HC_2 + CO_2$. In contrast, the isomeric $^-C_3O_2H$ radicals were found to access both stable C_3O_2H and a competitive dissociative pathway, which proceeds through excited C_3O_2H to form $C_3O + OH$.[24] However, their calculations and analysis were limited to the ground electronic states and did not examine the barriers to dissociation. Consequently, additional calculations were carried out to obtain more accurate electron affinities for the accessible electronic states of the three isomers. In

addition, product asymptotes and barriers to dissociation for each isomer were also carried out to aide in interpretation of the dissociative channel.

The simplest analogue to propiolyl is the formyloxyl radical, which possesses four electronic states with C_{2V} symmetry, all lying within a range of ~4.0 eV. The lowest-lying $^2A_1$ and $^2B_2$ states are nearly degenerate, making the identity of the ground state highly dependent on the level of theory and, therefore, a matter of much debate.[7-10, 12-17] High-level calculations predict that the $^2A_1$ state is the ground state for both HCO_2 and its isotopolog DCO_2.[5, 17] Further complexity may arise from asymmetric deformation/stretching in the carboxyl group ($–CO_2$), resulting in additional electronic states $^2A'$ and $^2A''$ with C_s symmetry,[8, 16] although the experimental data to date can be explained by the C_{2V} electronic states.[1, 5, 6]

One unique property of the formyloxyl radical is that the energy spacing of the O–C–O bending mode in the nascent neutral is nearly degenerate with the O–C–O bending spacing in the resulting CO_2 fragment, in large part due to the similarity in their respective reduced masses. Thus this is an ideal candidate for the study of state-to-state dissociation dynamics, and accordingly we recently published a study of product-state distributions for each populated vibrational level in the neutral.[6] Regardless of internal excitation in the neutral, the CO_2 product always forms with considerable vibrational excitation in the O–C–O bending mode. Full-dimensional quantum-dynamics simulations of this system using the LTSH surface did not adequately predict these product-state distributions,[18] while more recent quantum dynamics simulations carried out on a new

global potential energy surface[25] are in good agreement with our study, emphasizing the importance of having an accurate potential energy surface.

Similar to HCO_2, the more complex acetyloxyl radical, CH_3CO_2, also possesses multiple low-lying electronic states and a ground state that is nearly degenerate with the first excited electronic state.[7, 11, 15] Although the methyl group in the acetyloxyl radical adds additional complexity owing due to its torsional degrees of freedom, similarities of the two simple systems suggest a general trend, and the propiolyl radical, HC_3O_2, presents an ideal system to continue the exploration of carboxyl free radicals and an excellent test case for theory. Specifically, highly-accurate theoretical predictions of the photodetachment spectrum of propiolate are expected to be challenging for several reasons. First, this molecule is related to the formyloxyl radical, where profound vibronic mixing between the two lowest $^2A_1$ and $^2B_2$ electronic states is observed; similarly strong coupling can therefore be anticipated for propiolate. In addition, HC_3O_2 has 35 electrons and a dozen normal modes of vibration, which means that both accurate electronic structure and all-mode vibronic calculations are difficult and require significant computational resources.

In the following sections we present a photoelectron-photofragment coincidence (PPC) spectroscopy study of the propiolate anion at 4.80 eV. Photodetachment accesses the three lowest electronic states, $^2B_2$, $^2A_2$, and $^2A_1$, of the propiolyl radical, while dissociative photodetachment (DPD) probes the dissociation dynamics of the $^2A_1$ excited electronic state. Analysis of the experimental results are aided by high-level calculations, including a highly-accurate Franck-Condon simulation of the photodetachment spectrum

and the electron kinetic energy dependence of the photodetachment cross sections in excellent agreement with the experimental results.

4.2. Experimental Methods

This study was performed on a fast ion-beam PPC spectrometer, discussed in detail elsewhere.[26, 27] Anion precursors were synthesized using the combination of a coaxial pulsed discharge acting upon a supersonic expansion of O_2 passed over liquid propiolic acid held at room temperature and a 1-keV electron beam crossing the expansion. The resulting anions were skimmed, accelerated to 7 keV, re-referenced to ground, mass-selected by time-of-flight, and then confined in a cryogenically cooled electrostatic-ion-beam trap (EIBT) for 100 ms. The oscillating ion packet was phase-locked to the output of a Ti:Sapphire regenerative amplifier (Clark MXR CPA-2000; λ = 775.5 nm, repetition rate 1037 Hz, pulse width 1.1 ps) by an RF oscillator and the anions were probed with third-harmonic radiation (258.5 nm, 4.80 eV). The resulting detached photoelectrons were extracted on an event-by-event basis, orthogonal to the plane of the laser and ion beams, by means of an electrostatic velocity-map imaging lens coupled to a time- and position-sensitive photoelectron detector. Arrival time and position provide information on the center-of-mass (CM), electron kinetic energy (eKE), and laboratory-frame recoil angle for each photoelectron. For optimum resolution, photoelectrons with minimal z-velocity were selected by equatorially slicing the resulting photoelectron spectrum. The signal-intensity distribution of the photoelectron spectrum was affected by this imposed effective detector-acceptance function (DAF), resulting in a reduced apparent intensity at higher photoelectron velocities. Therefore, a DAF-corrected

intensity distribution, $P(eKE)$, was obtained by dividing the experimental intensity distribution, $N(eKE)$, by the acceptance function of the z-velocity slice.[28] Calibration of the photoelectron detector using F^- showed a sliced *z*-velocity component resolution of $\Delta E/E \sim 3.6$ % at 1.4 eV electron kinetic energy.

After photodetachment, the resulting neutral species recoiled out of the trap and were detected in coincidence with the photoelectron using a four-quadrant time- and position-sensitive multiparticle detector. Stable and dissociative photoelectron spectra were extracted by selecting for only those photoelectrons detected in coincidence with either one neutral particle (stable) or two neutral particles (dissociative). For dissociative processes, product masses and the product kinetic energy release (KER) distribution, *N(KER)*, were determined for momentum-matched neutral particles on an event-by-event basis. Unlike for the HCO_2 experiments were the where the angular acceptance of coincidence events on the neutral-particle detector was small due to the large difference in mass of the fragments,[3, 6] the angular acceptance is expected to be large for propiolyl due to the relatively small difference in mass between fragments HC_2 and CO_2 and as such no detector acceptance function corrections are needed. Calibration of the multiparticle neutral detector by dissociative photodetachment of O_4^- yielded a KER resolution of $\Delta E/E \sim 10\%$.[26]

4.3. Theory

Analysis of the experimental data has been greatly aided by extensive computations including the energetics of possible isomers and available low-lying electronic states, as well as Franck-Condon (FC) simulations and photodetachment cross

sections for the low-lying electronic states of the propiolyl radical.[24] Due to the complexity of the system, these computations were carried out at two different levels of theory. Exploration of C_3O_2H isomers including FC simulations were carried out using the CTQD method outlined below. The initial calculations for the low-lying electronic states of the propiolyl radical using this approach were not in good agreement with the experimental results, necessitating additional calculations using the EOMIP-CCSD(T)(a) method, also outlined in detail below. Photodetachment cross sections were included for the final FC simulations, resulting in excellent agreement with experiment.

Coupled cluster calculations were initially carried out at the CCSD(T)-F12a level in order to identify potentially relevant isomers and dissociation pathways. The computed electron affinities for syn- and anti-C_3O_2H, the propiolyl radical (HC_3O_2), and the corresponding excited electronic states are listed in Table 4.1. Dissociation pathways and energetics for HC_3O_2 and isomers at this level of theory are summarized in Table 4.2. Geometries were optimized at the CCSD(T)-F12a/aug-cc-pVDZ level and basis, and single-point energies were then evaluated at these geometries using the aug-cc-pVQZ basis. Zero-point vibrational, anharmonic vibrational, relativistic, diagonal Born-Oppenheimer, and (when appropriate) spin-orbit energies were calculated by various methods and using different programs. Vibrational corrections were calculated at the corresponding optimized geometry; all other energy contributions were calculated at the CCSD(T)-F12a/aug-cc-pVDZ optimized geometry. Anharmonic and Born-Oppenheimer calculations were found to be negligible compared to the expected errors for polyatomic molecules, and were not calculated beyond the diatomic species. Energy values

Table 4.1. Calculated AEAs for the four lowest electronic states of propiolyl radical (HC_3O_2) and the two lowest electronic states of each of the related isomers, syn- and anti-C_3O_2H. Energies are presented for both CTQD and EOMIP levels of theory and include zero-point energy corrections except where noted: *no ZPE, **B3LYP ZPE correction.

Isomer	Electronic State	CTQD AEA (eV)	EOMIP AEA (eV)
HC3O2	2B2	3.91	3.57
	2A2	4.46	3.60
	2A1	4.54	4.27
	2B1	4.77	–
Anti-C3O2H	2A’	3.87	–
	2A”	4.42	–
Syn-C3O2H	2A’	4.07	–
	2A”	4.63	–

Table 4.2. Dissociative pathways calculated at CTQD without zero-point energy corrections. The EOMIP value for the dissociation of $HC_3O_2 \rightarrow H_2C + CO_2$ is reported in parentheses. Bond dissociation energies (BDE) are reported relative to each respective neutral. KE_{max} values are determined by $KE_{max} = h\nu - AEA - BDE$, where $h\nu = 4.80$ eV and the AEAs correspond to those of the respective parent species as reported in Table 4.1.

Parent	Fragment 1	Fragment 2	BDE (eV)	KE_{max} (eV)
Anti-$CCCO_2H$	Cis-HOCO	CC	4.32	-3.39
	Trans-HOCO	CC	4.25	-3.32
	CCCO	OH	1.47	-0.54
	$CCCO_2$	H	3.80	-2.87
	Anti-CCO_2H	C	6.85	-5.92
	Syn-CCO_2H	C	6.88	-5.96
Syn-$CCCO_2H$	Cis-HOCO	CC	4.23	-3.50
	Trans-HOCO	CC	4.16	-3.43
	CCCO	OH	1.38	-0.65
	$CCCO_2$	H	3.71	-2.97
	Anti-CCO_2H	C	6.76	-6.02
	Syn-CCO_2H	C	6.79	-6.06
$HCCCO_2$	OCO	HCC	0.44	0.45 (1.01)
	HCCCO	O	4.18	-3.29
	$CCCO_2$	H	4.80	-3.92
	CCO_2	CH	6.17	-5.29

calculated this way, including zero-point and relativistic corrections (and spin-orbit when relevant), are referred to hereafter as "CTQD" energies. The CTQD energetics are used primarily to rule out the presence of the anti- and syn-C_3O_2H isomers and to estimate the dissociation barrier to $HC_2 + CO_2$ from the $^2A_1$ state of the propiolyl radical.

Assignment of the stable spectrum proved to be nontrivial and, as discussed later, is beyond the capabilities of the CTQD method. Accordingly, an extensive set of additional electronic structure, vibronic, and photodetachment cross-section calculations were undertaken based on the equilibrium geometry and force field calculated by the CCSD[29] method in the frozen-core approximation, using the atomic natural orbital basis set designated as ANO0.[30] At this geometry, best estimates of vertical detachment energy (VDE) were made by combining EOMIP-CCSD(T)(a) calculations,[31] as extrapolated to the basis set limit, with higher-order correlation corrections obtained with EOMIP-CCSDTQ[32, 33] and the ANO0 basis. In particular, best estimate VDEs were calculated as VDE= (VDE(EOMIP-CCSDTQ/ANO0) – VDE(EOMIP-CCSD(T)(a)/ANO0) + VDE(EOMIP-CCSD(T)(a)), where the last term in the sum is from the aforementioned basis-set-limit extrapolation. The resulting VDEs are 4.305 eV ($^2B_2$), 4.627 eV ($^2A_1$), and 4.743 eV ($^2A_2$), all of which carry a (conservative) uncertainty of perhaps 0.05 eV.

Using these estimated VDEs, the vibronic coupling model of Köppel, Domcke and Cederbaum (KDC)[34] was used to simulate the photoelectron spectrum. Apart from VDE differences, parameters for the model are the diabatic potential energy functions for the three electronic states as well as couplings between them, all expressed as polynomials in the dimensionless normal coordinate representation of the neutral. The

adiabatic parametrization method of Ref. [35] was used, and the electronic structure calculations used to this end were done at the EOMIP-CCSD/ANO0 level of theory.[36] The (electronically) diagonal diabatic potentials, expanded to second order in displacement, were obtained by adjusting the directly computed adiabatic potentials for the effects of diabatic couplings, as described in Ref. [17]. The coupling constants were computed analytically, using the quasidiabatic coupled-cluster ansatz of Ref. [37]. Diagonalization of the full diabatic potential obtained by this procedure reproduces the geometry and quadratic force fields of all adiabatic states (as computed by EOMIP-CCSD/ANO0 when the corresponding VDEs are used); this adiabatic parametrization of the KDC Hamiltonian has been shown to be essential for obtaining high-quality simulated spectra in cases where geometry changes (vertical → adiabatic) are large, as they are (especially for the $^2B_2$ state) in this system.

Finally, cross-sections for photodetachment were computed by the EOMIP-CCSD(T)(a) method, using the approach described in Ref. [38]. The d-aug-cc-pVTZ basis set[39] was used since adequate diffuse functions are essential for such computations. Full documentation of the parameters and fitted functional forms for the photodetachment cross-sections is available in the supplementary material. With the Hamiltonian parameters in hand, diagonalization of the KDC Hamiltonian provides the vibronic eigenvalues of the system. For propiolate, which has 12 vibrational modes, a full-multimode calculation is challenging, but was nevertheless performed in the present work with a recent massively parallel implementation of the KDC model.[40] For the full simulation of the stable channel included in the discussion section, the results were

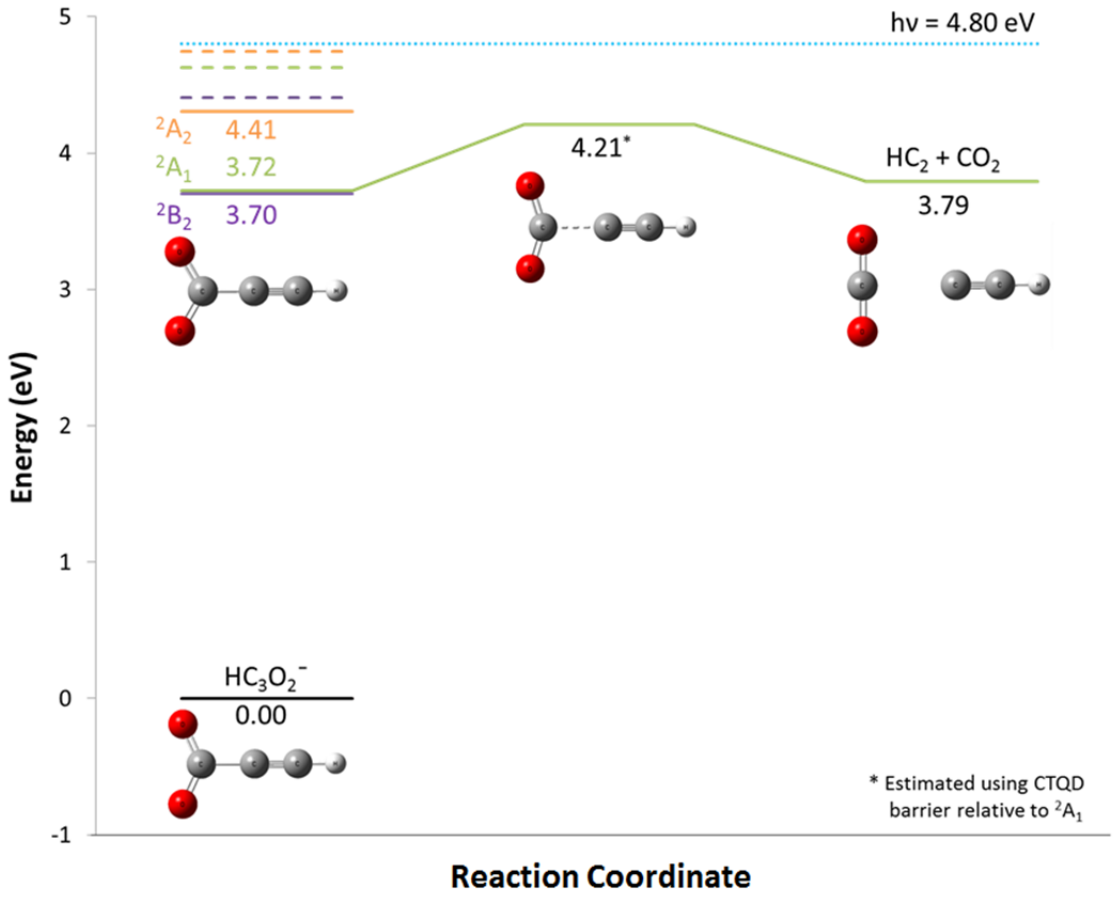

Figure 4.2. Energetics for photodetachment from the $HC_3O_2^-$ anion at hν = 4.80 eV (blue dotted line). All three low-lying electronic states ($^2B_2$, $^2A_1$, and $^2A_2$) are accessible and the $^2A_1$ can dissociate to form HC_2 + CO_2. The dashed lines correspond to the calculated VDE for each electronic state. With the exception of the barrier, all values are calculated using CCSD/EOMIP-CCSD/ANO0/FC with ZPE. The barrier is calculated using CTQD relative to the $^2A_1$ and has been adjusted relative to the EOMIP AEA.

obtained with a KDC Hamiltonian of dimension 2,972,712,960, which was deemed sufficient to obtain a fully converged spectral envelope. Diagonalization was done by the Lanczos procedure,[41] with 5000 iterations. Intensities were obtained by projecting the final-state eigenvectors onto the ground-state vibrational wavefunction followed by convolution with the calculated photodetachment cross-sections. Calculations reported here were performed with the CFOUR program system,[42] and greatly facilitated by new modules for CCSDTQ calculations (XNCC) and large-scale KDC calculations (XSIM_HPC).

4.4. Results

Experimental results for the stable and dissociative pathways of the propiolyl radical and possible isomers, syn- and anti-C_3O_2H, are presented in the following sections. Analysis of these experimental results is aided by the energetics listed in Tables 4.1 and 4.2 and shown in Figure 4.2.

4.4.1. Stable Pathway

The bulk (~96%) of the data collected upon photodetachment results in a distinct stable channel (Figure 4.3(a)). In this case, a stable photoelectron spectrum was extracted by selecting only those photoelectrons detected in coincidence with one neutral particle. These stable species must necessarily have a lifetime longer than the flight time between the interaction region and the neutral particle detector ($\Delta t \sim 9.7$ μs for m/z 69 in a 7 keV beam), or be associated with dissociative events with very low KER. The stable channel features a broad peak centered near eKE = 0.65 eV and three well-resolved features

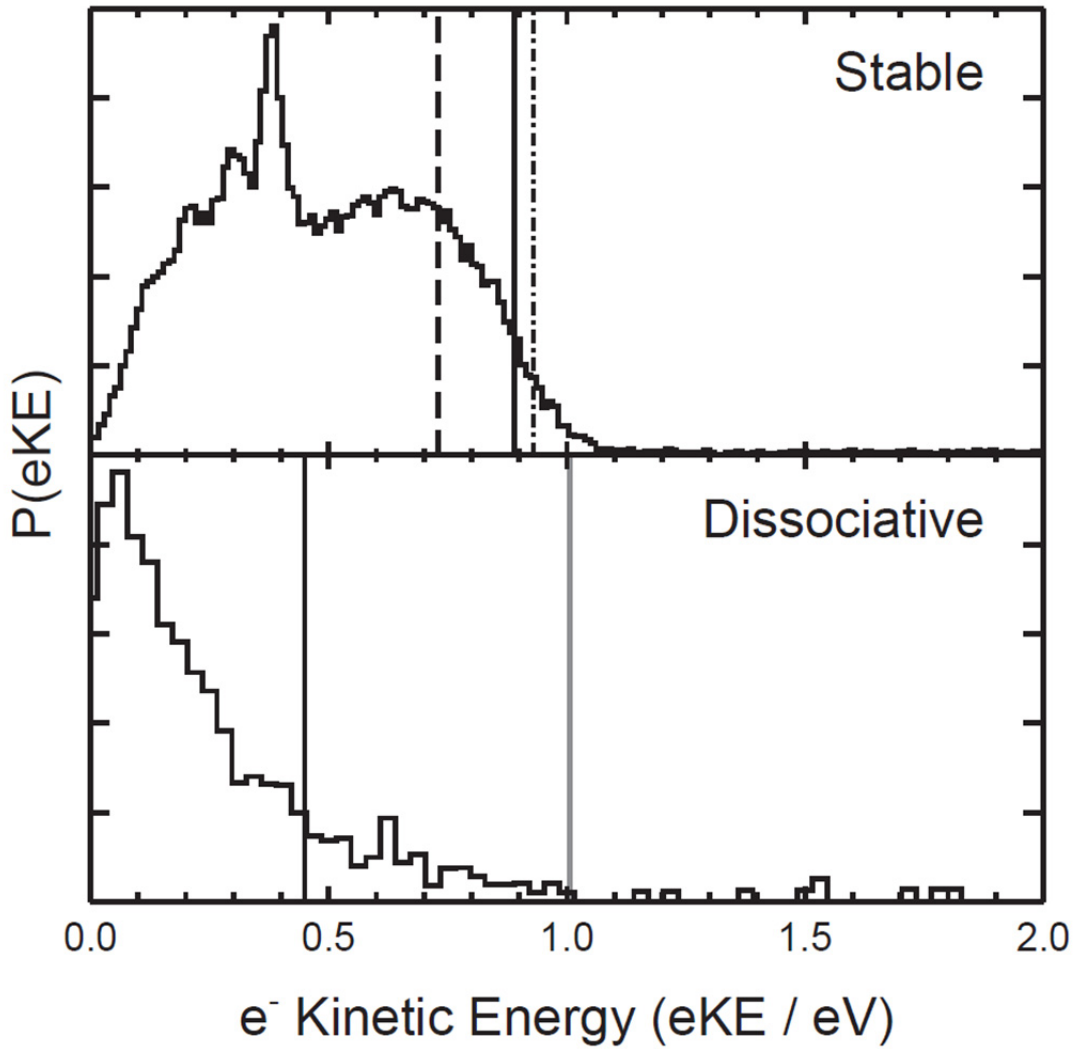

Figure 4.3. Photoelectron kinetic energy spectra of $HC_3O_2^-$ and isomers at 258 nm for (a) the stable channel, a photoelectron in coincidence with one neutral particle, and (b) the dissociative channel, a photoelectron in coincidence with two neutral particles. In the top panel, vertical lines correspond to the calculated (CTQD) AEA for the propiolyl radical (solid) and for the anti- and syn-HC_3O_2 isomers (dash and dash-dot-dot respectively). In the bottom panel, the solid black vertical line corresponds to the calculated KE_{max} (CTQD) for the dissociation reaction $HC_3O_2 \rightarrow HC_2 + CO_2$, and the grey vertical line corresponds to the calculated KE_{max} using CCSD/EOMIP-CCSD/ANO0/FC, without ZPE.

below 0.5 eV. On the other hand, the dissociative channel (Figure 4.3(b)) exhibits markedly different behavior, growing in as the stable channel drops off at lower eKE with a peak near zero eV. The shift in peak intensity to lower eKE (higher internal energies) in the dissociative channel suggests that dissociation of the nascent radical requires significant internal energy, indicating a reasonably large barrier to dissociation.

CTQD adiabatic electron affinities (AEAs) for each of the three possible anion isomers are indicated by vertical lines in Figure 4.3(a). All three AEAs fall above the bulk of the data, and thus are in qualitative agreement with the experimental results. However, the signal above these calculated AEAs is significant, implying either that these energetics are not in good agreement with the data or that the contribution from hot anions (hot bands) is large. Based on these CTQD results, it is not possible to either definitively assign the observed signal to any one species, or to rule out the presence of any isomer based solely on energetics.

Interestingly, the prominent peak progression observed below 0.5 eV in the stable photoelectron spectrum cannot be attributed to any of the computed ground states of the three radical isomers shown in Figure 4.1 based on these AEAs, strongly indicating the presence of at least one excited electronic state. As outlined in the introduction, the propiolyl radical is expected to have four low-lying electronic states due to its C_{2V} symmetry. As shown in Table 4.1, these low-lying electronic states are found to lie within roughly 1.0 eV of each other, and at the experimental photon energy of 4.80 eV the $^2B_2$ ground state and the $^2A_2$ and $^2A_1$ excited states are all energetically available. In addition, the syn- and anti-C_3O_2H isomers each have low-lying electronic states, also

listed in Table 4.1, that are calculated to be energetically available in our experiment. Based on these CTQD AEAs, the signal below 0.5 eV could potentially arise from accessing the $^2A_2$ state in the propiolyl radical or the ^2A" state in anti-C_3O_2H, although both have calculated AEAs too low to adequately describe the most prominent peak near 0.4 eV. Based on energetics alone, it is therefore not possible to directly identify which isomer and/or electronic state gives rise to this very prominent stable channel. Disentanglement of contributing species and identification of resolved features in this spectrum are possible with Franck-Condon simulations, as discussed further in the discussion section.

4.4.2. Dissociative Pathway

Unlike the case for the metastable formyloxyl radical,[3, 6] the photoelectron spectra for the stable and dissociative channels are noticeably different for the propiolyl radical as shown in Figure 4.3. Although the dissociative channel here accounts for only a surprisingly small ~4% of the overall experimental signal, the resulting resolved kinetic energy release spectrum (Figure 4.4) is very similar to that observed for the completely dissociative formyloxyl radical. [3, 6] Based on the CTQD bond dissociation energies (BDE) listed in Table 4.2, there is only one energetically available dissociative pathway at the experimental photon energy (4.80 eV), the photodetachment decarboxylation pathway: $HC_3O_2^- + h\nu \rightarrow HC_2 + CO_2 + e^-$. The progression of resolved peaks in Figure 4.4 has an average spacing of ~55 meV, consistent with excitation in the O–C–O bending mode of the CO_2 product. To first order, this makes qualitative sense given the fairly dramatic geometry change of the CO_2 group from the bent structure of the dissociative

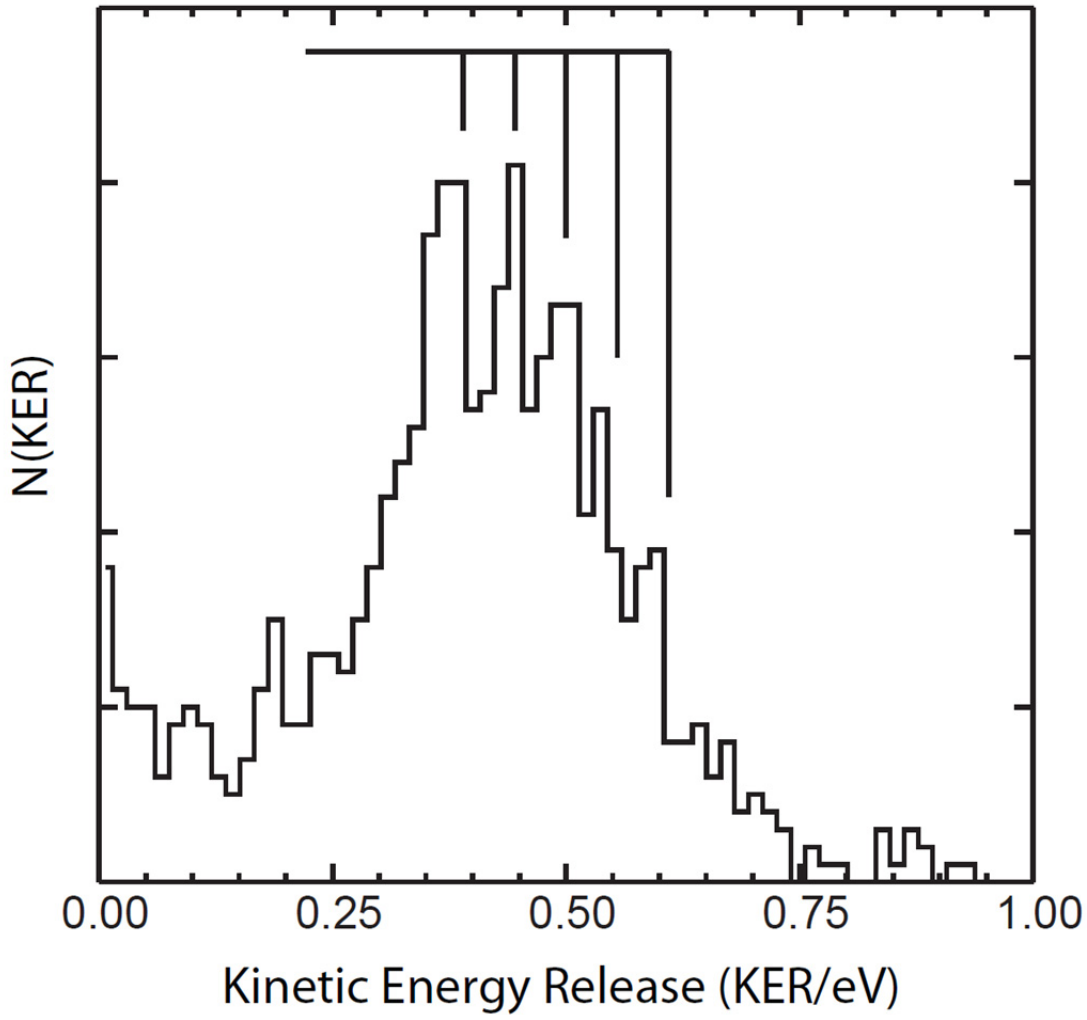

Figure 4.4. Kinetic energy release spectrum for the reaction $HC_3O_2^- + h\nu \rightarrow HC_2 + CO_2 + e^-$ at 258 nm. Vibrational comb spacing is 55 meV.

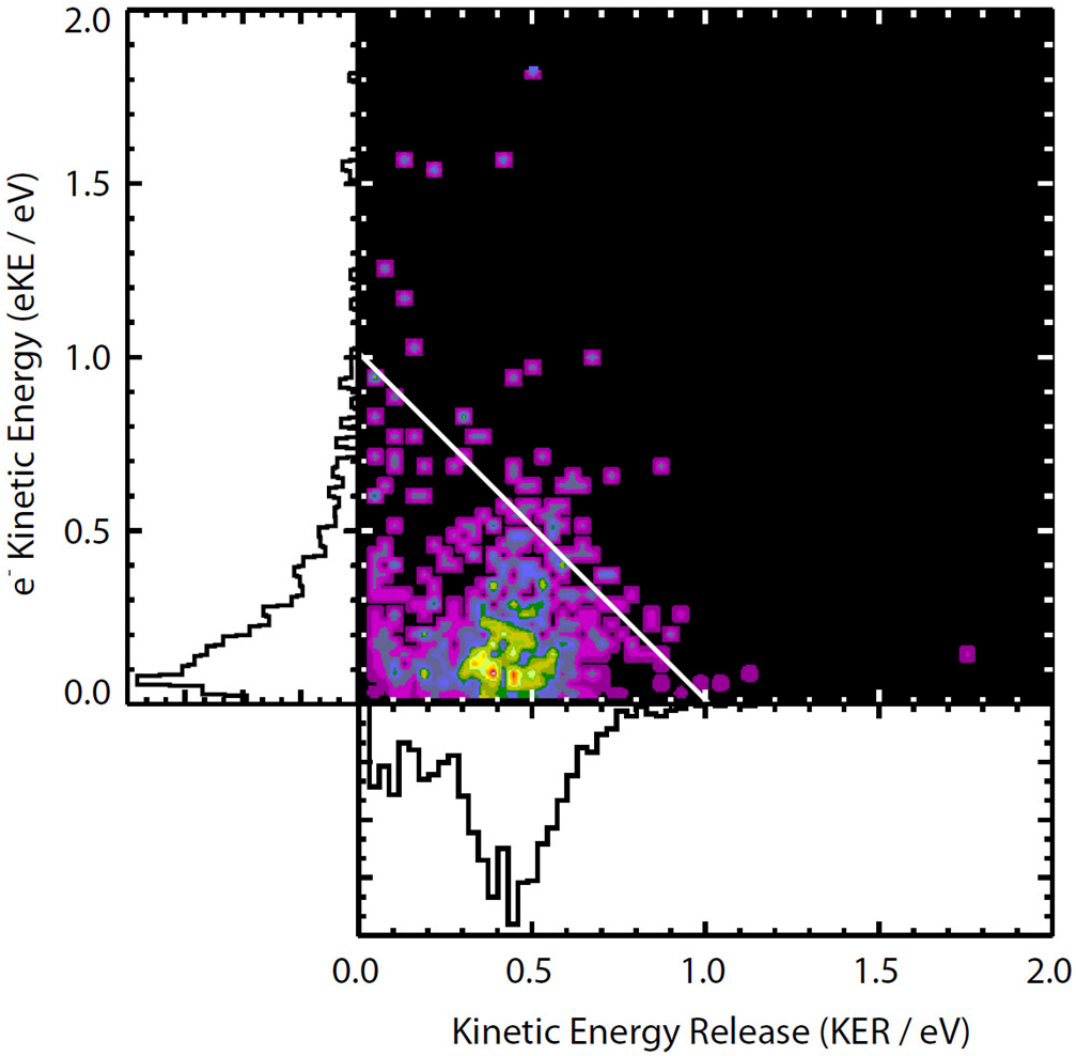

Figure 4.5. Photoelectron-photofragment coincidence spectrum for dissociation of the propiolyl radical at 258 nm. The diagonal line corresponds to the calculated maximum total kinetic energy for the $HCCCO_2^- + h\nu \rightarrow HC_2 + CO_2 + e^-$ dissociation channel, where the products form in their ground vibrational and rotational state.

$^2A_1$ state ($\angle OCO = 138^\circ$) to linear structure upon dissociation. This observed resolution in the *N(KER)* spectrum supports the HC_2 fragment being produced with limited vibrational or rotational excitation. This implies that HC_2 acts as a spectator to the dissociative process, and thus the *N(KER)* spectrum is dominated by bending excitation of the CO_2 product. The dissociation pathway must lie along a linear H-CCC axis, or significant rotational excitation of the products would be expected.

The PPC spectrum for $HC_3O_2^- + h\nu \rightarrow HC_2 + CO_2 + e^-$ (Figure 4.5) offers a more complete picture of the dissociation dynamics of this system. The two-dimensional histogram provides information on the correlation between the product *N(KER)* and *P(eKE)*, while the individual kinetic energy release spectrum (horizontal axis) and electron kinetic energy spectrum (vertical axis) result from integration over the conjugate variable. The diagonal line in the coincidence plot indicates the maximum kinetic energy release (KE_{max}) calculated at CCSD/EOMIP-CCSD/ANO0/FC, where the HC_2 and CO_2 products are produced in their ground rotational, vibrational, and electronic states ($KE_{max} = h\nu - EA - \Delta D_o = 1.01$ eV). The bulk of the data falls below this calculated KE_{max} diagonal, indicating that the predicted KE_{max} is in good agreement with the experimental data. The CTQD KE_{max} of 0.45 eV (not shown), listed in Table 4.2, is significantly too small, falling below the bulk of the dissociative data. Interestingly, the bulk of the data is centered at low eKE and high KER, appearing in the far-right corner of the energetically available coincidence region. This is consistent with probing near the top of a significant barrier to dissociation.

4.5. Discussion

As noted in the introduction, the study and analysis of even simple carboxyl free radicals are complicated by the presence of low-lying electronic states, making these systems an excellent test for theory. The propiolyl radical has proven to be an important and challenging addition to our previous studies of the dissociation dynamics of the formyloxyl radical[3, 6] and the acetyloxyl radical.[4] Specifically, its dissociative channel exhibits the general trend of fragmentation to bend-excited CO_2 and a free radical $R\cdot$, and our results indicate a substantial barrier to dissociation.

Although metastable and stable channels were observed for the smaller carboxyl free radicals, [3, 4, 6] the contribution of stable signal remained relatively small for these systems. In contrast, the propiolyl system has a massive stable channel (~96%), constituting the bulk of the experimental data. Similar to the acetyloxyl radical, where the CH_2CO_2H isomer was energetically available and could not be directly ruled out,[4] the isomeric anti- and syn-C_3O_2H are calculated to be energetically available (Table 4.1) and stable (Table 4.2) under experimental conditions and could contribute substantially to this stable channel. Discussion of this stable channel will outline the CTQD results used to ultimately rule out the presence of these isomers and their excited electronic states. Although useful for determination of isomeric composition, the CTQD method lacked the accuracy needed to fully identify the contributions of the low-lying electronic state of the propiolyl radical. Therefore the final fit of the stable channel will be discussed using results from the EOMIP-CCSD method, weighted by the calculated cross sections.

4.5.1. Non-dissociative Channels

The photoelectron spectrum for the substantial stable channel (Figure 4.3(a)) is clearly distinct from that for the dissociative channel (Figure 4.3(b)), with a broad distribution above 0.5 eV and a clear peak progression below 0.5 eV that drops toward zero signal intensity as the dissociative spectrum grows in at low energies. Unlike the metastable HCO_2, where spectra for both the stable and dissociative channels are identical,[6] the distinct difference observed here is indicative of accessing a truly stable channel. The question now is which isomers and which electronic states account for this stable pathway.

The CTQD results suggest that a number of stable pathways are energetically accessible at the experimental photon energy of 4.80 eV, which necessarily complicates analysis of the stable experimental spectrum. These pathways include three low-lying electronic states, all with C_{2V} symmetry, in the propiolyl radical: $^2B_2$, $^2A_2$, and $^2A_1$. The related syn- and anti-$CCCO_2H$ isomers must be included in the initial analysis of this stable signal, assuming that anions were created in our source using proton abstraction by O^- from propiolic acid to potentially form either $HC_3O_2^-$ or $^-C_3O_2H$. Both the anti- and syn-C_3O_2H anion isomers have CTQD calculated electron affinities within 0.2 eV of that for the propiolate anion, and are well within our experimental energy range. Additionally, the isomeric C_3O_2H (syn- and anti-) radicals also each have an energetically accessible excited electronic state: ^2A". (The CTQD EAs for each accessible state are listed in Table 1). To first order, then, this gives us a total of eight possible isomers and/or electronic states to consider.

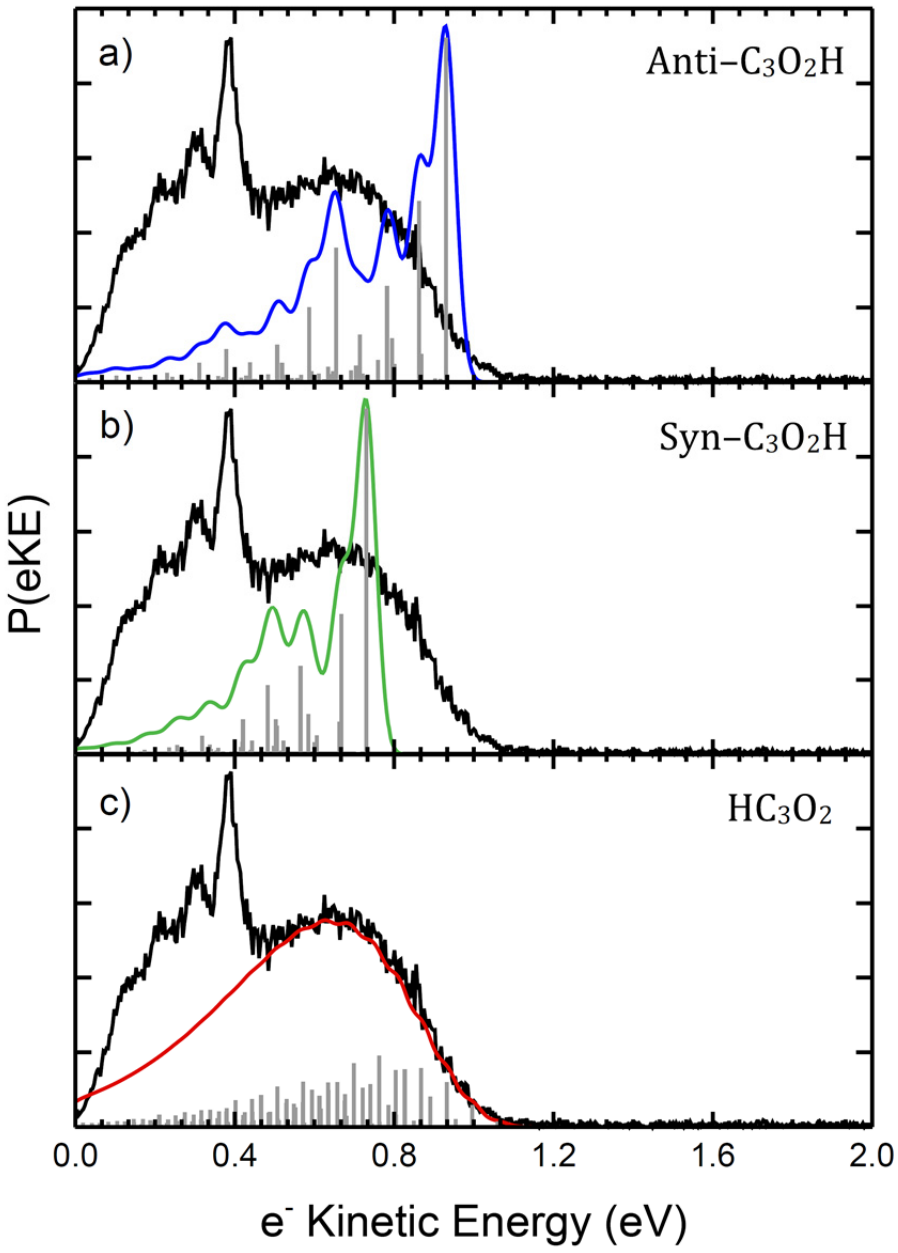

Figure 4.6. CTQD Franck-Condon simulations for photodetachment from the three possible anion precursors: a) anti- (blue) and b) syn-HC_3O_2 (green) carbanions, and c) propiolate (red), overlaid on the experimental data (black). Here photodetachment from propiolate accesses the ground $^2B_2$ state, shifted by +0.2 eV for best fit to the experimental data.

To better understand the anion-beam composition and to disentangle the information in the stable photoelectron spectrum shown in Figure 4.3(a), Franck-Condon simulations of the CTQD results for each of the ground electronic states of three possible anion isomers were performed using the program PESCAL.[43] In each case, the experimental spectrum was simulated by convoluting each FC transition with a Gaussian (FWHM = 0.05 eV). The convoluted spectra for each isomer are shown overlaid on the stable photoelectron spectrum in Figure 4.6. The simulated spectrum for the $^2B_2$ ground electronic state of the propiolyl radical (Figure 4.6(c)) consists of a broad distribution of convoluted peaks with a relatively weak ground-state transition, consistent with poor Franck-Condon overlap. The best fit to the experimental data was achieved by shifting the spectrum by 0.2 eV, so that the simulated signal slowly grows in at higher eKE and peaks at ~0.6 eV. Although the general shape of the simulation is in good agreement with the experimental data, the FC spectrum of this ground electronic state slightly overestimates the slope of the rise in intensity near the shifted EA (0.81 + 0.2 eV) and does not capture the pronounced vibrational progression seen below 0.5 eV. The large shift of 0.2 eV needed to achieve a good fit to the experiment also suggested that additional computational efforts were needed.

CTQD simulated spectra for photodetachment from the carbanion isomers anti- and syn-C_3O_2H are shown in Figure 4.6(a) and (b), respectively. Consistent with better Franck-Condon overlap than the propiolyl radical, both isomers demonstrate strong transitions at the electronic origin, with a series of clearly resolved peaks dropping to low intensity by 0.5 eV. In both cases, the overall simulation is a poor match to the

experimental data, peaking at much higher energies and exhibiting substantially different shapes than observed. With no energetically available dissociative pathways for either of these isomers, they are expected to appear only in the stable channel. Scaling the FC simulations to the experimental data (not shown) and using the assumption that the photodetachment cross-section for all anionic isomers is approximately identical leads to the conclusion that these two isomers contribute negligibly, if at all, to the overall experimental spectrum.

Fitzgerald *et al.* found the barrier to isomerization between the carbanion isomers and propiolate on the anion surface to be fairly substantial (>1 eV relative to anti-$C_3O_2H^-$), and propiolate is calculated to be ~0.9 eV more stable than either carbanion.[24] The pulsed-discharge ion source used in these experiments has previously been shown to readily make less-stable anion isomers, including cis- and trans-$HOCO^-$ anions that are ~1.5 eV less stable than the isomeric HCO_2^-.[44] Previous photodetachment work on the related 2-propyn-1-oxide ($HCCCH_2O^-$) showed that the acetylide isomer 3-hydroxy-1-propyn-1-ide ($^-$:$CCCH_2OH$) was formed readily by proton abstraction from propargyl alcohol by O^- in the pulsed-discharge ion source.[45] Consideration of the gas-phase acidity of the precursor propiolyl radical protons is useful in this analysis. In this experiment, precursor anions were formed using the robust gas-phase base O^- for proton abstraction from propiolyl alcohol. Gas-phase acidities of the acetylenic and carboxylic protons were calculated at CTQD and are listed in Table 4.3, presented relative to formation of the propiolyl radical for comparison. The acidities of the acetylenic proton (in either the anti- or syn- conformation) are considerably larger (by ~1.0 eV) than for the carboxylic

Table 4.3. CTQD gas-phase acidities for propiolic acid hydrogen atoms. Energies are reported relative to neutral propiolic acid and include zero-point energy corrections.

Acid Dissociation Pathway	ΔE (eV)
$HC_3O_2H \rightarrow HC_3O_2^- + H^+$	15.21
$HC_3O_2H \rightarrow {}^-C_3O_2H$ (anti) $+ H^+$	16.26
$HC_3O_2H \rightarrow {}^-C_3O_2H$ (syn) $+ H^+$	16.16

proton. Based on the relative stabilities of the anions, these calculated gas-phase acidities, and the CTQD Franck-Condon simulations, it is reasonable to conclude that the carbanion species do not contribute to the observed spectra. Further analysis of the stable photoelectron spectrum therefore focuses solely on the ground and low-lying excited states of the propiolyl radical.

The experimental photoelectron spectrum is fit well by the shifted CTQD simulation of the $^2B_2$ ground electronic state of the propiolyl radical above 0.5 eV (Figure 4.6(c)), the simulated spectrum quickly drops toward zero signal intensity at lower electron kinetic energies and does not explain the progression of clearly resolved peaks observed below 0.5 eV. This indicates that the resolved features arise from at least one low-lying excited electronic state of the propiolyl radical. However, the CTQD calculated EAs for the $^2A_1$ and $^2A_2$ are far too low to explain these features, while the EA for the $^2B_1$ state is too high (barely even accessible under experimental conditions). So, although the CTQD method is useful for identification of which isomer is present, it is not sufficient for a full analysis of this stable channel. Therefore, it was determined that the more extensive EOMIP-CCSD(T)(a) calculations with higher-order corrections were needed. These include calculations of electronic structures, vibronic coupling, and photodetachment cross-sections.

The calculated photodetachment cross-sections for the three lowest-lying electronic states of the propiolyl radical are shown in Figure 4.7; the EOMIP-CCSD(T)(a) simulated spectrum for these three electronic states is shown in Figure 8. As outlined briefly above, equilibrium geometries (Table 4.4) and force-field calculations

Table 4.4. CCSD/EOMIP-CCSD/ANO0/FC Geometries for HC_3O_2, HC_2 and CO_2 fragments.

	R(CO)	**R(CC*)**	**R(C*C**)**	**R(C**H)**	**A(OCO)**
Anion	1.246	1.537	1.226	1.069	131.12
$^2B_2$	1.255	1.449	1.215	1.070	113.37
$^2A_1$	1.246	1.489	1.212	1.070	138.07
$^2A_2$	1.270	1.458	1.215	1.070	121.04
HC_2	–	–	1.219	1.070	–
CO_2	1.166	–	–	–	180.00

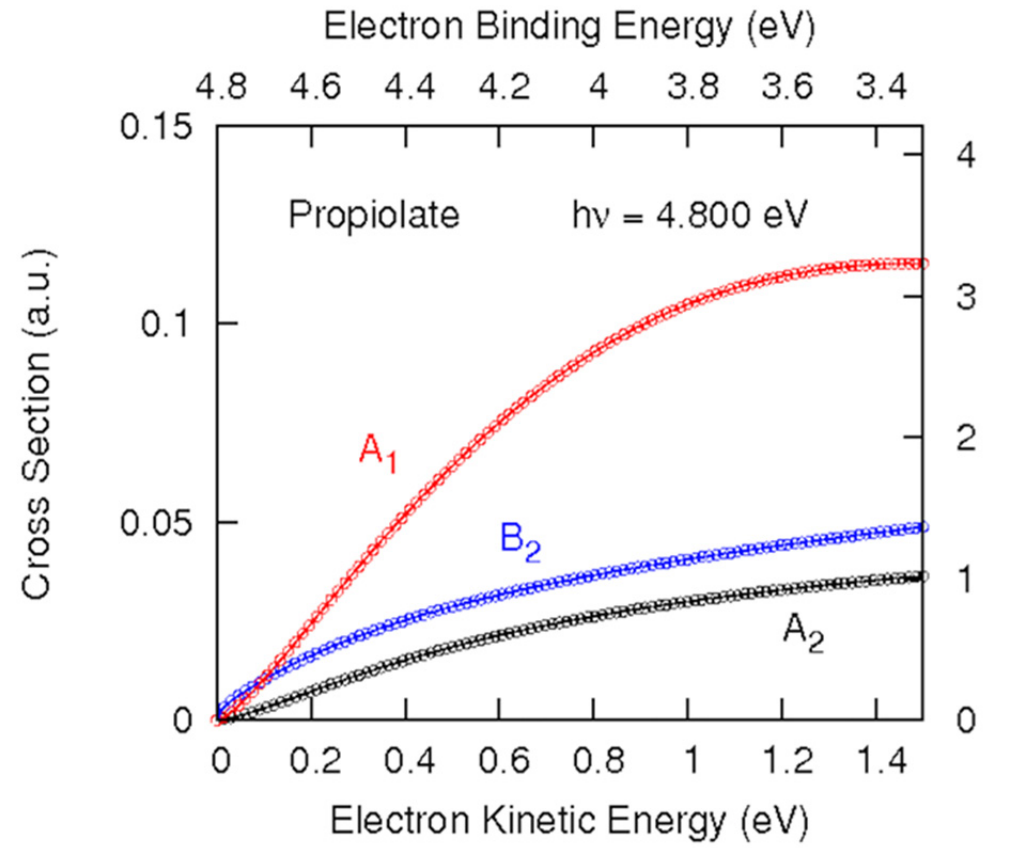

Figure 4.7. Calculated cross-sections for photodetachment to the $^2B_2$, $^2A_1$, and $^2A_2$ electronic states.

were carried out at the CCSD/ANO0 level of theory. To refine the energetics, EOMIP-CCSD(T)(a) computations, including higher-order correlation corrections from EOMIP-CCSDTQ and ANO0 basis, found VDEs for the three lowest-lying electronic states of 4.305 eV ($^2B_2$), 4.627 eV ($^2A_1$), and 4.743 eV ($^2A_2$), all with a (conservative) uncertainty of ~ 0.05 eV. Coupling between the (σ, in-plane) $^2A_1$ and $^2B_2$ states, as determined using the KDC model,[34] is very strong, and an important aspect of the electronic structure of this system, while couplings between the (π, out-of-plane) $^2A_2$ state and the two σ states are much smaller and were not included in the simulations.

The simulated spectrum, with the inclusion of calculated cross-sections, is in amazingly good agreement with the experimental data (Figure 4.8). Previous computational efforts completely failed to explain the resolved features below 0.5 eV, as clearly evident even in the calculated EAs listed in Table 4.1. The very strong coupling between the $^2A_2$ and $^2B_2$ states was key to fully capturing the experimental results, where the resolved peaks are now well described by the $^2A_1$ electronic state. The simulated spectrum also does a remarkably good job of capturing the relative intensity of these resolved peaks. This is consistent with the stable signal corresponding to photodetachment to the propiolyl radical, supporting the earlier conclusion that the other anion isomers are not present in our beam. Interestingly, this means that, unlike the simpler carboxyl free radicals, the lower lying states of the propiolyl radical are much more stable. In any case, as discussed below, the $^2B_2$ and $^2A_2$ states do not dissociate under our experimental conditions.

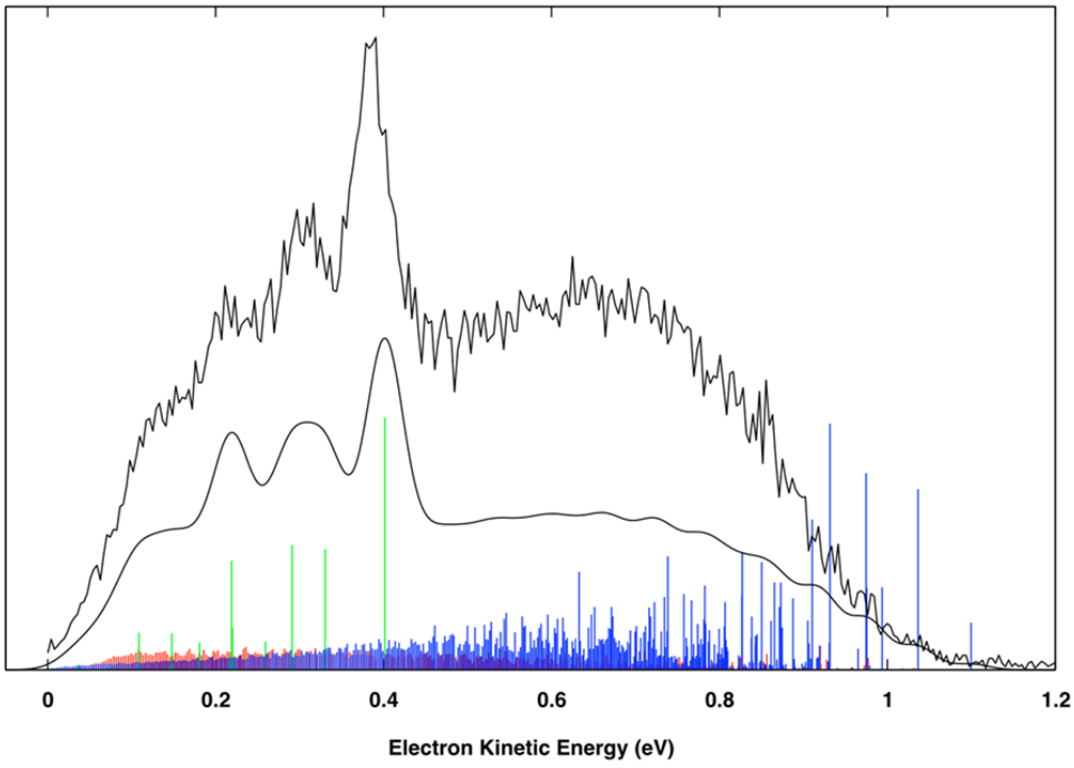

Figure 4.8. CCSD/EOMIP-CCSD/ANO0/FC Franck-Condon simulations for photodetachment to the $^2B_2$, $^2A_1$, and $^2A_2$ electronic states and sum fit.

The broad nature of the $^2B_2$ portion of the simulated spectrum indicates poor FC overlap, which, in this case, arises from the rather large geometry change in the O–C–O bond angle between the anion (132.0°) and the neutral $^2B_2$ (113°). Although convoluted, the peaks are dominated by modes corresponding to O–C–O bending and symmetric stretching, consistent with this large geometry change. Conversely, the $^2A_1$ state has much better FC overlap with the anion, as evidenced by the prominent, resolved peaks. The $^2A_1$ state has an O–C–O bond angle of 138°, comparable to that of the anion. Thus, it is reasonable to expect less vibrational excitation in the O–C–O bending mode, although this mode still dominates the spectrum.

4.5.2. Dissociative Channels

Although the presence of the isomers anti- and syn-C_3O_2H was ruled out in the discussion of the stable channel above, possible dissociative pathways for these isomers, in addition to the propiolyl radical, are listed in Table 2. The only energetically available dissociation pathway upon photodetachment is calculated to be $HC_3O_2^- + h\nu \rightarrow HC_2 + CO_2 + e^-$, so dissociation of only propiolyl radical is considered here. The photoelectron spectrum for the dissociative channel differs significantly from that for the stable channel as shown in Figure 3, peaking at small eKE and growing in just as the stable photoelectron spectrum drops toward zero signal intensity. A logical interpretation is that, at these low electron kinetic energies (and correspondingly higher internal energies) the dissociative channel opens and competes effectively with the stable channel, consistent with probing near the top of a dissociation barrier.

Similar to the DPD of DCO_2^-, resolved vibrational structure is observed in the KER spectrum (Figure 4). The average peak spacing is 55 meV, consistent with primarily O–C–O bending excitation in the CO_2 product and comparable to the 71 meV average peak spacing for vibrational progression observed in the KER for DCO_2.[6] State-resolved structure in the KER spectrum shows that the HC_2 product must act as a spectator, forming with little to no vibrational or rotational excitation. This is supported by the resulting conformational changes of the products from the nascent neutral radical. Comparison of the geometries of the HC_2 moiety of the propiolyl radical and the HC_2 fragment indicates that conformational changes are relatively small upon dissociation, regardless of electronic state, as shown in Table S4. In particular, the C–H bond for both the $^2A_1$ state and the HC_2 fragment are 1.069 Å, while the C≡C bond length goes from 1.212 Å in the $^2A_1$ state to 1.219 Å in the HC_2 fragment. Similar to the case for simpler carboxyl radicals, the O–C–O bond angles for the various electronic states range from ~113° for $^2B_2$ to ~138° for $^2A_1$. Given that free CO_2 is linear, it is therefore reasonable to expect the CO_2 fragment to originally form with considerable bending excitation upon dissociation, similar to what is observed for HCO_2.[6]

Interestingly, the signal intensity in the KER spectrum (Figure 4) peaks at ~0.4 eV, well below the calculated KE_{max} (1.01 eV), indicating a fairly substantial barrier to dissociation. This peak intensity implies a barrier to dissociation of at least 0.4 eV relative to the HC_2 + CO_2 product asymptote. Given that there are two polyatomic fragments that can be excited in the dissociation, this KER determination of the barrier is a lower limit, placing this at 4.24 eV relative to the propiolate anion, well below the

available photon energy. At the CTQD level of theory, only the $^2A_1$ state is found to be dissociative, with a calculated barrier (without ZPE) of 0.485 eV above the AEA for $^2A_1$. Using the EOMIP AEA value from Table 1 with the CTQD barrier gives a calculated barrier height of 4.21 eV relative to the anion. This calculated barrier is therefore 0.414 eV above the EOMIP products, in remarkably good agreement with the observed approximate experimental barrier of ~0.4 eV. As discussed above for the stable channel and for determination of the dissociative KE_{MAX}, CTQD calculations have consistently underestimated the stability of both the propiolyl radical and its fragments upon dissociation, and therefore this calculated barrier (like our approximation) should be taken as a lower limit.

With the understanding that photodetachment is a vertical process and relying on the Born-Oppenheimer approximation, we can gain a general idea of where on the neutral surface we are probing by comparing the anion and neutral geometries. This is easily done by focusing on the C(2)–C(3) bond length and the O–C–O bond angle, taking the reaction coordinate to be along the C(2)–C(3) bond, coupled to the O–C–O bond angle (which opens up as one proceeds toward products). The anion has a C(2)–C(3) bond length of 1.54 Å and a O–C–O bond angle of 132°. The $^2B_2$ ground state has a slightly shorter C(2)–C(3) bond length of 1.45 Å and a considerably smaller O–C–O bond angle of 113°. As observed for the stable channel, these conformational changes result in poor FC overlap with the bottom of the $^2B_2$ well. Based on the overall geometries of the various electronic states, the $^2A_1$ state has the largest O–C–O bond angle at 138°, lying closer to the final linear CO_2 structure than do either of the other electronic states, or even

the anion. This strongly suggests that, as for the simpler HCO_2, the $^2A_1$ electronic state is dissociative.

4.6. Conclusion

In conclusion, we report a study of the photodetachment and dissociative photodetachment of the propiolate anion, $HC_3O_2^-$, using PPC spectroscopy. Unlike the metastable species HCO_2 and CH_3CO_2 previously studied,[3, 4, 6] photodetachment of the propiolate anion predominantly forms stable propiolyl radicals, accounting for ~96% of the experimental data, with a minor dissociative channel arising from predissociation of the $^2A_1$ excited state. The HC_2 group acts as a spectator in the process, resulting in a distinct partitioning of internal energy in the products dominated by considerable excitation in the bending mode of CO_2, resulting in a resolved progression in the KER spectrum. This is consistent both with the expected geometry changes upon dissociation and with the observed dissociation dynamics of simpler carboxyl free radicals. The peak of the KER signal at 0.45 eV represents a lower limit to the barrier to dissociation, in good agreement with the relative CTQD calculated barrier of 0.395 eV.

The spectrum for the stable channel reveals photodetachment of the propiolate anion, accessing the three lowest-lying electronic states in the propiolyl radical, $^2B_2$, $^2A_1$, and $^2A_2$. The anion's syn- and anti-C_3O_2H isomers were excluded from analysis based on CTQD Franck-Condon simulations of the photoelectron spectrum for the stable channel. Fitting of the experimental photoelectron spectrum for the stable channel proved to be complicated, requiring sophisticated computational work. We present here a truly *ab initio* photoelectron spectrum, calculated by CCSD/EOMIP-CCSD/ANO0/FC, that is in

remarkable agreement with the experimental spectrum for the stable channel. Similar to the case for the simple formyloxyl radical, the $^2B_2$ and $^2A_1$ electronic states of the studied propiolate anion exhibit strong vibronic coupling that had to be accounted for accurately in the FC simulation. Energetics were determined using high-level vertical detachment energies (VDEs), with the relative contribution of each electronic state then adjusted using the calculated photodetachment cross-sections. Both the broad distribution in the photoelectron spectrum above eKE = 0.5 eV (arising from the $^2B_2$ and $^2A_1$ electronic states) and the well-defined peaks below eKE = 0.5 eV (arising from the $^2A_2$ electronic state) are well captured by the simulation. This was not the case using lower levels of theory, necessitating the push for ever-more-complicated theory and proving a good test case for the CCSD/EOMIP-CCSD/ANO0/FC method employed here.

Acknowledgements

This material is based on work supported by the U.S. Department of Energy, Office of Science, Office of Basic Energy Sciences under award numbers DE-FG03-98ER14879 (AWR and REC)

4.7. References

1. Kim, E. H.; Bradforth, S. E.; Arnold, D. W.; Metz, R. B.; Neumark, D. M., Study of HCO_2 and DCO_2 by Negative Ion Photoelectron Spectroscopy. *The Journal of Chemical Physics* **1995,** *103* (18), 7801-7814.

2. Ruscic, B.; Schwarz, M.; Berkowitz, J., A Photoionization Study of the COOH Species. *The Journal of Chemical Physics* **1989,** *91* (11), 6780-6785.

3. Clements, T. G.; Continetti, R. E., Predissociation dynamics of Formyloxyl Radical Studied by the Dissociative Photodetachment of HCO_2^- /DCO_2^- + hν → H/D + CO_2 + e^-. *The Journal of Chemical Physics* **2001,** *115* (12), 5345-5348.

4. Lu, Z.; Continetti, R. E., Dynamics of the Acetyloxyl Radical Studied by Dissociative Photodetachment of the Acetate Anion. *The Journal of Physical Chemistry A* **2004,** *108* (45), 9962-9969.

5. Garand, E.; Klein, K.; Stanton, J. F.; Zhou, J.; Yacovitch, T. I.; Neumark, D. M., Vibronic Structure of the Formyloxyl Radical (HCO_2) via Slow Photoelectron Velocity-Map Imaging Spectroscopy and Model Hamiltonian Calculations. *The Journal of Physical Chemistry A* **2009,** *114* (3), 1374-1383.

6. Ray, A. W.; Shen, B. B.; Poad, B. L. J.; Continetti, R. E., State-Resolved Predissociation Dynamics of the Formyloxyl Radical. **2014,** *592* (0), 30-35.

7. Peyerimhoff, S. D.; Skell, P. S.; May, D. D.; Buenker, R. J., Configuration Interaction Study of the Three Lowest Electronic States in the Formyl and Acetyl Radicals. *J. Am. Chem. Soc.* **1982,** *104* (17), 4515-4520.

8. Feller, D.; Huyser, E. S.; Borden, W. T.; Davidson, E. R., MCSCF/CI Investigation of the Low-Lying Potential Energy Surfaces of the Formyloxyl Radical, $HCO_2\cdot$. *J. Am. Chem. Soc.* **1983,** *105* (6), 1459-1466.

9. McLean, A. D.; Lengsfield III, B. H.; Pacansky, J.; Ellinger, Y., Symmetry Breaking in Molecular Calculations and the Reliable Prediction of Equilibrium Geometries. The Formyloxyl Radical as an Example. *The Journal of Chemical Physics* **1985,** *83* (7), 3567-3576.

10. Burton, N. A.; Yamaguchi, Y.; Alberts, I. L.; Schaefer Iii, H. F., Interpretation of Excited State Hartree-Fock Analytic Derivative Anomalies for NO_2 and HCO_2 Using the Molecular Orbital Hessian. *The Journal of Chemical Physics* **1991,** *95* (10), 7466-7478.

11. Rauk, A.; Yu, D.; Armstrong, D. A., Carboxyl Free Radicals: Formyloxyl (HCOO·) and Acetyloxyl (CH3COO·) Revisited. *J. Am. Chem. Soc.* **1994,** *116* (18), 8222-8228.

12. Rauk, A.; Yu, D.; Borowski, P.; Roos, B., CASSCF, CASPT2, and MRCI Investigations of Formyloxyl Radical (HCOO·). *Chemical Physics* **1995,** *197* (1), 73-80.

13. Stanton, J. F.; Kadagathur, N. S., Pseudorotational Interconversion of the $^2A_1$ and $^2B_2$ States of HCOO. *Journal of Molecular Structure* **1996,** *376* (1–3), 469-474.

14. Ayala, P. Y.; Schlegel, H. B., A Nonorthogonal CI Treatment of Symmetry Breaking in Sigma Formyloxyl Radical. *The Journal of Chemical Physics* **1998,** *108* (18), 7560-7567.

15. Kieninger, M.; Ventura, O. N.; Suhai, S., Density Functional Investigations of Carboxyl Free Radicals: Formyloxyl, Acetyloxyl, and Benzoyloxyl Radicals. *International Journal of Quantum Chemistry* **1998,** *70* (2), 253-267.

16. Feller, D.; Dixon, D. A.; Francisco, J. S., Coupled Cluster Theory Determination of the Heats of Formation of Combustion-Related Compounds: CO, HCO, CO_2, HCO_2, HOCO, HC(O)OH, and HC(O)OOH. *The Journal of Physical Chemistry A* **2003,** *107* (10), 1604-1617.

17. Klein, K.; Garand, E.; Ichino, T.; Neumark, D.; Gauss, J.; Stanton, J., Quantitative Vibronic Coupling Calculations: the Formyloxyl Radical. *Theor Chem Acc* **2011,** *129* (3-5), 527-543.

18. Ma, J.; Guo, H., Full-Dimensional Quantum State Resolved Predissociation Dynamics of HCO_2 Prepared by Photodetaching HCO_2^-. *Chemical Physics Letters* **2011,** *511* (4–6), 193-195.

19. Corchado, J. C.; Espinosa-Garcia, J.; Li, J.; Guo, H., CO_2 Vibrational State Distributions From Quasi-Classical Trajectory Studies of the HO + CO → H + CO_2 Reaction and H + CO_2 Inelastic Collision. *The Journal of Physical Chemistry A* **2012**.

20. Li, J.; Wang, Y.; Jiang, B.; Ma, J.; Dawes, R.; Xie, D.; Bowman, J. M.; Guo, H., Communication: A Chemically Accurate Global Potential Energy Surface for the HO + CO → H + CO_2 Reaction. *The Journal of Chemical Physics* **2012,** *136* (4), 041103-4.

21. Li, J.; Brill, T. B., Spectroscopy of Hydrothermal Reactions 20: Experimental and DFT Computational Comparison of Decarboxylation of Dicarboxylic Acids Connected by Single, Double, and Triple Bonds. *The Journal of Physical Chemistry A* **2002,** *106* (41), 9491-9498.

22. Poad, B. L. J.; Kirk, B. B.; Hettiarachchi, P. I.; Trevitt, A. J.; Blanksby, S. J.; Clark, T., Direct Detection of a Persistent Carbonyloxyl Radical in the Gas Phase. *Angewandte Chemie International Edition* **2013,** *52* (35), 9301-9304.

23. Sasahara, A.; Uetsuka, H.; Ishibashi, T.-a.; Onishi, H., A Needle-Like Organic Molecule Imaged by Noncontact Atomic Force Microscopy. *Applied Surface Science* **2002,** *188* (3–4), 265-271.

24. Fitzgerald, M.; Bowie, J. H.; Schröder, D.; Schwarz, H., The Formation of Neutral $CCCO_2H$ and $HCCCO_2$ Molecules from Anionic Precursors in the Gas Phase: A Joint Experimental and Theoretical Study. **2005,** *19* (24), 3705-3712.

25. Zou, L.; Li, J.; Wang, H.; Ma, J.; Guo, H., State-Resolved Quantum Dynamics of Photodetachment of HCO_2^-/DCO_2^- on an Accurate Global Potential Energy Surface. *The Journal of Physical Chemistry A* **2015,** *119* (28), 7316-7324.

26. Hanold, K.; Luong, A.; Clements, T.; Continetti, R., Photoelectron-Multiple-Photofragment Coincidence Spectrometer. *Review of Scientific Instruments* **1999,** *70* (5), 2268-2276.

27. Johnson, C.; Shen, B.; Poad, B.; Continetti, R., Photoelectron-Photofragment Coincidence Spectroscopy in a Cryogenically Cooled Linear Electrostatic Ion Beam Trap. *Review of Scientific Instruments* **2011,** *82* (10), 105105.

28. Bowen, M. S.; Continetti, R. E., Photodetachment Imaging Study of the Vinoxide Anion. *The Journal of Physical Chemistry A* **2004,** *108* (39), 7827-7831.

29. Purvis, G. D.; Bartlett, R. J., A Full Coupled-Cluster Singles and Doubles Model: The Inclusion of Disconnected Triples. *The Journal of Chemical Physics* **1982,** *76* (4), 1910-1918.

30. Almlöf, J.; Taylor, P. R., General Contraction of Gaussian Basis Sets. I. Atomic Natural Orbitals for First- and Second-Row Atoms. *The Journal of Chemical Physics* **1987,** *86* (7), 4070-4077.

31. Matthews, D. A.; Stanton, J. F., A New Approach to Approximate Equation-of-Motion Coupled Cluster with Triple Excitations *Journal of Chemical Physics* **2016**, Accepted.

32. Kamiya, M.; Hirata, S., Higher-Order Equation-of-Motion Coupled-Cluster Methods for Ionization Processes. *The Journal of Chemical Physics* **2006,** *125* (7), 074111.

33. Matthews, D. A.; Stanton, J. F., Non-Orthogonal Spin-Adaptation of Coupled Cluster Methods: A New Implementation of Methods Including Quadruple Excitations. *The Journal of Chemical Physics* **2015,** *142* (6), 064108.

34. Köppel, H.; Domcke, W.; Cederbaum, L. S., Multimode Molecular Dynamics Beyond the Born-Oppenheimer Approximation. In *Advances in Chemical Physics*, John Wiley & Sons, Inc.: 1984; pp 59-246.

35. Ichino, T.; Gianola, A. J.; Lineberger, W. C.; Stanton, J. F., Nonadiabatic Effects in the Photoelectron Spectrum of the Pyrazolide-d3 Anion: Three-State Interactions in the Pyrazolyl-d3 radical. *The Journal of Chemical Physics* **2006,** *125* (8), 084312.

36. Stanton, J. F.; Gauss, J., Analytic Energy Derivatives for Ionized States Described by the Equation-of-Motion Coupled Cluster Method. *The Journal of Chemical Physics* **1994,** *101* (10), 8938-8944.

37. Ichino, T.; Gauss, J.; Stanton, J. F., Quasidiabatic States Described by Coupled-Cluster Theory. *The Journal of Chemical Physics* **2009,** *130* (17), 174105.

38. Gozem, S.; Gunina, A. O.; Ichino, T.; Osborn, D. L.; Stanton, J. F.; Krylov, A. I., Photoelectron Wave Function in Photoionization: Plane Wave or Coulomb Wave? *J. Phys. Chem. Lett.* **2015,** *6* (22), 4532-4540.

39. Woon, D. E.; Dunning, T. H., Gaussian Basis Sets for Use in Correlated Molecular Calculations. IV. Calculation of Static Electrical Response Properties. *The Journal of Chemical Physics* **1994,** *100* (4), 2975-2988.

40. Rabidoux, S. M.; Eijkhout, V.; Stanton, J. F., Parallelization Strategy for Large-Scale Vibronic Coupling Calculations. *The Journal of Physical Chemistry A* **2014,** *118* (51), 12059-12068.

41. Lanczos, C., An Iteration Method for the Solution of the Eigenvalue Problem of Linear Differential and Integral Operators. *Journal of Research of the National Bureau of Standards* **1950,** *45* (4), 255-282.

42. CFOUR, Coupled-Cluster techniques for Computational Chemistry, a quantum chemical program package written by Stanton, J. F.; Gauss, J.; Harding, M. E.; Szalay, P. G.; with contributions from Auer, A. A.; Bartlett, R. J.; Benedikt,U.; Berger. C.;

Bernholdt, D. E.; Bomble, Y. J.; Cheng, L.; Christiansen, O.; Heckert, M.; Heun, O.; Huber, C.; Jagau,T. –C.; Jonsson, D.; Jusélius, J.; Klein, K.; Lauderdale, W. J.; Lipparini, F.; Matthews, D. A.; Metzroth, T.; Mück, L. A.; O'Neill, D. P.; Price, D. R.; Prochnow, E.; Puzzarini, C.; Ruud, K.; Schiffmann, F.; Schwalbach, W.; Simmons, C.; Stopkowicz, A.; Tajti, A.; Vázquez, J.; Wang, F.; Watts, J. D. and the integral packages MOLECULE (Almlöf, J.; Taylor, P. R.), PROPS (Taylor, P. R.), ABACUS (Helgaker, T.; Jensen, H. J. Aa.; Jørgensen, P.; Olsen, J.), and ECP routines by Mitin, A. V. and van Wüllen, C. For the current version see, http://www.cfour.de.

43. Ervin, K. M.; Ho, J.; Lineberger, W. C., Ultraviolet Photoelectron Spectrum of Nitrite Anion. *J. Phys. Chem.* **1988,** *92* (19), 5405-5412.

44. Dixon, D. A.; Feller, D.; Francisco, J. S., Molecular Structure, Vibrational Frequencies, and Energetics of the HCO, HOCO, and HCO_2 Anions. *The Journal of Physical Chemistry A* **2003,** *107* (1), 186-190.

45. Alconcel, L.-N. S. Energetics and Dissociation Dynamics of Reactive Organic Intermediates. University of California, San Diego, 2002.

Chapter 5: Effects of Vibrational Excitation on the F + H_2O → FH + OH Reaction: Dissociative Photodetachment of Overtone-Excited $[F–H–OH]^-$

5.1. Introduction

The effects of vibrational excitation on the rates and dynamics of chemical reactions in the gas phase are the focus of considerable interest. In the case of atom-diatom reactions, Polanyi's rules explain the differing effects of reactant vibration and translational energy as a function of reaction energetics,[1] and recent work has extended these concepts toward polyatomic systems.[2, 3] Considerable experimental effort has been devoted toward exploration of mode-selective chemistry involving polyatomic molecules both in the gas phase[2, 4-12] and at surfaces.[13, 14] These studies indicate that excitation of vibrational modes with large displacements along a reaction coordinate can preferentially promote surmounting specific barriers, giving rise to mode-selective chemistry. The present work is a study of the effect of anion vibrational excitation on the dynamics of the neutral F + H_2O → HF + OH reaction by means of direct IR absorption. Photodetachment initiates this reaction near the transition state for the bimolecular reaction by photodetachment of $F^-(H_2O)$.[15] Excitation of a suitable mode in the precursor anion changes the Franck-Condon overlap with the neutral surface, and in favorable cases should provide considerable control over product branching ratios and dynamics. Here we examine the effects of excitation of the first overtone of the F–H–OH proton-transfer

mode in $F^-(H_2O)$ prior to carrying out photoelectron-photofragment coincidence (PPC) spectroscopy. This study was made possible by our demonstration of the successful coupling of an infrared laser system into the ion beam line of the PPC spectrometer.[16]

Most previous studies of the effects of vibrational excitation on reaction dynamics have used gas cell or crossed-beam techniques, but another important approach to examining neutral reaction dynamics is by neutralization of ionic species. Photodetachment photoelectron spectroscopy of negative ions has been used as a spectroscopy of the neutral transition state in isomerization[17, 18] and bimolecular reactions.[19] These experiments probe neutral configurations as determined by the ground state anion precursor. To go beyond this restriction, Lineberger and coworkers, using negative ion-neutral-positive ion (NeNuPo) charge reversal spectroscopy, probed a broad portion of the neutral surface of Ag_3 by photodetachment of Ag_3^- followed by femtosecond photoionization to probe the time dependence of the neutral wavepacket.[20] An alternative approach to sampling other configurations on the neutral surface is to vibrationally excite the anion precursor prior to photodetachment. Neumark and coworkers have demonstrated this approach by using stimulated Raman excitation of C_2^- as demonstrated by photoelectron spectroscopy.[21, 22] However, stimulated Raman pumping is limited to those anion systems with optically accessible excited states below their detachment threshold. Other approaches including stimulated Raman-adiabatic passage (STIRAP) may also be applied,[23] however in our laboratory we have taken the more general approach of direct absorption of infrared radiation used in a number of prior crossed beam studies.

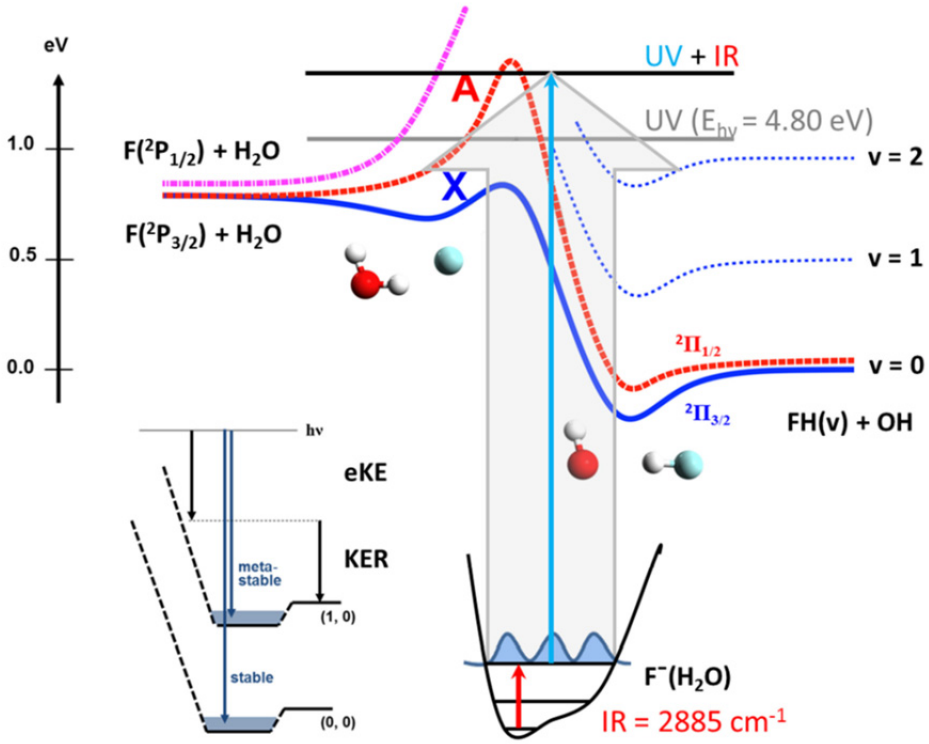

Figure 5.1. Potential energy diagram for the ground (X) and excited (A) states of the F + H_2O → HF + OH reaction and a 1D potential energy slice along the ionic hydrogen bond (IHB) of the F^-H_2O anion. Anion and neutral surfaces not necessarily to scale.

The prototypical hydrogen-abstraction reaction $F + H_2O \rightarrow FH_2O^* \rightarrow HF + OH$ has recently been studied in our lab in conjunction with full 6D quantum-dynamics simulations on *ab initio* potential energy surfaces.[15] This reaction provides an excellent test case for precursor-anion excitation in PPC experiments. The reaction is characterized by three low-lying potential energy surfaces (PES), shown schematically in Figure 5.1. Asymptotically, the ground state $F(^2P_{3/2})$ correlates adiabatically to $HF + OH(^2\Pi_{3/2})$ along the ground (X) state and also accesses the higher-lying excited (A) state, leading to formation of spin-orbit-excited $HF + OH(^2\Pi_{1/2})$.[24-27] The third surface corresponds to the endothermic reaction of spin-orbit-excited $F(^2P_{1/2}) + H_2O$ to adiabatically form electronically excited $OH(^2\Sigma^+) + HF$ products. Reaction barriers separate reactant-channel and product-channel van der Waals (vdW) complexes on both the X and A states,[28, 29] and the pre-reactive $F–H_2O$ complex was recently shown to possibly exert a strong influence on the overall reactivity.[30]

Kinetics measurements on this system suggested a tunneling-mediated reaction at low temperatures, based in part on the observed kinetic-isotope effect and the observation of no temperature dependence.[31] Wang and coworkers carried out the first photoelectron spectroscopy experiments on the $F^-(H_2O)$ anion at 6.42 eV,[32] and the resulting fragmentation processes were studied by direct molecular-dynamic simulations.[33] Nesbitt and coworkers carried out an extensive series of cross-beam experiments on the $F + H_2O/D_2O$ reaction using a combination of laser-induced fluorescence[25, 27] and high-resolution IR-laser absorption techniques for product detection.[26] Despite the collision energies (~ 0.25 eV) of these experiments falling well below the adiabatic barrier to the higher-lying A state, both $OH(^2\Pi_{3/2})$ and $OH(^2\Pi_{1/2})$ products were observed with a

branching ratio of 0.69:0.31, suggesting that nonadiabatic surface-hopping occurs in the exit channel.[25] The HF products were found to exhibit a vibrational population inversion, with the OH product behaving essentially as a spectator to the reaction.

The structure and energetics of the $F^-(H_2O)$ anion itself have garnered significant attention, including a number of experimental [34-36] and theoretical studies [37-42]. Experimentally, Johnson and coworkers used vibrational predissociation of $F^-(H_2O)\cdot Ar$ complexes to study this system experimentally over the range 600–3800 cm^{-1}, producing spectra dominated by the ionic hydrogen bond/ ionic OH stretch (IHB). Interestingly, they showed that features attributed to the fundamental and overtone of this mode are strongly blue-shifted upon complexation with Ar, while $Cl^-(H_2O)\cdot Ar$ and $Br^-(H_2O)\cdot Ar$ are slightly red-shifted for the comparable mode.[35] This strong blue shift is attributed to the fact that, in the ground state, charge is localized on F^-, giving the anion a $F^-\cdots$H-OH character, while any vibrational excitation in this ionic OH stretch induces charge delocalization to give a $FH\cdots OH^-$ intramolecular-proton-transfer-type structure. The competing nature of these differing charge states is attributed to the increased complexity of the $F^-(H_2O)\cdot Ar$ spectrum, and the large blue shift contributes to the fairly large uncertainty in the position of the IHB-overtone peak position in neat $F^-(H_2O)$.

Theoretical studies of the anion have focused largely on the experimentally dominant ionic hydrogen bond/OH stretch in these halide-water anions due in part to their large oscillator strengths and to sensitivity to specific interactions between the water molecule and the ion of interest. As observed experimentally, $F^-(H_2O)$ exhibits particularly large anharmonicity due in large part to the change in charge-localization

induced by excitation of this vibrational mode, making theoretical treatments challenging and highlighting the need for accurate potential energy surfaces and for a full treatment of coupled motions.[36] One dimensional cuts along the proton transfer coordinate shows this delocalized charge state as a shelf in the potential, not as a true minimum, contributing strongly to the anharmonic character of this IHB mode. This delocalized-charge-structure shelf appears at greater energies for the less-electronegative $Cl^-(H_2O)$ and $Br^-(H_2O)$ clusters,[35] which can therefore be fairly accurately described with a simple Morse potential near the bottom of the potential wells. Although calculated vibrational frequencies using this reduced-dimensionality approach yield reasonable results, Horvath and coworkers determined that a 2D model including both OF stretch/distance and bound OH stretch modes gives the most accurate results compared to the available experimental data for the $F^-(H_2O)$ system.[36] Recent full dimensional computational work simulated photodetachment spectra of vibrationally excited $F^-(H_2O)$, showing that pumping of the IHB accesses the more charge delocalized $FH\cdots OH^-$ structure of the anion results in a change in the photoelectron spectrum.[42] Excitation of this anion IHB mode is an efficient way to probe the effects of OH-stretching excitation on the overall neutral reaction for photodetachment experiments.

In the following, we present an experimental study of the effect of vibrational excitation of precursor anions on neutral-dissociation dynamics using PPC spectroscopy. As outlined above, the neutral reaction coordinate is essentially along the motion of the shared proton between fluorine and oxygen. Thus, excitation of the overtone of the IHB in the precursor $F^-(H_2O)$ anion is expected to have a significant impact on the reactivity. The resulting PPC spectra show clear signs of excitation, indicating that we have

successfully excited the precursor ions. The effects of this precursor anionic vibrational excitation on the dissociation dynamics of the neutral $F \cdot H_2O$ system are presented and discussed.

5.2. Experimental Methods

Experiments were carried out on a purpose-built PPC spectrometer, shown schematically in Figure 5.2, and described in detail elsewhere. [16, 43, 44] Precursor anions were synthesized in a coaxial-pulsed plasma discharge, stabilized/activated by a 1-keV electron beam acting on a supersonic expansion of C_2F_6/HeNe (20%/80%) passed over a 10% NH_4OH/H_2O mixture. The resulting ions were skimmed, accelerated to 7 keV, re-referenced to ground in a 30 cm long cylindrical electrode, and mass-selected by time-of-flight (TOF). The ion packet was then injected into a cryogenically cooled electrostatic ion-beam trap (EIBT), where it was phase-locked to the output from a Ti:Sapphire regenerative amplifier (Clark MXR CPA-2000; λ = 775.5 nm, repetition rate 1037 Hz, pulse width 1.1 ps) using an RF oscillator. The ion packet was then repetitively probed perpendicularly using third-harmonic radiation (258.5 nm, 4.80 eV) over a 50-ms trapping period. The resulting photoelectrons were collected on an event-by-event basis, extracted orthogonal to the ion- and laser-beam axis, and velocity-map-imaged onto a time- and position-sensitive detector.

Information on the center-of-mass (CM) electron kinetic energy (eKE) and laboratory-frame recoil angle were obtained from the arrival time and position for each photoelectron. When appropriate, optimal resolution was achieved by equatorially slicing

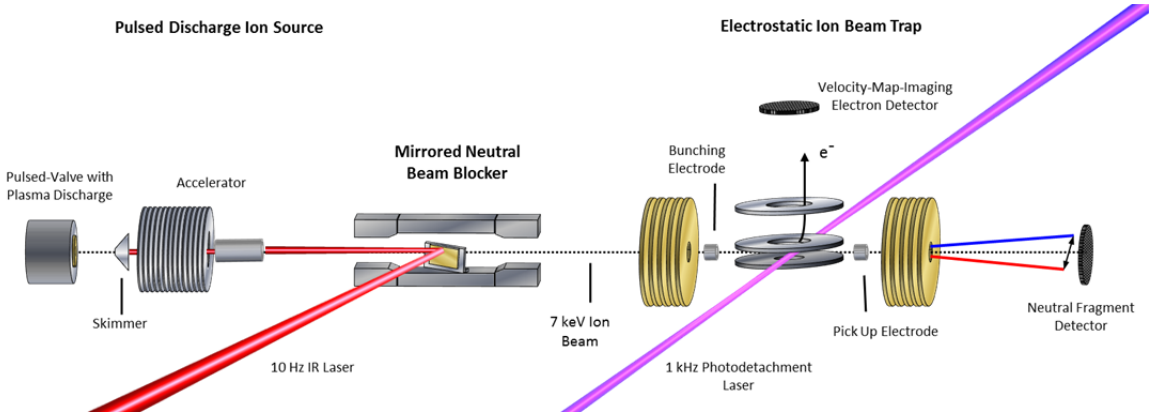

Figure 5.2. Schematic overview of the PPC spectrometer with mirrored neutral beam blocker. Ions are produced using a pulsed-valve with plasma discharge, accelerated to 7 keV and re-referenced to ground. The fast ion-beam is then irradiated with a 10 Hz laser pulse using a gold mirror placed along the beam axis. The ions are "bumped" over this mirror before proceeding to the EIBT where the PPC experiments are then carried out.

the resulting photoelectron spectrum, ensuring selection of only those photoelectrons with minimal z-velocity. This imposed detector acceptance function (DAF) necessarily results in a reduction of signal intensity at larger photoelectron velocities, which can be corrected for by dividing the experimental intensity distribution, $N(eKE)$, by the acceptance function of the z-velocity slice to provide DAF-corrected intensity distributions, $P(eKE)$.[45] Calibration of the photoelectron detector using F^- resulted in a sliced *z*-velocity component resolution of $\Delta E/E \sim 3.8$ % (unsliced $\Delta E/E \sim 7.2$ %) at 1.4 eV electron kinetic energy.

Neutral photofragments recoil out of the EIBT in a cone along the propagation direction of the ion beam, impinging on a four-quadrant time- and position-sensitive multiparticle detector, allowing the resulting neutral species to be detected in coincidence with the photoelectron.. This allows calculation of the product masses and kinetic energy release (KER) for each event containing momentum-matched neutral particles. Calibration of the multiparticle neutral detector using the dissociative photodetachment of O_4^- yielded a kinetic energy release resolution of $\Delta E/E \sim 10\%$.[43]

Observation of the effect of vibrational excitation of precursor ions was achieved by irradiating the ion packet with infrared (IR) light coaxially in a counter-propagating fashion prior to injection into the EIBT as described in ref. [16] and shown in Figure 5.2. The anion packet was irradiated at 2885 cm^{-1}, 2872 cm^{-1}, or 2900 cm^{-1} using the tunable output of a 10-Hz Nd:YAG (Surelite III EX) pumped KTP/KTA optical-parametric oscillator/optical-parametric amplifier (OPO/OPA) system (Laser Vision, 100–300 mW, 5 ns FWHM, bandwidth ~3 cm^{-1}). The IR wavelength λ was set using the

OPO signal and idler wavelength, measured using a spectrometer (Ocean Optics HR2000+) and independently calibrated using photoacoustic spectroscopy. Counter-propagation of the IR pulse relative to the fast-ion packet gives rise to a Doppler shift of 2cm^{-1}, corrected for prior to data collection. Source fluctuations were mitigated by data collection in an interleaved fashion, where ion source and PPC measurements were run at a 20-Hz duty cycle, all the while synchronized with the 10-Hz IR laser system such that every other 48 ms trapping cycle was carried out on an IR-irradiated anion packet. IR-irradiation of the anions occurred ~10 μs before the first photodetachment laser shot in the EIBT. These interleaved IR on/off data sets were separated during post-processing, calibrated, and analyzed in the usual way. Effects of IR excitation are analyzed by taking difference plots (IR On – IR Off), and the experimental uncertainty for each is determined for a bin by bin basis, using $\sqrt{N_{IR} + N_{noIR}}$, where N_{IR} and N_{noIR} correspond to the number of events in the IR and no-IR spectra. Based on analysis of the stable channel detailed in the discussion, a best estimate for the excitation fraction of the anion packet is ~4%. Note, although optimal photoelectron resolution in our system is typically achieved by slicing along the *z*-velocity component, the subsequent DAF correction resulted in increased noise at larger eKE when determining the difference spectra. Consequently, all difference-plot spectra presented here contain unsliced data.

5.3. Results

Due to limitations in the IR-laser tunable range, it was necessary to probe the overtone of the anion internal F−H−OH stretch. Unfortunately, the exact position of this feature is not directly known, with reported experimental values in the range 2815–2930

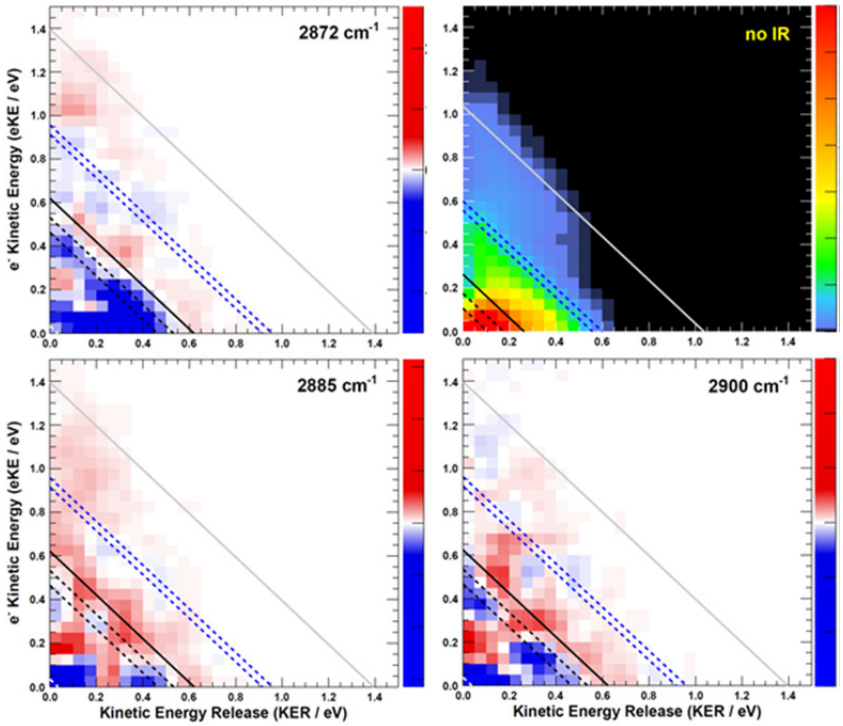

Figure 5.3. Difference (IR – noIR) PPC plots taken at various IR wavelengths and cold/no IR PPC plot for F^-H_2O (top right). All PPC plots were taken at 4.80 eV. The grey and black solid lines indicate the energetic limits, KE_{MAX}, for dissociation into HF + OH and F + H_2O fragments, respectively. The dashed lines indicate vibrationally excited product states. For the difference plots, these energetic limits have been shifted by the corresponding IR energy relative to the no IR PPC spectrum. The blue areas indicate suppression and the red enhancement relative to the no IR spectrum.

cm^{-1}.[34-36] Theoretical values, which are highly sensitive to level of theory and anharmonic treatment, cover the even larger range 2844–3055 cm^{-1}.[36, 38-42] The data presented here were taken at $h\nu_{IR}$ = 2885 cm^{-1}, extrapolated back to the unperturbed neat F^-H_2O cluster using vibrational-predissociation spectra of $F^-H_2O{\cdot}Ar_n$ clusters.[34, 35] Note that our extrapolated value of 2885 cm^{-1} for the IHB overtone in the anion is slightly lower than the reported value of 2905(20) cm^{-1} for the neat F^-H_2O given by Johnson and coworkers,[35] although the extrapolated-fit value still falls within the stated experimental uncertainty. A recent high-level theory paper from Bowman and coworkers calculated this overtone to be at 2872 cm^{-1}.[41] Thus, although the clearest effects were observed at 2885 cm^{-1}, additional data was collected both to the blue at 2900 cm^{-1} and to the red at 2872 cm^{-1}, as shown in Figure 5.3.

5.3.1. *Dissociative Channel*

Taking advantage the unique ability of PPC spectroscopy separately examine stable and dissociative channels, changes in dissociation dynamics brought on by vibrational excitation of the precursor anions (using $h\nu_{IR}$ = 2885 cm^{-1}) are shown in Figure 5.4(b). For reference, the PPC spectrum of F^-H_2O without IR excitation is shown in Figure 5.4(a). All energetic limits for the dissociative pathways for both the no-IR and IR cases are tabulated in Table 5.1. These energetics are indicated as diagonal lines in both panels of Figure 5.4 – the no-IR energetics are indicated in Figure 5.4(a) while the diagonals in Figure 5.4(b) are adjusted for the addition of $h\nu_{IR}$ such that $h\nu = h\nu_{uv} + h\nu_{IR}$. In both frames, the rightmost diagonal line corresponds to the energetic limit for the HF + OH products formed in their ground rotational and vibrational states, denoted KE_{MAX}^{UV} for

Table 5.1. Energetic limits for the various dissociative pathways for both the cold spectrum and the IR excited spectrum. The maximum kinetic energies are reported for neutral products formed in their ground rotational and vibrational states. In general, $KE_{MAX} = h\nu - \Delta D^{o}(F^{-}H_2O) - AEA(OH^{-})$ for the product side and $KE'_{MAX} = h\nu - \Delta D'^{o}(F^{-}H_2O) - AEA(F^{-})$ for the reactant side. The adiabatic electron affinities (AEA) for F^{-} and OH^{-} are well known.(NIST) The product side, HF + OH, pathway is labeled **.**extrapolated from the cold spectrum by addition of the added IR energy, such that $h\nu = h\nu_{UV} + h\nu_{IR}$, effectively treating the excitation as if all additional energy is partitioned into translational motion. Product and reactant asymptotes for IR excited values are indicated as KE^{IR}_{MAX} and KE'''_{MAX}, respectively.

Energetic Pathway	**Cold Energy (eV)**	**IR Excited Energy (eV) 2885 cm^{-1}**
Product KE_{MAX} (HF + OH): (0,0)	1.03	1.39
Reactant KE'_{MAX} ($F + H_2O$)	0.26	0.62
(0,1)	0.59	0.95
(1,0)	0.52	0.87
(1,1)	0.08	0.44
(0,2)	0.17	0.53
(2,0)	0.10	0.46
(0,3)	--	0.12

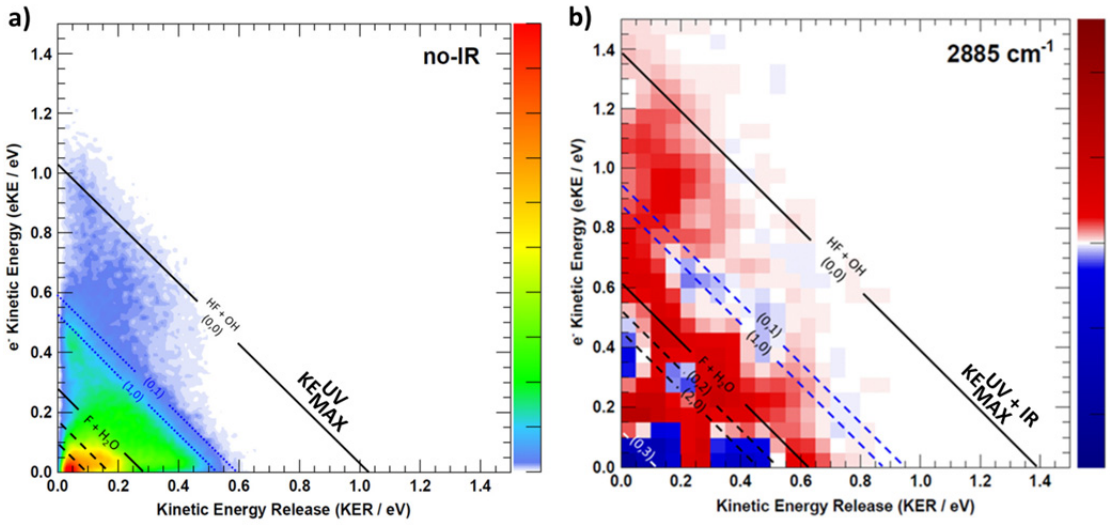

Figure 5.4. Photoelectron photofragment coincidence (PPC) plot for photodetachment from no-IR $F^{-}H_2O$ (left) and difference (IR – no-IR) PPC plot for precursor anions excited with IR = 2885 cm^{-1} (right). For the no-IR spectrum (left), black solid diagonal lines indicate the energetic limits, KE_{MAX}^{UV}, for dissociation into HF + OH + e^{-} and F + H_2O + e^{-} fragments, respectively; dashed lines indicate vibrationally excited product states. For the difference plots (right), these energetic limits have been shifted by the corresponding IR energy relative to the no-IR PPC spectrum; blue areas indicate suppression and red areas indicate enhancement relative to the no-IR spectrum.

the no-IR case and KE_{MAX}^{UV+IR} for the IR-excited case. For convenience, product states are referenced herein in the general form (v_{HF}, v_{OH}). The energetics for formation of HF(v = 0) + OH(v = 1) and HF(v = 1) + OH(v = 0) products, denoted (0, 1) and (1, 0) respectively, are denoted in the difference plot by dotted blue lines. The white diagonal line at 0.26 eV in the no-IR PPC spectrum, and black diagonal at 0.62 eV in the difference plot correspond to formation of the reactants F + H_2O. The no-IR PPC spectrum in Figure 5.4(a) is dominated by diagonal bands, consistent with the HF product fragment being formed with considerable internal excitation, in agreement with previous experimental studies.[15, 26]

The difference plot in Figure 5.4(b) shows a clear effect from IR irradiation of the IHB overtone (2←0) of the precursor anions. The clearest change is the red band of new events falling above the cold-product KE_{MAX}^{UV} (1.03 eV, not shown on the difference plot for clarity) and below the IR-excited product KE_{MAX}^{UV+IR} line (solid black diagonal line). This new band in the IR excitation difference spectrum is consistent with accessing the ground vibrational state of the HF + OH dissociation pathway, where the additional energy from the IR photon has been partitioned into translational motion of the resulting photoelectron, appearing at greater eKE. Interestingly, this band consists of two broad features, one closer to the KE_{MAX}^{UV+IR} line at higher eKE and smaller KER, and a second, weaker feature appearing at lower eKE, just above the energetic limit for HF(v = 0) + OH(v = 1) (blue dashed line), with a long tail extending out to KER = 0.65 eV. The first feature cuts off at KER = 0.40 eV, as in the no-IR PPC spectrum. The second feature, with the long KER tail, is consistent with rotational excitation in at least one of the HF

and/or OH products. The high KER tail observed just above the (0, 1) energetic limit (still within the (0, 0) band) may be the result of increased Franck-Condon overlap with the more-repulsive A-state barrier that plays an important role in the (0, 1) and (1, 0) channels for the reaction with no vibrational excitation.[15] Alternatively, it is possible that through the effects of intramolecular vibrational relaxation (IVR) that the FC overlap with the neutral surface is changing with excited anion lifetime.

The next prominent diagonal band of enhanced (red) signal in Figure 5.4(b) appears below the energetic limits for both (1, 0) or (0, 1), lying just above the adjusted energetic limit for the F + H_2O reactant channel. As in the no-IR spectrum, this band covers the full range of allowed eKE and KER, notably without the distinct KER cutoff seen in the (0, 0) features. The peak enhancement signal falls below the energetic limits for the (1, 0) or (0, 1) product states by 0.2 – 0.3 eV, indicating that these vibrationally excited products are accompanied by significant rotational excitation.

Owing to limited product mass resolution under the current experimental conditions, the F + H_2O reactant channel cannot be separated from the HF + OH product channel. The energetic limit for formation of the F + H_2O reactant-channel products is denoted by the solid black diagonal line. The energetic limits for production of the (0, 2) and (2, 0) final states are denoted by black dashed diagonal lines. This convoluted portion of the difference spectrum is dominated by "depletion" (blue) signal. The depletion observed here corresponds directly to the most intense portions of the no-IR PPC spectrum, where the feature near eKE = 0.4 eV is attributed to the no-IR (1, 0) band and the long horizontal band covering the range KER = 0.0–0.4 eV has previously been

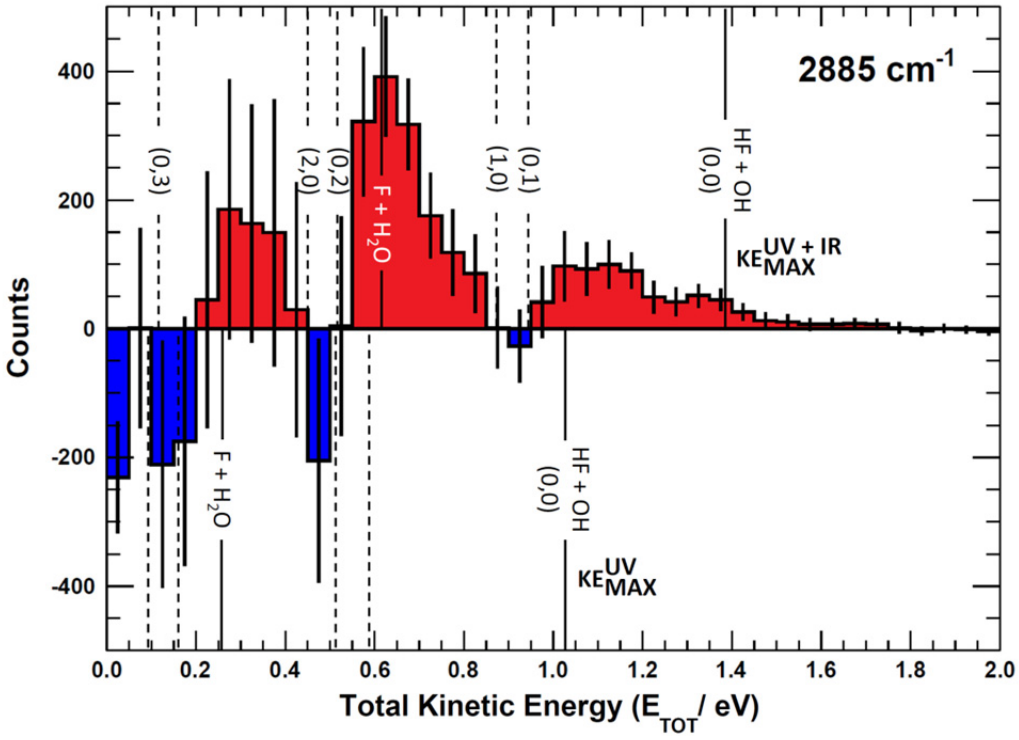

Figure 5.5. Total kinetic energy (E_{TOT}) difference (IR – no-IR) plots for IR = 2885 cm^{-1}, showing IR-excited (top) and no-IR (bottom) energetic limits. Blue and red areas indicate suppression and enhancement, respectively, relative to the no-IR spectrum. Error bars correspond to $\sqrt{N_{IR} + N_{noIR}}$ for each bin.

observed in the no-IR (2, 0) band.[15] Because these peak signal intensities have been shifted by IR excitation, with less intense signal to take their place, it is reasonable to propose that these regions appear as depletion signal in the straight difference plot.

Integrating along the diagonal produces a total kinetic energy (E_{TOT} = eKE + KER on an event-by-event basis) difference plot, shown in Figure 5.5, and provides additional information on the relative populations in each state. The energetic limits for dissociation to the respective pathways are the same as for the PPC spectra, and are indicated here with vertical lines. The vertical lines in the top panel correspond to IR-excited energetics and, for comparison the bottom panel includes no-IR energetic lines. Error bars represent the experimental uncertainty and are calculated for each bin using$\sqrt{N_{IR} + N_{noIR}}$. Again, the red-enhancement data above the no-IR KE_{MAX}^{UV} at E_{TOT} = 1.03 eV provides clear evidence for successful IR excitation of the precursor anions. Here it is more readily apparent that the data peaks away from the IR-excited product KE_{MAX}^{UV+IR} indicating substantial rotational excitation in one or both of the diatomic products. This is also true for the data in the (1, 0) channel, which peaks almost on top of the energetic limit for the F + H_2O channel. Interestingly, this rotational-excitation trend does not appear to carry through to the (2, 0) channel, which peaks closer to the (2, 0) limit.

Both the (0, 1) and (0, 2) OH-excitation pathways are now dominated by suppression, most clearly evident as blue suppression features appearing at 0.87 eV and 0.53 eV in the E_{TOT} difference plot in Figure 5.5. That said, these suppression features are on the same order as the estimated experimental uncertainty (error bars). It is not clear

whether this arises because (i) the populations of OH (v > 0) remain the same relative to the no-IR case and are therefore a relatively smaller fraction of the overall signal or (ii) this actually indicates a decrease in the populations of OH (v > 0). In either case, the decreased signal observed here is consistent with the previously observed spectator nature of the OH moiety in the proton-abstraction reaction.[24-27]

5.3.2. Stable Channel

A unique aspect of the PPC experiment is that it allows one to distinguish between photoelectrons arising from stable and dissociative events. Therefore, in addition to studying the effects of vibrational excitation on the dissociation dynamics, we also explored these effects on long-lived complexes of FH_2O produced by photodetachment. In our previous study of cold anions, a product-channel vdW complex was observed above the KE_{MAX}^{UV} limit (1.03 eV) as well as long-lived vibrational Feshbach resonances that in the cold spectrum near eKE = 0.4 eV and 0.0 eV. In the latter case, we define long-lived/stable photoelectrons as those collected in coincidence with a single heavy particle, giving a lifetime of 7 μs as determined by the time of flight between the interaction region and the neutral-particle detector. Note that, owing to the finite resolution of the neutral-particle detector, dissociative events with very small KER cannot be directly distinguished from true stable events.

Figure 5.6 shows the effect of anion vibrational excitation on this stable photoelectron spectrum, along with a difference plot for the dissociative photoelectron spectrum. For reference, the energetic limits, both IR-excited and no-IR, for dissociation to HF + OH and F + H_2O channels are indicated on each difference plot by solid and

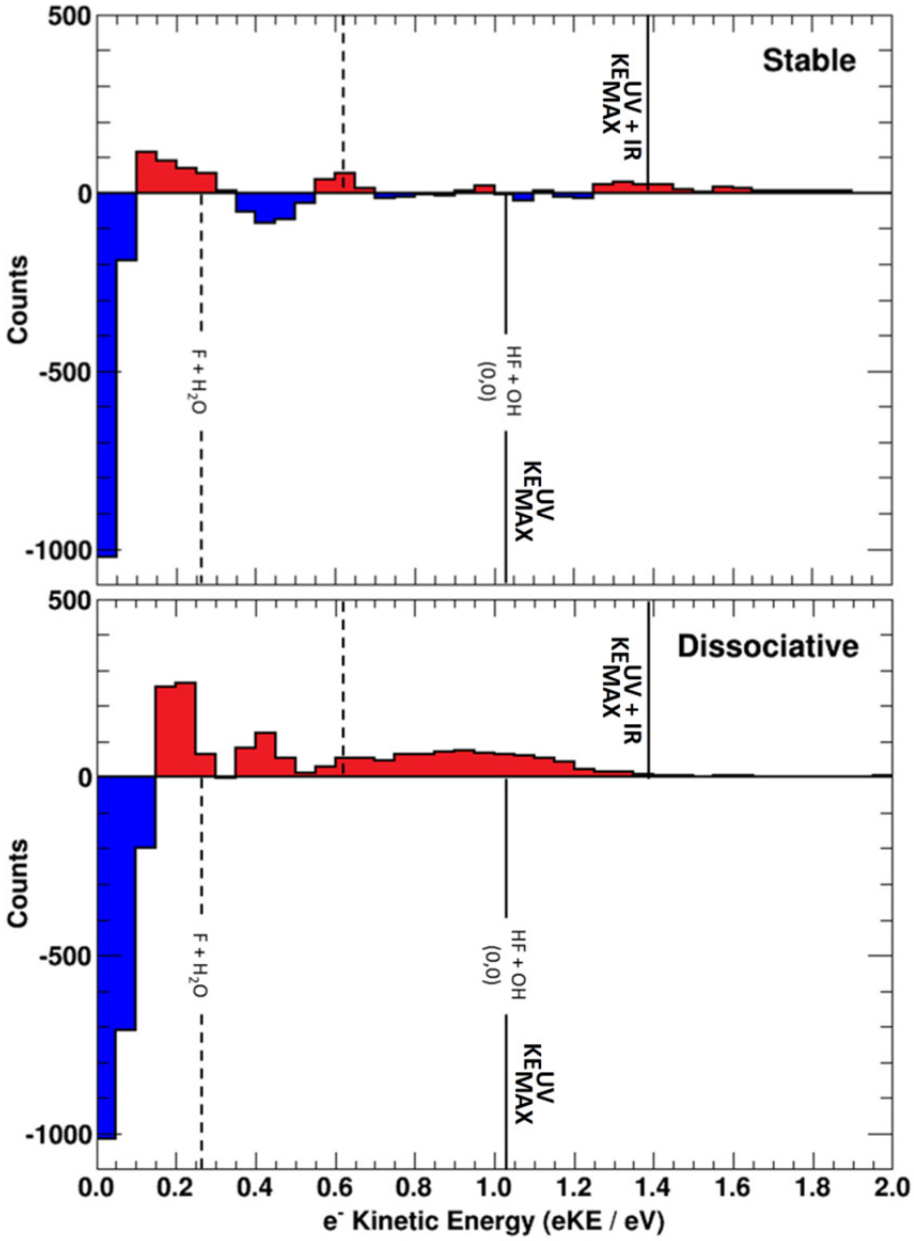

Figure 5.6. Difference (IR – no-IR) plots for the stable and dissociative photoelectron spectra, showing IR-excited (top) and no-IR (bottom) energetic limits. Blue and red areas indicate suppression and enhancement, respectively, relative to the no-IR spectrum. Solid and dashed vertical lines correspond to limits for dissociation to HF + OH and F + H_2O, respectively. Error bars correspond to $\sqrt{N_{IR} + N_{noIR}}$ for each bin.

dashed vertical lines, respectively. Focusing on the stable component for the moment, clear enhancement regions are evident near eKE = 0.2, 0.6, and >1.2 eV. The highest-energy feature appearing near and even above the KE_{MAX}^{UV+IR} is easily explained as accessing the stable product-channel vdW complex where excess energy imparted by vibrational excitation of the precursor anions has been dispersed as kinetic energy. The suppression features near eKE = 0.0, 0.4, and >1.0 eV are easily recognizable as the areas of greatest intensity in the no-IR spectrum, and the feature at eKE > 1.0 eV is again identified as the product-channel vdW complex. The lower-energy features are attributed to long-lived internally excited complexes. Interestingly, the enhancement features at eKE = 0.2 and 0.6 eV have matching features in the dissociative difference plot, as does the strong suppression feature near eKE = 0.0 eV.

5.3.3. *Changing Dynamics with Excited Anion Lifetime*

Finally, we acquired data as a function of trapping time to look for effects related to radiative cooling and intramolecular vibrational redistribution in the vibrationally excited precursor anion. Figure 5.7 shows difference plots for PPC data (dissociative channel) and stable photoelectron spectra for the beginning and end of the EIBT trap cycle. Spectra labeled “early” are for the first one-sixth (0-8 ms) of the full trap time; those labeled “late” are for the last one-sixth (40-48 ms) of that time. For both the stable and dissociative channels, the early data is dominated by enhancement while late data is dominated by suppression, demonstrating that there is an effect from radiative relaxation and/or intramolecular vibrational redistribution.

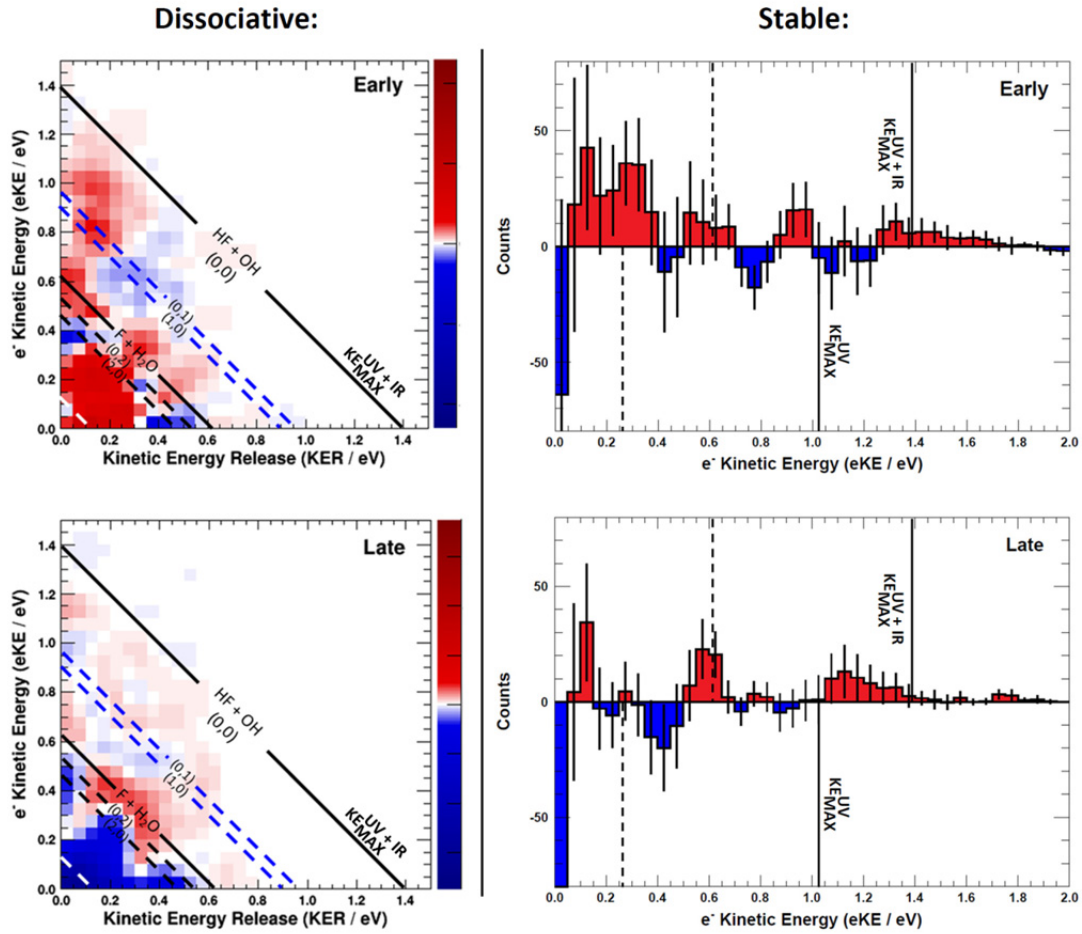

Figure 5.7. Comparison of early- (0-8 ms) and late- (40-48 ms) trap-time PPC difference (IR – no-IR) plots and stable photoelectron spectra. Blue and red areas indicate suppression and enhancement, respectively, relative to the no-IR spectrum. Error bars correspond to $\sqrt{N_{IR} + N_{noIR}}$ for each bin.

5.4. Discussion

In the following we will first examine the effect of vibrational excitation on the dissociative channel, the formation of long-lived complexes and finally the trapping time dependence. From a simple energetic standpoint, addition of an IR photon to the $F^-(H_2O)$ anion gives a total available energy fixed by the photodetachment photon energy of 4.80 eV plus $h\nu_{IR}$ = 0.36 eV. The additional energy available to the system is far above the X-state barrier and reaches very close to the top of the calculated barrier on the A-state as shown in Figure 5.1. A more detailed consideration of this problem must take into account the change in the Franck-Condon overlap induced by the initial vibrationally excited wavefunction, as well as the change in the electronic structure of the anion to a more charge delocalized proton-transfer $FH\cdots OH^-$ geometry,[36] as was recently observed in a full dimensional computational study of this system.[42] This latter effect in particular is expected to result in increased Franck-Condon overlap with the product-channel side of the neutral surface, Noting these factors, however, it remains useful to first order to examine the data from the perspective of the total available energy, by shifting the energetic limits by the IR photon energy and assigning the distribution of product states from the partitioning of the available kinetic energy between eKE and KER.

In the anion ground state, the negative charge is located primarily on the F atom, giving the anion a $F^-\cdots H\cdots OH$ type structure. Photodetachment from this ground state probes near the transition-state geometry on the neutral surface. This process has been well studied previously in our lab[15] and is included for comparison, labeled as the "no-IR" PPC spectrum, in Figure 5.4(a). With additional internal energy in IHB mode, the

anion can assume a more charge-delocalized structure, $FH\cdots OH^-$. Visualized using a 1D slice along the IHB mode, as in Figure 5.1, this charge-delocalized geometry is represented by a shelf in the potential energy surface that grows in slightly before the fundamental for the IHB mode.[36] Thus, probing the overtone of this mode should increase the proton-transfer $FH\cdots OH^-$ character of the anion wave function to ~58%, allowing direct probing of a greater portion of the neutral potential energy surface. This increased $FH\cdots OH^-$ character should provide better Franck-Condon overlap with the product-channel FH–OH vdW well and the product-channel asymptote. Possibly complicating matters, however, the additional available energy in the system now probes well above the X-state barrier and accesses near the top of the A-state barrier as shown in Figure 5.1.

5.4.1. *Dissociative Channel*

The enhancement signal observed in the difference plot in Figure 5.4(b), appearing below the IR-excited KE_{MAX}^{UV+IR} and above the no-IR KE_{MAX}^{UV}, can come only from ground-state HF + OH products accessed after vibrational excitation of the precursor anions. Beyond serving as proof of concept for successful preparation of the first overtone of the proton transfer vibration in $F^-(H_2O)$, this band is largely consistent with the cold experiment. The ground-state-product signal grows in starting at the energetic limit for (0, 0) and appears as a fairly broad diagonal band comprised of two distinct features. The smaller-KER cutoff observed at larger eKE is consistent with greater FC access to the product side of the X-state barrier, as expected from the increased $FH\cdots OH^-$ character of the anion upon excitation.[36, 42] The second feature,

appearing just above the energetic limit for (0, 1) has a larger KER cutoff as the result of probing higher on a barrier. As indicated in Figure 5.1, the addition of IR-excitation probes well above the X-state barrier and this lower-energy band suggests increased access to the excited A-state barrier. The fact that this band appears well below the product KE_{MAX}^{UV+IR} indicates that these species are formed with considerable rotational excitation in at least one of the product fragments.

As previously mentioned, in the cold data the OH group acts like a spectator and the suppression signal observed in Figure 5.5 implies that this OH product is insensitive to the changes in reaction dynamics induced by IR excitation. In comparison, the HF product is particularly sensitive to changes in reaction dynamics. In the no-IR PPC spectrum (Figure 5.4(a)), HF(v=1) signal dominates, appearing as an intense spot near eKE = 0.4 eV, with a band covering the full range of available KER.[15]. In the difference PPC plot, the signal for this channel falls noticeably below (1, 0), with enhancement signal observed as a prominent red band that extends past the reactant KE_{MAX}^{UV+IR} = 0.62 eV value in the IR case (Figure 5.4(b) solid black line, Figure 5.5 dashed black line). Although it is not possible to unambiguously separate the product and reactant channels, excitation of the precursor anion results in a more delocalized-charge structure, as indicated in Figure 5.1, should increase FC overlap with the product (HF + OH) side of the neutral potential energy surface. Therefore it a priori makes sense to see a decrease in the reactant F + H_2O population upon IR excitation. As such, the enhancement-signal peaking at the reactant-pathway energetic limit in the difference spectra is attributed to

the (1, 0) channel where products are formed with substantial rotational excitation in at least one product-channel fragment.

Population analysis was carried out on the difference plot in Figure 5.4(b) by summing over all enhancement (positive events only), with the caveat that the population fraction in the IR-excited (0, 0) to (0, 1) band is an over-estimation and any signal below the no-IR KE_{MAX}^{UV} (1.03 eV) is an under-representation of the true signal due to subtraction of the no-IR spectrum without scaling for excitation fraction when making the difference plot. This excitation fraction is not directly known, but likely falls somewhere between 3% and 5%, as discussed in more detail for the stable channel below. Thus, these populations in the IR-excited data should be taken as an upper limit for the (0, 0) ground state and a lower limit for all other channels. We find that, upon IR excitation of the precursor anions, the population in the (0, 0) ground state is now 23%, a comparatively smaller 46% of enhancement events now fall in the energetic range between (1, 0) and (2, 0) for the IR-excited case, and a dramatically increased 31% of enhancement events now fall in the energetic range between (2, 0) and 0.0 eV. To reiterate, the data falling below the (2, 0) limit includes contributions from both the F + H_2O reactant channel and the HF(v=2) channel, further serving to make the reported population fraction an upper limit for this channel.

5.4.2. *Stable Channel*

Again, in the simplest case, additional IR energy is carried away by the photoelectron, shifting the observed eKE features in the photoelectron spectrum by the IR-photon energy. Similar to the no-IR case, the stable vdW well in the HF + OH product

channel appears as two enhancement peaks near/slightly above KE_{MAX}^{UV+IR}, shown in the stable-channel difference plot in the upper panel of Figure 5.6. The higher energy enhancement peak appears at eKE = 1.6 eV, or roughly 0.2 eV higher in energy than KE_{MAX}^{UV+IR}, consistent with the no-IR stable photoelectron spectrum. [15] An estimate of the fraction of the precursor-ion packet excited by IR-laser irradiation can be determined by comparing the signal for the vdW complex in the difference plot to the no-IR stable eKE spectrum. As shown in Figure 5.8, a model system was used where the excited spectrum was estimated using a combination of the no-IR spectrum and the no-IR spectrum shifted by the IR wavelength and scaled by the excitation fraction, f, such that IR_{model} = (no-IR + $h\nu_{IR}$) + (1-f)*no-IR). A simulated difference plot was then taken by subtracting IR_{model} from the no-IR signal using the relationship model = IR_{model} – f*no-IR. This model difference plot was then compared to the experimental difference plot in the region corresponding to the stable vdW complex (above 1.0 eV). The excitation factor f was determined by scaling until integrated signal in the model and experimental difference plots were the same. Using this model system, ~ 4% of the anion packet is determined to excited for the $h\nu_{IR}$ = 2885 cm^{-1} data shown here. However, this determination assumes that FC overlap of excited anions with stable vdW-product-channel complex is unchanged and that additional energy in the IR-excited systems is partitioned into translational energy of the photoelectron, and therefore this excitation fraction should be treated as an estimate only. Although an exact excitation fraction is needed to extract a "pure" IR spectrum, it was determined through Monte Carlo simulations (Chapter 2) that an excitation fraction as small as 2% yields a clearly visible difference in the simulated

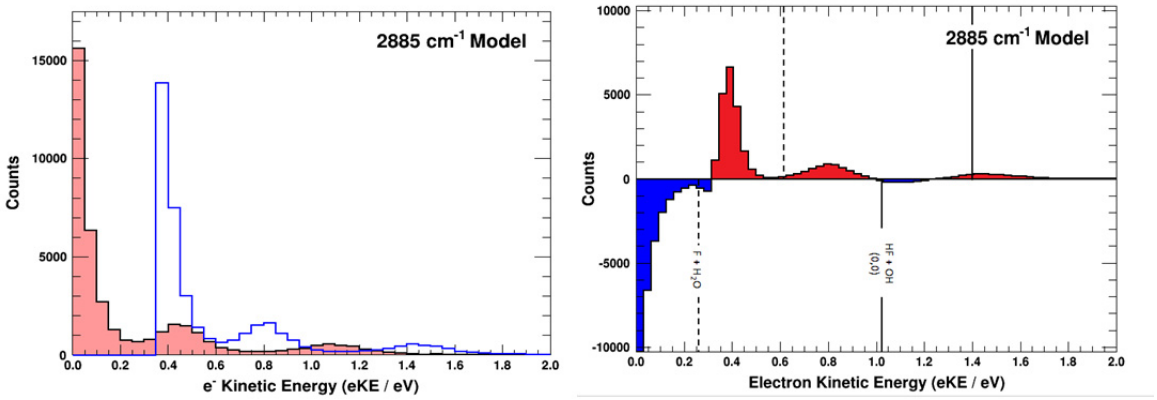

Figure 5.8. The Model: The IR excited spectrum is estimated by shifting the no-IR spectrum (red fill) by the IR photon energy to product the blue spectrum. A simulated difference plot, right, is then produced using the following equation: IR_{model} = (no-IR + $h\nu_{IR}$) + (1-f)*no-IR). The excitation fraction, f, can then be adjusted as needed. The spectrum on the left is simulated using an excitation fraction of 4%.

PPC difference plots. As such, an excitation fraction of ~ 4% is more than enough to produce the observed differences.

Beyond this vdW complex, the most striking feature in the stable-channel difference plot is the absence of any real enhancement between eKE = 0.6 and 1.3 eV. In the no-IR stable spectrum, the feature centered near 0.5 eV was attributed to a metastable FH(v = 1)–OH Feshbach resonance[15] and upon excitation this feature would be shifted to near 0.8 eV provided that all additional energy is carried away by the photoelectron. In addition, this area of the no-IR spectrum has signal near the baseline,[15] so any enhancement near 0.8 eV is expected to be readily observable in the difference plot. However, the difference plot shows no clear difference at this location, indicating that, unlike the stable vdW complex, the HF(v=1)–OH Feshbach resonance is no longer as stable as in the no-IR case .The enhancement feature at 0.6 eV, is consistent with accessing the FH(v = 2)–OH complex, while the suppression feature at 0.45 eV likely arises from the no-IR HF(v=1)–OH Feshbach resonance discussed above as appear near 0.5 eV in the no-IR spectrum. Although the dissociative asymptote for HF(v = 3) + OH is not energetically accessible under the no-IR experimental conditions, the metastable FH(v = 3)–OH complex is now accessible, appearing as enhancement signal at 0.2 eV. Both of these metastable complexes are less intense relative to the stable vdW complex than observed in the no-IR spectrum,[15] while the lower-energy FH(v = 1)–OH complex is essentially absent, implying that all of the metastable states are less stable than in the no-IR case. Note that the enhancement features at 0.2 and 0.6 eV also appear in the dissociative-photoelectron difference plot (Figure 5.6, bottom), consistent with a decaying metastable state producing a range of KER dependent on lifetime.

The dissociative difference spectra (Figures 5.4 and 5.5) are clearly dominated be enhancement with the stable eKE spectra (Figure 5.6) is dominated by suppression, suggesting a decrease in the stable channel contribution upon IR excitation of the precursor anions. This is supported by comparison of enhancement-to-suppression signal where the dissociative spectra are dominated by enhancement signal with a ratio of ~2:1, while the stable-channel difference spectrum is dominated by suppression signal with a ratio of ~ 0.44:1. As expected, the bulk of the data comes from the dissociative channel, with only 8.3% of measured events in the cold experiment coming from the stable channel. In the IR-on case, the stable fraction is slightly reduced to 8.1%; however, note that this fraction has not been adjusted for the IR-excited fraction and is therefore dominated by the background unexcited signal. Although the increased $FH\cdots OH^-$ character of the anion should increase the Franck-Condon overlap with the product-channel vdW well, the additional energy in the system along the reaction coordinate may be sufficient to reduce the lifetimes of the metastable FH(v = 1, 2)–OH complexes relative to the cold system, supporting the decrease in signal for these states in the stable channel difference plot (Figure 5.6).

The higher-energy features in the stable eKE spectrum correspond to true stable minima on the neutral potential energy surface and are observed to have lifetimes greater than our experimental limit of 7 μs. In contrast, the lower-energy features in the spectrum have previously been identified as coming from long-lived, metastable FH(v = 1, 2)–OH vibrational Feshbach resonances in the exit channel. These complexes are best thought of as internally excited FH–OH complexes where the internal energy has been partitioned to modes/degrees of freedom/motions not along the reaction coordinate. For our purposes,

the lifetime of these Feshbach resonances is dependent on the amount of time it takes for the system to undergo IVR and then "shuffle" this internal energy into a mode along the reaction coordinate, leading ultimately to dissociation. In the no-IR spectrum decay of these metastable states is observed as a horizontal band in the PPC spectrum where the system has a fixed eKE value and a lifetime indicated by the spread of observed KER values.[15] That is, events that dissociate immediately upon photodetachment of the precursor anion exhibit the "true"/largest KER, while events with lifetimes of less than the TOF from the interaction region to the detector are observed to have lower KER due to the reduced flight time from dissociation. Systems with lifetimes longer than the TOF to the detector are observed in the stable eKE spectrum.

It is therefore reasonable to expect the truly stable exit-channel vdW complex, with a life time considerably longer than our experiment, to follow the so-called "simplest case" model described above. The higher-energy metastable complexes, on the other hand, should exhibit more complex behavior due to their finite lifetimes. It is also reasonable to expect that pumping the internal F–H–OH bond, which imparts additional motion approximately along the neutral reaction coordinate, can dramatically change the dynamics and lifetimes of these metastable complexes. Unfortunately, though, this behavior is necessarily complicated by the fact that, in our experimental setup, vibrational excitation occurs more than 7 μs before photodetachment in the interaction region, providing time for precursor anions to undergo radiative decay and/or IVR, possibly producing competing changes in the dissociation dynamics and/or affecting the lifetimes of the metastable complexes. It is not possible to directly disentangle these potentially competing effects, but the effects of IVR on the measured differences can be explored by

analyzing how these effects change with increasing anion lifetime. Inclusion of the EIBT in our experiment allows us, during the course of a single experiment, to take data over a range of anion lifetimes dictated by the length of time during which the anion packet is trapped. Results presented so far cover the full EIBT trapping range of 48 ms. It is instructive to compare the effects of IR excitation on anions early and late in their trapping cycle.

5.4.3. *Effects of Intramolecular Vibrational Relaxation*

One known complication to investigating vibrational excitation is the finite lifetime of the excited vibrational mode. Key to previous studies of the effects of vibrational excitation on the reaction dynamics of systems was to measure the system within picoseconds of excitation of precursor ions to ensure a strong effect.[6, 7] Due to instrumental constraints, however, photodetachment measurements were not carried out until at least ~ 7 μs after IR-excitation. Therefore, beyond needing to accept a certain amount of loss of excited-state signal due to spontaneous emission, analysis of the excited-anion results may also be complicated by IVR. Using the calculated vibrational frequencies of McCoy and coworkers, we estimate that there are ~50 available states and combinations of states accessible at the IR-photon energies used in this experiment, offering a rich density of states to which energy may partition.[36] Thus, two assumptions are reasonable: (i) the clearest effects of pumping the anion IHB overtone should be observed in the early data, and (ii) difference spectra from the late trap time should provide valuable information about how IVR can affect dissociation dynamics.

In the early-trap-time difference spectrum (Figure 5.7), many of the most prominent enhancement features observed in the full-trap-time difference spectrum (Figure 5.4(b)) also appear. In the latter, the intense enhancement signal in the (0, 0) band covers the range from the energetic limit for HF + OH to the energetic limit where the (0, 1) band opens up. In the early-trap-time difference spectrum this enhancement signal cuts off near KER = 0.4 eV, although the lower-energy feature, appearing just above the (0, 1) limit, with a larger KER cut off observed in the full-trap-time difference plot is now absent. The observed enhancement signal at relatively large eKE and small KER in the ground-state band indicates that, at early trap times, we are probing low on the dissociation barrier, consistent with the expected increased FC overlap with the product HF + OH asymptote. As discussed above, this is expected for an increase in $FH\cdots OH^-$ character of the anion upon excitation with the IR laser.[36, 42] Peaking of the enhancement signal away from KE_{MAX}^{UV+IR}still indicates that one or more resulting fragments is formed with considerable rotational excitation.

At late trap times (Figure 5.7), the enhancement signal in the ground-state (0, 0) band now cuts off at larger KER (KER = 0.65 eV), consistent with the lower eKE/high KER tail observed in the full-trap-time difference spectrum (Figure 5.4). The enhancement data covers the full energetic of this channel, peaking below the energetic limit, indicating once again rotational excitation in at least one resulting fragment. This larger-KER cutoff indicates that we are actually probing higher on a dissociation barrier at later trap times, as a result of changing FC overlap with changing anion wave function. The enhancement signal in the (0, 1) band now peaks at even smaller total energies, indicating additional rotational excitation for this channel.

The most striking difference in this late spectrum is the substantial suppression signal after the F + H_2O channel opens up. The early spectrum shows enhancement in the (0, 2) region that is noticeably absent in the late-trap-time difference spectrum. Because this portion of the spectrum is particularly convoluted, it is not possible to disentangle whether this depletion at late trap times corresponds to a decrease in the (0, 2) channel in addition to a reduction in the F + H_2O reaction channel. Theoretical work on the anion potential surface by McCoy and coworkers indicates that anion populations in v'_{IHB} = 1, 2 have dramatically increased their proton-transfer character ($FH\cdots OH^-$ anionic structure) to ~58% and ~53% respectively, while the comparable value for the ground-state anion is only ~15%.[36] Dissociative photodetachment from the ground-state anion is known to probe near the transition state of the neutral surface.[15, 32, 33] Increased proton-transfer character in the anion wave function thus increases the FC overlap with the product side of the neutral surface. It is therefore reasonable to attribute this suppression signal to the F + H_2O channel. Whereas the early-time PPC difference spectrum shows sufficient enhancement in the HF(v = 2) product channel to overcome this F + H_2O suppression signal, the late-trap-time spectrum shows the suppression signal dominates this portion of the spectrum, consistent with the overall reduction in enhancement signal observed at these longer anion lifetimes.

Like in the time-sliced PPC difference plots (Figure 5.7), the early stable-channel plot is also clearly dominated by enhancement signal, with a ratio of positive/negative events of 1.85 or ~ 2:1 for the stable channel. In contrast, the late stable-channel plot is dominated by suppression/negative events at a ratio of 0.60:1, indicating a dramatic change in dynamics over the course of the anion lifetime. Enhancement features near 0.1

and 0.55 eV appear in both early and late plots, while enhancement features near 0.3 and 0.95 eV appear in only the early plot. Interestingly, the feature appearing in the early plot above 1.3 eV, identified as the product vdW complex, appears to have shifted to lower energies in the later plot, growing in closer to 1.05 eV. This enhancement feature now falls below the product KE_{MAX}^{UV+IR}, although still above the no-IR KE_{MAX}^{UV}. This late-trap-time, high-energy enhancement signal is now more consistent with access to the product-side vdW well from anion populations in $v'_{IHB} = 1$, indicating that over the course of the excited anion lifetime IVR plays a significant role, changing the FC region and thus the dissociation dynamics..

In the early-trap-time PPC difference spectrum (Figure 5.7), the suppression features near 0.0, 0.4, and >1.0 eV correlate with the prominent features in the no-IR eKE spectrum. However, the suppression feature near 0.8 eV, and its relative intensity, is surprising. In the no-IR eKE spectrum, signal does not reach zero in the region between the prominent features at 0.4 and ~1.0 eV, but there is also no strong feature present at eKE = 0.8 eV. In the simplest case where all additional energy is removed by the photoelectron, we would expect to see *enhancement* here, not suppression. These suppression features above 0.7 eV are noticeably absent in the late-trap-time difference spectrum, although the suppression features near 0.0 and 0.4 eV are now more prominent. This is consistent with decreased access to the FH(v=2)–OH product-channel complex at later trap times due to IVR changing the FC region, resulting in less enhancement to counteract the no-IR spectrum/suppression. The decreased access to the Feshbach resonances and change in overall dissociation dynamics between early- and late-trap times provides clear evidence for the effects of IVR during the course of our experiment.

At early trap times the observed effects of vibrational excitation of the precursor anions is to increase the overlap with the product HF + OH asymptote while decreasing overlap with the reactant F + H_2O asymptote. At late trap times, these dynamics have changed dramatically producing products with much larger KER consistent with probing a steeper dissociative curve, consistent with probing a different portion of the neutral surface. The decreased access to the product channel Feshbach resonances at late trap times also indicates that, through IVR, the additional energy in the anions has partitioned into other degrees of freedom that dramatically decrease access to/lifetimes of these resonances. As such, the early-trap-time spectra represent the most direct effects of the IR-excitation of the precursor anions on the dissociation dynamics, while the late-trap-time spectra offer an opportunity to monitor how these effects change with IVR in the anion.

5.5. Conclusion

We successfully demonstrated vibrational excitation of anion precursors prior to carrying out photoelectron-photofragment coincidence experiments on the F^-H_2O system. Pumping the overtone of the anion internal-hydrogen-bond overtone decreases Franck-Condon access to the reactant F + H_2O channel and concurrently increases access to the HF + OH product channel. These HF + OH products form with considerably more rotational excitation than is the case for comparable cold/no-IR experiments. In addition, vibrational-population inversion of the HF fragment is enhanced upon vibrational excitation of the precursor anions, with increased access to HF(v=2). Taking advantage of the additional information provided by trapping anions in an EIBT, we were able to analyze the effects of excited-anion lifetime and the effect of IVR on dissociation

dynamics. At early trap times/shorter anion lifetimes, dissociative photodetachment probes close to the product-side complexes. With increasing anion lifetime, photodetachment instead probes near the top of a barrier, most likely that of the higher-lying A state, indicating a change in the Frank-Condon region with increasing anion lifetime.

Acknowledgements

This material is based upon work supported by the U.S. Department of Energy, Office of Science, Office of Basic Energy Sciences under award number DE-FG03-98ER14879. We acknowledge helpful discussions with H. Guo.

5.6. References

1. POLANYI, J. C., Some Concepts in Reaction Dynamics. *Science* **1987,** *236* (4802), 680-690.

2. Xie, Z.; Bowman, J. M., Quasiclassical Trajectory Study of the Reaction of Fast H Atoms with C–H Stretch Excited CHD_3. *Chemical Physics Letters* **2006,** *429* (4–6), 355-359.

3. Guo, H.; Jiang, B., The Sudden Vector Projection Model for Reactivity: Mode Specificity and Bond Selectivity Made Simple. *Acc. Chem. Res.* **2014,** *47* (12), 3679-3685.

4. Zare, R. N., Laser Control of Chemical Reactions. *Science* **1998,** *279* (5358), 1875-1879.

5. Camden, J. P.; Bechtel, H. A.; Ankeny Brown, D. J.; Zare, R. N., Comparing Reactions of H and Cl with C–H Stretch-Excited CHD_3. *The Journal of Chemical Physics* **2006,** *124* (3), 034311.

6. Crim, F. F., Vibrational State Control of Bimolecular Reactions: Discovering and Directing the Chemistry. *Acc. Chem. Res.* **1999,** *32* (10), 877-884.

7. Crim, F. F., Chemical Dynamics of Vibrationally Excited Molecules: Controlling Reactions in Gases and on Surfaces. *Proceedings of the National Academy of Sciences of the United States of America* **2008,** *105* (35), 12654-12661.

8. Yan, S.; Wu, Y.-T.; Zhang, B.; Yue, X.-F.; Liu, K., Do Vibrational Excitations of CHD_3 Preferentially Promote Reactivity Toward the Chlorine Atom? *Science* **2007,** *316* (5832), 1723-1726.

9. Yan, S.; Wu, Y.-T.; Liu, K., Tracking the Energy Flow Along the Reaction Path. *Proceedings of the National Academy of Sciences of the United States of America* **2008,** *105* (35), 12667-12672.

10. Proctor, D. L.; Davis, H. F., Vibrational vs. Translational Energy in Promoting a Prototype Metal–Hydrocarbon Insertion Reaction. *Proceedings of the National Academy of Sciences of the United States of America* **2008,** *105* (35), 12673-12677.

11. Duncan, W. T.; Truong, T. N., Thermal and Vibrational-State Selected Rates of the $CH_4 + Cl \leftrightarrow HCl + CH_3$ Reaction. *The Journal of Chemical Physics* **1995,** *103* (22), 9642-9652.

12. Palma, J.; Echave, J.; Clary, D. C., The effect of the Symmetric and Asymmetric Stretching Vibrations on the $CH_3D + O(^3P) \rightarrow CH_3 + OD$ Reaction. *Chemical Physics Letters* **2002,** *363* (5–6), 529-533.

13. Killelea, D. R.; Campbell, V. L.; Shuman, N. S.; Utz, A. L., Bond-Selective Control of a Heterogeneously Catalyzed Reaction. *Science* **2008,** *319* (5864), 790-793.

14. Beck, R. D.; Maroni, P.; Papageorgopoulos, D. C.; Dang, T. T.; Schmid, M. P.; Rizzo, T. R., Vibrational Mode-Specific Reaction of Methane on a Nickel Surface. *Science* **2003,** *302* (5642), 98-100.

15. Otto, R.; Ma, J.; Ray, A. W.; Daluz, J. S.; Li, J.; Guo, H.; Continetti, R. E., Imaging Dynamics on the $F + H_2O \rightarrow HF + OH$ Potential Energy Surfaces from Wells to Barriers. *Science* **2014,** *343* (6169), 396-399.

16. Otto, R.; Ray, A.; Daluz, J.; Continetti, R., Direct IR Excitation in a Fast Ion Beam: Application to NO^- Photodetachment Cross Sections. *EPJ Techniques and Instrumentation* **2014,** *1* (1), 3.

17. Ervin, K. M.; Ho, J.; Lineberger, W. C., A Study of the Singlet and Triplet States of Vinylidene by Photoelectron Spectroscopy of $H_2C{=}C^-$, $D_2C{=}C^-$, and $HDC{=}C^-$. Vinylidene–Acetylene Isomerization. *The Journal of Chemical Physics* **1989,** *91* (10), 5974-5992.

18. Wenthold, P. G.; Hrovat, D. A.; Borden, W. T.; Lineberger, W. C., Transition-State Spectroscopy of Cyclooctatetraene. *Science* **1996,** *272* (5267), 1456-1459.

19. Neumark, D. M., Transition State Spectroscopy of Bimolecular Chemical Reactions. *Annu. Rev. Phys. Chem.* **1992,** *43* (1), 153-176.

20. Boo, D. W.; Ozaki, Y.; Andersen, L. H.; Lineberger, W. C., Femtosecond Dynamics of Linear Ag_3. *J. Phys. Chem. A* **1997,** *101* (36), 6688-6696.

21. de Beer, E.; Zhao, Y.; Yourshaw, I.; Neumark, D. M., Stimulated Raman Pumping of C_2^- Probed via Resonant Two-Photon Detachment. *Chemical Physics Letters* **1995,** *244* (5–6), 400-406.

22. Furlanetto, M. R.; Pivonka, N. L.; Lenzer, T.; Neumark, D. M., Vibrational Spectroscopy of Anions by Stimulated Raman Pumping–Photoelectron Spectroscopy. **2000,** *326* (5–6), 439-444.

23. Bergmann, K.; Vitanov, N. V.; Shore, B. W., Perspective: Stimulated Raman Adiabatic Passage: The status after 25 years. *The Journal of Chemical Physics* **2015,** *142* (17), 170901.

24. Deskevich, M. P.; Nesbitt, D. J.; Werner, H.-J., Dynamically Weighted Multiconfiguration Self-Consistent Field: Multistate Calculations for $F + H_2O \rightarrow HF + OH$ Reaction Paths. *The Journal of Chemical Physics* **2004,** *120* (16), 7281-7289.

25. Ziemkiewicz, M.; Wojcik, M.; Nesbitt, D. J., Direct Evidence for Nonadiabatic Dynamics in Atom + Polyatom Reactions: Crossed-Jet Laser Studies of $F + D_2O \rightarrow DF + OD$. *The Journal of Chemical Physics* **2005,** *123* (22), 224307.

26. Zolot, A. M.; Nesbitt, D. J., Crossed Jet Reactive Scattering Dynamics of F + H_2O → HF(v,J) + OH: HF(v,J) Product Quantum State Distributions Under Single-Collision Conditions. *The Journal of Chemical Physics* **2008,** *129* (18), 184305-9.

27. Ziemkiewicz, M.; Nesbitt, D. J., Nonadiabatic Reactive Scattering in Atom + Triatom Systems: Nascent Rovibronic Distributions in F + H_2O → HF + OH. *The Journal of Chemical Physics* **2009,** *131* (5), 054309.

28. Li, J.; Dawes, R.; Guo, H., An ab initio Based Full-Dimensional Global Potential Energy Surface for FH_2O (X^2A') and Dynamics for the F + H_2O → HF + HO Reaction. *Journal of Chemical Physics* **2012,** *137* (9), 094304.

29. Li, J.; Jiang, B.; Guo, H., Spin-Orbit Corrected Full-Dimensional Potential Energy Surfaces for the Two Lowest-Lying Electronic States of FH_2O and Dynamics for the F + H_2O → HF + OH Reaction. *The Journal of Chemical Physics* **2013,** *138* (7), 074309.

30. Li, J.; Jiang, B.; Guo, H., Enhancement of Bimolecular Reactivity by a Pre-reaction van der Waals Complex: the case of F + H_2O → HF + HO. *Chem. Sci.* **2013,** *4* (2), 629-632.

31. Stevens, P. S.; Brune, W. H.; Anderson, J. G., Kinetic and Mechanistic Investigations of Fluorine Atom + Water/Water-d2 and Fluorine Atom + Hydrogen/Deuterium Over the Temperature Range 240-373 K. *J. Phys. Chem.* **1989,** *93* (10), 4068-4079.

32. Yang, X.; Wang, X.-B.; Wang, L.-S., Photodetachment of $F^-(H_2O)n$ (n=1–4): Observation of Charge-Transfer States [$F^-(H2O)_n^+$] and the Transition State of F + H_2O Hydrogen Abstraction Reaction. *The Journal of Chemical Physics* **2001,** *115* (7), 2889-2892.

33. Ishikawa, Y.; Nakajima, T.; Yanai, T.; Hirao, K., Ab initio Direct Molecular Dynamics Study of the Fragmentation of $F(H_2O)$ Complex Generated by Photodetachment of $F^-(H_2O)$ Anion Complex. **2002,** *363* (5–6), 458-464.

34. Ayotte, P.; Kelley, J. A.; Nielsen, S. B.; Johnson, M. A., Vibrational Spectroscopy of the $F^-\cdot H_2O$ Complex via Argon Predissociation: Photoinduced, Intracluster Proton Transfer? **2000,** *316* (5–6), 455-459.

35. Roscioli, J. R.; Diken, E. G.; Johnson, M. A.; Horvath, S.; McCoy, A. B., Prying Apart a Water Molecule with Anionic H-Bonding: A Comparative Spectroscopic Study of the $X^-\cdot H_2O$ (X = OH, O, F, Cl, and Br) Binary Complexes in the 600−3800 cm^{-1} Region. *J. Phys. Chem. A* **2006,** *110* (15), 4943-4952.

36. Horvath, S.; McCoy, A. B.; Roscioli, J. R.; Johnson, M. A., Vibrationally Induced Proton Transfer in $F^-(H_2O)$ and $F^-(D_2O)$. *J. Phys. Chem. A* **2008,** *112* (48), 12337-12344.

37. Weis, P.; Kemper, P. R.; Bowers, M. T.; Xantheas, S. S., A New Determination of the Fluoride Ion−Water Bond Energy. *J. Am. Chem. Soc.* **1999,** *121* (14), 3531-3532.

38. Yates, B. F.; Schaefer, H. F.; Lee, T. J.; Rice, J. E., Infrared spectrum of $F^-\cdot H_2O$. *J. Am. Chem. Soc.* **1988,** *110* (19), 6327-6332.

39. Chaban, G. M.; Xantheas, S. S.; Gerber, R. B., Anharmonic Vibrational Spectroscopy of the $F^-(H_2O)_n$ Complexes, n = 1, 2. *J. Phys. Chem. A* **2003,** *107* (24), 4952-4956.

40. Toffoli, D.; Sparta, M.; Christiansen, O., Vibrational Spectroscopy of Hydrogen-Bonded Systems: Six-Dimensional Simulation of the IR Spectrum of $F^-(H_2O)$ Complex. *Chemical Physics Letters* **2011,** *510* (1–3), 36-41.

41. Kamarchik, E.; Toffoli, D.; Christiansen, O.; Bowman, J. M., Ab initio Potential Energy and Dipole Moment Surfaces of the $F^-(H_2O)$ Complex. *Spectrochimica Acta Part A: Molecular and Biomolecular Spectroscopy* **2014,** *119*, 59-62.

42. Punyain, W.; Takahashi, K., Theoretical Calculation of the Vibrational State Dependent Photodetachment Spectra of X^-H_2O, X = F, Cl, Br. *Phys. Chem. Chem. Phys.* **2016**.

43. Hanold, K.; Luong, A.; Clements, T.; Continetti, R., Photoelectron-Multiple-Photofragment Coincidence Spectrometer. *Rev. Sci. Instrum.* **1999,** *70* (5), 2268-2276.

44. Johnson, C.; Shen, B.; Poad, B.; Continetti, R., Photoelectron-Photofragment Coincidence Spectroscopy in a Cryogenically Cooled Linear Electrostatic Ion Beam Trap. *Rev. Sci. Instrum.* **2011,** *82* (10), 105105.

45. Bowen, M. S.; Continetti, R. E., Photodetachment Imaging Study of the Vinoxide Anion. *J. Phys. Chem. A* **2004,** *108* (39), 7827-7831.

Chapter 6: Energetics and Transition-State Dynamics of the $F + HOCH_3 \rightarrow HF + OCH_3$ Reaction

6.1. Introduction

Studies of the exothermic reactions of fluorine atoms with small molecules, such as the F + H_2 reaction,[1, 2] have provided a foundation for the development of multidimensional potential energy surfaces and theories of chemical reaction dynamics. These systems exhibit both direct and resonance-mediated reactive processes, providing a rich ground for examining aspects of molecular reaction dynamics.[3] Extending these studies beyond triatomic systems to higher dimensionality, our recent studies of the F + $H_2O \rightarrow HF + OH$[4] and $OH + CO \rightarrow H + CO_2$ reactions[5, 6] represent systems with six degrees of freedom at the frontier of both quantum chemistry and quantum dynamics computations.[7-14] In the present work, we extend these efforts to even higher dimensionality by carrying out PPC studies on $F^-(HOCH_3)$, nominally producing the $F(HOCH_3)$ complex in the vicinity of the submerged barrier on the $F + HOCH_3 \rightarrow HF + OCH_3$ potential energy surface. This system, with 7 atoms and 15 degrees of freedom, remains a challenge for full-dimensionality quantum dynamics computations, but is a tractable system for high accuracy electronic structure computations.[15] The photodetachment and dissociative photodetachment (DPD) of $F^-(HOCH_3)$ will be presented, and compared to new electronic structure computations. Insights into the dynamics of the $F + HOCH_3 \rightarrow HF + OCH_3$ reaction from the partitioning of energy in

DPD will also be discussed, as well as the role played by long-lived complexes and vibrational Feshbach resonances (reactive and/or non-reactive).

The exothermic hydrogen abstraction from methanol by fluorine atoms is widely used as a means to produce methoxy radicals and/or rovibrationally excited HF.[16-19] As such, this reaction has been the focus of a number of kinetic studies,[19]and has been probed using a combination of laser-induced fluorescence (LIF) and/or infrared chemiluminescence techniques.[20-23] On the neutral potential energy surface, two hydrogen-abstraction reactions are possible: abstraction either from the hydroxyl to form methoxy radicals, OCH_3, or from the methyl group to form hydroxymethyl radical, H_2COH.

$$F + HOCH_3 \rightarrow HF + OCH_3 \quad (6.1)$$

$$F + CH_3OH \rightarrow HF + H_2COH \quad (6.2)$$

Both reactions are highly exothermic (-1.39 ± 0.04 and -1.78 ± 0.13 eV, respectively[24]) and are expected to proceed via a minimal barrier to products.[25] Formation of the hydroxymethyl radical (reaction 6.2) is expected to be favored both thermodynamically and statistically (3:1) and would be expected to be the dominant product. Counter to expectation, however, at room temperatures (and above), methoxy has been found to account for an anomalously large fraction of the final products (~ 0.6).[25] In addition to branching ratios between these two competing pathways, considerable attention has been directed toward measuring product-state distributions. Energy partitioning in the HF and OCH_3 fragments has been studied by infrared chemiluminescence and laser induced

fluorescence, respectively.[20-22, 26, 27] The HF product is formed with considerable internal excitation, with distributions peaking at v = 2 (the deuterated isotopologue, DF, peaks at v = 4 due to smaller vibrational-energy spacing). In this case, population distributions of HF correspond to products formed via both reactions 6.1 and 6.2 for the $F(HOCH_3)$ and perdeuterated $F(DOCD_3)$ complexes. Selective deuteration, used to disentangle these results, showed that hydrogen abstraction from the methyl group (reaction 6.2) leads to clear population inversion in the HF fragment, and thus greater internal energy, than abstraction from the hydroxyl group (reaction 6.1). Correspondingly, only a small amount of energy is partitioned into internal energy in the methoxy radical (reaction 6.2), with about 2% of the available energy partitioning into the C–O stretching mode (ν_3).[21, 22] Thus, methoxy is largely considered a "spectator" to the reaction.

In addition to experimental interest in this system, the neutral surface has been studied computationally,[15, 24] including the recent high-level potential energy surfaces for both reaction pathways described by Schaefer and coworkers.[15] The reaction was computed to proceed via a shallow reactant-channel complex, a submerged barrier (relative to the reactant asymptote), and a product-channel hydrogen-bonded complex that is stable relative to the HF + OCH_3 product asymptote. The greatest discrepancy between available computational studies is the computed barrier height, which decreases with higher levels of theory.[15, 24, 28]

The present study of the energetics and transition-state dynamics of $F(HOCH_3)$ and reaction (6.1) $F + HOCH_3 \rightarrow HF + OCH_3$ is based on earlier work by Neumark and coworkers using photoelectron spectroscopy of the $F^-(HOCH_3)$ anion at a wavelength of

213 nm (5.82 eV).[29] They found this to be an ideal system for transition-state spectroscopy by photodetachment as the anion geometry is similar to the calculated transition state for the neutral reaction. They observed signal attributed to both reactants ($F + HOCH_3$) and products ($HF + OCH_3$), probing both the reactant and product channels of the neutral potential energy surface of reaction 6.1. The resulting photoelectron spectrum was found to be dominated by broad, shelf-like peaks attributed to vibrational excitation in the HF fragment. It was concluded that the methoxy-radical product was formed primarily in its ground vibrational state from the small conformational changes between the anion and the free methoxy radical. This is consistent with the inferences from kinetics and dynamics studies of the neutral reaction mentioned above. Low-lying electronic states and spin-orbit splitting effects were also posited to play an important role in the full understanding of the $F(HOCH_3)$ system due, in part, to their roles in photodetachment of the simpler FHO^- system[29] as well as the more recently studied $F^-(H_2O)$ systems.[4]

Using the photodetachment and dissociative photodetachment of a cluster anion to study neutral reaction transition-state dynamics requires knowledge of the anion structure and potential energy surface. The $F^-(HOCH_3)$ potential energy surface has been explored by a number of experimental[30] and theoretical studies.[31, 32] The reactivity and stability of the $F^-(HOCH_3)$ anion has been studied using Fourier-transform ion cyclotron resonance (FT-ICR) techniques, giving an experimental binding energy of 1.28 ± 0.02 eV.[33] The anion potential energy surface has been examined computationally, with computed stationary points for the SN_2 reaction $F^- + HOCH_3 \rightarrow HF + OCH_3^-$ yielding a binding

energy for F^-−$HOCH_3$ in good agreement with experiment.[32] The related $[F{-}CH_3{-}OH]^-$ intermediate complex in the $F^- + CH_3OH \rightarrow FCH_3 + OH^-$ bimolecular SN_2 reaction has also been studied, but was found to have significantly lower binding energies of ~ 0.56 eV.[32, 34] In all cases, no corresponding stable anion for interactions of F^- with any hydrogen on the methyl group in methanol ($F{-}H{-}CH_2OH$) was found and therefore only reaction 6.1 is expected to be accessed by photodetachment of the $[F{-}H{-}OCH_3]^-$ anion.

In the following sections, studies of the neutral $F + HOCH_3 \rightarrow HF + OCH_3$ reaction via PPC spectroscopy at a photon energy of 4.80 eV will be presented. The PPC technique provides a means for separating photodetachment processes that lead to stable and dissociative neutral products. Much like the simpler $F^-(H_2O)$ system,[4] the dissociative channel is dominated by vibrationally excited HF products. The distinct stable photoelectron spectra provide evidence for a population of both reactant- and product-channel complexes, in addition to long-lived vibrational Feshbach resonances. Interpretation of the results is aided by new high-quality zero-point-corrected *ab initio* results extrapolated to the CCSDT(Q)/CBS level of theory.

6.2. Experimental Methods

This study was carried out on a fast-ion-beam PPC spectrometer, discussed in detail elsewhere.[35, 36] Briefly, the anion precursor $F^-(HOCH_3)$ was synthesized in a supersonic expansion of C_2F_6/HeNe (25% C_2F_6) passed over methanol ($HOCH_3$), acted upon by a coaxial pulsed discharge and crossed by a 1-keV electron beam. The resulting

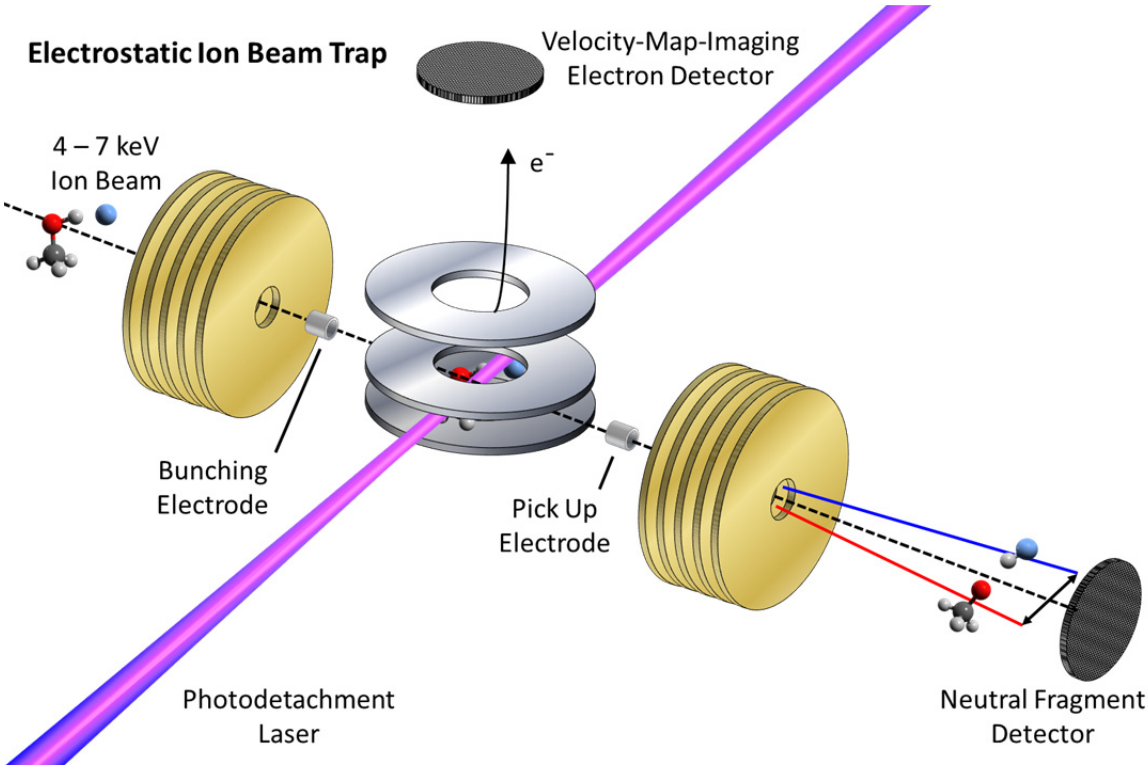

Figure 6.1. Simplified schematic of the PPC spectrometer. The fast-ion beam is injected into the Electrostatic Ion Beam Trap (EIBT), bunched and synchronized to the photodetachment laser using an RF signal on the bunching electrode, thereby ensuring that photodetachment occurs when the ions are traveling towards the neutral particle detector. Photoelectrons are velocity-map-imaged onto the electron detector and collected in coincidence with the recoiling neutral fragments.

anions were skimmed, accelerated to either 4.0 or 7.0 keV, re-referenced to ground, and mass-selected by time-of-flight. The anions of interest were subsequently confined for 100 ms to 1 s in a cryogenically cooled electrostatic-ion-beam trap (EIBT), shown schematically in Figure 6.1, and phase-locked to the output of a Ti:sapphire regenerative amplifier (Clark MXR CPA-2000; λ = 775.5 nm, repetition rate 1037 Hz, pulse width 1.1 ps) using an RF oscillator. The oscillating ion packet was then repetitively probed using either second-harmonic radiation (387.8 nm, $E_{h\nu}$ = 3.20 eV) or third-harmonic radiation (258.5 nm, $E_{h\nu}$ = 4.80 eV). The resulting detached photoelectrons were extracted on an event-by-event basis orthogonal to the plane of the laser and ion beams by means of an electrostatic velocity-map-imaging lens coupled to a time- and position-sensitive detector.

The center-of-mass (CM) electron kinetic energy (eKE) and laboratory-frame recoil angle for each photoelectron were determined from the arrival time and impact position on the detector. Optimum resolution was obtained by selecting those photoelectrons with minimal z-velocity by equatorially slicing the resulting photoelectron spectrum. This imposed detector-acceptance function (DAF) alters the signal-intensity distribution of the photoelectron spectrum, reducing the apparent intensity at greater photoelectron velocities. DAF-corrected intensity distributions, *P(eKE)*, are obtained by dividing the experimental intensity distribution, *N(eKE)*, by the acceptance function of the z-velocity slice.[37] Calibration of the photoelectron detector using I^- showed a sliced z-velocity component resolution of ΔeKE/eKE ~ 3.5 % at 0.797 eV and ΔeKE/eKE ~ 2.5 % at 1.74 eV electron kinetic energy.

After photodetachment, the resulting neutral species recoiled out of the EIBT and were detected, in coincidence with the photoelectron, 1.35 m downstream on a four-quadrant time- and position-sensitive multiparticle detector.[35] CM kinetic energy release (KER) and product masses for the momentum-matched neutral particles were determined on an event-by-event basis. For the current experimental kinematics, the angular acceptance of events in coincidence on the neutral-particle detector was expected to be large due to the relatively small difference in mass between fragments (HF and OCH_3) and therefore no DAF correction was applied to these neutral-particle results. One advantage of the PPC technique is the ability to separate apparently stable and dissociative events by enforcing coincidence between the photoelectron and a single neutral particle. The photoelectron spectrum corresponding to photodetachment processes that yield a free electron and a single molecular product are defined as those detected in coincidence with a single heavy particle arriving at the time and position expected for the neutralized parent anion beam. This will be referred to as the stable photoelectron spectrum while the dissociative photoelectron spectrum consists of the photoelectrons detected in coincidence with two momentum-matched heavy particles. The lifetime of any stable or metastable species must therefore be greater than the TOF between the laser interaction region and the neutral detector (~ 8.4 μs for 7.0 keV ion beam). Although this discrimination breaks down in the case of dissociative events with an extremely low kinetic energy release, this coincidence technique can still be extremely useful for the separation of prompt dissociative events from stable or long-lived metastable product states. For prompt dissociation, the multiparticle neutral detector was calibrated using the

dissociative photodetachment of O_4^-, yielding a translational energy release resolution $\Delta KER/KER \sim 10\%$.[35]

6.3. Computational Methods

Ab initio computations were carried out to determine the stationary points on the F($HOCH_3$) neutral potential energy surface as well as the corresponding anion surface, with the zero-point corrected energetics and structures shown in Figure 6.2. All energies are reported relative to the precursor anion. Equilibrium structures were obtained from geometry optimization using coupled cluster theory with single, double, and perturbative triple excitations [CCSD(T)],[38-40] as implemented in CFour 2.0.[41] All atoms were described with Dunning's augmented, correlation-consistent, valence, triple-ζ aug-cc-pVTZ basis-set.[42] Aligned with the design of this basis set, the 1s-like electrons on carbon, oxygen, and fluorine atoms were excluded from post Hartree-Fock computations (i.e., "frozen-core"). Reference energies (RHF or UHF) were considered converged when the maximum change in density-matrix elements was less than 10^{-9}. Coupled-cluster amplitudes were also converged to 10^{-9}, and the RMS force for geometric parameters were converged to less than 10^{-9} Hartree/Bohr.

Relative electronic energies were determined using the focal point approach,[43, 44] whereby single-point energy computations are extrapolated to the complete-basis-set (CBS) limit using a three-parameter fit for Hartree-Fock energies[45] and a two-parameter fit for correlation energies.[46, 47] Coupled-cluster computations with full triples [CCSDT(Q)] were performed with MRCC,[48, 49] as interfaced with CFour. Relative enthalpies at zero Kelvin were obtained by appending the relative zero-point vibrational

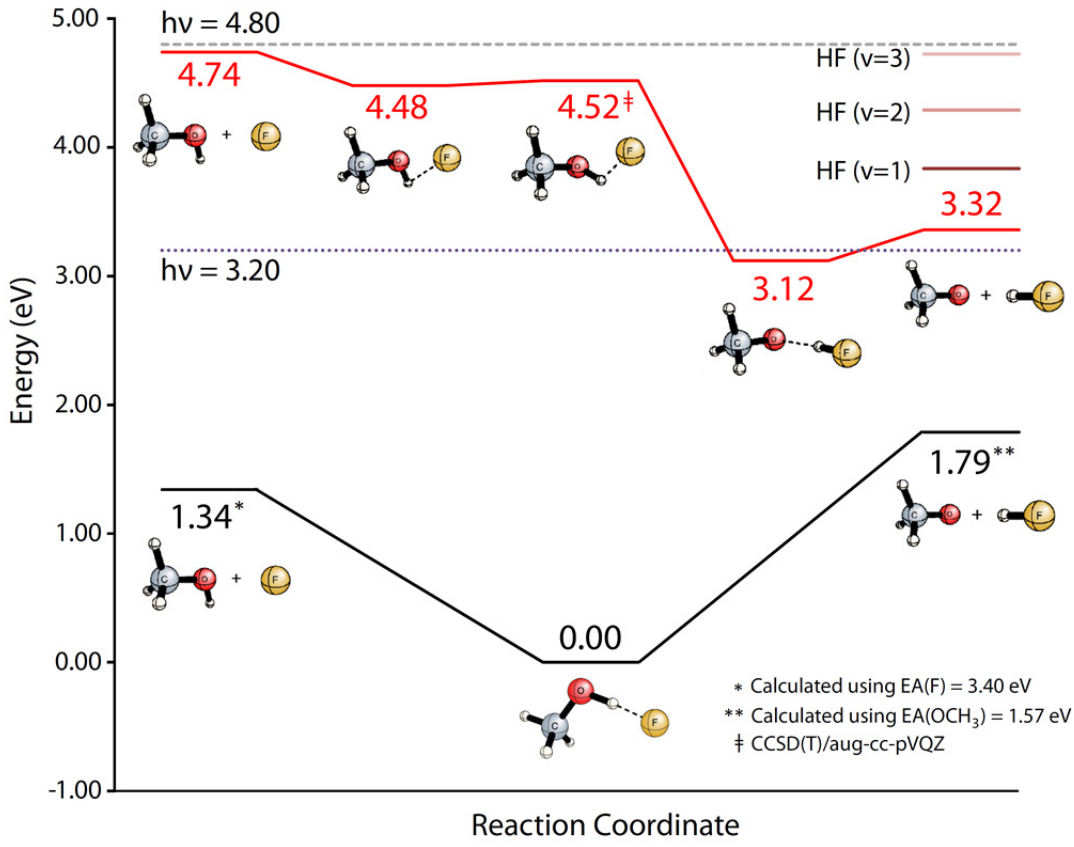

Figure 6.2. Energy diagram for stationary points along the neutral F + $HOCH_3$ → HF + OCH_3 potential energy surface. Zero-point-corrected CCSDT(Q)/CBS energetics are reported in eV relative to the $F^-(HOCH_3)$ anion. The experimental photon energies used, 4.80 and 3.20 eV, are indicated by dashed and dotted lines respectively.

energy (ZPVE), determined at the same level as geometry optimization, to the extrapolated electronic energy.

6.4. Results

PPC spectroscopy is ideal for examining the transition state dynamics of the $F(HOCH_3)$ system, allowing for separation of photodetachment processes for the $F^-(HOCH_3)$ precursor anion that lead to stable neutral complexes from dissociative photodetachment (DPD) processes that yield a photodetached electron and two (or more) neutral photofragments. As discussed earlier, the stable channel is taken to be those with photoelectrons detected in coincidence with a single neutral particle arriving at a time and position on the neutral particle detector as expected for the incident precursor anion beam. Dissociative events correspond to detection of a photoelectron in coincidence with two momentum-matched neutral particles. Experimental results for each channel are detailed in the following sections, followed by a discussion of the new *ab initio* results.

6.4.1. Dissociative Channel

Figure 6.3 shows the PPC spectrum for the $F + HOCH_3 \rightarrow HF + OCH_3$ reaction, providing information on the event-by-event correlation of eKE with the KER between neutral products. Analysis of the fraction of coincidence events indicates that DPD of $F^-(HOCH_3)$ is the dominant pathway (84%), with 16% yield for photoelectrons and one stable product. The PPC spectrum is dominated by diagonal bands, dropping off quickly as KER increases each with a cut off by KER = 0.5 eV. The uppermost diagonal line at 1.48 eV corresponds to the calculated KE_{MAX} for dissociation to products ($HF + OCH_3$)

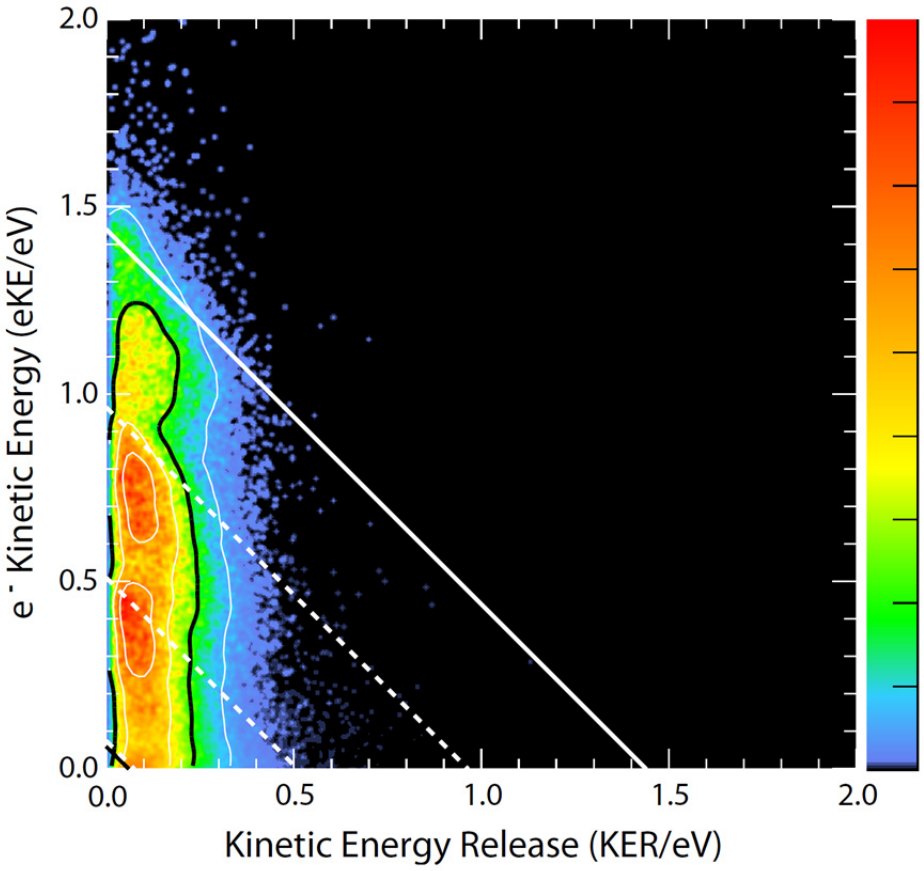

Figure 6.3. PPC spectrum of the F + $HOCH_3$ → HF + OCH_3 reaction using a photon energy of 258 nm (4.80 eV). The rightmost diagonal indicates the maximum kinetic energy (KE_{MAX}) when the HF + OCH_3 products are formed in their vibrational and rotational ground states. The dashed diagonals correspond to vibrational excitation in the HF fragment; the black diagonal corresponds to the KE'_{MAX} for dissociation to the reactants F + $HOCH_3$. All calculated values presented here contain ZPE corrections.

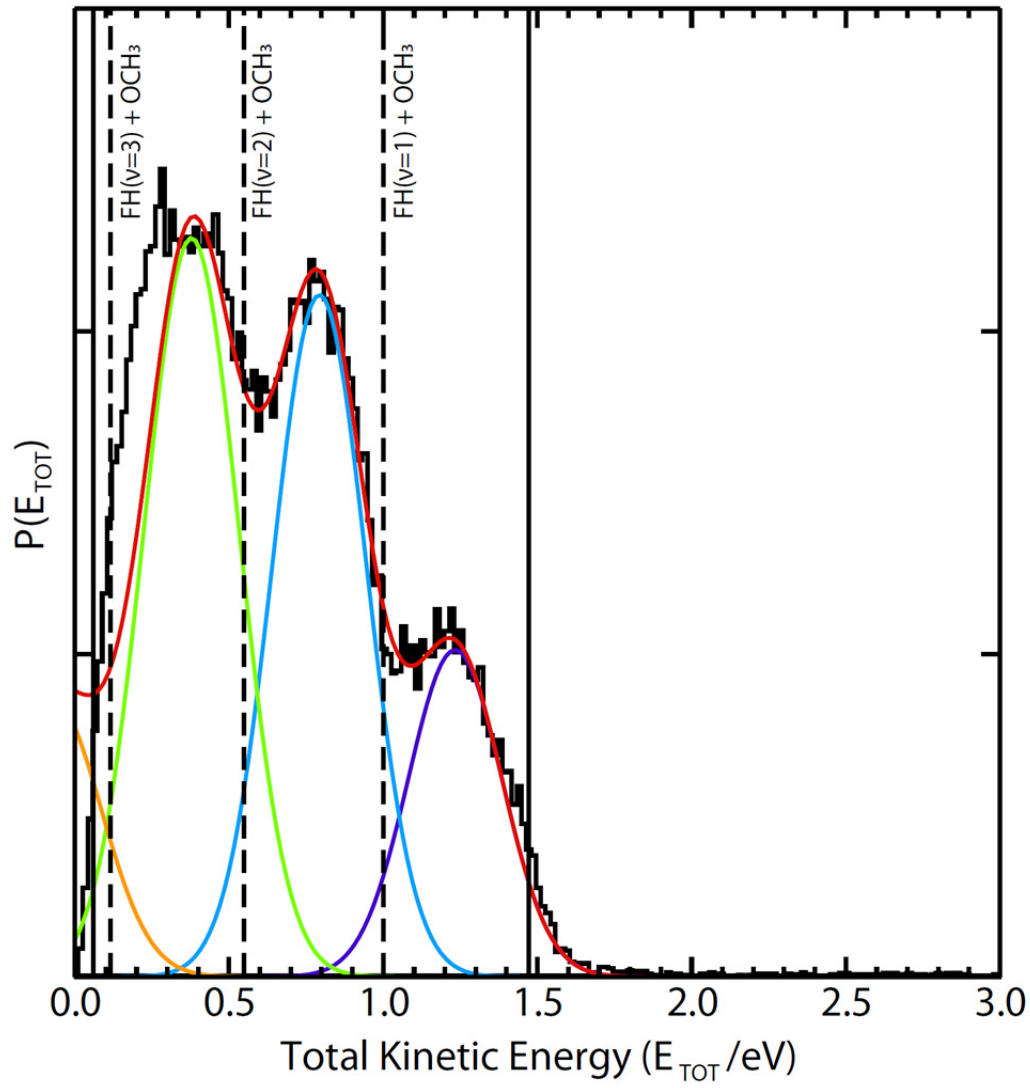

Figure 6.4. Total kinetic energy spectrum $N(E_{TOT})$, where E_{TOT} = KER + eKE as determined on an event-by-event basis, for $F^-(HOCH_3)$ at $E_{h\nu}$ = 4.80 eV. Vertical lines denote the energetic limits for HF(v = 0, 1, 2, 3) + OCH_3 + e^- final states, and each state is fit with a Gaussian and the overall combined fit shown in red.

in their ground vibrational and rotational states. The bulk of the data falls below this calculated line, indicating good agreement with the experimental results assuming internally cold anions. Dissociation to the reactant-channel ($F + HOCH_3$) is calculated to be barely accessible at this photon energy as indicated by the black diagonal line at $KE'_{MAX} = 0.06$ eV. Unfortunately, given the similarity in masses of the two dissociative pathways, these pathways cannot be individually resolved in the lowest-energy portion of the PPC spectrum. The dashed diagonal lines correspond to the energetic limits accounting for vibrational excitation in the HF product, and are a good match to the observed diagonal bands in the spectrum. In the case of the HF(v=1,2) bands, the data is most intense just below the diagonal line, while in the ground state HF(v=0) the distribution peaks away from the KE_{MAX} diagonal but still above the HF(v=1) limit. Another way to view the dissociative data recorded in this coincidence measurement is by examination of the total kinetic energy, E_{TOT}, where $N(E_{TOT}) = \Sigma_i(eKE_i + KER_i)$ is calculated on an event-by-event basis. The E_{TOT} spectrum is shown in Figure 6.4 and has a regular structure consistent with the production of HF(v) product vibrational states. This is an additional signature of the diagonally limited features seen in the PPC spectrum.

6.4.2. Stable Channel

As noted earlier, stable events are extracted from the data set by selecting for those photoelectrons in coincidence with only one neutral particle arriving at the time and position of the center-of-mass, thus selecting for species with lifetimes longer than the flight time between the laser-interaction region and the neutral-particle detector ($\Delta t \sim 8.4$

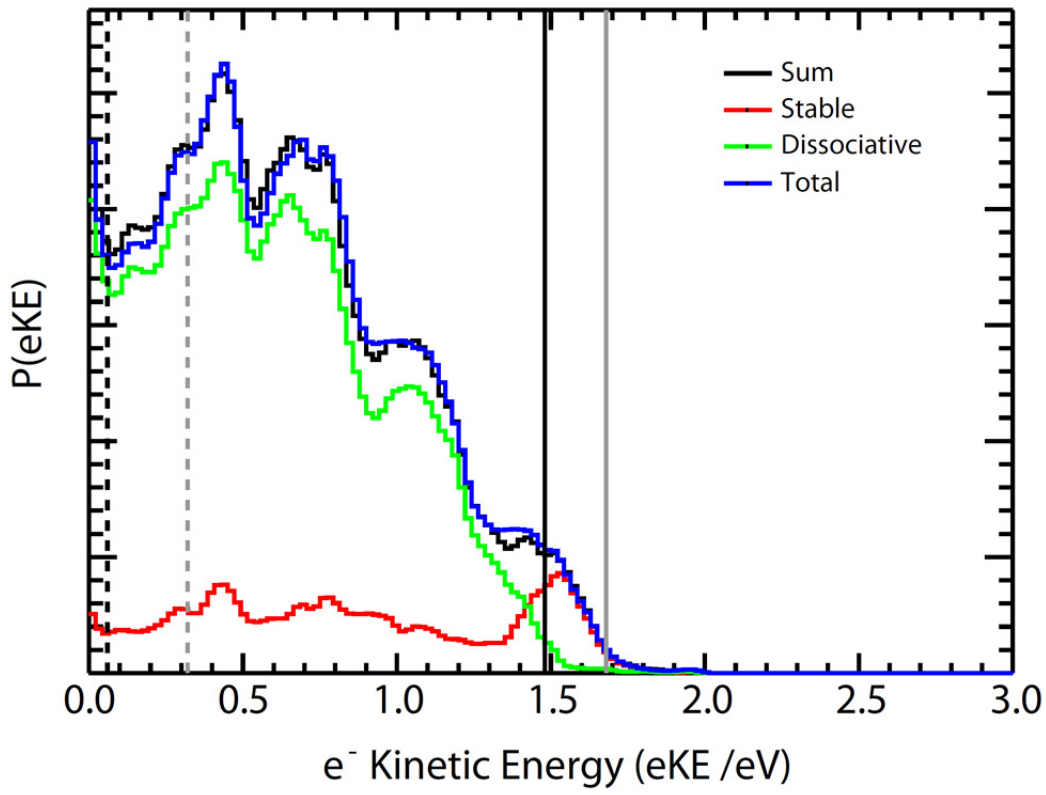

Figure 6.5. Comparison of the total photoelectron spectrum (photoelectron + 1 or more heavy particles with no center-of-mass gating) and the decomposition of this total spectrum into the photoelectron spectra for the stable (e^- + 1 neutral particle, center-of-mass gated) and dissociative (e^- + 2 neutral particles, center-of-mass gated) channels of the $F^-(HOCH_3)$ system, taken at 258 nm (4.80 eV). The grey vertical lines indicate ZPE-corrected calculated EAs for the reactant- (dashed) and product-channel (solid) complexes. The black vertical lines indicate calculated KE_{MAX} and KE'_{MAX} for dissociation to either reactants (dashed) or products (solid), respectively. These represent products formed in their vibrational and rotational ground states. All CCSDT(Q)/CBS calculated energetic limits presented here include ZPE corrections.

μs for a 7 keV beam), or dissociation events with very low kinetic energy release between the molecular fragments. Given the detection efficiency of the neutral-particle detector (~50%),[50] any stable signal necessarily contains a small contribution from dissociative events where only one neutral particle was collected in an event with a very low KER; but, if a true stable channel exists, the photoelectron spectra in coincidence with one heavy particle should look noticeably different than those in coincidence with two momentum-matched heavy particles.

Figure 6.5 shows a comparison of the total photoelectron spectrum (photoelectron + one or more heavy particles with no center-of-mass gating) and the decomposition of this total spectrum into stable and dissociative components. The blue total photoelectron spectrum consists of four broad features that are increasingly resolved as eKE decreases, as well as a peak at eKE = 0.00 eV. This spectrum is in good agreement with earlier photoelectron spectra recorded by Neumark and coworkers at a higher photon energy.[29] The red stable spectrum consists of a peak at eKE = 1.55 eV, a second feature peaking slightly under 0.8 eV and a poorly resolved doublet at 0.45 and 0.30 eV. The green dissociative spectrum consists of three broad features and a peak near 0.00 eKE, with some evidence of fine structure. The most striking difference is the prominent peak at 1.55 eV in the stable spectrum that is noticeably absent from the dissociative spectrum. This feature peaks just above the KE_{max} limit for the dissociative channel (black vertical line), consistent with formation of the stable hydrogen-bonded complex in the product channel. In comparison the bulk of the dissociative signal falls below this limit, consistent with dissociation leading to internal excitation in one or more of the resulting

neutral dissociative products. The broad peaks correspond to the diagonal bands observed in the coincidence spectrum (Figure 6.3) and are consistent with vibrational excitation in the HF product as resolved in the E_{TOT} spectrum in Figure 6.4. The width of these broad peaks can be explained either by vibrational excitation in the OCH_3 product and/or rotational excitation in one or both of the HF + OCH_3 products.

6.4.3. Complex Lifetime Effects

Once distinct dissociative and stable photoelectron spectra are observed, it is useful to examine in further detail the lifetime of any metastable complexes formed in the photodetachment of $F^-(HOCH_3)$. This can be done by examining the KER dependence of the eKE spectra at a given energy, as well as the dependence of the stable eKE spectra on the incident ion beam energy. At a 7.0 keV beam energy the flight time from the laser-ion-beam interaction region to the QXDL is 8.4 μs, and any dissociative events that occur on a timescale < 8.4 μs but greater than ~100 ns will lead to a degrading of the measured KER to lower values. Thus, one approach to examining the differences between the stable and dissociative channels is by comparing the stable eKE spectrum with that generated by integrating over the lowest KER portion (KER = 0.00 – 0.05 eV) of the PPC spectrum. Figure 6.6 (upper panel) shows, in green, a plot of the corresponding low-KER eKE spectrum compared to the stable eKE spectrum. The low-KER spectrum has more in common with the stable than dissociative spectrum, again showing five features at 1.40, 1.05, 0.80, 0.45 and 0.30 eV, marked A – E, respectively. Most interesting of these is peak A at 1.40 eV, appearing at lower eKE than in the stable spectrum and peaking just below the calculated KE_{MAX} vertical line. This corresponds to probing at the top of the

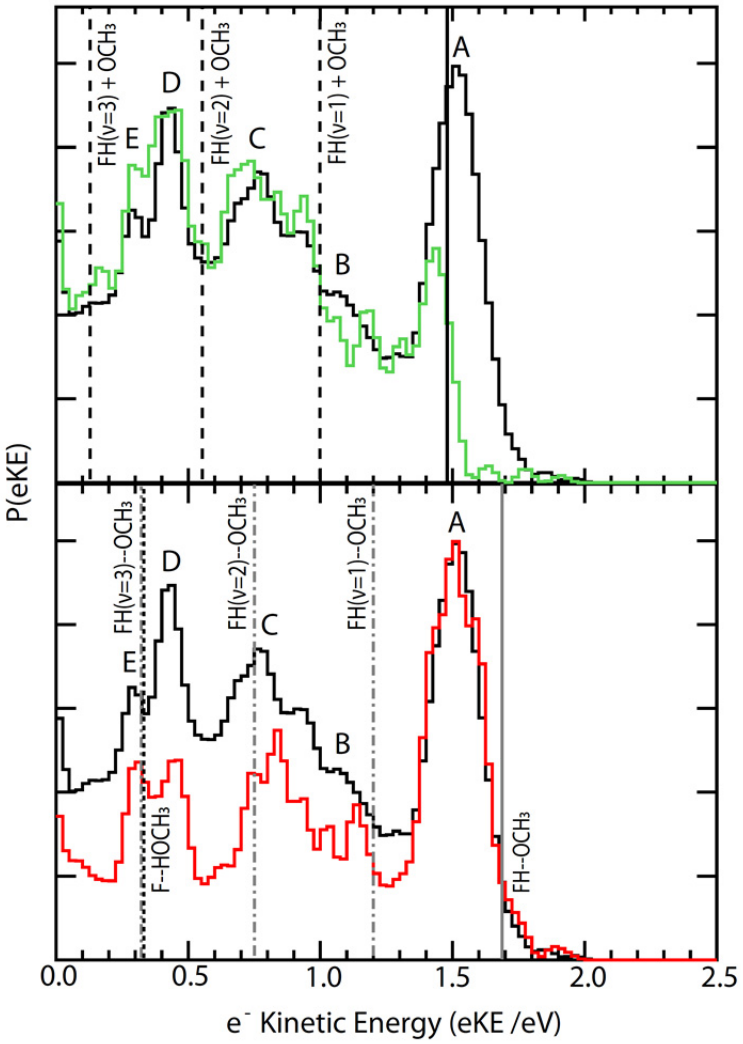

Figure 6.6. Photoelectron spectrum of the stable (e^- + 1TAC) channel, taken at 7.0 keV beam energy (flight time ~ 8.4 μs, black trace) vs. the low-KER slice (KER = 0.00 – 0.02 eV, green trace) from the dissociative spectrum (e^- + 2TAC), top panel. The effect of dropping the beam energy to 4.0 keV (flight time ~ 11 μs, red trace), normalized to the stable signal at 1.55 eV at 7.0 keV, is shown in the bottom panel. The black vertical line corresponds to the calculated KE_{MAX} to form HF + OCH_3 products in their ground vibrational and rotational states (eKE = 1.48 eV with ZPE correction included) while the black dotted line in the lower panel corresponds to the calculated KE'_{MAX} for dissociation to F + $HOCH_3$ products (eKE = 0.32 eV with ZPE correction included). In the top panel the dashed lines correspond to the energetic limits for HF(v = 0, 1, 2, 3) + OCH_3 + e^- final states. The grey vertical line in the lower panel corresponds to the product-channel hydrogen-bonded complex well (eKE = 1.68 eV with ZPE correction) and the grey dash-dot-dash lines represent the estimated well-depths for the metastable vdW resonances corresponding to excitation in HF.

stable product-channel hydrogen-bonded complex well, leading to HF(v=0) + OCH_3 products via a slow dissociation process that, by energy conservation, can only produce a small KER.

A more direct test of the lifetime of metastable complexes is to vary the incident ion beam kinetic energy, and examine the intensity dependence of the stable and metastable peaks in the photoelectron spectrum. In the present experiments this was done by lowering the experimental beam energy from 7.0 to 4.0 keV, lengthening flight times of the resulting neutrals after photodetachment from 8.4 to 11.0 μs. The lower panel in Figure 6.6 shows, in red, the 4.0 keV stable photoelectron spectrum, normalized to the height of peak A at 1.55 eV in the 7.0 keV spectrum (in black). This highlights the increase in relative intensity of both peak A and peak E in the 4.0 keV spectrum. As noted above, peak A is assigned to the stable product-channel hydrogen-bonded complex. Peak E evidently has a longer lifetime than the other features in the stable photoelectron spectrum, and is tentatively assigned to production of the weakly bound reactant-channel van der Waals complex F—$HOCH_3$. This complex is metastable, but is expected to only slowly dissociate by tunneling through the barrier, evidently on a timescale commensurate with the 11.0 μs flight time.

6.4.4. Product-Channel Hydrogen-Bonded Complex Well

To further probe the stable product-channel complex, data was collected near threshold at $E_{h\nu}$ = 3.20 eV, allowing probing near the bottom of the product complex well and completely closing off the dissociative channel. Figure 6.7 shows the resulting photoelectron spectrum, which peaks near eKE = 0.00 eV, with a progression of poorly

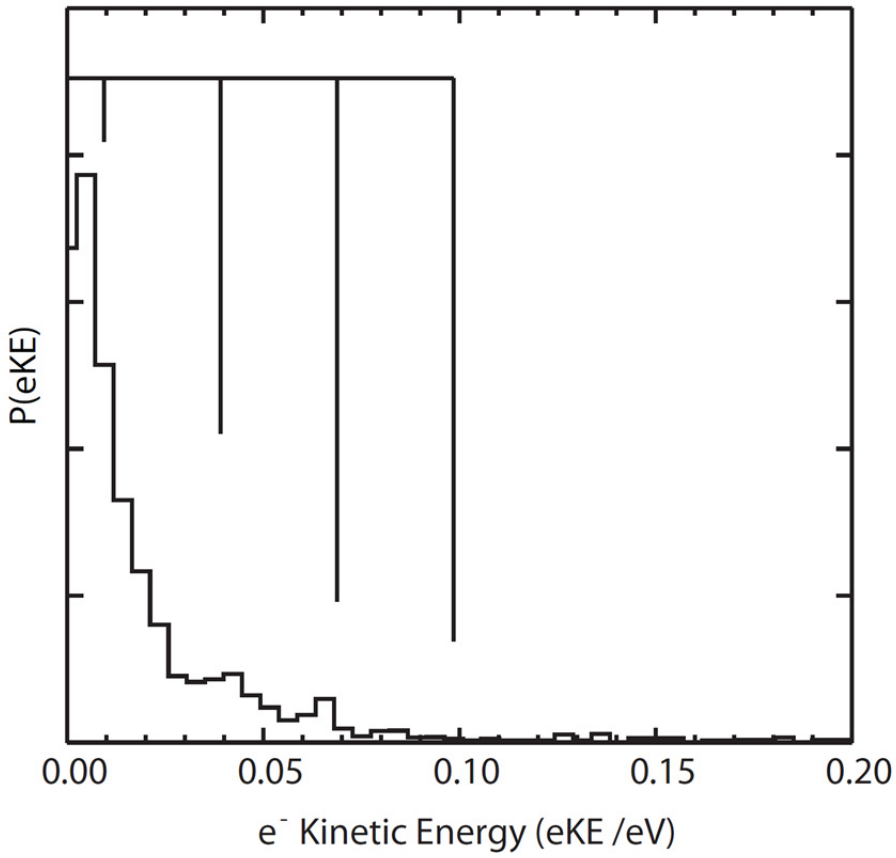

Figure 6.7. Near-threshold photoelectron spectrum of the product hydrogen-bonded complex FH—OCH_3, taken at 388 nm. The vibrational comb corresponds to the calculated F–HO stretch with an OCH_3 rock mode (241.3 cm^{-1}), shifted for best fit by 0.02 eV from the maximum eKE = 0.08 eV as determined by the calculated zero-point-corrected AEA (3.12 eV).

resolved features with an average spacing of ~25 meV. The calculated AEA appears at eKE = 0.08 eV at this wavelength, in reasonable agreement with experimental data. The best Franck-Condon overlap is more clearly seen to peak away from the bottom of the well. Note that the calculated frequency of the internal F−H−O asymmetric stretching mode of 3751 cm^{-1} (0.47 eV) is significantly larger than the calculated well depth of 0.24 eV for this product complex and, although expected to contribute to the dissociative channel discussed above, this mode is not energetically available at 388 nm. Instead, the vibrational progression is in decent agreement with the calculated frequency for the υ_3 mode of 241.3 cm^{-1} (29.9 meV), corresponding to the F−H stretch and an H−O−C rocking motion. This calculated frequency is plotted as an overlaid vibrational comb, starting at the calculated AEA + 0.02 eV.

6.4.5. Ab Initio Results

Figure 6.2 shows the stationary points for the anion and neutral potential energy surfaces, with energies extrapolated to the CCSDT(Q)/CBS level of theory. These energies include zero-point energy corrections, and are presented relative to the anion. As noted earlier, geometry optimizations and frequencies were determined at the CCSD(T)/aug-cc-pVTZ level. No stable $F^-(HCH_2OH)$ geometry was found, eliminating the need to consider reaction 6.2 and simplifying analysis of the experimental data. Accordingly, only the stationary points related to reaction 6.1 are considered here.

Table 6.1 lists calculated vibrational frequencies used for zero-point energy corrections, for the neutral reactant-channel well, transition state, and product-channel hydrogen-bonded complex well. A more detailed discussion of the calculated geometries

Table 6.1. Calculated vibrational frequencies for the reactant-channel vdW complex, transition state, and product-channel hydrogen-bonded complex at the CCSD(T)/aug-cc-pVTZ level of theory.

Mode	F–$HOCH_3$	TS1	FH–OCH_3	Description
ν_1	116.627	72.8	71.901	H-C-H rock/rotation (YZ)
ν_2	186.691	197.3	83.955	C-O-F bend
ν_3	349.465	421.9	241.279	OCH_3 rock and O-HF stretch
ν_4	468.383	1012.8	602.514	H-C-H rock/rotation (XZ)
ν_5	1028.587	1095.1	751.181	O-H-F bend (+/-)/ H(O) wag
ν_6	1066.771	1154.8	939.979	H-C-H rock/rotation (XZ)
ν_7	1165.713	1311.9	1059.210	C-O stretch
ν_8	1355.939	1456.6	1108.164	H-C-O bend with H wag
ν_9	1465.119	1481.4	1382.505	CH_3 umbrella
ν_{10}	1503.868	1510.2	1398.914	CH_3 H rotation
ν_{11}	1511.434	3042.0	1517.487	H-C-H and H bend
ν_{12}	3036.551	3115.5	2931.717	CH_3 symmetric stretch
ν_{13}	3116.778	3138.9	3036.087	H-C-H rock (YZ)
ν_{14}	3159.399	3156.9	3095.673	CH_3 asymmetric stretch
ν_{15}	3797.992	800.2i	3751.282	O--H--F asymmetric stretch

for these stationary points have been previously reported,[15] and the geometries are included in Figure S1 in the supplementary material. The new energetic results presented here were carried out on the previous CCSD(T)/aug-cc-pVTZ optimized geometries using CCSDT(Q) and extrapolated to the complete basis set limit. In addition, zero-point-energy corrections have now been included.

Briefly, the reactant-channel complex, F—$HOCH_3$, is calculated to be stable relative to both the reactants and the submerged reaction barrier, although this well is shallow, only 0.04 eV relative to the barrier. In contrast, the product-channel complex is calculated to be stable relative to the products by 0.24 eV. This product-channel well is in good agreement with the peak at 1.55 eV in the stable photoelectron spectrum. The calculated dissociative-channel asymptotes were used to determine KE_{MAX} values for our PPC plots, also in excellent agreement with the experimental data. There are features observed in the spectra consistent with production of the metastable reactant-channel F—$HOCH_3$ complex as well, noted above and discussed in more detail below.

6.5. Discussion

These experiments show that photodetachment of the $F^-(HOCH_3)$ anion leads to prompt DPD to HF + OCH_3 + e^-, the stable FH—OCH_3 product-channel hydrogen-bonded complex as well as a significant fraction of quasi-bound complexes with microsecond time-scale lifetimes and/or product kinetic energy distributions upon dissociation that are strongly peaked near KER = 0.00 eV. This is consistent with observations made in our study of the analogous $F^-(H_2O)$ system,[4] illustrating in a larger polyatomic system that at a minimum both resonant and direct pathways play a

significant role in DPD processes. Again, these results provide a sensitive probe for multidimensional potential energy surfaces and many particle reaction dynamics. Comparison of the calculated minimum on the anion potential energy surface and the transition state and reactant- and product-channel complexes on the neutral surface qualitatively indicates that photodetachment of the $F^-(HOCH_3)$ primarily probes near the product channel of the transition state for the neutral reaction, albeit with a very large change along the O–H–F hydrogen atom transfer coordinate and a significant lengthening of the O–F distance. This is consistent with the conclusions of Neumark and coworkers in their study of the photodetachment of $F^-(HOCH_3)$.[29] In the following paragraphs the experimental observations of direct and resonance-mediated dynamics on the neutral $F(HOCH_3)$ potential energy surface will be discussed in light of the electronic structure computations carried out here, as well as the analogy to the much more extensive reaction dynamics computations that have been carried out on the $F(H_2O)$ system.[4, 51]

6.5.1. *Dissociative Channel*

PPC spectroscopy was originally developed for the examination of direct DPD processes where dissociation is prompt (on the nanosecond timescale), and the $F^-(HOCH_3)$ system exhibits a major direct DPD channel. Given the energetics in Figure 6.2, at a photon energy of 4.80 eV, the dissociative signal is dominated by formation of the products ($HF + OCH_3$), with clear indications of vibrational excitation in the HF fragment as evidenced by the diagonal bands in the coincidence spectrum (Figure 6.3). These resolved features, consistent with HF vibrational excitation, appear as broad features in the E_{TOT} spectrum in Figure 6.4 as well as the dissociative eKE spectrum

(Figure 6.5). In Figure 6.3, the maximum KER extends out to a remarkably constant ~ 0.5 eV in all of the states. An insight into the nature of this limit can be seen by examining the distribution of events above and below the diagonal limit corresponding to HF(v=1) + OCH_3. At eKE > 1.0 eV, where only HF(v=0) + OCH_3 products are accessible, a significant number of events occur at the corresponding maximum KER. At eKE = 1.0 eV, however, this behavior breaks off, simultaneous with the opening of the HF(v=1) + OCH_3 channel. This is observed in the PPC spectrum as the 'bending-in' towards lower KER of the 20% contour line right above the HF(v=1) + OCH_3 energetic limit. This can explain the general trend wherein the KER limit on each band corresponds roughly to the energy spacing between HF vibrational states and thus the opening of the next available HF vibrational state. It is interesting to note that the same 'bending-in' of the contour line does not occur below the HF(v=1) limit, a result possibly related to the decay of metastable vibrational Feshbach resonances or tunneling through the submerged barrier further discussed below.

In general the widths of each band are consistent with the photoelectron spectrum of $F^-(HOCH_3)$ reported by Neumark and coworkers, who concluded that the OCH_3 product is produced vibrationally cold but with significant rotational excitation.[29] This is similar to the case for $F^-(H_2O)$, where the product HF + OH channel dominates the spectrum, HF carries away considerable vibrational excitation, and the OH product acts primarily as a spectator, remaining vibrationally cold.[4] This finding can be understood by considering the vibrational degrees of freedom in the $F(HOCH_3)$ complex enumerated in Table 6.1. As for the simpler $F(H_2O)$ system, the reaction coordinate is primarily the

internal hydrogen bond, F−H−O. Two normal modes have considerable amplitude along the reaction coordinate: the F−H−O asymmetric stretch, ν_{15}, and the FH−O stretch coupled to an O−CH_3 rocking mode, ν_3. Dissociation coupled to the ν_3 mode, for example, is expected to impart fairly substantial rotational excitation in the OCH_3 fragment in addition to producing vibrationally excited HF. The features observed in the near-threshold photoelectron spectrum in Figure 6.7 are consistent with excitation of this ν_3 mode, supporting its importance to the dissociation dynamics of this system.

Focusing on the HF fragment, with the assumption that OCH_3 is produced without significant vibrational excitation, vibrational population distributions were extracted from the E_{TOT} spectrum by fitting each peak with a Gaussian distribution, as shown in Figure 6.4, and relative populations are presented in Table S1. As these features are not fully resolved and are convoluted with the HF rotational distributions as well as the internal energy distribution of the OCH_3 products, these populations are only approximate. Only 16% of the HF is found in v = 0, in reasonably good agreement with the value of 23% in the ground state reported by Dill and Heydtmann using IR chemiluminescence.[20] It should be noted that those researchers observed both HF + OCH_3 (reaction 6.1) and HF + CH_2OH (reaction 6.2), while our results are limited to reaction 6.1. The fit to the E_{TOT} spectrum shows that the majority of the HF products are vibrationally excited, with 33% in HF(v=1) and 37% in HF(v=2), indicating a significant HF-product vibrational population inversion. Although energetically available, the signal for HF(v=3) falls in the congested portion of the spectrum where dissociation back to reactants, F + $HOCH_3$, also appears and it is not possible to disentangle these results owing to the limited

photofragment mass resolution. The combined F + $HOCH_3$ and HF(v=3) signal accounts for the remaining roughly 14% of the observed events.

6.5.2. *Product and Reactant Complexes and Metastable Resonances*

As noted before, in addition to characterizing DPD processes, PPC spectroscopy also allows determination of the stable photoelectron spectrum by examining those events where one electron is detected in coincidence with one neutral particle at the time and position of impact expected for the neutralized parent anion. As noted earlier, Figure 6.5 shows that the stable photoelectron spectrum differs significantly from that for the dissociative pathway. In particular, the prominent peak A, centered at 1.55 eV, is absent from the dissociative spectrum. Peak A is best explained by photodetachment to the stable complex in the product channel, with a calculated stabilization 0.24 eV lower in energy than the product asymptote. The bulk of peak A falls above the calculated KE_{MAX} for dissociation to HF + OCH_3 (solid black line) and below the calculated AEA of 3.12 eV for the product-channel complex (solid grey line) relative to the $F^-(HOCH_3)$ precursor anion, in very good agreement with the calculated values.

The comparison between the stable and the low-KER portion of the dissociative spectrum shown in the upper panel of Figure 6.6 provides additional insight into photodetachment production of the stable product-channel complex. The peak at 1.4 eV in the low-KER (green) spectrum peaks just below the calculated KE_{MAX} vertical line, corresponding to production of complexes with internal energies just above the dissociation asymptote. Energy conservation dictates that these complexes will dissociate with very low KER and may also dissociate on a long timescale. In contrast, the

corresponding peak A in the stable channel (black) peaks above the calculated KE_{MAX}, indicating that this calculated value is in excellent agreement with experimental results and captures where the dissociative channel opens. The fact that the stable channel peaks so close to the KE_{MAX} and away from the AEA line indicates that the best Franck-Condon overlap is nearer the top of the well, as expected based on the geometries of the precursor anion and the product-channel complex. This is confirmed by the near-threshold photoelectron spectrum at $E_{h\nu}$ = 3.20 eV shown in Figure 6.7.

Lowering the anion beam energy from 7.0 to 4.0 keV increased the flight time between the laser interaction region and the neutral-particle detector from ~8.4 μs to ~11 μs, aiding in the differentiation between long-lived complexes and metastable resonance states. Shown in red in the lower panel of Figure 6.6, the 4.0 keV spectrum is normalized to peak A which, like peak E, increased in relative intensity as might be expected for a longer-lived species with a lifetime greater than 11 μs. In contrast, peaks C and D do not exhibit this same behavior, but instead decrease in relative intensity, as expected for a dissociative species with a comparatively shorter lifetime. The fact that peak E behaves differently from its neighboring peak D, behaving like the stable product-channel complex, supports the conclusion that this feature is a result of formation of the reactant-channel vdW complex, F—$HOCH_3$. As shown in the theoretical results, the reactant-channel vdW complex is also calculated to be accessible and stable relative to dissociation to F + $HOCH_3$, although this well is fairly shallow (~ 0.04 eV) with respect to the submerged barrier. The ZPE-corrected KE_{MAX} for dissociation to reactants and the reactant-channel vdW complex EA are plotted as black and grey dashed vertical lines,

respectively, in Figure 6.5. Feature E at eKE = 0.30 eV is in good agreement with the calculated value for the bottom of the reactant-channel van der Waals complex well at 0.32 eV. With this assignment, it can be concluded that the theoretical predictions for the stability of the reactant- and product-channel complexes relative to the $F^-(HOCH_3)$ precursor are in excellent agreement with experiment, serving to benchmark the energetics of the neutral potential energy surface. It must be noted, however, that feature E also appears in the dissociative spectra. This is not surprising given that this complex can decay by tunneling through the low reactive barrier to products, and essentially plays the role of a shape resonance in the reaction.

The features B, C and D, at 1.05, 0.80 and 0.45 eV, respectively, cannot be directly explained by any calculated stationary point or barrier on the neutral potential energy surface. Instead, these peaks are consistent with long-lived metastable states corresponding to the product-channel hydrogen-bonded complex wells correlating to HF(v=1,2, and 3) products, respectively. The energetic limits for these metastable complexes (grey dash-dot-dashed vertical lines in the lower panel of Figure 6.6) were determined using the known HF(v) vibrational spacing and assumed a well depth equal to that of the calculated ground state complex. Interestingly, the v = 2, 3 peaks C and D appear at eKE's greater than these limits, hinting at an increase in well depth with increasing HF product vibration. Although we can largely disentangle stable and dissociative photoelectron spectra by enforcing coincidence with one or two heavy particles at the neutral-particle detector, metastable complexes can present challenges. The finite resolution of the neutral-particle detector means that very low KER

dissociative events may appear "stable." Here, peak C is comparable to the broad shelf-like peak at 0.7 eV in the dissociative spectrum, but shifted to slightly larger eKE as would be expected for a stabilized complex with a modest well depth. The importance of quasi-bound states in the reactant-channel vdW complex of the F + CH_4 reaction has recently been demonstrated[52-54] and similar metastable vibrationally excited product-channel complexes have been observed in the simpler F + H_2 reaction. [1, 55] At high enough energies these resonances are also expected to become more reactive (that is, their wavefunctions extend to both reactant and product channels) as is observed in the related F + H_2O system.[14] Interestingly, stability of these complexes relative to their respective product asymptotes has been shown to increase with additional vibrational excitation. This increasing complex well-depth with internal excitation results in a shift in observed vibrational frequencies and is expected to have an effect on complex lifetimes. This, combined with the product-population inversion already seen in the dissociative data, helps explain why features correlated with HF(v=2,3) appear so prominently in our nominally stable spectrum, consistent with an assignment of these features to vibrational Feshbach resonances based on metastable product-channel hydrogen-bonded complexes.

6.6. Conclusion

In this work the F + $HOCH_3$ → HF + OCH_3 potential energy surface has been studied using PPC spectroscopy at E_{hv} = 4.80 eV using the $F^-(HOCH_3)$ anionic precursor. The experimental results provide evidence for Franck-Condon excitation to reactant- and product-channel complexes, metastable product-channel vibrational Feshbach resonances, and direct dissociation. The observed dissociation dynamics are dominated

by the exothermic product channel of the neutral surface and excitation of HF product vibrations. In addition to the dissociative pathway, we observed the stable ground-state product-channel hydrogen-bonded complex as well as the long-lived reactant-channel complex with a lifetime on the order of 11 μs or more. The near-threshold photoelectron spectrum for the product-channel complex has features consistent with excitation of the low frequency ν_3 mode. Thus, the internal hydrogen-bond F−H−O asymmetric stretch, ν_{15}, and the ν_3 mode which couples the F−H stretch with and H−O−C rocking motion should be considered when discussing reaction dynamics on this potential energy surface.

The recent PPC experiments on the comparatively simpler $F + H_2O \rightarrow HF + OH$[4] and $OH + CO \rightarrow H + CO_2$ reactions[5, 6] represent benchmarks for full-dimensionality quantum dynamics computations for six dimensional systems. Although full 15-dimensional quantum dynamics computations for the $F + HOCH_3 \rightarrow HF + OCH_3$ reaction remain out of reach, the new high accuracy electronic structure computations (extrapolated to CCSDT(Q)/CBS) presented here represent a substantial effort and are in excellent agreement with the current experimental results. The calculated product asymptote is in agreement with the dissociative data, while the calculated product-channel complex AEA perfectly captures the high-energy peak at 1.55 eV in the stable photoelectron spectrum. Although the reactant-channel vdW complex appears in a more convoluted portion of the experimental spectrum, increasing the time-of-flight of the resulting nascent neutral products by lowering the ion beam energy made identification of this complex possible as well. This reactant-channel vdW complex is also in excellent agreement with the calculated energetics, despite the complexity of this system and the

shallowness of the well. Thus, in this single experiment, the neutral potential energy surface is simultaneously sampled in the reactant and product channels as well as the transition state.

Acknowledgments

This material is based upon work supported by the U.S. Department of Energy, Office of Science, Office of Basic Energy Sciences under award numbers DE-FG03-98ER14879 (AWR, BBS and REC) and DE-FG02-00ER14748 (JA and HFS III). Helpful discussions with J. Stanton are acknowledged.

Chapter 6, in full, is a reprint of the material as it appeared in Ray, A. W.; Agarwal, J.; Shen, B. B.; Schaefer, H. F.; Continetti, R. E. "Energetics and Transition-State Dynamics of the F + $HOCH_3$ → HF + OCH_3 Reaction," *Physical Chemistry Chemical Physics*, in press (2016); doi: 10.1039/c6cp06409d. The dissertation author is the primary author and the dissertation advisor is the corresponding author.

6.8. References

1. Kim, J. B.; Weichman, M. L.; Sjolander, T. F.; Neumark, D. M.; Kłos, J.; Alexander, M. H.; Manolopoulos, D. E., Spectroscopic Observation of Resonances in the F + H_2 Reaction. *Science* **2015,** *349* (6247), 510-513.

2. Yang, X.; Zhang, D. H., Dynamical Resonances in the Fluorine Atom Reaction with the Hydrogen Molecule. *Acc. Chem. Res.* **2007,** *41*, 981-989.

3. Liu, K., Quantum Dynamical Resonances in Chemical Reactions: From A + BC to Polyatomic Systems. In *Advances in Chemical Physics*, Rice, S. A.; Dinner, A. R., Eds. Wiley: Hoboken, NJ, 2012; Vol. 149, pp 1-46.

4. Otto, R.; Ma, J.; Ray, A. W.; Daluz, J. S.; Li, J.; Guo, H.; Continetti, R. E., Imaging Dynamics on the F+ H_2O → HF+ OH Potential Energy Surfaces from Wells to Barriers. *Science* **2014,** *343*, 396-399.

5. Johnson, C. J.; Poad, B. L. J.; Shen, B. B.; Continetti, R. E., Communication: New Insight into the Barrier governing CO_2 Formation from OH + CO. *J. Chem. Phys.* **2011,** *134* (17), 171106.

6. Johnson, C. J.; Otto, R.; Continetti, R. E., Spectroscopy and Dynamics of the HOCO Radical: Insights Into the OH + CO → H + CO_2 Reaction. *Phys. Chem. Chem. Phys.* **2014,** *16* (36), 19091-19105.

7. Li, G.; Zhou, L.; Li, Q.-S.; Xie, Y.; Schaefer, H. F., The Entrance Complex, Transition State, and Exit Complex for the F + H_2O → HF + OH Reaction. Definitive Predictions. Comparison with Popular Density Functional Methods. *Phys. Chem. Chem. Phys.* **2012,** *14* (31), 10891-10895.

8. Li, J.; Wang, Y.; Jiang, B.; Ma, J.; Dawes, R.; Xie, D.; Bowman, J. M.; Guo, H., Communication: A Chemically Accurate Global Potential Energy Surface for the HO + CO → H + CO_2 Reaction. *J. Chem. Phys.* **2012,** *136* (4), 041103-4.

9. Li, J.; Dawes, R.; Guo, H., An *ab initio* Based Full-Dimensional Global Potential Energy Surface for $FH_2O(X^2A')$ and Dynamics for the F + H_2O → HF + HO Reaction. *The Journal of Chemical Physics* **2012,** *137* (9), 094304.

10. Li, G.; Li, Q.-S.; Xie, Y.; Schaefer, H. F., F + $(H_2O)_2$ Reaction: The Second Water Removes the Barrier. *J. Phys. Chem. A* **2013,** *117*, 11979-11982.

11. Li, J.; Jiang, B.; Guo, H., Spin-Orbit Corrected Full-Dimensional Potential Energy Surfaces for the Two Lowest-Lying Electronic States of FH_2O and Dynamics for the F + H_2O → HF + OH Reaction. *J. Chem. Phys.* **2013,** *138*, 074309.

12. Nguyen, L.; Li, J.; Dawes, R.; Stanton, J. F.; Guo, H., Accurate Determination of Barrier Height and Kinetics for the F + H_2O → HF + OH Reaction. *J. Phys. Chem. A* **2013,** *117*, 8864-8872.

13. Ma, J.; Li, J.; Guo, H., Tunneling Facilitated Dissociation to H + CO_2 in $HOCO^-$ Photodetachment. *Phys. Rev. Lett.* **2012,** *109* (6), 063202.

14. Ma, J.; Guo, H., Reactive and Nonreactive Feshbach Resonances Accessed by Photodetachment of FH_2O^-. *The Journal of Physical Chemistry Letters* **2015,** *6* (23), 4822-4826.

15. Feng, H.; Randall, K. R.; Schaefer, H. F., Reaction of a Fluorine Atom with Methanol: Potential Energy Surface Considerations. *J. Phys. Chem. A* **2015,** *119* (9), 1636-1641.

16. Jacox, M. E., The Reaction of Excited Argon Atoms and of F Atoms with Methanol. Vibrational Spectrum of CH_2OH Isolated in Solid Argon. *Chem. Phys.* **1981,** *59* (1–2), 213-230.

17. Dyke, J. M.; Ellis, A. R.; Jonathan, N.; Keddar, N.; Morris, A., Observation of the CH_2OH Radical in the Gas Phase by Vacuum Ultraviolet Photoelectron Spectroscopy. *Chem. Phys. Lett.* **1984,** *111* (3), 207-210.

18. Dyke, J. M., Properties of Gas-Phase Ions. Information to be Obtained From Photoelectron Spectroscopy of Unstable Molecules. *J. Chem. Soc. Faraday Trans. 2* **1987,** *83* (1), 69-87.

19. Biggs, P.; Canosa-Mas, C. E.; Fracheboud, J.-M.; Shallcross, D. E.; Wayne, R. P., Kinetics of the Reaction of F Atoms with CH_3ONO and CH_3O, and the Reaction of CH_3O with a Number of Hydrocarbons. *J. Chem. Soc. Faraday Trans.* **1997,** *93* (15), 2481-2486.

20. Dill, B.; Heydtmann, H., Infrared Chemiluminescent Reactions of Fluorine Atoms with Methanol and Some Deuterated Analogs. *Chem. Phys.* **1980,** *54* (1), 9-20.

21. Agrawalla, B. S.; Setser, D. W., Energy Disposal in Hydrogen Atom Abstraction Reactions: Energy in the Radical Fragment by Laser-Induced Fluorescence. *J. Phys. Chem.* **1984,** *88* (4), 657-660.

22. Agrawalla, B. S.; Setser, D. W., Infrared Chemiluminescence and Laser-Induced Fluorescence Studies of Energy Disposal by Reactions of Fluorine and Chlorine Atoms with Hydrogen Sulfide, Deuterium Sulfide, Hydrogen Selenide, Water, Water-d2, and Methanol. *J. Phys. Chem.* **1986,** *90* (11), 2450-2462.

23. Bogan, D. J.; Kaufman, M.; Hand, C. W.; Sanders, W. A.; Brauer, B. E., Laser-Induced Fluorescence Study of Methoxy Radical Formation from the Reactions of

Fluorine(^{2}P) Atoms with Methanol (CH_3OH, CD_3OH, and CH_3OD). *J. Phys. Chem.* **1990,** *94* (21), 8128-8134.

24. Glauser, W. A.; Koszykowski, M. L., Anomalous Methoxy Radical Yields in the Fluorine + Methanol Reaction. 2. Theory. *J. Phys. Chem.* **1991,** *95* (26), 10705-10713.

25. Durant, J. L., Anomalous Methoxy Radical Yields in the Fluorine + Methanol Reaction. 1. Experiment. *J. Phys. Chem.* **1991,** *95* (26), 10701-10704.

26. Wickramaaratchi, M. A.; Setser, D. W.; Hildebrandt, H.; Kōrbitzer, B.; Heydtmann, H., Evaluation of HF Product Distributions Deduced from Infrared Chemiluminiscence. II. F Atom Reactions. *Chem. Phys.* **1985,** *94* (1–2), 109-129.

27. Macdonald, R. G.; Sloan, J. J.; Wassell, P. T., The Dynamics of Hydrogen Abstraction from Polyatomic Molecules by Fluorine Atoms. *Chem. Phys.* **1979,** *41* (1–2), 201-208.

28. Jodkowski, J. T.; Rayez, M.-T.; Rayez, J.-C.; Bérces, T.; Dóbé, S., Theoretical Study of the Kinetics of the Hydrogen Abstraction from Methanol. 1. Reaction of Methanol with Fluorine Atoms. *J. Phys. Chem. A* **1998,** *102* (46), 9219-9229.

29. Bradforth, S. E.; Arnold, D. W.; Metz, R. B.; Weaver, A.; Neumark, D. M., Spectroscopy of the Transition State: Hydrogen Abstraction Reactions of Fluorine. *J. Phys. Chem.* **1991,** *95* (21), 8066-8078.

30. DeTuri, V. F.; Ervin, K. M., Competitive Threshold Collision-Induced Dissociation: Gas-Phase Acidities and Bond Dissociation Energies for a Series of Alcohols. *J. Phys. Chem. A* **1999,** *103* (35), 6911-6920.

31. Wladkowski, B. D.; East, A. L. L.; Mihalick, J. E.; Allen, W. D.; Brauman, J. I., The Proton-Transfer Surface of CH_3OHF^-. *J. Chem. Phys.* **1994,** *100* (3), 2058-2088.

32. Gonzales, J. M.; Pak, C.; Cox, R. S.; Allen, W. D.; Schaefer Iii, H. F.; Császár, A. G.; Tarczay, G., Definitive *ab initio* Studies of Model SN_2 Reactions $CH_3X + F^-$ (X=F, Cl, CN, OH, SH, NH_2, PH_2). *Chem. Eur. J.* **2003,** *9* (10), 2173-2192.

33. Yang, Y.; Linnert, H. V.; Riveros, J. M.; Williams, K. R.; Eyler, J. R., Photodetachment of Singly Solvated Halide Ions. *J. Phys. Chem. A* **1997,** *101* (13), 2371-2378.

34. Sun, L.; Song, K.; Hase, W. L.; Sena, M.; Riveros, J. M., Stationary Points for the $OH^- + CH_3F \rightarrow CH_3OH + F^-$ Potential Energy Surface. *Int. J. Mass Spec.* **2003,** *227* (3), 315-325.

35. Hanold, K.; Luong, A.; Clements, T.; Continetti, R., Photoelectron-Multiple-Photofragment Coincidence Spectrometer. *Rev. Sci. Instrum.* **1999,** *70* (5), 2268-2276.

36. Johnson, C.; Shen, B.; Poad, B.; Continetti, R., Photoelectron-Photofragment Coincidence Spectroscopy in a Cryogenically Cooled Linear Electrostatic Ion Beam Trap. *Rev. Sci. Instrum.* **2011,** *82* (10), 105105.

37. Bowen, M. S.; Continetti, R. E., Photodetachment Imaging Study of the Vinoxide Anion. *J. Phys. Chem. A* **2004,** *108* (39), 7827-7831.

38. Raghavachari, K.; Trucks, G. W.; Pople, J. A.; Head-Gordon, M., A Fifth-Order Perturbation Comparison of Electron Correlation Theories. *Chem. Phys. Lett.* **1989,** *157* (6), 479-483.

39. Bartlett, R. J.; Watts, J. D.; Kucharski, S. A.; Noga, J., Non-Iterative Fifth-Order Triple and Quadruple Excitation Energy Corrections in Correlated Methods. *Chem. Phys. Lett.* **1990,** *165* (6), 513-522.

40. Stanton, J. F., Why CCSD(T) Works: a Different Perspective. *Chem. Phys. Lett.* **1997,** *281* (1–3), 130-134.

41. CFOUR, a. q. c. p. p. w. b. S., J. F.; Gauss, J.; Watts, J. D.; Szalay, P. G.; Bartlett, R. J. with contributions from Auer, A. A.; Bernholdt, D. E.; Christiansen, O.; Harding, M. E.; Heckert, M.; Heun, O.; Huber, C.; Jonsson, D.; Jusélius, J.; Lauderdale, W. J.; Metzroth, T.; Michauk, C.; O'Neill, D. P.; Price, D. R.; Ruud, K.; Schiffmann, F.; Tajti, A.; Varner, M. E.; Vázquez, J. and the integral packages: MOLECULE (Almlöf, J.; Taylor, P. R.), PROPS (Taylor, P. R.), ABACUS (Helgaker, T.; Jensen, H. J. Aa.; Jørgensen, P.; Olsen, J.), and ECP routines by Mitin, A. V. and van Wüllen, C. For the current version see, http://www.cfour.de.

42. Dunning, T. H., Gaussian Basis Sets for Use in Correlated Molecular Calculations. I. The Atoms Boron Through Neon and Hydrogen. *J. Chem. Phys.* **1989,** *90* (2), 1007-1023.

43. East, A. L. L.; Allen, W. D., The Heat of Formation of NCO. *J. Chem. Phys.* **1993,** *99* (6), 4638-4650.

44. Császár, A. G.; Allen, W. D.; Schaefer, H. F., In Pursuit of the *ab initio* Limit for Conformational Energy Prototypes. *J. Chem. Phys.* **1998,** *108* (23), 9751-9764.

45. Feller, D., The Use of Systematic Sequences of Wave Functions for Estimating the Complete Basis Set, Full Configuration Limit in Water. *J. Chem. Phys.* **1993,** *98*, 7059-7071.

46. Helgaker, T.; Klopper, W.; Koch, H.; Noga, J., Basis-Set Convergence of Correlated Calculations on Water. *J. Chem. Phys.* **1997,** *106*, 9639-9646.

47. Halkier, A.; Helgaker, T.; Jorgenson, P.; Klopper, W.; Koch, H.; Olsen, J.; Wilson, A. K., Basis-Set Convergence in Correlated Calculations on Ne, N_2, and H_2O. *Chem. Phys. Lett.* **1998,** *286*, 243-252.

48. Kállay, M.; Surján, P. R., Higher Excitations in Coupled-Cluster Theory. *J. Chem. Phys.* **2001,** *115* (7), 2945-2954.

49. Kállay, M.; Gauss, J., Approximate Treatment of Higher Excitations in Coupled-Cluster Theory. *J. Chem. Phys.* **2005,** *123* (21), 214105.

50. Sherwood, C. R.; Hanold, K. A.; Garner, M. C.; Strong, K. M.; Continetti, R. E., Translational Spectroscopy Studies of the Photodissociation Dynamics of O_4^-. *J. Chem. Phys.* **1996,** *105* (24), 10803-10811.

51. Li, J.; Guo, H., Quasi-classical Trajectory Study of F + H_2O → HF + OH Reaction: Influence of Barrier Height, Reactant Rotational Excitation, and Isotopic Substitution. *Chin. J. Chem. Phys.* **2013,** *26*, 627-634.

52. Westermann, T.; Eisfeld, W.; Manthe, U., Coupled Potential Energy Surface for the $F(^2P)$ + CH_4 → HF + CH_3 Entrance Channel and Quantum Dynamics of the CH_4-F^- Photodetachment. *J. Chem. Phys.* **2013,** *139*, 014309.

53. Westermann, T.; Kim, J. B.; Weichman, M. L.; Hock, C.; Yacovitch, T. I.; Palma, J.; Neumark, D. M.; Manthe, U., Resonances in the Entrance Channel of the Elementary Reaction of Fluorine and Methane. *Angew. Chem. Int. Ed.* **2014,** *53*, 1122-1126.

54. Schapers, D.; Manthe, U., Quasi-Bound States of the F·CH_4 Complex. *J. Phys. Chem. A* **2016,** *120*, 3186-3195.

55. Yacovitch, T. I.; Garand, E.; Kim, J. B.; Hock, C.; Theis, T.; Neumark, D. M., Vibrationally Resolved Transition State Spectroscopy of the F + H_2 and F + CH_4 Reactions. *Faraday Discuss.* **2012,** *157* (0), 399-414.